Impacts of gateways and climate on regional hydrology and carbon cycle processes: A view from the Miocene sediments of Malta.

Ray Zammit

School of Earth and Environmental Sciences

Cardiff University

Thesis submitted in partial fulfilment of the requirements for the degree of

Doctor of Philosophy

October 2022

BLANK PAGE

Abstract

The Miocene represents a key interval in the transition to our modern bipolar icehouse world. The early Miocene climate (23.0 Ma to 19.2 Ma) was typified by a cool-arid climate with large swings in global benthic $\delta^{18}O$ records. This climate regime changed to a gradually warming trend (19.2 Ma to 17.0 Ma) until it was replaced by the relative warmth of the Miocene Climatic Optimum from 17.0 Ma to 14.7 Ma. Climate subsequently cooled in a step-wise manner, with a major expansion of the Antarctic ice sheet occurring at 13.8 Ma. In addition to these climatic shifts, a major change in oceanic circulation also occurred during the Miocene. This was due to the restriction of water flow through the Mesopotamian Seaway that connected the Mediterranean with the Indian Ocean. This flow restriction occurred in two steps, one during the early Miocene (19.0 to 20.2 Ma) and the second and complete disconnection between 13.8 Ma and 13.6 Ma. The Miocene deposits of Malta are temporally and spatially ideally situated to investigate local and global paleoenvironmental changes during the Miocene.

Lithological and geochemical changes from the Early Miocene il-Blata section outcropping in Malta indicate a regional shift from a cold arid climate to a warm humid climate following the first Miocene restriction of the Mesopotamian Seaway. A marked shift in sedimentation rate at ~19.1 Ma coincident with a change to organic-rich clays and changes in bulk $CaCO_3$, Sr/Ca, K/Al, Ti/Al, Zr/Al and Si/Ti support this interpretation. The closure of the Mesopotamian Seaway and consequent diversion of warm intermediate waters into the Atlantic Ocean is a plausible mechanism for the intensification of the hydrological cycle over North Africa. This transition to a humid regime and associated influence of terrigenous sediment delivery likely helped in the termination of the extensive Early Miocene phosphorites of Malta.

Planktic and benthic foraminiferal geochemical records from the Ras il-Pellegrin section (Malta) indicate changes in regional hydroclimate following the Middle Miocene expansion of the Antarctic ice sheet at 13.82 Ma. Foraminiferal Mg/Ca was used to generate temperature records, which enabled the generation of surface and bottom seawater $\delta^{18}O$, and in turn an estimate of sea surface salinity variability. These records show that a significant input of freshwater occurred following the Middle Miocene expansion of the Antarctic icesheet and the closure of the Mesopotamian Seaway.

The input of freshwater is precession and obliquity driven and indicates that a strong seasonal, monsoonal type climate was emplaced over North Africa.

A new planktic foraminiferal B/Ca record was used with previously published $\delta^{13}C$ records from the composite Marsalforn (Gozo Island) and Ras il-Pellegrin sections to investigate carbon cycle dynamics in the Central Mediterranean from 14.4 Ma to 12.8 Ma. The vertical seawater $\delta^{13}C$ gradient coupled with B/Ca, Mn/Ca, and calculated $[B(OH)_4^-]/[DIC]$, indicates a highly active biological pump following the Antarctic ice sheet expansion at 13.82 Ma and coinciding with the global CM-6 $\delta^{13}C$ excursion. These records also cast doubt on the interpretation of the pCO_2 records from Malta published in Badger et al. (2013), and suggests that low latitude shallow water zones are particularly important in carbon cycle dynamics as zones of enhanced carbon burial.

Overall, this thesis highlights the importance of the tectonic closure of the Mesopotamian Seaway on regional climate, with possible effects on global climate and cryospheric feedbacks. It confirms the Maltese Islands as a natural laboratory for investigating the Miocene climate. This thesis also underlines the importance of considering the Miocene as a geological time suitable for investigating global environments and climate feedbacks at near-future pCO_2 levels.

Acknowledgements

First and foremost, I would like to thank my main supervisor Carrie Lear who from the onset of this study was always encouraging and supportive. Your perseverance and infectious sense of optimism has ensured that this project flowed smoothly through some really testing times. I would also wish to thank you for your exemplary work ethic and unparalleled eye for detail which have ensured that the work presented here and published in peer review is of the utmost scientific quality. If I could point out just one thing that I learned from working with you is the need to strive for excellence in written work.

I am greatly indebted to Or Bialik for many great discussions, fieldwork, fruitful collaborations and for being a true friend. Your passion for science and dedication to the work is truly remarkable.

I would also like to extend my gratitude to the fantastic scientists who helped in this thesis and with whom I published my first main author paper. It has been a privilege and a great learning experience working with you. Paul Pearson, Elias Samankassou, Aaron Micallef and Lucas Lourens, I can only hope to have such fine co-authors as yourselves in my future work.

Extended gratitude goes to the hard-working staff at The School of Earth and Environmental Sciences, Cardiff University without whom this thesis would have been impossible. Sandra Nederbragt for generating all stable isotope records and for many useful discussions and guidance. Iain Macdonald is thanked for many hours of guidance and technical support in generating element data. Amy Thomas-Sparkes is thanked for instruction in using the Clean Lab, and for generating some of the foraminifera trace element data. Gratitude also goes to Anabel Morte-Rodenas, Sophie Slater and Matthew Dumont for analysing trace metal samples on the mass spectrometer.

Finally, I need to send a big hug to my wife Allison for always being supportive throughout these seven years of PhD study. Many times, you took upon yourself all house and parenting duties while I was away on fieldwork, lab. work, conferences and while I was writing this thesis. During this time, we have seen our two children Adelia and Alexander grow from toddlers to cool kids. I wish that my time away from them is compensated by a sense of inspiration and passion for science which I hope to have inspired in them by this work. As the first person from a large extended family to ever attend a University (let alone do a PhD) this means a lot to me. They are the future from whom we are borrowing this beautiful planet, I dedicate this thesis to them in the hope that they grow as adults with a sense of duty and care towards our Planet.

List of abbreviations

AAC	Antarctic Circumpolar Current
AMOC	Atlantic Meridional Overturing Circulation
BCfm	Blue Clay formation
BWT	Bottom Water Temperature
CM	Carbon Maximum event
CenoGRID	Cenozoic Global Reference benthic foraminifer carbon and oxygen Isotope Dataset
CRI	Clay-Rich Interval
DIC	Dissolved Inorganic Carbon
DSDP	Deep Sea Drilling Project
GLfm	Globigerina Limestone formation
GSSP	Global Boundary Stratotype Section and Point
ITCZ	Intertropical Convergence Zone
LIP	Large Igneous Province
LGLm	Lower Globigerina Limestone member
MCIE	Monterey Carbon Isotope Excursion
MCO	Miocene Climatic Optimum
MGLm	Middle Globigerina Limestone member
MMCT	Middle Miocene Climate Transition
MRSF	Marsalforn Section (Malta)
MSR-1	Mesopotamian Seaway Restriction 1
MSR-2	Mesopotamian Seaway Restriction 2
ODP	Ocean Drilling Project

OMT	Oligocene-Miocene Transition
pCO_2	Atmospheric partial pressure of carbon dioxide
PSU	Practical Salinity Units
RIP	Ras il-Pellegrin Section (Malta)
SEM	Scanning Electron Microscope
SSS	Sea Surface Salinity
SST	Sea Surface Temperature
TB	Transition Bed between the Globigerina Limestone Formation and the Blue Clay Formation (Malta)
TISW	Tethyan Intermediate Seawater
UGLm	Upper Globigerina Limestone member
WAM	West African Monsoon

Contents

Research statement:

Chapter 3 in this thesis has been published in its entirety as:

> Zammit, R., Lear, C. H., Samankassou, E., Lourens, L. J., Micallef, A., Pearson, P. N., & Bialik, O. M. (2022). Early Miocene Intensification of the North African Hydrological Cycle: Multi-Proxy Evidence From the Shelf Carbonates of Malta. *Paleoceanography and Paleoclimatology*, *37*(9). https://doi.org/10.1029/2022PA004414

While working on this thesis I have contributed to the following research which has been published in peer-review articles. Results from these works are cited where necessary.

> Bialik, O. M., Frank, M., Betzler, C., Zammit, R., & Waldmann, N. D. (2019). Two-step closure of the Miocene Indian Ocean Gateway to the Mediterranean. *Scientific Reports*, *9*(1), 8842. https://doi.org/10.1038/s41598-019-45308-7

> Bialik, O. M., Zammit, R. and Micallef, A. (2021) Architecture and sequence stratigraphy of the Upper Coralline Limestone formation, Malta—Implications for Eastern Mediterranean restriction prior to the Messinian Salinity Crisis, *The Depositional Record*. John Wiley & Sons, Ltd, 7(2), pp. 256–270. doi: 10.1002/DEP2.138.

Funding:

This work was partly funded by the ENDEAVOUR Scholarships Scheme (Group B) National Funds Malta. And partly funded by Cardiff University Match Funding scheme.

"There are no stories without a meaning. And I am one of those men who can find it even when others fail to see it. Afterwards the story becomes the book of the living, like a blaring trumpet that raises from the tomb those who have been dust for centuries ….. Still it takes time, you have to consider the events, arrange them in order, find the connections, even the least visible ones."

Niketas Choniates

Umberto Eco 'Baudolino'

Chapter 1

Introduction

Chapter 1 – Introduction

1.1 The Cenozoic – From Greenhouse to Icehouse

The Cenozoic Era (66 Ma to present) represents a geological interval during which global climate switched from a Greenhouse to an Icehouse (Thomas, 2008; Westerhold et al., 2020; Zachos et al., 2001). The Cenozoic follows the Cretaceous-Paleogene (K/Pg) mass extinction event that was induced by an extra-terrestrial impact (Alvarez et al., 1980). The Cenozoic Era is divided into three periods, the Paleogene (66.0 Ma to 23.03 Ma), the Neogene (23.03 Ma to 2.58 Ma) and the Quaternary (2.58 Ma to present) (Figure 1.1) (Gradstein et al., 2020).

During the early Paleogene the poles lacked ice sheets, and significant hyperthermal events are recorded in the deep sea-record, including the Paleocene-Eocene Thermal Maximum (PETM) (Thomas, 2008; Westerhold et al., 2020). These hyperthermal events are associated with large negative excursions in foraminiferal $\delta^{13}C$ and $\delta^{18}O$ records and have been associated with the release of vast amounts of greenhouse gases over a geologically short timeframe (Figure 1.1) (Cohen et al., 2007). Following the Early Eocene Climatic Optimum (EECO) (~53 Ma to ~49 Ma), global climate started to follow a generally cooling trend that typifies the general long term trend of the Cenozoic (Zachos et al., 2001).

Punctuated over the long-term Cenozoic cooling trend are episodes of abrupt climate change generally associated with expansion of the Antarctic Ice Sheet and global cooling detected as positive excursions in the deep sea $\delta^{18}O$ record (Westerhold et al., 2020). The main episodes of Antarctic Ice sheet expansion are the glaciation at the Eocene-Oligocene boundary (EOT – Eocene-Oligocene transition, Oi-1 oxygen isotope excursion), the transient glaciation at the Oligocene-Miocene boundary (OMT – Oligocene-Miocene transition, Mi-1 oxygen isotope excursion) and the glaciation at the Langhian-Serravallian boundary (MMCT- Mid-Miocene Climate transition, Mi-3b oxygen isotope excursion) (Miller et al., 1991; Zachos et al., 2001). Both the glaciation at the EOT and the OMT represent the emplacement of a full-scale ice sheet over

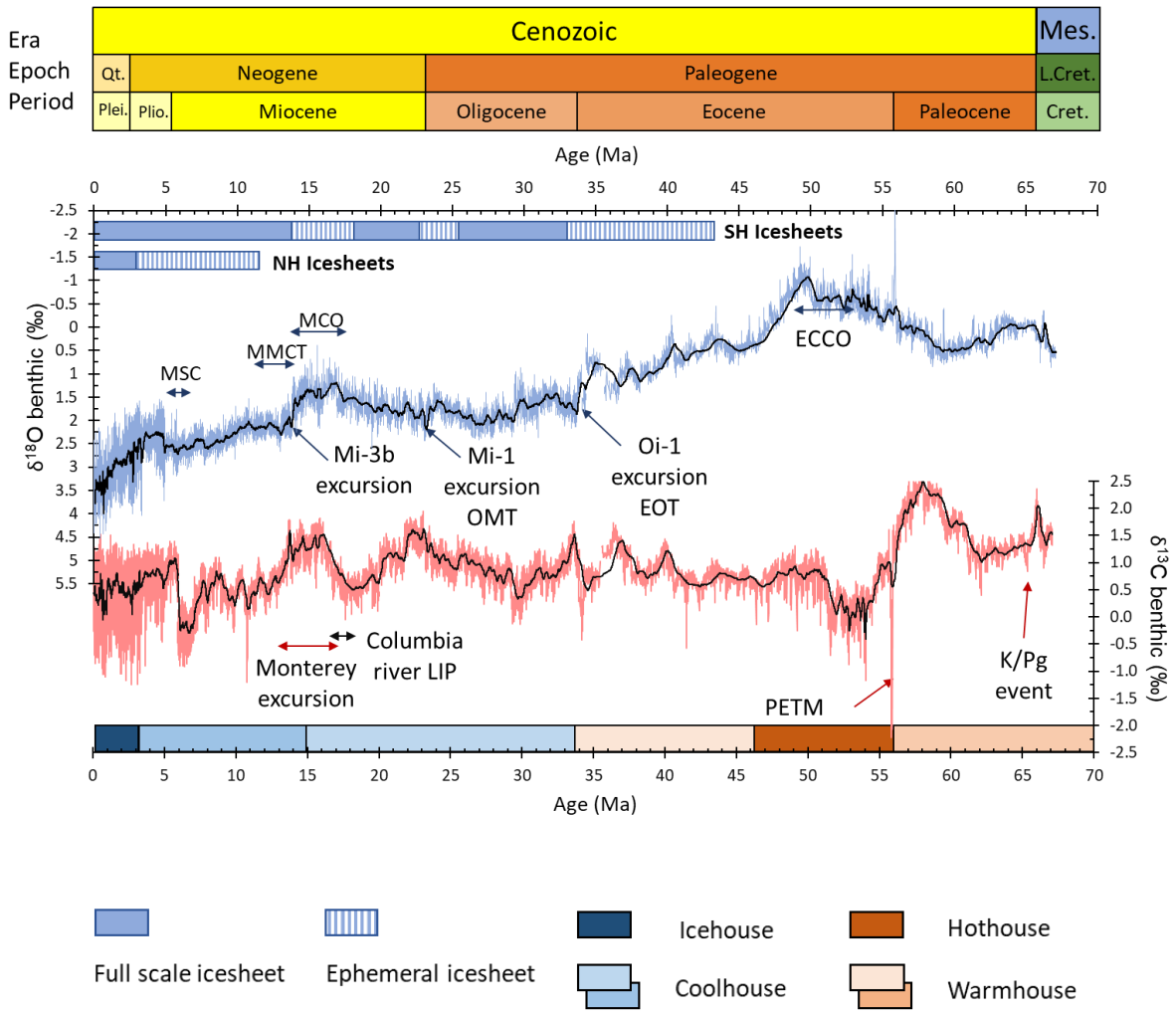

Figure 1.1 Global benthic stable isotope $\delta^{18}O$ (blue) and $\delta^{13}C$ (red) compilation for the Cenozoic (Westerhold et al., 2020). Southern Hemisphere (SH) ice sheets first appear during the Eocene and become full scale features during the Eocene-Oligocene Transition (EOT). The second Cenozoic temporary large-scale glaciation coincided with the Oligocene-Miocene Transition (OMT). Retreat of SH ice sheets occurs during the Late Oligocene and the Miocene Climatic Optimum (MCO) with full and permanent ice cover over Antarctica from the Middle Miocene Climate Transition (MMCT). Northern Hemisphere (NH) permanent ice cover starts during the Pliocene. Abbreviations: Mes – Mesozoic, L.Cret – Late Cretaceous, Cret.- Cretaceous, Qt- Quaternary, Plio-Pliocene, Plei-Pleistocene.

Antarctica, however these conditions changed to ephemeral ice cover occurring during the Late Oligocene and the Middle Miocene (Figure 1.1) (Thomas, 2008). Permanent Southern Hemisphere glaciation occurred during the Middle Miocene Climatic Transition (MMCT), from 13.8 Ma and persists till the present day. Therefore, the Miocene epoch represents an important time in the understanding of the evolution of climate and cryosphere when atmospheric pCO_2 was at times similar to near future predictions (Steinthorsdottir et al., 2020).

1.2 The Miocene – A natural laboratory for near future climate scenarios

The Miocene represents a lengthy and highly varied geological interval spanning around 18 million years during which global climate varied significantly. The base of the Miocene is the base of the Aquitanian stage (23.03 Ma) for which the GSSP is found at Lemme-Carrosio in North West Italy (Steininger et al., 1997). The base of the Miocene also coincidences with the boundary between the Paleogene and the Neogene and is coincident with a positive excursion in the global benthic $\delta^{18}O$ record at the Oligocene-Miocene transition. This excursion is associated with a large scale increase in Antarctic Ice volume and subsequent retreat (Mawbey & Lear, 2013). This excursion is the first of a number of positive oxygen-isotope excursions during the early Miocene (Aquitanian to early Burdigalian stage), with the last of these early Miocene excursions peaking at around 19.2 Ma (Westerhold et al., 2020).

The earliest Burdigalian (~20 Ma to ~18 Ma) is a poorly investigated interval during the Miocene, which has not attracted a lot of attention since there seems to be no major climatic event during this time. However, it has recently been shown that significant restriction of water flow through the Mesopotamian Seaway that connected the Indo-Pacific realm to the Mediterranean and Atlantic realms (Figure 1.2) occurred during this interval (Bialik et al., 2019). Restriction of the Mesopotamian Seaway occurred in two distinct steps, one during the Early Miocene (~20 Ma) here termed Mesopotamian Seaway Restriction-1 (MSR-1) and a final and complete disconnection around the MMCT (~14 Ma), here termed Mesopotamian Seaway Restriction-2 (MSR-2) (Bialik et al., 2019). A major shark extinction event has also been recorded around this time, suggesting the possibility of a yet unknown major oceanic perturbation at the time (Sibert and Rubin, 2021).

A gentle warming trend is observed in the benthic $\delta^{18}O$ records from around 18.5 Ma (Westerhold et al., 2020) preceding the emplacement of the Columbia River Large Igneous Provence (LIP) which occurred from 16.7 Ma to 15.9 Ma (Kasbohm & Schoene, 2018). The eruption of the Columbia River Basalts and the ensuing release of CO_2 into the atmosphere is seen as a primary driver for the for the exceptionally warm interval known as the Miocene Climatic Optimum (MCO) (Sosdian et al., 2020). This warm interval is also associated with the Monterey Carbon Isotope Excursion (MCIE), an extended positive excursion in the $\delta^{13}C$ record (Vincent & Berger, 1985). The MCO is terminated by the Middle Miocene Climate Transition (MMCT). This is a phase of step-wise increases in $\delta^{18}O$ in the global benthic records and is associated with the permanent, large-scale expansion of the Antarctic Ice sheet (Holbourn et al., 2013). The Mesopotamian Gateway connecting the Indo-Pacific realm with the proto-Mediterranean also closes permanently around this time (MSR-2) (Bialik et al., 2019). Towards the end of the Miocene (5.59 Ma to 5.50 Ma) an extreme climatic event occurs when the Mediterranean basin underwent wholesale desiccation, an event known as the Messinian Salinity Crisis (MSC) (Krijgsman et al., 1999). The MSC was triggered by a combination of tectonic closure of the Atlantic Gateway and periods of low insolation and general dryness over the Mediterranean region (Krijgsman et al., 1999).

Although the continental configuration was different during the early parts of the Miocene, the closure of Mesopotamian Seaway during the Middle Miocene represents a turning point in global tectonic history. Low latitude circum-global circulation had been a feature of ocean circulation since ~ 100 Ma (Barron & Peterson, 1989) and the closure of the Mesopotamian Seaway during the Miocene terminated this long-standing system (Bialik et al., 2019). Therefore, it is during the Miocene that the circulation patterns similar to the modern world were facilitated by this new continental configuration. Another important feature of Miocene climate is that atmospheric pCO_2 levels during parts of the Miocene are similar to near future predictions. This makes the Miocene ideal as a natural laboratory to test near future climate predictions in the context of anthropogenic global warming (Steinthorsdottir et al., 2020).

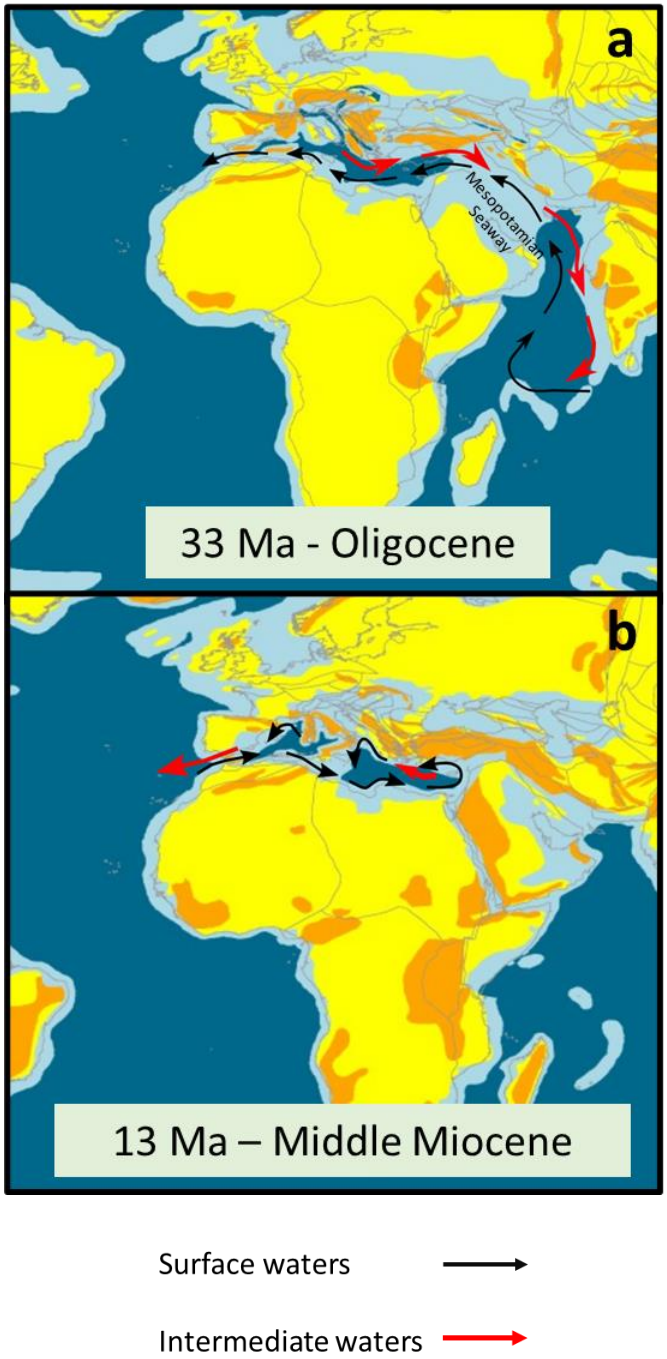

Figure 1.2 Low latitude water flows during the Oligocene (a) and following the MMCT (b). The longstanding open Mesopotamian Seaway resulted in a generally E-W low latitude flow of surface waters and a transfer of saline intermediate waters into the Indian Ocean. The closure of the Mesopotamian Seaway during the Miocene resulted in the cessation of the low latitude surface E-W flow and the advection of intermediate saline waters into the Atlantic. Palaeomaps adapted from (Cao et al., 2017, Bialik et.al., 2019)

1.3 The pelagic to hemi-pelagic deposits of the Maltese Islands

The Maltese Islands (Central Mediterranean) consist of marine deposits that formed during the Late Oligocene and throughout the Miocene (Figure 1.2, 1.3). Their location is ideal for investigating oceanographic changes in the Tethys Seaway during this time of changing gateway configuration (Bialik et al., 2019; Kocsis et al., 2008). Their position close to North Africa also makes them suitable for investigating hydrological changes over the continent in response to climate change (John et al., 2003).

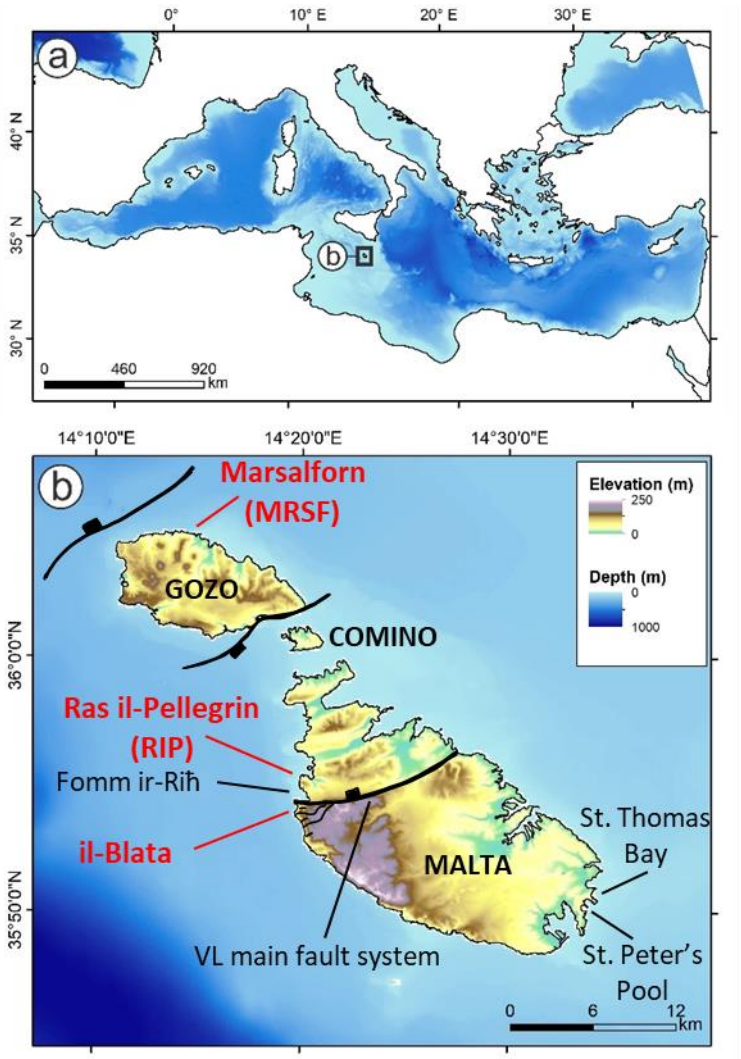

Figure 1.3 (a) The Central Mediterranean Islands of Malta lie on the northernmost part of the African Plate. The geology of the Islands consists of mixed-carbonate siliciclastic marine sediments deposited under varying sea-level regimes. The il-Blata, Ras il-Pellegrin (RIP) and Marsalforn (MRSF) sections have been investigated during this study.

The Oligo-Miocene sedimentary deposits exposed above sea-level consist of shallow water carbonates and deeper water units of mixed carbonate-siliciclastic nature (Figure 1.4) (Baldassini & Di Stefano, 2017; Föllmi et al., 2008; Gatt & Gluyas, 2012; Pedley & Bennett, 1985). The general stratigraphy is rather simple with shallow water units at the base and the top of the sequence and deeper water units in between. These have been lithostratigraphically (Figure 1.4) divided into five formations and, from oldest to youngest consist of:

1. The Lower Coralline Limestone Formation (LCLfm). This formation consists of shallow water carbonate deposits of Late Oligocene age. The base of the formation exposed above sea-level is approximately 28 Myr (Gatt & Gluyas, 2012).

2. The Globigerina Limestone Formation (GLfm). This formation represents deposition in a deeper water environment and is classically subdivided into three lithostratigraphic members (Pedley et al., 1976). The Lower Globigerina Limestone member (LGLm), the Middle Globigerina Limestone member (MGLm) and the Upper Globigerina Limestone member (UGLm). Separating each member are well-developed condensed beds (C_1 and C_2) containing autochthonous and allochthonous phosphorite material (Pedley & Bennett, 1985). This formation was deposited between the Late Oligocene and the Middle Miocene (Baldassini & Di Stefano, 2015).

3. The marly Blue Clay Formation (BCfm) is poor in carbonate content and consists of alternate bands of pale and dark grey marls deposited at a depth of around 500 m (Abels et al., 2005; Bellanca et al., 2002). The banding reflects the varying carbonate content. The transition bed between this formation and the underlying GLfm hosts the base Serravallian (13.82 Ma) (GSSP) (Hilgen et al., 2009).

4. The very thin Greensand Formation (GSfm) consists of poorly cemented glauconitic limestones associated with significant, rapid shallowing of the carbonate platform (Pedley et al., 1976, 1978).

5. The succession is capped by the shallow water units pertaining to the Upper Coralline Limestone Formation (UCLfm). This formation represents carbonate sediment deposited in very shallow waters and includes two episodes of emergence of the carbonate platform above sea level prior to the Messinian Salinity Crisis (Bialik et al., 2021)

These sedimentary deposits have been shown to respond well to climatic and hydrologic changes during the Oligocene and the Miocene (Abels et al., 2005; Gatt & Gluyas, 2012; Jacobs et al., 1996; John et al., 2003). The pelagic to hemi-pelagic units in particular have garnered significant interest for several reasons. Jacobs et al., (1996) demonstrated that the GLfm and the BCfm hold a geochemical record of the MCIE in the Mediterranean thus identifying a carbon cycle response to the Monterey Event in the Mediterranean. The response of these deposits to hydroclimate over North Africa was demonstrated by analysing mineralogical changes within these units (John et al., 2003). It was shown that sedimentology and minerology over Malta can be used to identify changes in hydrological regime over North Africa during the Middle Miocene (John et al., 2003). Bulk carbonate stable oxygen isotope and K/Ca records from the Ras il-Pellegrin Section allowed for the identification of the main step in the MMCT in the transition bed between the GLfm and the BCfm correlatable with the global Mi-3b oxygen isotope excursion (Figure 1.1) (Abels et al., 2005). This led to the proposal and eventual ratification of the GSSP for the Serravallian to be placed in the transition bed between the GLfm and the BCfm at the Ras il-Pellegrin Section in Malta (Hilgen et al., 2009). Using both planktic and benthic foraminiferal specimens from the UGLm (Marsalforn Section (MRSF)) and the BCfm (Ras il-Pellegrin Section (RIP)), Mourik et al., (2011) were able to produce a detailed astronomically-tuned stable isotope stratigraphy for the Middle Miocene deposits of Malta. It has been suggested that increased river run-off occurred at the onset of the BCfm indicating a strong continental influence on the depositional environment over Malta during the MMCT (Bellanca et al., 2002; Mourik et al., 2011). Using exceptionally well-preserved foraminifera from the Ras il-Pellegrin section, Badger et al., (2013) determined a record of atmospheric CO_2 during the final stage of the MCIE. Detailed nannofossil stratigraphy has allowed for these pelagic to hemi-pelagic units to be compared with

open ocean stable isotope records and allow for precise correlation of the sedimentary units with global Miocene isotopic excursions (Baldassini & Di Stefano, 2015, 2017).

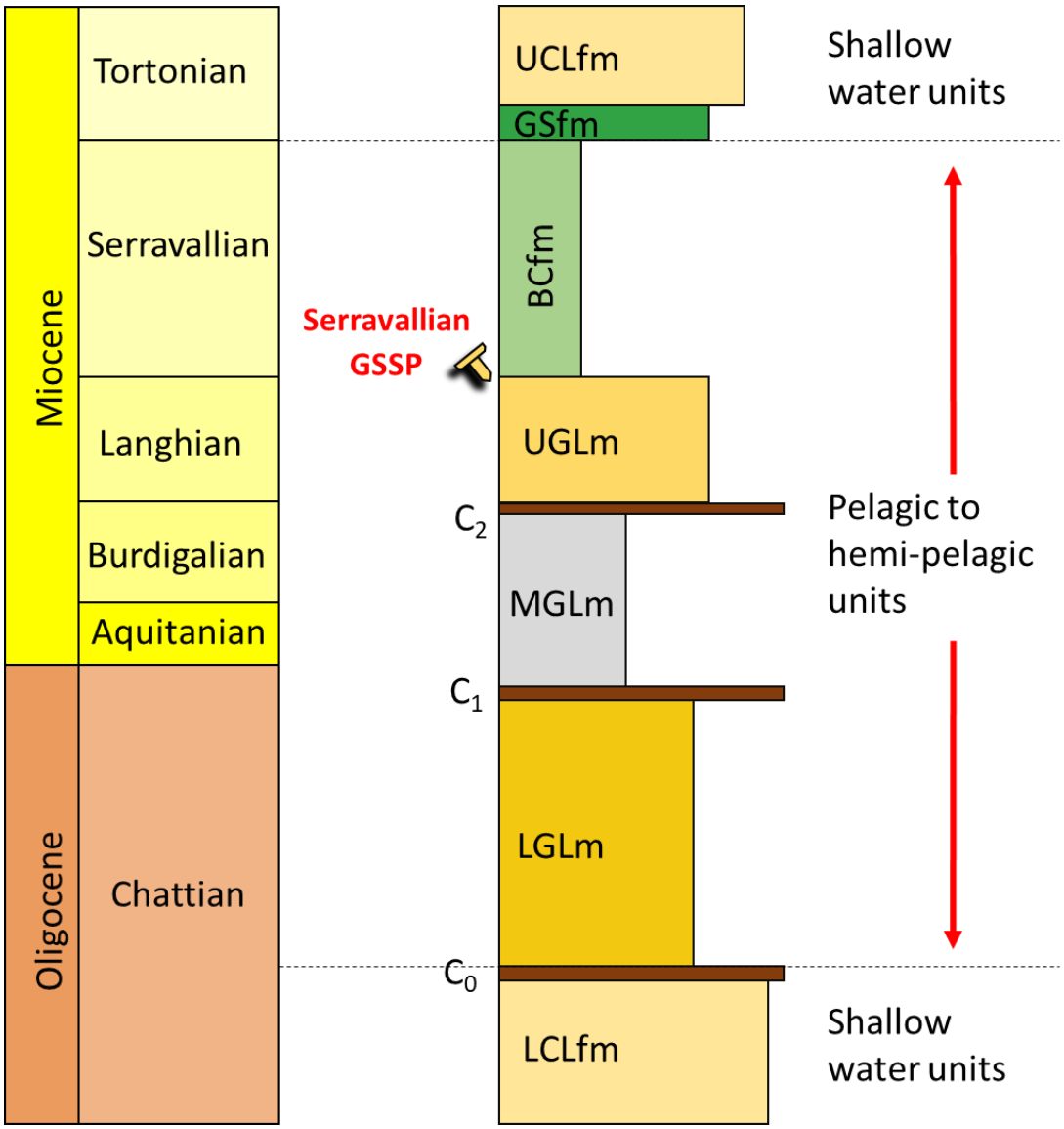

Figure 1.4 General stratigraphy of the Maltese sedimentary deposits. The Lower Coralline Limestone Formation (LCLfm), the Greensand Formation (GSfm) and the Upper Coralline Limestone Formation (UCLfm) represent shallow water carbonates while the three members of Globigerina Limestone Formation: Lower Globigerina Limestone member (LGLm), Middle Globigerina Limestone member (MGLm), Upper Globigerina Limestone member (UGLm) and the Blue Clay Formation (BCfm) represent pelagic to hemi-pelagic units. C_0 represents a phosphatic hardground that is not present at all locations while C_1 and C_2 consist of ubiquitous condensed beds containing phosphatic material including gravity flow clasts and hardgrounds. The base Serravallian GSSP is set at the RIP section in the transition bed between the Globigerina Limestone Formation and the Blue Clay Formation.

1.4 Aims and objectives and thesis outline

This study aims to refine current knowledge of climate and carbon cycle dynamics during the Miocene by utilising the mixed carbonate-siliciclastic deposits from the Maltese Islands. The general methodology employed is described in Chapter 2 with specific methodology presented in chapters 3, 4 and 5 as required.

The research questions being addressed are:

i. What is the temporal correlation between the phosphorite-bearing Early Miocene deposits from the il-Blata section and the global stable isotope records?
ii. What is the influence of climate and/or the restriction of the Mesopotamian Gateway on the hydrological regime of North Africa during the Early and Middle Miocene?
iii. Is there a relationship between surface salinity and continental run-off during the MMCT associated with the permanent closure of the Mesopotamian Seaway?
iv. Is there a relationship between changes in the regional hydrologic regime and the carbon cycle?

To address these questions, the following objectives have been set and achieved:

i. Produce a detailed lithostratigraphy and a new age model for the il-Blata section.
ii. Utilise a multiproxy approach (lithostratigraphy and geochemistry) to identify hydrological changes in the il-Blata records and correlate these with the MSR-1 event. Use planktic and benthic foraminifera from the RIP section to produce a Mg/Ca surface and bottom water temperature record for the Middle Miocene.
iii. Use the Mg/Ca temperature records in conjunction with foraminiferal $\delta^{18}O$ records from the RIP section to produce surface and bottom seawater $\delta^{18}O$ and surface salinity record for the Middle Miocene.
iv. Produce foraminiferal B/Ca, Mn/Ca and stable carbon isotopes from the MRSF and the RIP section and use these to discuss carbon cycle dynamics in the Central Mediterranean during the MMCT.

The influence of global climate and tectonic forcing on regional hydrology in the Central proto-Mediterranean during the Early Miocene is investigated in Chapter 3. Detailed lithostratigraphy, together with a new $^{87}Sr/^{86}Sr$ age model for the il-Blata section outcropping in SW Malta is utilised in conjunction with bulk stable isotope records and major element ratios. These records are used to identify changes in hydrological regime over western North Africa during the Early Miocene (~23 Ma to ~18 Ma). The newly produced age model allows for correlation between the stratigraphy of the il-Blata section and the MSR-1 event allowing discussion into possible mechanisms relating a hydrological shift in North Africa with changes in ocean circulation induced by the MSR-1 event. The formation and demise of the Early Miocene phosphorite beds over Malta is also discussed in relation to hydrological and ocean circulation changes in the Central Mediterranean. The chapter presented here was published as a peer-reviewed journal article in Palaeoceanography and Paleoclimatology on the 13th September 2022 (Zammit et al., 2022).

In Chapter 4, well preserved benthic and planktic foraminifera from the RIP section are used to generate bottom water and surface water Mg/Ca temperature records for the interval following the Mi-3b oxygen isotope excursion. A new age model that does not assume astronomical tuning for the Middle Miocene deposits of Malta is presented. New and previously published (Mourik et al., 2011) stable oxygen isotope records are used to produce a sea surface salinity record which demonstrates the influence of western North African river systems on the Central Mediterranean following the Middle Miocene permanent expansion of the Antarctic Ice Sheet. Spectral analysis is used to identify dominant orbital cycles on the hydrological activity over North Africa and link this to monsoonal activity in the region.

Regional carbon cycle changes are investigated in Chapter 5 by making use of foraminiferal B/Ca, Mn/Ca and stable carbon isotopes from the MRSF and RIP sections. The records suggest major changes in local export productivity associated with the changes in regional hydrology. The records from Malta are compared with records from the Indian Ocean (ODP 761) and allow for a new interpretation of the Malta pCO_2 record published in Badger et al., (2013), with implications for our

understanding of feedbacks in the carbon cycles associated with major global climate change.

Synthesis of the main findings of this study together with suggestions for future work is presented in chapter 6.

‘

Chapter 2

Materials and Methods

Chapter 2 – Materials and Methods

2.1 Study Site – The Maltese Islands

The central Mediterranean archipelago of Malta consists of two main islands and a number of small islets. The main islands of Malta and Gozo host a number of Late Oligocene and Miocene outcrops of mixed carbonate and siliciclastic sediment. These outcrops have been shown to provide an ideal site for testing ideas related to the palaeoclimate and palaeoceanography of the Oligocene and the Miocene. The main reasons for this are (i) the islands rest on an isolated carbonate platform away from continental volcanic influence, (ii) the clay rich intervals host exceptionally well preserved foraminifera, (iii) ease of accessibility of sites, (iv) Early Miocene sites in the Mediterranean are extremely rare.

2.1.1 The outcrops: Il-Blata, Marsalforn and Ras il-Pellegrin

Three different outcrops in Malta and Gozo were selected for this study (Figure 1.3). The oldest of the three is the il-Blata outcrop, which lies along the southwestern coast of Malta. The section is exposed along a slope (base at 35.9004˚N, 14.3309˚E, top at 35.9000˚N, 14.3314˚E) and is almost identical to the section described by Baldassini and DiStefano (2015). It comprises around 40 m of exposed marine rocks of Late Oligocene to Early Miocene age. The studied lithology pertains to the Globigerina Limestone Formation, in particular to the Lower Globigerina Limestone member and the Middle Globigerina Limestone member.

The Marsalforn (MRSF) section is exposed along the northern coast of the island of Gozo (36.072662˚N, 14.265167˚E). Sampling was carried out in previous expeditions (Mourik et al., 2011). The Upper Globigerina Limestone member as well as the Blue Clay Formation are exposed at this site.

The youngest outcrop considered in this study is the Ras il-Pellegrin (RIP) outcrop. This lies at the headland of Fomm ir-Riħ bay along the south west coast of Malta (35.914355˚N, 14.335691˚E). The Ras il-Pellegrin site was sampled in previous studies (Abels et al., 2005; Badger et al., 2013; Mourik et al., 2011). The upper part

of the Globigerina Limestone Formation and the entirety of the Blue Clay Formation is exposed here.

2.1.2 Field work and sampling

Numerous field expeditions between 2016 and 2019 were conducted at the il-Blata site in order to produce a detailed lithostratigraphy and collect samples for analysis. No sampling and field work was conducted at MRSF and RIP during this study since samples collected by Badger et al., (2013) archived at Cardiff University and samples collected Mourik et al, (2011) archived University of Utrecht were used for foraminiferal picking. During the il-Blata field work, ~40 m of outcrop pertaining to the Lower and Middle Globigerina Limestone members was logged at high resolution. During sampling the first few cm of the oxidised surface was removed using a combination of traditional geological hammer and battery-operated hammer-drill. Approximately 20 g of sample was collected, wrapped in aluminium foil, and placed in labelled plastic bags. Sampling intervals varied throughout the section ranging from one sample every 10 cm to one sample every 50 cm depending on the accessibility of the outcrop. In total, 142 samples were collected from the il-Blata section.

2.2 Laboratory methods

2.2.1 Bulk rock analysis

About 10g of each il-Blata sample was powdered and homogenized using a pestle and mortar. These powders were dried overnight at 40°C and stored in glass vials. The powders were eventually used to determine the following geochemical data: percentage carbonate content, bulk carbonate stable isotopes $\delta^{13}C$ and $\delta^{18}O$, bulk sediment major elemental composition and bulk carbonate radiogenic strontium isotope ratio $^{87}Sr/^{86}Sr$.

2.2.1.1 Calcimeter

The percentage carbonate of all samples was measured using a digital calcimeter. About 1 g of powdered, homogenised, and dry sample was weighed and transferred

into a 50 ml sample bottle. A clean, dry glass cuvette was filled with 6 M HCl, placed in the bottle, and connected to a FOGL digital calcimeter. The digital calcimeter was standardised using an in-house carbonate standard with average precision of 2 % (1 s.d.).

2.2.1.2 Stable isotope stratigraphy

Approximately 5g of bulk sediment material from all collected samples was crushed and homogenised using an agate pestle and mortar and dried for 24 hours at 40°C. Carbon and oxygen isotope ratios were measured on ~500 µg of this powder using a Gasbench II coupled to a Thermo Delta V Advantage isotope ratio mass spectrometer at the School of Earth and Environmental Sciences, Cardiff University. Results are expressed in ‰ in the δ-notation on the Vienna Pee Dee Belemnite (VPDB) scale. The long-term precision of an in-house carbonate standard is ≤0.06 ‰ (1 s.d.) for $\delta^{18}O$ and ≤0.05 ‰ for $\delta^{13}C$.

2.2.1.3 Major element analysis

A total of 114 samples of the crushed and dried samples were selected for major element analysis using X-ray florescence. Analysis was performed using a hand-held Olympus Delta Innov-X XRF gun at the School of Earth and Environmental Sciences, Cardiff University. The instrument was standardised using in-house carbonate and silica standards. The following ratios were calculated to act as palaeoproxies, Ti/Al, Zr/Al (aeolian fluxes), Sr/Ca (shelf export), K/Al (riverine fluxes), Si/Ti (biogenic silica production). In general, these metal ratios represent the influx of different minerals into the sedimentary system. The elements Ti and Zr are associated with the terrigenous input to the system and by normalizing these to Al allows to differentiate between the coarse (wind) and fine (riverine) terrestrial inputs (Govin et al., 2012). The source of K is usually the minerals illite and K-feldspar which are associated with dry, low chemical weathering times (Govin et al., 2012). Sr tends to be incorporated in marine sediment during the formation of aragonite that occurs in periplatform regions and the increase in Sr/Ca in pelagic deposits indicates an increase in delivery of periplatform material during times of sea-level rise (Bialik et al., 2020). Normalising Si with Ti (both of which are typically found in siliciclastic

component of sediment) allows for the identification biogenic sources of silica as opposed to lithogenic sources (Kylander et al., 2011). The [Ca] was used to indicate the marine component while the [S] indicates redox conditions. All X-ray fluorescence data are semi-quantitative. Detailed explanation of the rationale for utilizing these proxies is given in Chapter 3.

2.2.1.4 $^{87}Sr/^{86}Sr$ stratigraphy

The strontium isotope ratio $^{87}Sr/^{86}Sr$ of dissolved strontium in the world's oceans has changed over geological time and this allows for comparison of sedimentary $^{87}Sr/^{86}Sr$ with established calibration curves of $^{87}Sr/^{86}Sr$ -stratigraphy (McArthur et al., 2012). This method can be applied on marine carbonates with foraminiferal calcite and nannofossil ooze (McArthur et al., 2012). The pelagic to hemipelagic records from Malta consist of foraminiferal and nannofossil rich limestones and therefore bulk rock from these deposits combined with other dating methods (such as nannofossil biostratigraphy) can be used to determine age models for outcrops in Malta. Indeed, previous studies from Malta (Föllmi et al., 2008; Jacobs et al., 1996; Stille et al., 1996) have employed this methodology with variable degrees of success. The interpretation of the $^{87}Sr/^{86}Sr$ record can be complicated by the preferential leaching of Sr from silicates during chemical weathering and therefore the $^{87}Sr/^{86}Sr$ records should always be compared with other age models for the same site (eg. nannofossil biostratigraphy, stable isotope stratigraphy) to ensure a robust age model (McArthur et al., 2012).

A total of 16 samples were selected from the il-Blata succession for $^{87}Sr/^{86}Sr$ analysis. The samples were selected as close as possible to main sedimentary hiatuses as observed in the field to time constrain the different sedimentary packages. For each sample, 30 milligrams of powdered bulk sediment were dissolved in 2.2 M high-purity acetic acid for 1–2 hours at room temperature (22-24°C) in conical 2 ml vials. The solutions were centrifuged, and the supernatant was recovered and transferred to Teflon vials, where it was dried to a residue on a hot plate. The residue was re-dissolved in a few drops of 14 M HNO_3 and dried again prior to Sr separation from the matrix using Sr-Spec resin. The Sr separate was re-dissolved in 5 ml ~2% HNO_3 solution, and the ratios were measured using a Thermo

Neptune PLUS Multi-Collector inductively coupled plasma mass spectrometer in static mode at the University of Geneva. The $^{88}Sr/^{86}Sr$ ratio (8.375209) was used to monitor internal fractionation during the run. Interferences at masses 84 (^{84}Kr), 86 (^{86}Kr), and 87 (^{87}Rb) were corrected in-run by monitoring ^{83}Kr and ^{85}Rb. SRM987 standard was used to check external reproducibility, which, on the long term (more than 100 measurements in one year), had a reproducibility of 10 ppm. The internally corrected $^{87}Sr/^{86}Sr$ values were further corrected for external fractionation by a value of -0.025‰ per amu, because a systematic difference between measured and nominal standard ratios of the SRM987 of $^{87}Sr/^{86}Sr$ was 0.71024 (McArthur et al., 2001). The $^{87}Sr/^{86}Sr$ were converted into numerical ages using the LOWESS 5 fit (McArthur et al., 2012).

2.2.2 Microfossil analysis

About 10 g of sample from the Blata section was broken and placed in jars filled with deionized water and rotated on a vertical spinner for about 12 to 14 hours. Samples that remained strongly lithified following spinning were broken down mechanically by pestle and mortar and subsequently dried. All samples were dry sieved through a 355, 250, 100 and 63 µm sieve stack. Each sample from the 250 to 355 µm range was spread on a picking tray and observed through an optical microscope in order to determine the presence of foraminifera.

The dry samples from the Marsalforn and Ras il-Pellegrin sections were dry sieved through a standard stack. The 250 to 355 µm fraction was gently spread over a picking tray and three species of foraminifera were picked using fine paintbrushes. The species selected were the planktonic species *Trilobatus trilobus* and the two benthic species *Uvigerina spp*. and *Heterolepa dutemplei*. Specimens of *Trilobatus trilobus* and *Uvigerina spp.* (Figure 2.1) were prepared for trace metal analysis while specimens of *Trilobatus trilobus* and *Heterolepa dutemplei* were prepared for stable isotope analysis.

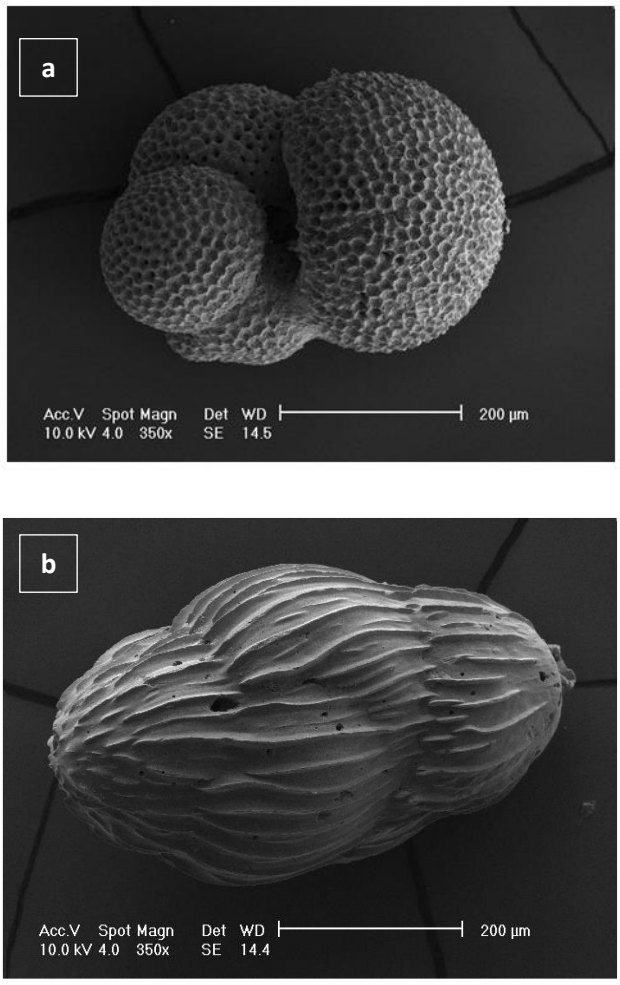

Figure 2.1 SEM images of foraminifera used for trace element analysis. (a) *Trilobatus trilobus*, (b) *Uvigerina* spp.

2.2.2.1 Foraminiferal stable isotope analysis

Stable isotope ($\delta^{18}O$ and $\delta^{13}C$) analysis was carried out on benthic and planktic specimens from the Ras il-Pellegrin section. This was carried out at the School of Earth and Environmental Sciences, Cardiff University. About 3 to 4 specimens of the benthic species *Heterolepadutemplei* were used while 5 to 7 specimens of the planktic species *Trilobatus trilobus*-(~ 88 to 120 µg) were utilized. Results were expressed in ‰ in the δ notation on the Vienna Pee Dee Belemnite (VPDB) scale. Analysis was carried out on MAT 253/Kiel IV carbonate device. Long term precision of in-house standard (BCT63) is ≤ 0.04 ‰ (1 s.d.) in $\delta^{18}O$ and ≤ 0.03 ‰ (1 s.d.) in $\delta^{13}C$.

2.2.2.2 Trace metal analysis

About 25 to 30 samples of the planktic species *T. trilobus* (~ 440 µg to 530 µg of total carbonate material) and 10 to 15 samples of *Uvigerina spp*. were first crushed in order to open the tests following the in-house modified method after Boyle & Keigwin (1985). The lab bench, microscope stage and sample box were thoroughly cleaned with D.I water (18 MΩ cm). Two glass slides were cleaned with D.I. water and acetone. One slide was set on the microscope stage while the other was set aside. A drop of D.I. water was placed on the slide resting on the microscope stage and 3 individual foraminiferal specimens were picked by fine paint brush and placed in the drop. The foraminifera were cracked open by pressing them between two clean slides. Foraminifera chambers were opened and inspected under light microscope. Infill material (clay, pyrite) was gently removed using a fine brush. Pristine foraminiferal fragments were set aside, dried using a dry brush and scooped into a labelled, acid-cleaned 500 µl centrifuge tube. This was repeated until sufficient material was collected for each sample. A total of 84 samples containing planktic foraminifera from the RIP section and 68 from the MRSF section were utilized. 34 samples containing benthic foraminifera from the RIP section were utilized.

The crushed foraminiferal samples were cleaned under clean laboratory conditions at The School of Earth and Environmental Sciences, Cardiff University, following the in-house modified method of Boyle & Keigwin (1985). The following cleaning steps were performed in order:

i. Removal of clays by ultrasonication in D.I. water (3 times), methanol (2 times), D.I. water (3 times). This whole step was performed six times in order to remove as much of the clay content as possible due to the clay-rich lithology of the RIP section and parts of the MRSF section.
ii. Organic removal phase by addition of a solution of 20 ml 0.1 N NaOH and 50 µl H_2O_2 to the samples. The samples were placed in a hot water bath for 5 min and the procedure was repeated three times.
iii. Dilute acid leaching step. 250 µl of 0.002 N HNO_3 was used. The samples in acid were subject to ultrasonication 3 times.

iv. The samples were rinsed in D.I. water, removing as much water as possible and stored.

The cleaned and dry samples were dissolved in 120 µl of ultra-pure 0.065 M HNO_3. The dissolution process was aided by placing each tube on a vortex mixer. The solutions were placed in an ultra-centrifuge and centrifuged at 30 000 rpm. An aliquot of 10 µl from the centrifuged solution was gently pipetted and placed in a clean centrifuge tube to be diluted and used for calcium analysis while an aliquot of 100 µl was pipetted and placed in a clean tube to be diluted and used for trace element analysis. Trace element and calcium analysis were carried out using a Thermo Element XR High Resolution – Inductively Coupled Plasma – Mass Spectrometer (HR-ICP-MS) at the Cardiff Earth Laboratory for Trace Element and Isotope Chemistry (CELTIC) at Cardiff University. Long-term precision for trace element to calcium ratios (rsd): Mg/Ca ≤ 1%, B/Ca ≤ 2%, Mn/Ca ≤ 1%, Sr/Ca ≤ 1%, Ba/Ca ≤ 4 %, Fe/Ca ≤ 4%, U/Ca ≤ 2%.

2.2.2.3 SEM images

Intact and crushed planktic (*T.trilobus*) and benthic (*Uvigerina* spp.) specimens from the RIP and MRSF sections were used to generate Scanning Electron Microscope (SEM) images. The fragments were cleaned with D.I. water and acetone using fine paint brushes in order to remove any infill material. Whole specimens and fragments were placed on SEM mounting stubs and held in place by carbon adhesive tape. Prior to imaging, the samples were coated with gold and palladium. Imaging was performed using a FEI XL 30 Field Emission Gun Environmental Scanning Electron Microscope in high vacuum mode with a beam voltage between 10 to 20 kV using a Secondary Electron Detector at the School of Earth and Environmental Sciences, Cardiff University.

2.3 Methodology contributions to this thesis

The following is a list of external contributions to the generation of data presented in this thesis.

i. All laboratory work associated with the generation of $^{87}Sr/^{86}Sr$ data set was performed by Elias Samakassou at the Department of Earth Sciences, University of Geneva.
ii. Field sampling and sediment washing for the RIP section was conducted during previous studies by Marcus P. Badger (Badger, 2010; Badger et al., 2013) at Cardiff University.
iii. Field sampling and sediment washing for the MRSF section was conducted during previous studies by Anja Mourik and Hemmo Abels (Mourik et al., 2011) at Utrecht University.
iv. The new age model for the composite MRSF-RIP section was devised by Lucas J. Lourens, Utrecht University.
v. Laboratory training in foraminiferal cleaning and sample preparation was provided by Amy Thomas-Sparkes, Cardiff University.
vi. Laboratory training in bulk element analysis was provided by Iain Macdonald, Cardiff University.
vii. Measurement of bulk carbonate stable isotope data for the il-Blata section was performed by Alexandra Nederbragt, Cardiff University.
viii. Mass spectrometry analysis of RIP and MRSF foraminiferal trace metal samples was conducted by Anabel Morte Rodenas, Sophie Slater, and Matthew Dumont.

Chapter 3

Early Miocene intensification of the North African hydrological cycle: multi-proxy evidence from the shelf carbonates of Malta

This chapter has been published in its entirety in Paleoceanography and Paleoclimatology (AGU publications)

https://agupubs.onlinelibrary.wiley.com/doi/full/10.1029/2022PA004414

Individual author contributions as follows:

- Conceptualization: R.Zammit, C.H. Lear, O.M. Bialik
- Formal analysis: R.Zammit, E.Samakassaou
- Funding acquisition: R.Zammit, C.H. Lear, O.M. Bialik
- Investigation: All authors
- Methodology: R.Zammit, C.H. Lear, O.M. Bialik, E.Samakassou
- Resources: R.Zammit, C.H. Lear, A.Micallef
- Writing – original draft: R.Zammit
- Writing – review & editing: All authors

Early Miocene intensification of the North African hydrological cycle: multi-proxy evidence from the shelf carbonates of Malta

R. Zammit[1], C.H. Lear[1], E. Samankassou[2], L.J. Lourens[3], A. Micallef [4,5], P.N. Pearson[1], O.M. Bialik [4]

[1]School of Earth and Environmental Sciences, Cardiff University

[2]Department of Earth Sciences, University of Geneva

[3]Faculty of Geosciences, Utrecht University

[4]Department of Geosciences, University of Malta

[5]Helmholtz Centre for Ocean Research Kiel

Corresponding author:

Ray Zammit (zammitR2@cardiff.ac.uk) , (raymond.zammit@um.edu.mt)

Key Points:

- The climate over the central Mediterranean shifted from a cool-arid to a humid regime during the Early Miocene around 19.0 Ma.
- The transition to more humid conditions may have been a consequence of the first Miocene restriction of the Mesopotamian Seaway (MSR-1).
- Circulation changes in the proto-Mediterranean coupled with changes in the sedimentation may have terminated regional phosphorite episodes.

Abstract

During the Miocene (23.0 to 5.3 Ma) North Africa experienced both humid and arid intervals, but the underlying cause of these transitions is unknown. Earth's climate was characterised by a unipolar icehouse with a dynamic Antarctic ice sheet, which may have influenced regional hydrology through atmospheric teleconnections. However, the Miocene also witnessed the restriction of the Mesopotamian Seaway, which may have had significant climatic impacts. The Maltese il-Blata section (Central Mediterranean) comprises Late Oligocene to Early Miocene marine deposits previously used to constrain the timing of the Mesopotamian Seaway restriction using the εNd tracer. The location of this section also makes it sensitive to climatic changes in the North African region, and biogeochemical changes in the central Mediterranean. Here, we present lithological and geochemical records of the il-Blata section. We find a marked shift in lithology and an increase in sedimentation rate coeval with the Early Miocene (~19 to 20 Ma) restriction of the Mesopotamian Seaway. Concomitant changes in bulk sediment $CaCO_3$, Sr/Ca, K/Al, Ti/Al, Zr/Al, and Si/Ti support a major humid climate transition and associated intensification of river systems over western North Africa. We propose that these changes in North African hydroclimate reflect either a tipping point effect in a gradually warming global climate or are the result of the initial restriction of the Mesopotamian Seaway, perhaps through consequent changes in Atlantic Meridional Overturning Circulation and the West African Monsoon. We also suggest the restriction of the Mesopotamian Seaway inhibited phosphorite deposition at low latitudes.

Plain language summary

The climate over the densely populated areas of North Africa and the Central Mediterranean is influenced by the West African Monsoon system. Climate data from the region is limited and models fail to make consistent predictions in the context of Anthropogenic global warming. Therefore, it is important to examine the geological past when atmospheric carbon dioxide levels were similar to values predicted for the end of the century. The il-Blata section in Malta (central Mediterranean) holds a geological record from 25 to 18 million years ago. This time interval is not well represented elsewhere in the region. Geological records from this section indicate a large increase in regional humidity around 19 million years ago. This humid transition followed a tectonic event that resulted in the closure of the Mesopotamian Seaway which connected the Indian Ocean with the Mediterranean Sea. This may reflect an important role for tectonic forcing in the evolution of the West African Monsoon system through changes in ocean circulation patterns. The change to a wetter climate also occurred against a backdrop of gradually warming global climate, so an alternative interpretation is that it reflects a regional tipping point in the climate system.

Keywords

Aquitanian-Burdigalian transition, Tethys Seaway, Globigerina Limestone Formation, Mediterranean, West African Monsoon, Maltese Islands

3.1 Introduction

3.1.1 Early to Mid-Miocene climate

The Miocene epoch (20.03 Ma to 5.33 Ma) witnessed several important climate transitions (Figure 3.1), and has been proposed as a test-bed for exploring moderate to high pCO_2 climates (Steinthorsdottir et al., 2020). The Miocene is also a time of large scale tectonic changes that resulted in reorganization of ocean basins and subsequent changes in global heat transport (Hamon et al., 2013; Potter & Szatmari, 2009). The base of the Miocene (23.03 Ma) is marked by a transient glaciation event known as the Oligocene-Miocene Transition (OMT; Figure 3.1), during which the Antarctic Ice-Sheet advanced and retreated on orbital timescales (Miller et al., 1991; Naish et al., 2001; Zachos et al., 2001; Mawbey and Lear, 2013; Mudelsee et al., 2014). For around 3 million years following the OMT, the marine benthic foraminiferal oxygen isotope ($\delta^{18}O$) record exhibits a strong eccentricity signal (De Vleeschouwer et al., 2017; Liebrand et al., 2011) with rather consistent glacial and interglacial values and ~1‰ variability (Liebrand et al., 2011; Westerhold et al., 2020). This interval was terminated by an unusually warm interglacial at ~19.6 Ma, followed by an unusually cool glacial maximum at ~19.4 Ma (Figure 3.1). Between 19.4 Ma and 17.0 Ma, both the glacial and interglacial values display a gradual warming trend (Figure 3.1; Cramer et al., 2009; De Vleeschouwer et al., 2017; Westerhold et al., 2020), followed by a relatively abrupt warming into the Miocene Climatic Optimum (MCO), which was also associated with the 'Monterey' positive $\delta^{13}C$ isotope excursion (Vincent & Berger, 1985; Holbourn, et al., 2007; Diester-Haass et al., 2009, 2013; Sosdian et al., 2020). The MCO was terminated by the middle Miocene climatic transition (MMCT), marked by declining pCO_2, a step-wise increase in $\delta^{18}O$ (14.6 Ma to 13.8 Ma) (Holbourn et al., 2014), and a permanent increase in global ice volume from 13.8 Ma (Abreu & Anderson, 1998; Flower & Kennett, 1994; Lear et al., 2015; Zachos et al., 2001). While the details of the climatic events of the OMT, MCO and the MMCT are becoming relatively well known, regional and global climate regimes between the OMT and the MCO (~23 Ma to ~17 Ma) are currently poorly investigated despite modern to near-future CO_2 concentrations (Steinthorsdottir et al., 2021). Possible reasons for this

include the limited number of sections that span this time interval without large hiatuses, as evidenced by the absence of base-Burdigalian and base-Langhian Global Boundary Stratotype Sections and Points (GSSPs) (Foresi et al., 2011; Iaccarino et al., 2011; Gradstein et al., 2012; Foresi et al., 2014; Fabbrini et al., 2019; Gradstein et al., 2020).

3.1.2 Evolution of Mediterranean climate during the Early Miocene

The present semi-enclosed nature of the Mediterranean Sea formed during the Miocene (Rögl, 1998; Kocsis et al., 2008; Cornacchia et al., 2021). Throughout the Cenozoic, the northward movement of the African and Arabian Plates continued to fragment the Tethys Ocean and generate smaller basins. This eventually resulted in the restriction of the Mesopotamian Seaway that connected the Indian Ocean to the proto-Mediterranean and led to the termination of low latitude circum-global halo-thermal circulation (de la Vara and Meijer, 2016). Recent work using the εNd tracer has revealed that the restriction of the Mesopotamian Seaway occurred in two distinct steps (Bialik et al., 2019). The initial Mesopotamian Seaway restriction (MSR-1) occurred during the Early Miocene ~20 Ma, while the final complete disconnection (MSR-2) occurred during the MMCT (~13.8 Ma) (Bialik et al., 2019). Intermittent reconnections and pre MSR-1 flow levels may have occurred between these two steps (Cornacchia et al., 2018; Sun et al., 2021).

In addition to these large scale tectonic and circulation changes, the Mediterranean region also shifted from a warm arid to a warm humid climate during the Early to Middle Miocene (John et al., 2003). However, the timing of this climatic shift is uncertain. John et al. (2003) noted a significant increase in the kaolinite/smectite ratio of sediments in Malta, and used an oxygen and carbon isotope stratigraphy to infer that the transition to more humid conditions and intense chemical weathering occurred close to the onset of the MCO at ~17 Ma. It has been suggested that the clay rich interval (CRI) in the Maltese Upper Globigerina Limestone member (UGLm) represents fully humid conditions (John et al., 2003). Subsequent age models (Mourik et al., 2011) suggest that the CRI, and hence the establishment of the humid phase, occurred later, at

around 14.6 Ma. The North African humid climate regime intensified further after the MMCT at 13.8 Ma (John et.al., 2003).

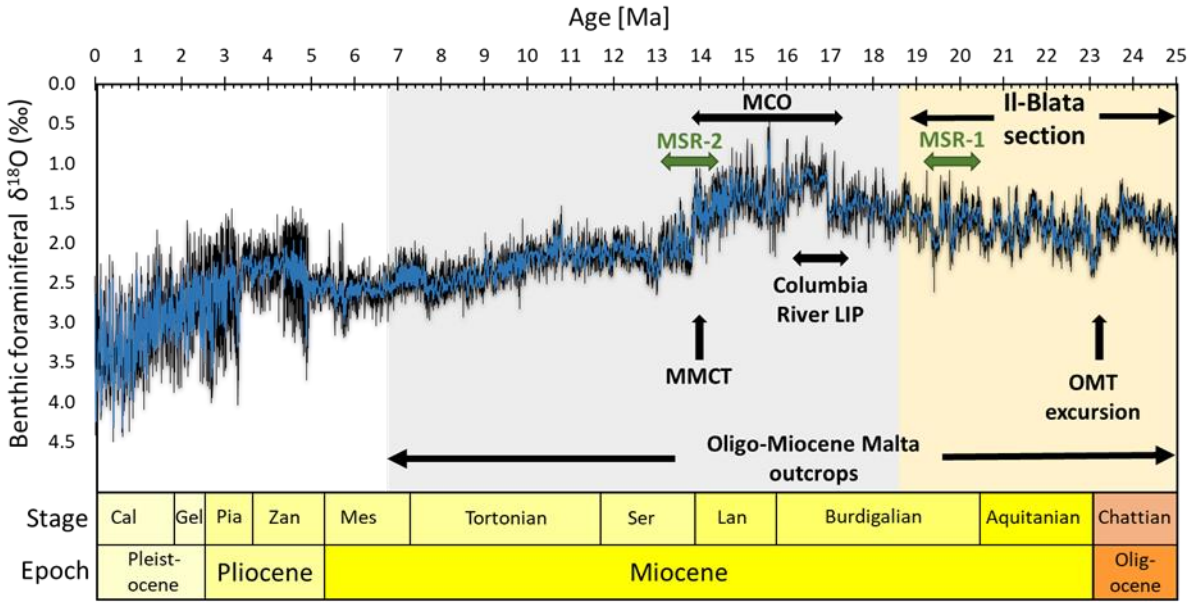

Figure 3.1 Benthic foraminiferal oxygen isotope record (Westerhold et.al. 2020) of the last 25 Myr and significant oceanographic and climatic events during this interval. The sedimentary deposits outcropping on the Maltese Islands were deposited during different climatic regimes from the Late Oligocene to the Late Miocene. The two major steps of the Mesopotamian Seaway restriction are highlighted [MSR-1 and MSR-2, the latter coinciding with the Middle Miocene Climate Transition (MMCT)]. Oligocene-Miocene transition (OMT), Large igneous province (LIP), Miocene Climatic Optimum (MCO). Abbreviations for stages: Langhian (Lan) ,Serravallian (Ser), Messinian (Mes), Zanclean (Zan), Piacenzian (Pia), Gelasian (Gel), Calabrian (Cal).

It has been suggested that this increase in humidity was due to a northward migration of the ITCZ over Africa in response to cooling and ice growth in Antarctica (John et al., 2003; Mutti et al., 2006). However, the Early and middle Miocene restriction events of the Mesopotamian Seaway raise the possibility of a tectonically mediated mechanism. Understanding the mechanisms behind past changes in hydrology of the North African region is important because this region is currently poorly constrained in future climate simulations (Masson-Delmotte et al., 2021).

3.1.3 Study site (Malta) and objectives

The pelagic to hemi-pelagic phosphorite bearing deposits of the Maltese Islands have repeatedly provided a reliable lithological, palaeontological and geochemical record of regional and global climatic and oceanographic changes during the late Oligocene (c. 28 to 23 Ma) and throughout the Miocene (23 to 5.3 Ma) (Jacobs et al., 1996; Abels et al., 2005; Hilgen et al., 2009; Mourik et al., 2011; Badger et al., 2013; Bialik et al., 2019; Bialik et al., 2021). The Maltese Islands, located on an isolated carbonate platform at the northern edge of the African plate (Figure 3.2), provide an opportunity to investigate changes in the hydrological regime over North Africa during the Oligo-Miocene. Here we present high-resolution lithostratigraphic and geochemical records from the Late Oligocene through Early Miocene il-Blata section outcropping along the south-west coast of Malta (Figure 3.2). We also construct a new age model for this site based on $^{87}Sr/^{86}Sr$. This allows us to confirm the temporal correlation of the phosphorite deposits at il-Blata (Föllmi et al., 2008; Baldassini and Di Stefano, 2015) with the deposition of the global low latitude Late Oligocene to Early Miocene phosphorites (Schöllhorn et al., 2019). We use a multiproxy approach to infer changes in the sedimentation rate and palaeoceanographic conditions at il-Blata during the Early Miocene. Calcium concentrations and $CaCO_3$ [%] are used to quantify the marine carbonate component in the sediment. Aluminium normalised proxies are used to indicate changes in fluvial and aeolian sediment fluxes (Ti/Al, Zr/Al) and chemical weathering intensity (K/Al), while Si/Ti ratios are used to infer changes in palaeoproductivity. Sulphur concentrations are used to assess palaeoredox conditions, and bulk sediment Sr/Ca reflects the supply of shelf carbonate to the system, acting as a local sea-level indicator. We show that the regional hydrology shifted to more humid conditions ~19 Ma. This coincided with the initial restriction of the Mesopotamian Seaway during a time of general warming climate. We explore possible mechanisms for this change, which probably also caused the cessation of major phosphorite deposition in this region.

3.2 Materials and methods

3.2.1 Study site and field sampling

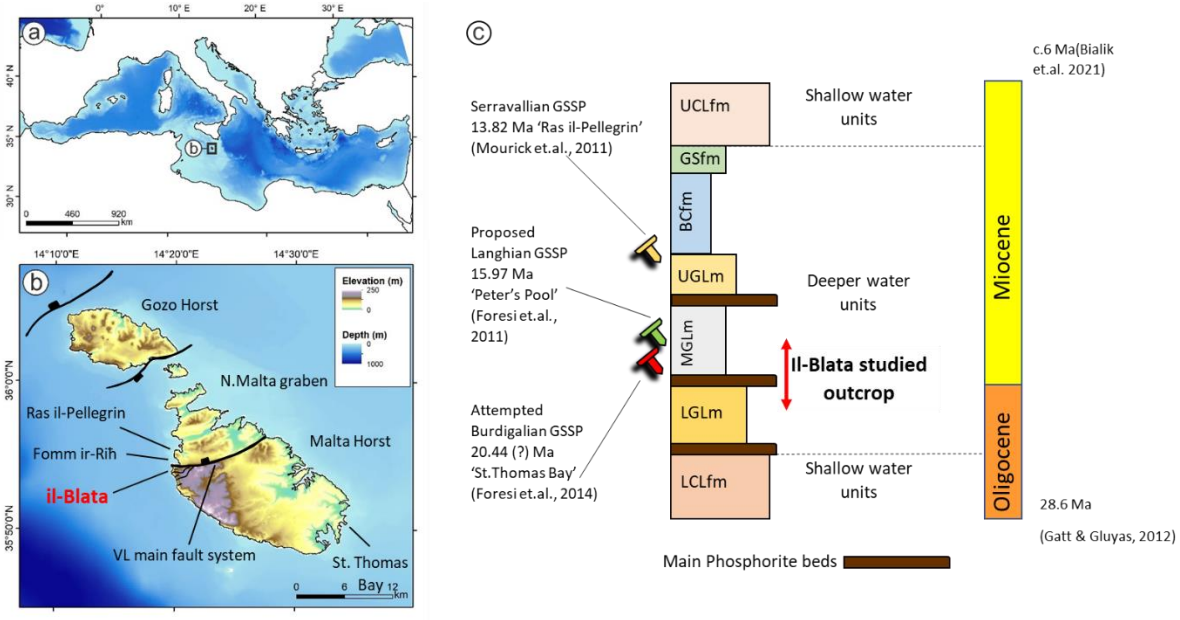

Figure 3.2 (a) The Maltese Archipelago lies in the central Mediterranean on the northern margin of the African plate. (b) The Maltese Islands represent the exposed part of a complex Oligo-Miocene tectonic regime dominated by a NE to SW trending horst-graben system (Dart et.al. 1993). The il-Blata study site lies at the edge of the North Malta graben close to the Victoria Lines (VL) main fault system. The Langhian-Serravallian GSSP at the Ras il-Pellegrin section lies across the Fomm ir-Riħ embayment to the north of the study site. The St. Thomas Bay section has been considered a candidate for the Burdigalian GSSP (Foresi et. al., 2014). (c) General lithostratigraphy of the Maltese Islands. LCLfm – Lower Coralline Limestone formation, LGLm – Lower Globigerina Limestone member, MGLm – Middle Globigerina Limestone member, UGLm – Upper Globigerina Limestone member, BCfm – Blue Clay formation, GSfm – Green Sand formation, UCLfm – Upper Coralline Limestone formation.

The Maltese Islands rest on the NE side of the Pantelleria rift, a deep trough that runs NE-SW for 100 km between the island of Sicily and the Tunisian tip of North Africa (Dart, et. al. 1993) (Figure 3.2). The Oligo-Miocene il-Blata section outcrops along the SW coast of the Island of Malta (Figure 3.2). The section is exposed along a slope (base at 35.9004˚N, 14.3309˚E, top at 35.9000˚N, 14.3314˚E) and is almost identical to the section described by Baldassini and DiStefano (2015). During sampling, the first few cm of the oxidised surface was removed using a hammer, and the samples were

collected from the visibly unoxidized part of the rock. Samples were wrapped in aluminium foil and placed in labelled plastic bags. It is highly unlikely that there was any significant aluminium contamination to our samples (Lewis & Christensen, 2016). Sampling intervals varied throughout the section, ranging from one sample every 10 cm to one sample every 50 cm depending on the accessibility of the outcrop. In total, 142 samples were collected from a ~40 m section of the Globigerina Limestone formation (GLfm).

3.2.2 Geochemistry and microfossils

3.2.2.1 Percentage carbonate

The percentage carbonate of all samples was measured using a digital calcimeter. About 1 g of powdered, homogenised, and dried sample was weighed and transferred to a 50 ml sample bottle. A clean, dry glass cuvette was filled with 6 M HCl, placed in the bottle, and connected to a FOGL digital calcimeter. The digital calcimeter was standardised using an in-house carbonate standard with average precision of 2 % (1 s.d.).

3.2.2.2 Stable isotope stratigraphy

Approximately 5g of bulk sediment material was crushed and homogenised using an agate pestle and mortar and dried for 24 hours at 40°C. Carbon and oxygen isotope ratios were measured on ~500 µg of this powder using a Gasbench II coupled to a Thermo Delta V Advantage isotope ratio mass spectrometer at the School of Earth and Environmental Sciences, Cardiff University. Results are expressed in ‰ using the δ-notation on the Vienna Pee Dee Belemnite (VPDB) scale. The long-term precision of an in-house carbonate standard is ≤0.06 ‰ (1 s.d.) for $\delta^{18}O$ and ≤0.05 ‰ for $\delta^{13}C$.

3.2.2.3 Major elements

A total of 114 samples of the crushed and dried samples were selected for major element analysis using X-ray florescence. Analysis was performed using a hand-held Olympus Delta Innov-X XRF gun at the School of Earth and Environmental Sciences, Cardiff University. The instrument was standardised using in-house carbonate and

silica standards. The following ratios were calculated to act as palaeoproxies: Ti/Al and Zr/Al for aeolian flux (Krom et al., 1999; Govin et al., 2012; Hennekam et al., 2015; Martín-Puertas et al., 2010; Martinez-Ruiz et al., 2015) , Sr/Ca for sea-level controlled export of shelf carbonate material (Bialik et al., 2020), K/Al for chemical weathering (Clift et al., 2014), and Si/Ti for biogenic silica production (Brown et al., 2007; Kylander et al., 2011). The bulk [Ca] was used to indicate the marine carbonate component while the bulk [S] indicates redox conditions (Passier & de Lange, 1998; Wei et al., 2009; Filippidi & Lange, 2019). All X-ray fluorescence data are semi-quantitative.

3.2.2.4 Radiogenic strontium isotopes

A total of 16 samples were collected from the succession for strontium isotope analysis. The samples were selected as close as possible to the main sedimentary hiatuses observed in the field in order to time constrain the different sedimentary packages (Figure 3.3). For each sample, 30 milligrams of powdered bulk sediment was dissolved in 2.2 M high-purity acetic acid for 1–2 hours at room temperature (22-24°C) in conical 2 ml vials. The solutions were centrifuged, and the supernatant was recovered and transferred to Teflon vials, where it was dried to a residue on a hot plate. The residue was re-dissolved in 14 M HNO_3 and dried again prior to Sr separation from the matrix using Sr-Spec resin. The Sr separate was re-dissolved in 5 ml ~2% HNO_3 solution, and the ratios were measured using a Thermo Neptune PLUS Multi-Collector inductively coupled plasma mass spectrometer in static mode at the University of Geneva. The $^{88}Sr/^{86}Sr$ ratio (8.375209) was used to monitor internal fractionation during the run. Interferences at masses 84 (^{84}Kr), 86 (^{86}Kr), and 87 (^{87}Rb) were corrected in-run by monitoring ^{83}Kr and ^{85}Rb. An SRM987 standard was used to check external reproducibility, which, on the long term (more than 100 measurements in one year), was 10 ppm. The internally corrected $^{87}Sr/^{86}Sr$ values were further corrected for external fractionation by a value of -0.025‰ per amu, because a systematic difference between measured and nominal standard ratios of the SRM987 of $^{87}Sr/^{86}Sr$ was 0.71024 (McArthur et al., 2001). The $^{87}Sr/^{86}Sr$ were converted into numerical ages using the LOWESS 5 fit (McArthur et al., 2012).

3.2.3 Microfossils

About 10 g of sample was broken and placed into jars filled with deionized water and rotated on a vertical spinner for about 12 to 14 hours. Samples that remained strongly lithified following spinning were broken down using pestle and mortar and subsequently dried. All samples were dry sieved and examined with a binocular microscope in order to determine the presence of foraminifera.

3.3 Results

3.3.1 Lithostratigraphy

The lithostratigraphy of the studied section (Figure 3.3) is broadly similar to that described in previous studies for the il-Blata section (Baldassini and Di Stefano, 2015) and the related Fomm ir-Riħ section (Jacobs, et al., 1996; Föllmi et al., 2008; Gruszczynski et al., 2008). The description of the MGLm (Middle Globigerina Limestone member) given here is more detailed than previous descriptions and, together with geochemical records and a robust age model, offers a new perspective for the interpretation of the Maltese depositional intervals in relation to Early Miocene oceanographic, tectonic, and regional climate changes. We divide the studied section into two intervals, which we term Depositional Interval 1 and Depositional Interval 2. This subdivision is based on general field observations (colour, grainsize, weathering features, lithology, and abundance of phosphatic beds) that indicate a significant depositional change at around 11 m from the base of the studied section (Figure 3.3). Each interval is further subdivided into smaller sedimentary packages (SP) based on facies changes observed in the field.

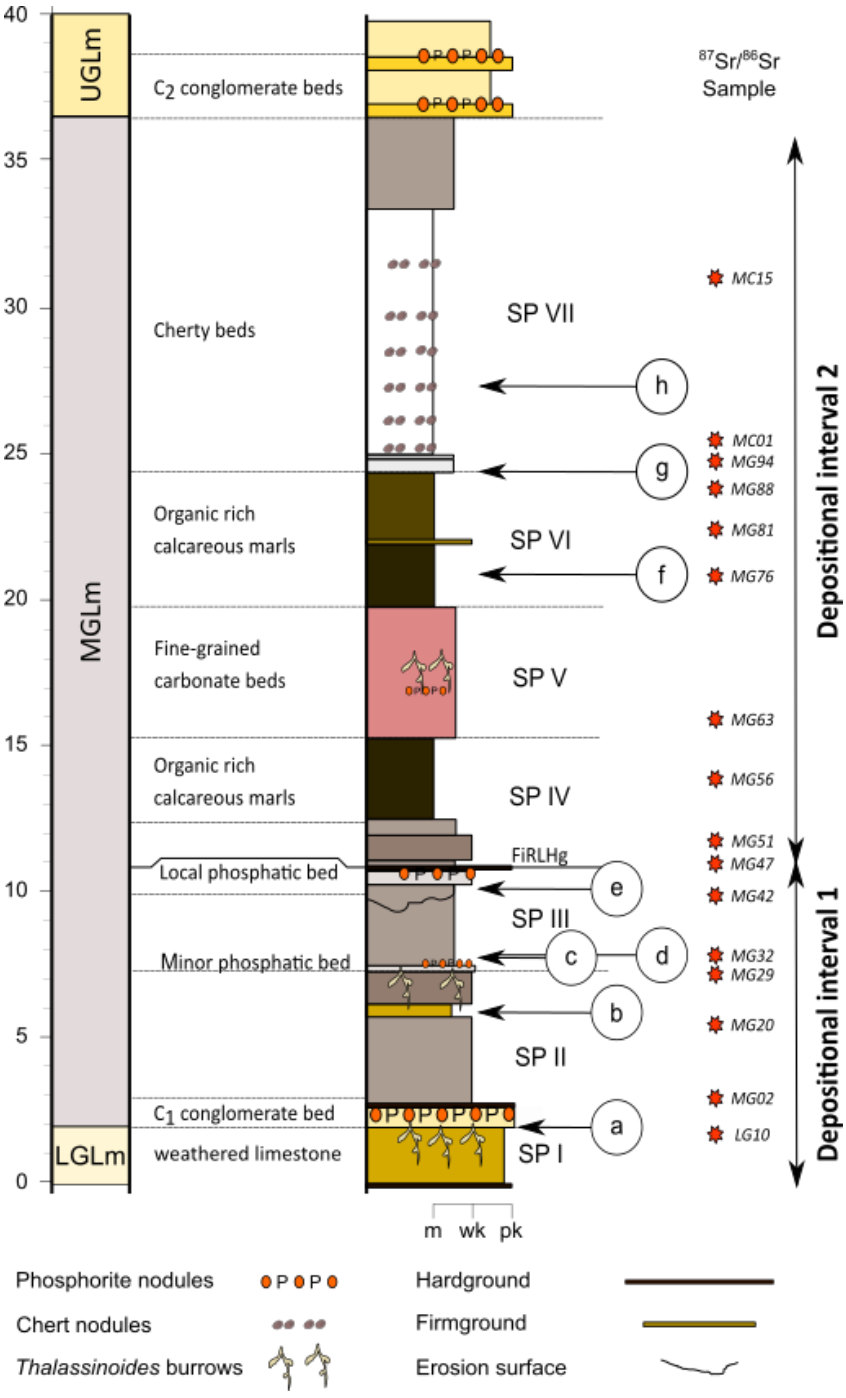

Figure 3.3 Lithostratigraphy of the il-Blata carbonate section pertaining to the Globigerina Limestone Formation. FiRLHg represents the Fomm ir-Riħ Local Hardground' of Gruszczynski et al., (2008). Samples taken for $^{87}Sr/^{86}Sr$ dating are indicated by red stars and constrain the main sedimentary packages. SP – Sedimentary package, LGLm – Lower globigerina limestone member, MGLm – Middle Globigerina Limestone member, UGLm - Upper globigerina limestone member. Sample naming: LG – Lower Globigerina Limestone, MG – Middle Globigerina Limestone, MC – Middle Globigerina Limestone cherty interval.

3.3.1.1 Depositional Interval 1 – Marine carbonates and phosphatic deposits

In general, the lower 2m of the section (SP I) is composed of highly weathered and bioturbated pale yellow wackestone/packstone facies associations within the Lower Globigerina Limestone member (LGLm; Figures 3.3 and 3.4a). This is capped by the ubiquitous condensed bed C_1 (Pedley and Bennett, 1985; Figure 3.4a). The beds towards the top of SP I display an increase in burrowing activity (*Thalassinoides*), an increase in broken *Pecten* bivalve shells, and a general increase in coarser grained material (Figure 3.4a). The base of C_1 is taken as the top of SPI.

The next sedimentary package (SPII) consist of the C_1 bed and the overlying 4.5m of fine grained, bedded, pale-grey mudstone/wackestone facies associations pertaining to the Middle Globigerina Limestone member (MGLm) (Figures 3.3 and 3.4b). This package displays coarsening upwards and terminates with a shallowing sequence of *Thalassinoides* ichonofacies, broken macrofossils, a 20 cm thick preferentially-weathered horizon (Figure 3.4b) and small phosphatic pebbles.

The next package, (SP III) lies unconformably on SP II. Its base comprises a limestone terrace containing a complex network of *Thalassinoides* ichonofacies, an erosional surface and a bed containing small phosphatic pebbles (Figure 3.4b, c, d). The overlying beds comprise 3 m of similar deposits to SP II. It is capped by an erosional surface (ES 1 *sensu* Baldassini and Di Stefano, 2015), which is filled by a phosphatic bed and capped by a phosphatic hardground (Figure 3.4e). We identify it as the Fomm ir-Riħ local hardground (FiRLHg) described by Baldassini and DiStefano (2015). It is relatable to phosphatic hardgrounds identified by other authors (Föllmi et al., 2008; Gruszczynski et al., 2008). This package is followed by a sedimentary unconformity and indicates the possibility of a large hiatus (Figure 3.3, 3.4e). Therefore, this unconformity was chosen to mark the top of Depositional Interval 1.

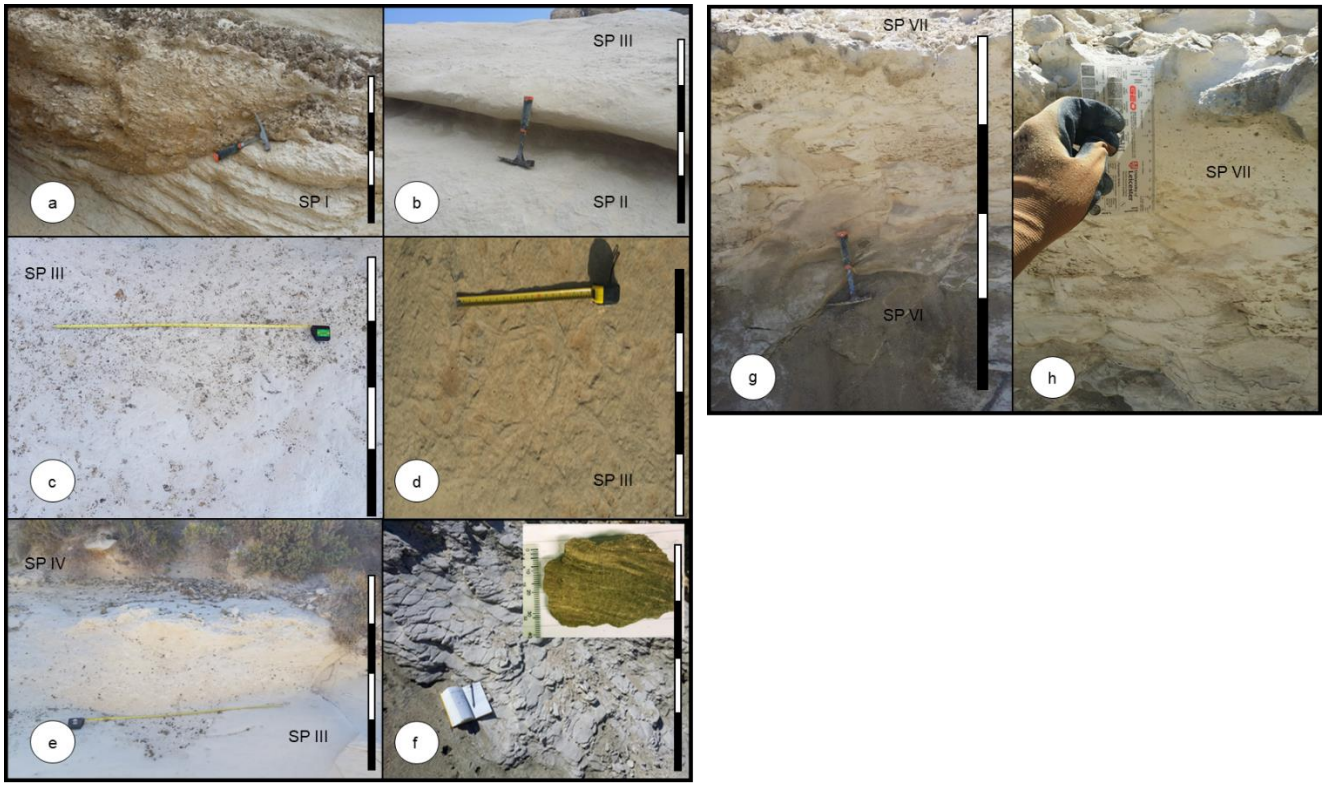

Figure 3.4 Sedimentological features of the il-Blata section. Black and white scale is 1 m. (a) Erosion surface at the top of SPI infill conglomerate material of gravity flow origin and phosphatic capping of the bed. (b) Notch between SP II and SPIII. (c) Erosion feature followed by minor phosphatic interval at the base of SP III resting on top of limestone terrace. (d)*Thalassinoides* ichonofacies associated with limestone terrace at the base of SPIII. (e) Erosion surface, phosphatic bed and planar hardground mark the end of depositional interval 1. (f) Dark, terrigenous-sediment rich mudstone facies SP VI, inset showing fine mm scale laminations. (g) Conformant transition from dark mudstones of SP VI to cherty deposits of SP VII transition. (h), Chert nodule SP VII.

3.3.1.2 Depositional Interval 2 – Calcareous organic-rich marls and cherty deposits

The packages overlying the Fomm ir-Riħ local hardground are significantly different from the underlying marine carbonates and have not previously been described in detail. Field observations indicate that, except for one unconformity at around 22 m from the base of the outcrop, this sequence is continuous. SP IV comprises 2.5m of fine-grained dark grey/green organic rich calcareous marls (Figure 3.3). These are overlain by coarser grained reddish lime mudstones/wackestone facies (SP V; Figure 3.3). This package contains a horizon with small (~1 cm) allochthonous phosphatic

pebbles at around 17 m above the base of the section, and evidence of bioturbation above this minor phosphatic layer. The transition to the next package (SP VI) is conformable. SP VI is similar to SP IV, and consists of finely-laminated, dark, organic-rich calcareous marls (Figure 3.4 f). A thin firmground (~2cm width) occurs at 22 m above the base of the section. SP VI transitions conformably with a striking colour change into a grey/white mudstone bed containing cm-scale siliceous intraclasts (Figure 3.4 g, h). This transitional bed is capped by a thick band of chert nodules that weathers proud and defines the shift from the calcareous marls to the pale grey/white beds of SP VII (Figure 3.4 h). SP VII consists of 9 m of very fine siliceous and carbonate sediment containing large chert nodules. The top of this package represents the termination of the studied section and is an unconformity that is capped by the yellow wackestone/packstone facies of the Upper Globigerina Limestone member (UGLm) and the associated C_2 phosphatic beds (Pedley & Bennett, 1985; Baldassini & Di Stefano, 2015, 2017).

3.3.2 Age model and sedimentation rate

The 16 samples of bulk sediment analysed for $^{87}Sr/^{86}Sr$ (Figure 3.3) display a generally consistent trend of increasing $^{87}Sr/^{86}Sr$ with height in the section, giving us confidence in using these data to obtain a reliable age model (Appendix 1.1) . The lowest $^{87}Sr/^{86}Sr$ value (0.708209) was recorded at 2.9 m above the base of the section (sample MG02), while the highest $^{87}Sr/^{86}Sr$ value (0.708515) was recorded at 24.0 m above the base of the section (sample MG88). The $^{87}Sr/^{86}Sr$ values suggest that the section was deposited between 24.9 Ma and 18.6 Ma (McArthur et al., 2012).

We note that this $^{87}Sr/^{86}Sr$ age model is in generally good agreement with the published nannofossil biostratigraphy of Baldassini and DiStefano (2015) for this section. The main points of disagreement between our age model and the nannofossil record of Baldassini and DiStefano (2015) relate to the duration of Depositional

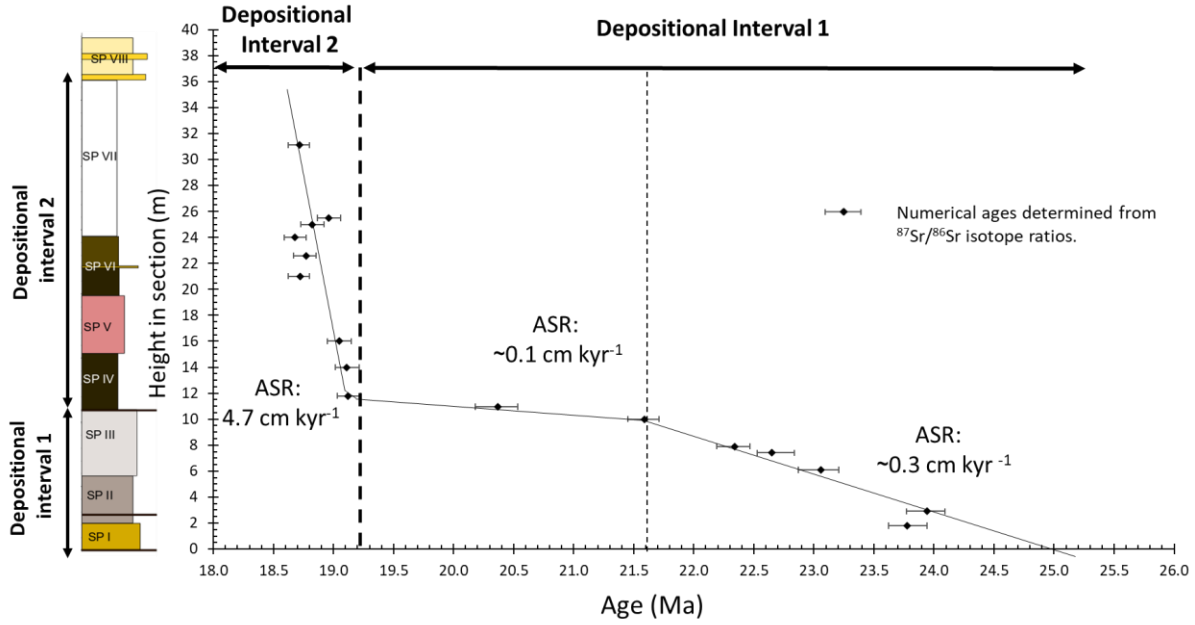

Figure 3.5 Numerical ages determined from $^{87}Sr/^{86}Sr$ ratios using LOWESS fit 5 model of McArthur et.al. (2012) with respect to height in the il-Blata section. Simplified graphic log relates the height in section with the main sedimentary packages (SP). The average sedimentation rate increases by an order of magnitude from Depositional Interval 1 to Depositional Interval 2. Average sedimentation rate (ASR).

Interval 1. The termination of Depositional Interval 1 is here determined to occur at 20.35 (+0.185, −0.170) Ma while the nannofossil record suggest a termination at ~21 Ma (no uncertainty provided) (Baldassini and Di Stefano, 2015). These discrepancies may be attributed to different sampling resolutions between the two studies and the difficulty in comparing the samples between the two studies due to the non-planar nature of the erosion surfaces at the site. Our $^{87}Sr/^{86}Sr$ data give an age of 19.121 (+ 0.102, −0.091) Ma to 18.526 (+0.085, −0.090) Ma for Depositional Interval 2, which is in excellent agreement with the nannofossil record (19.0 Ma to 18.5 Ma) (Figure 3.5).

Our age model shows that the sedimentation rate during Depositional Interval 1 is on average 0.3 cm kyr^{-1} between 0 and 10.0 m followed by a condensed section at the top with a sedimentation rate of 0.1 cm kyr^{-1}. This increases significantly to an average 4.7 cm kyr^{-1} throughout Depositional Interval 2 (Figure 3.5).

3.3.3 Geochemistry

3.3.3.1 Bulk carbonate stable isotopes

The bulk $\delta^{18}O$ and $\delta^{13}C$ records display a large negative excursion towards the top of SP I (Figure 3.6); this part of the record will not be discussed further since it can attributed to meteoric diagenesis (Oehlert & Swart, 2014). In addition, the presence of ankerite has been shown to shift $\delta^{18}O$ to more positive values within the section (John et al., 2003). The bulk $\delta^{18}O$ record will therefore not be further discussed.

Starting at 4 m from the base of the section, the bulk sediment $\delta^{13}C$ displays a generally decreasing trend through SP II and III, before increasing by ~0.4‰ across the hiatus between Depositional Intervals 1 and 2. Bulk sediment $\delta^{13}C$ subsequently decreases through SP IV and SP V, reaching a minimum value at around 22.0 m from the base, corresponding to an age of ~18.8 Ma and a minor local firmground. This is followed by a rapid rise of 1.2 ‰ within less than 0.15 Myr, reaching a maximum within the cherty beds of SP VII (Figure 3.6).

3.3.3.2 Carbonate content

There is a marked difference in carbonate content between Depositional Interval 1 and Depositional Interval 2. Carbonate content is high (~80%) throughout Depositional Interval 1, decreases to ~60% in the lower part of Depositional Interval 2 (SP IV), and increases slightly through SP V. Carbonate content generally decreases through SP VI and SP VII with the lowest value (30%) recorded within the cherty SP VII layer (Figure 3.6).

3.3.3.3 Major elements

Sediment [Ca] tends to covary with the carbonate record, reflecting the overall reduction in carbonate content from Depositional Interval 1 to Depositional Interval 2, with the lowest [Ca] occurring within the cherty layer SPVII (Figure 3.6). Bulk sediment Sr/Ca ratio covaries with bulk [Sr] except for a very short interval around 29 m from the base of the section (Figure 3.6). However, Sr/Ca does not covary with bulk $\delta^{18}O$, which is more susceptible to diagenetic influences. Bulk sediment Sr/Ca generally increases through the il-Blata section, with the main shifts associated with hiatuses and changes in sedimentary facies.

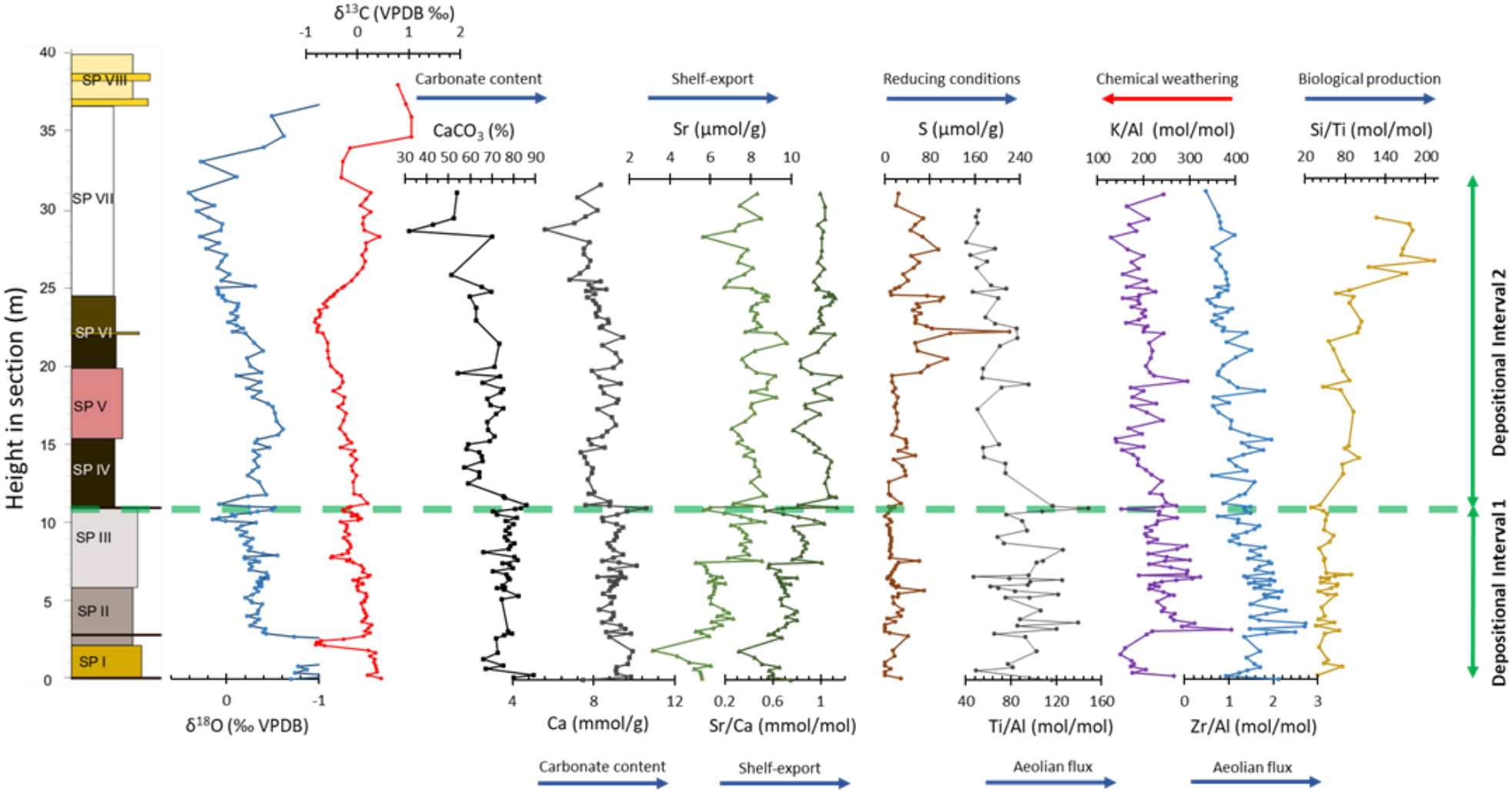
δ13C (VPDB ‰)
-1 0 1 2
Carbonate content
Shelf-export
Reducing conditions
Chemical weathering
Biological production
CaCO3 (%)
30 40 50 60 70 80 90
Sr (µmol/g)
2 4 6 8 10
S (µmol/g)
0 80 160 240
K/Al (mol/mol)
100 200 300 400
Si/Ti (mol/mol)
20 80 140 200
Height in section (m)
SP VIII
SP VII
SP VI
SP V
SP IV
SP III
SP II
SP I
0 5 10 15 20 25 30 35 40
Depositional Interval 2
Depositional Interval 1
0 -1
δ18O (‰ VPDB)
4 8 12
Ca (mmol/g)
0.2 0.6 1
Sr/Ca (mmol/mol)
40 80 120 160
Ti/Al (mol/mol)
0 1 2 3
Zr/Al (mol/mol)
Carbonate content
Shelf-export
Aeolian flux
Aeolian flux

Figure 3.6 Bulk stable isotopes, %$CaCO_3$ (marine sediment component), elemental abundances of Ca, Sr, (control on the Ca/Sr ratio), S (redox) and ratios Sr/Ca (shelf-export) , Ti/Al (aeolian flux), K/Al (chemical weathering), Zr/Al (aeolian flux), and Si/Ti (biogenic silica) with respect to height in section and lithology for the il-Blata section, Malta. Green dotted line delineates the hiatus between 20.0 Ma to 19.2 Ma and distinguishes the lithostratigraphy between the Depositional Interval 1 and Depositional Interval 2.

Bulk sediment [S] is generally very low and stable throughout Depositional Interval 1, after which an increase of ~40 µmol/g is recorded within SP IV, associated with a decrease in % carbonate and a general increase in clay content. A marked step increase of ~100 µmol/g coincides with the organic, clay rich interval of SP VI, with a notable spike (reaching values >200 µmol/g) around the firmground of Depositional Interval 2. Bulk sediment [S] decreases around the transition into the cherty interval but peaks around the middle of SP VII.

The Al normalized proxies Ti/Al, K/Al, and Zr/Al display a general decreasing trend from Depositional Interval 1 to Depositional Interval 2, likely reflecting the general increase in clay content up-section (Figures 3.6 and 3.8). Some of the values in interval 1 and interval 2 do overlap, however the average of these values changes from interval 1 to interval 2. The overlapping data points could reflect the inherent, short term climatic variability in the record (Figure 3.8). Bulk sediment Si/Ti records a step increase from Depositional Interval 1 to Depositional Interval 2. During Depositional Interval 2, the ratio further increases within SP VI, and more steeply in SP VII (Figure 3.6). The data presented does not all have the same resolution since the concentration of some elements was below the detection limit in a number of samples.

3.3.4 Microfossils

All samples within Depositional Interval 1 were found to be strongly lithified and could only be disaggregated by mechanical means. On visual inspection of the sediment under a light microscope we found no planktonic foraminifera and only a few poorly preserved benthic foraminifera.

We were able to disaggregate many samples from Depositional Interval 2 without resorting to mechanical methods. In general, foraminifera are rare throughout

Depositional Interval 2. No planktonic foraminifera were identified within the organic-rich sedimentary packages with very rare benthic specimens identified in the 100 to 250 µm size fraction. Very rare, well preserved planktic and benthic specimens were observed within the transitional bed between the organic-rich SP VI and the cherty SP VII. No specimens were found within the 250 to 355 µm size fraction for the cherty SP VII, while rare well-preserved benthic and planktic specimens were picked from the 100 to 255 µm size fraction. In general, within Depositional Interval 2, foraminifera tend to be very rare, well preserved, and small.

3.4 Discussion

3.4.1 Depositional history of the il-Blata section

Our results show that the depositional environment of the pelagic to hemi-pelagic il-Blata section (Baldassini & Di Stefano, 2015) changed significantly between Depositional Interval 1 and Depositional Interval 2. The lithology shows a change from marine carbonates and episodic phosphorites of Depositional Interval 1, to organic rich calcareous marls (SP IV and VI), fine grained carbonates (SP V) and chert-rich beds (SPVII) of Depositional Interval 2. Another important feature is the extreme change in the sedimentation rate (Figure 3.5). Depositional Interval 1 contains numerous hiatuses and condensed intervals (Figures 3.4 a, b, c, e), but an approximate sedimentation rate for the continuous episodes can be estimated from the $^{87}Sr/^{86}Sr$ data points at the top and bottom of the uninterrupted deposition for SP II (samples MG 02 and MG 20) and SP III (samples MG 32 and MG 42; Figure 3.3). These yield low sedimentation rates of ~0.3 cm kyr^{-1} (SP II) and ~0.1 cm kyr^{-1} (SP III). The sedimentation rate for Depositional Interval 2 is 4.7 cm ky^{-1} and compares well with the published sedimentation rate for the lower part of the MGLm at the St. Thomas outcrop (4.33 cm ky^{-1}) in the SE of Malta (Figure 3.2) (Foresi et al., 2014), and is in the same order of magnitude as typical Quaternary pelagic and hemi-pelagic sediments (1.7 to 2.3 cm kyr^{-1}) (Berger et al., 1993). This order of magnitude surge in sedimentation rate indicates a significant change in the depositional environment with a rapid increase in sediment supply and retention. The likely source and palaeoenvironmental implications of this enhanced sediment supply are discussed below (section 3.4.3).

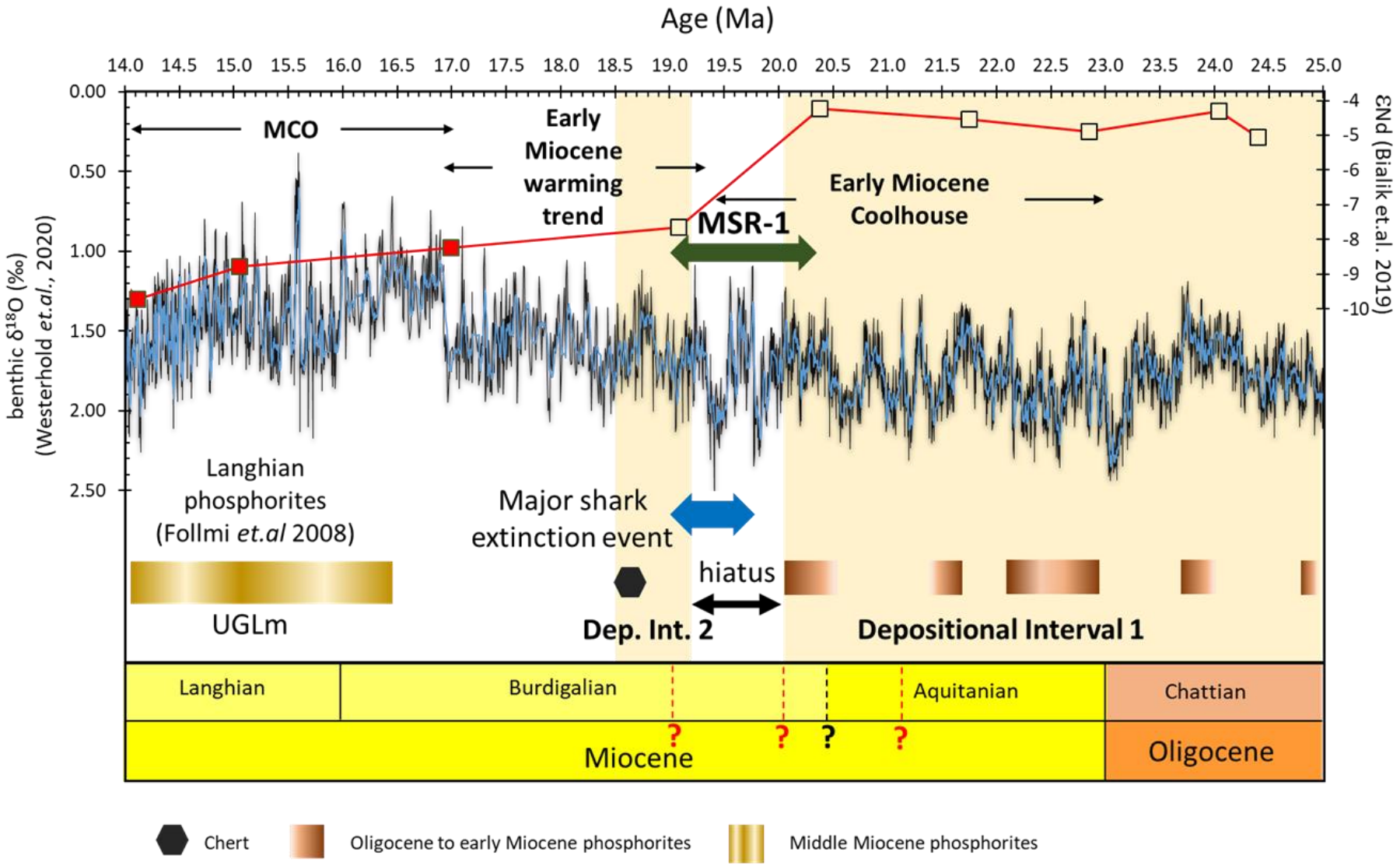
Age (Ma)
14.0 14.5 15.0 15.5 16.0 16.5 17.0 17.5 18.0 18.5 19.0 19.5 20.0 20.5 21.0 21.5 22.0 22.5 23.0 23.5 24.0 24.5 25.0
benthic δ18O (‰) (Westerhold et.al., 2020)
0.00 0.50 1.00 1.50 2.00 2.50
εNd (Bialik et.al. 2019)
-4 -5 -6 -7 -8 -9 -10
MCO
Early Miocene warming trend
MSR-1
Early Miocene Coolhouse
Langhian phosphorites (Follmi et.al 2008)
Major shark extinction event
hiatus
UGLm
Dep. Int. 2
Depositional Interval 1
Langhian
Burdigalian
Aquitanian
Chattian
Miocene
Oligocene
Chert
Oligocene to early Miocene phosphorites
Middle Miocene phosphorites

Figure 3.7 Timing of the Depositional Intervals at il-Blata, Malta compared with sedimentological characteristics, and the timing of the initial restriction of the Mesopotamian Seaway (MSR-1), and a shark extinction event (Sibert and Rubin, 2021). The age of the phosphatic horizons is only a rough approximation owing to the uncertainty in the $^{87}Sr/^{86}Sr$ and the non-planar nature of these beds. The age range of the various Langhian phosphorite episodes is from Föllmi et al. (2008). Onset of the chert horizons is marked by black hexagon. Solid symbols in the εNd record represent samples collected from other sections in Malta, while open symbols represent samples obtained from the il-Blata section (Bialik et al. 2019) and redated using the age model in this study. The base of the Burdigalian is still a matter of debate (indicated by '?') with the following four possible values still being considered 21.12 Ma, 20.43 Ma, 20.04 Ma and 19.03 Ma, with 20.43 being the current stated value (Gradstein et.al., 2012; Gradstein et al., 2020).

Depositional Interval 1 is interpreted to represent deposition in a well-oxygenated and well-mixed water column, subject to significant variations in sea-level and strong episodic upwelling currents. Indications of a periodically well oxygenated water column include the presence of the *Thalassinoides* ichonofacies (Savrda & Bottjer, 1989; Reolid & Betzler, 2019) and the formation of thick phosphatic hardgrounds (Schöllhorn et al., 2019). High amplitude sea-level oscillations are inferred from the general sedimentological pattern of deep water facies capped by erosion surfaces and followed by multiple, cyclic gravity flow deposits (Föllmi et al., 2008) rich in phosphatic material and capped by hardgrounds. The formation of the condensed sections are assumed to be the result of rapid sea-level rises (Baldassini and Di Stefano, 2015). These rapid transgressions are necessary to break pre-existing hardgrounds and carry material by gravity flows down a palaeo-slope. These phosphatic hard-grounds are assumed to have been in a palaeo-highground in the NW of the present archipelago (Pedley and Bennett, 1985; Carbone et al., 1987). Although we acknowledge the presence of a local tectonic component in the formation of the accommodation space (Dart et al., 1993), this cannot account for the rapid sea-level oscillations. We also note a good match between our Sr/Ca record and the general sedimentological pattern of deep water to shallow water facies with Sr/Ca values decreasing around phosphate-rich intervals and associated hiatuses (Figure 3.6). In general, Sr/Ca values are relatively low compared with open ocean pelagic carbonates of this age (Billups et al., 2004) which may reflect a more substantial contribution from inorganic calcite. This is consistent with the interpretation of increasing bulk sediment Sr/Ca reflecting

increased delivery of aragonite-rich shelf material during sea-level rise and marine transgressions (Renard, 1986; Bialik et al., 2020). The Sr/Ca record for Depositional Interval 2 remains consistently high, reflecting a significant shelf influence, with variations correlatable with the main sedimentary packages (Figure 3.6). The decrease in % $CaCO_3$, the general increase in fine grained sediments (muds and clays) and the surge in sedimentation rate suggests a significantly greater flux of terrigenous material into the area. The fine laminations, absence of bioturbation, dark colouration, scarcity of benthic foraminifera and generally organic-rich lithology within SP IV and VI indicate periods of seafloor suboxia/anoxia.

3.4.2 Enhanced siliceous productivity in a warming climate

The depositional system over Malta from the Late Oligocene through the Early Miocene was driven by global glacial-interglacial oscillations. In the earliest Miocene, sedimentation rates and productivity were low, with productivity most likely increasing during phosphorite deposition. The initiation of the phosphatic episodes is associated with eustatic lowstands and the overlying beds are deposited during the subsequent rapid transgression (Baldassini and Di Stefano, 2015). Our Sr/Ca record, age model and lithostratigraphy generally support this idea of a strong association of submarine erosional features, hardgrounds and condensed phosphatic beds with glacial maxima and sea-level lowstand followed by rapid post-glacial transgression (Figures 3.6 and 3.7). However, the condensed nature of the phosphatic intervals makes the precise temporal constraint of these episodes difficult and is beyond the scope of this work.

The onset of more humid conditions is associated with increased sedimentation rates, as well as the deposition of more organic- and silica-rich sediments, and follows the MSR – 1 step (20.35 Ma to 19.05 Ma) (Figures 3.5, 3.7 and 3.8). The concomitant large increase in Si/Ti indicates that the siliceous/chert interval (SP VII) is dominated by biogenic production rather than lithogenic input, since an increase in lithogenic silica would most likely also increase the Ti content (Brown et al., 2007) (Figure 3.8).

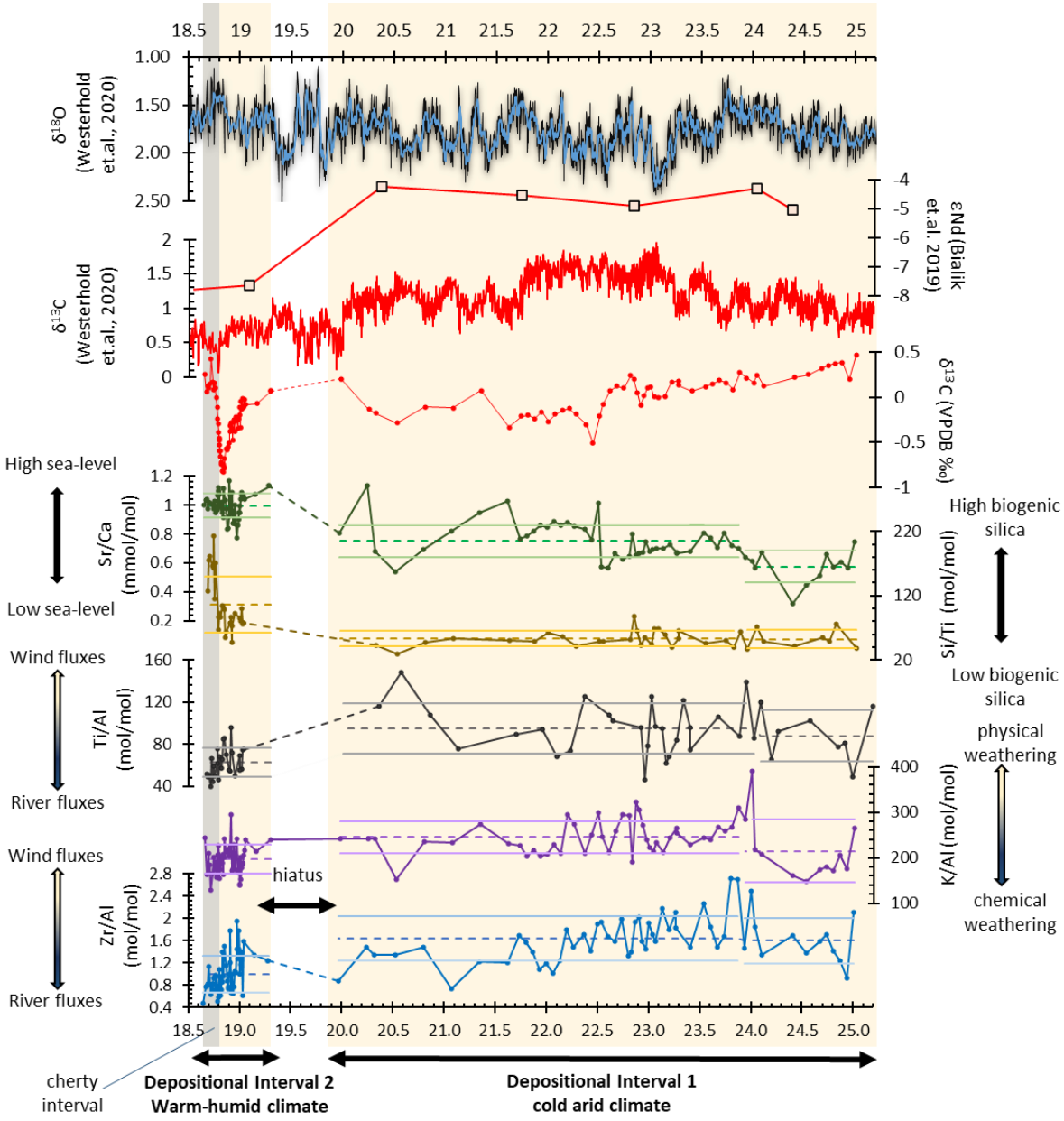

Figure 3.8 Aluminium normalized proxies Zr/Al, K/Al and Ti/Al used to indicate a decrease in wind-derived sediment fluxes and an increase in chemical weathering following the early Burdigalian hiatus. The surge in Si/Ti indicates an increase in biogenic silica production while the Sr/Ca indicates relative sea-level change at the site of deposition. Dotted lines indicate the mean of values within three selected intervals (25.0 Ma to 23.9 Ma, 23.9 Ma to 19.9 Ma and 19.3 Ma to 18.6 Ma) while dotted lines indicate 1 s.d. from this mean.

We interpret this as an increase in biological production in the central Mediterranean during the early Burdigalian. These chert deposits are likely contemporaneous with extensive radiolarian-rich biogenic silica deposits along the Western North African

Margin (Riahi et al., 2015; Ben Yahia et al., 2019; Essid et al., 2019) and diatomite-bearing biogenic siliceous beds of Central Italy (Amorosi et al., 1995), although poor age control of these Mediterranean deposits prevent a precise correlation.

The onset of the Miocene Climatic Optimum was marked by a relatively rapid shift to warmer conditions at ~17 Ma (Holbourn et al., 2015). However, the benthic oxygen isotope record also indicates an earlier decreasing $\delta^{18}O$ trend between ~19.5 Ma and ~17 Ma (Figure 3.7; De Vleeschouwer et al., 2017; Westerhold et al., 2020) which is correlatable with an Early Miocene warming trend from ~20 Ma as indicated by Mg/Ca temperature proxy (Cramer et al., 2011). Widespread decreases in deep ocean $CaCO_3$ mass accumulation rates have also been used to argue for increasing oceanic dissolved inorganic carbon (DIC) concentrations during this interval, suggesting that the gradual warming was caused by changes in the global carbon cycle (Drury et al., 2021). We note a step increase in chert horizons in the global oceanic records, starting around 19 Ma and terminating around 13 Ma (Muttoni & Kent, 2007). This may suggest that the Early Miocene Mediterranean cherts of Malta, Italy and Tunisia represent a regionally amplified signal of a more global phenomenon during this interval of global warmth. We therefore speculate that this interval of enhanced biogenic silica deposition represents a response to increased delivery of silica and other nutrients to the global oceans. In the Mediterranean region, the chemical weathering of Western North African mountains in a warming climate may have been particularly important (Penman et al, 2019).

3.4.3 A hydrologic shift in the North African region

The western and central regions of the southern Mediterranean currently receive wind-blown sediment from the Sahara Desert without any significant riverine input from North Africa due to its modern arid climate. During the Holocene, this region was also influenced by riverine fluxes from now extinct fluvial systems that mainly discharged into the Gulf of Sirte (Libya) or the Gulf of Gabez (Tunisia) (Wu et al., 2016, Wu et al., 2017). Sedimentological evidence suggests that Western North African fluvial systems have episodically influenced marine sedimentary environments over Malta as far back

as the late Oligocene (Gatt & Gluyas, 2012). In addition, sediments from Mega-Lake Fezzan in western Libya support the existence of an intermittent humid climate by the Early Miocene (23.0 Ma; Hounslow et al., 2017). The influence of fluvial systems in the Mediterranean was thought to have increased around ~17 Ma (John et al. 2003), with fully humid conditions in place during the deposition of the Clay Rich Interval (CRI) of the UGLm. However, subsequent age models have suggested that the CRI and hence the establishment of the humid phase occurred later, close to 14.6 Ma (Mourik et al., 2011). Humid conditions further intensified following the MMCT at 13.8 Ma (John et al., 2003). As described above, the change in lithology and sedimentation rate at il-Blata indicates a significantly greater influx of terrigenous material from ~19 Ma. The most likely explanation would be a hydrologic shift in the North African region at this time, and we use our multi-proxy records to explore this interpretation below.

3.4.3.1 An Early Miocene shift from aeolian to fluvial sediment fluxes

Aluminium normalised element proxies are here used to support the interpretation of a change in hydrological regime causing the dramatic changes in lithology and sedimentation rate. (Figures 3.5, 3.6 and 3.8). The Ti/Al proxy has been successfully applied to represent wind derived sediment fluxes due to dust storms from the Sahara into the Mediterranean during the Pliocene and the Pleistocene (Govin et al., 2012; Lourens et al., 2001). Zr/Al is also indicative of wind-blown Saharan sediment (Martín-Puertas et al., 2010; Martinez-Ruiz et al., 2015). Changes in sea-level would impact the proximity of our study area to the nearest land mass, potentially influencing the accumulation of heavy minerals that contain Ti and Zr. However, the river input for such heavy minerals tends to be very low, and we do not think this is a significant influence on our records (Kumar Warrier & Shankar, 2009). Ti/Al and Zr/Al mainly reflects grain size and hence can differentiate between the intensity of the aeolian/fluvial transport process (Zabel et al., 2001). Potassium is generally associated with the minerals illite and feldspar, both of which are indicative of low rates of chemical weathering and we interpret the K/Al ratio as increasing under arid regimes

(high physical weathering) and decreasing under more humid regimes (high chemical weathering) (Zabel et al., 2001; Govin et al., 2012).

There is considerable covariation between the Ti/Al and the Zr/Al records throughout the il-Blata section (Figures 3.6 and 3.8) and we interpret the decrease in both these records between Depositional Interval 1 and Depositional Interval 2 as indicating a decrease in wind-blown North African sediment over the central Mediterranean following the early Burdigalian hiatus. The associated increase in sedimentation rate and transition to more clay-rich sediments therefore reflects a shift to a predominantly fluvial sediment supply during the early Burdigalian (after 19.29 Ma), supported by the general decrease in the K/Al record. The shift from a wind dominated to a fluvial dominated sediment supply is consistent with a change from more arid to more humid climate conditions.

3.4.3.2 Early Miocene onset of humid conditions in North Africa was coincident with the initial restriction of the Mesopotamian Seaway

A recent study measured bulk sediment εNd at il-Blata (using sediments collected by us and published in Bialik et.al. (2019)) and other sites, revealing a two-stage restriction of the Mesopotamian Seaway, with the initial restriction occurring in the Early Miocene, and the final restriction associated with the Middle Miocene Climate Transition (Bialik et al., 2019). The scale of change in the εNd recorded in Malta cannot be ascribed to a change in weathering regime over North Africa (Bialik et. al. 2019). We can therefore confidently correlate MSR-1 with our lithologic and geochemical records, and our improved age model also enables us to better correlate MSR-1 with global records. MSR-1 is marked by a step change in the εNd record, reflecting a significantly reduced water flow from the Indian Ocean into the proto-Mediterranean. Our new Sr isotope-based age model suggests that MSR-1 occurred sometime between 20.35 (+0.185, −0.170) Ma and 19.05 (+0.100, −0.100) Ma. It is difficult to refine the chronology further since this interval includes the il-Blata hiatus (19.97 Ma to 19.29 Ma) that separates Depositional Interval 1 and Depositional Interval 2 (Figures 3.7 and 3.8). We note that the il-Blata hiatus also coincides with two large positive excursions in the global $\delta^{18}O$ record with $\delta^{18}O$ maxima at 19.8 Ma and 19.4

Ma (Figures 3.7 and 3.8; Westerhold et al., 2020). These events are assumed to be accompanied by eustatic drops in sea-level, with estimates suggesting sea-level minima of –10 m at 19.8 Ma and –25 m below present day levels at 19.4 Ma (Miller et al., 2020). It is therefore possible that the exact timing of the tectonically induced seaway restriction was also modified by these glacio-eustatic sea level changes. The global planktonic foraminiferal records do not suggest any significant oceanic turnover events at this time (Wade et al., 2011). However, a gap in the Mediterranean planktonic foraminiferal records from 20.66 Ma to 19.74 Ma has been noted, either side of which there appear to be significant changes in abundance of various taxa (Lirer et al., 2019). This could be a sampling gap, but it may also be indicative of a regional hiatus throughout much of the Mediterranean around the Aquitanian/Burdigalian boundary. This interval also coincides with a global mass extinction of pelagic shark populations (>70% of species) between ~20 Ma and ~18 Ma, focused between 19.75 and 19.00 Ma (Sibert and Rubin, 2021). It is therefore striking that the distinct change in depositional regime, representing the onset of more humid conditions in North Africa, is penecontemporaneous with the initial restriction of the Mesopotamian Seaway (Figure 3.7). We explore the potential mechanisms for this dramatic shift in North African hydrology in section 3.4.4.

3.4.3.3 A model for the termination of Late Oligocene to Early Miocene phosphorite deposition in the Mediterranean

The initial restriction of the Mesopotamian Seaway was also associated with the termination of the Late Oligocene-Early Miocene phosphorite deposition over Malta and elsewhere. These phosphorite episodes (Schöllhorn et al., 2019) started during the Late Oligocene (28 – 29 Ma) along the present day United States Pacific coast (Schöllhorn, et al., 2019). A belt of phosphorite deposits developed in a west-east trend with major phosphatic episodes occurring during the late Oligocene along the shallow marine coastal areas of California, Mexico (Föllmi et al., 2019; Schöllhorn et al., 2019), Puerto Rico, the Dominican Republic (Ortega-Ariza et al., 2015), and Florida (Schöllhorn et al., 2019). Across the Atlantic, phosphogenesis started later, and by ~25 Ma periodic phosphorite deposits are observed in Malta and Sicily (Pedley and Bennett, 1985; Föllmi et al., 2008; Gruszczyński et al., 2008; Carbone et al., 1987),

Central Italy (Auer et al., 2016), and Galicia bank along the Atlantic Spanish/Portuguese submarine coast (González et al., 2016).

These deposits require a combination of global and regional factors to facilitate their formation. From a regional perspective, these include a well-oxygenated water column, strong upwelling systems and low sedimentation rates to allow sufficient time for phosphorite lithification (Schöllhorn et al., 2019). From a global point of view, the rhythmic expansion and contraction of the Antarctic Ice-Sheet and associated glacio-eustatic sea-level oscillations likely facilitated the emplacement of these phosphorite deposits, with the glacial phases forcing wind-driven upwelling systems and the required productivity levels (Schöllhorn et al., 2019). A number of these low latitude phosphogenesis episodes terminate during the Early Miocene (Schöllhorn et al., 2019). The MSR-1-induced changes in Mediterranean circulation would have severely hampered the upwelling systems in the central Mediterranean during glacial maxima (Figure 3.9; de la Vara and Meijer, 2016). In addition, the more rapid sedimentation on the seafloor would have further inhibited the formation of phosphorites (Föllmi, 1996; Heggie et al., 1990). The global phosphorus cycle is tied to the carbon cycle and can potentially act as a negative or positive feedback on climate change (Föllmi, 1996). However, determining the wider impact of this cessation of regional phosphogenesis requires modelling that is beyond the scope of this paper.

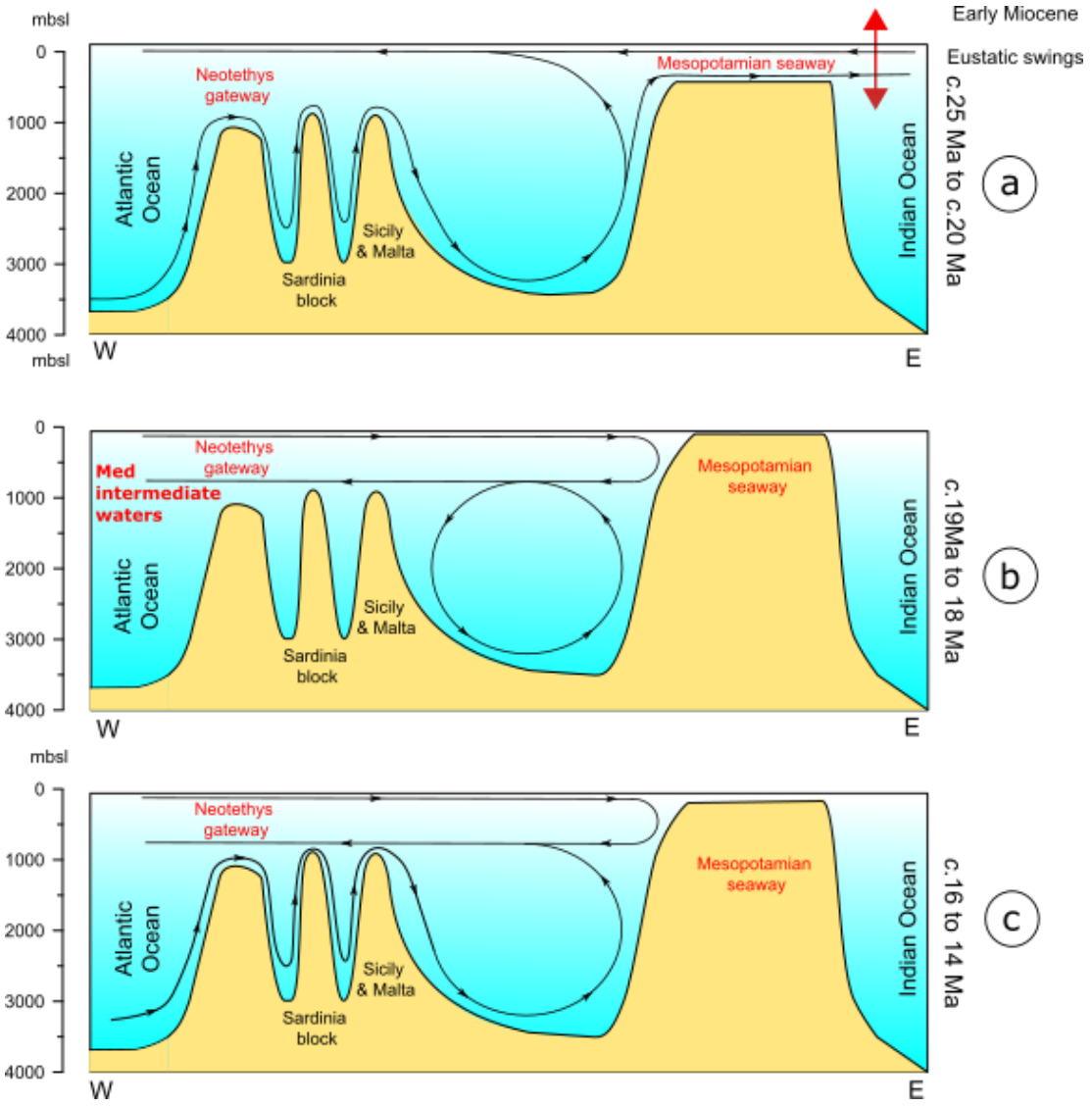

Figure 3.9 Proposed changes in ocean circulation in the Mediterranean region following the initial restriction of the Mesopotamian Seaway (MSR-1). (a) Between c.25 Ma to 20 Ma, the central Mediterranean would have been subject to episodic upwelling driven by the early Miocene high amplitude glacial-interglacial eustatic sea level changes. During this time interval, episodic allochthonous and autochthonous phosphorites were formed in the central Mediterranean aided by W-E upwelling currents. (b) Following MSR-1, these upwelling systems would have been cut off and warm, saline intermediate waters advected into the Atlantic Ocean. Consequent intensification of the Atlantic thermohaline circulation may had led to an enhanced monsoon system over western North Africa. (c) Possible reconnections may have been re-established during the MCO resulting in re-emergence of phosphatic episodes. Model adapted from (de la Vara and Meijer, 2016; Bialik et al., 2019).

3.4.4 A model for the onset of a North African humid interval in the Early Miocene

The il-Blata hiatus (19.97 Ma to 19.29 Ma) separates a cooler, more arid regional climate regime from subsequent warmer and more humid conditions in the North African region. We consider three possible mechanisms to account for this marked change in North African hydrology: (i) a northward shift in the ITCZ caused by Antarctic cooling, (ii) global warmth, and (iii) ocean-atmosphere response to water-flow restriction through the Mesopotamian Seaway.

It is thought that the shift of the North African climate from arid to humid during the middle Miocene at 14.6 Ma and subsequent intensification of the hydrological system during the MMCT (13.8 Ma) is likely to have been due to the northward migration of the ITCZ over Africa as a result of the expansion of the Antarctic Ice-Sheet in a unipolar world (John et al., 2003). We therefore initially consider a similar mechanism for the increased humidity at ~19 Ma. However, the deep sea benthic foraminiferal $\delta^{18}O$ record suggests reduced global ice volume following 19 Ma (Figure 3.7; Westerhold et al., 2020), so we discount this possibility as it is difficult to reconcile an increase in global ice volume with a trend towards lower $\delta^{18}O$ values. The second mechanism therefore is a response to global warmth. The gradual nature of the warming in the benthic foraminiferal $\delta^{18}O$ record compared with the onset of humid conditions might be used to argue against a global climate driver, although the hydrology of the North African region has been shown to be surprisingly sensitive to regional changes in albedo and vegetation, resulting in tipping point behaviour (Demenocal et al., 2000; Hopcroft & Valdes, 2021). Therefore, we consider it is impossible to rule out a global climate driver (e.g., increasing pCO_2) for the increased regional humidity at this time. However, we find it striking that the transition to more humid conditions in North Africa and the termination of phosphorite deposition coincide with the initial restriction of the Mesopotamian Seaway (Figure 3.7). Prior to the seaway restriction, low-latitude, circum-global circulation had been operating at least since the mid-Cretaceous (~100 Ma; Barron & Peterson, 1989). It is likely that following MSR-1 this low latitude E-W system (Figure 3.9 a) was shut down or severely restricted (de la Vara and Meijer,

2016; Bialik et al., 2019) and that the hot, saline intermediate waters of the proto-Mediterranean started to advect primarily into the Atlantic rather than the Indian Ocean (Figure 3.9 b). This injection of salt may have had a direct effect on Atlantic thermohaline circulation, enhancing the formation of Northern Component Water (NCW; Rogerson et al., 2006; Hamon et al., 2013). We note a shift towards non-radiogenic εNd at Ocean Drilling Program (ODP) Site 1090 around this time, possibly reflecting an increasing contribution of Northern Component Water into the Southern Ocean (Scher & Martin, 2008). Enhanced Atlantic thermohaline circulation may in turn have had a significant influence on the strength of the West African monsoon (WAM) by impacting tropical sea surface temperatures and the land-sea gradient (Chang et al., 2008; Latimer & Murray, 2007). Our data demonstrate an increased fluvial sediment supply via North-West African tributaries in the Gulf of Gabez and the Gulf of Sirte, accompanied by surges in sedimentation rate and biogenic silica production in response to a new, distinct climatic regime. We therefore hypothesize that this intensification of the hydrological regime over the region reflects the activation of a weak proto-WAM during the Early Miocene, perhaps favoured by the new ocean overturning regime, but we caution that further work is required to investigate these potential couplings.

3.4.4 Depositional regimes on Malta beyond the il-Blata section

A lengthy hiatus occurs at il-Blata following the cherty interval SP VII (Baldassini and Di Stefano, 2015, 2017), which may in part be attributed to the complex tectonic history of the Maltese Islands (Dart et al., 1993). Sedimentation continued towards the east of the Maltese Islands with the thick calcareous marls of the Middle Globigerina Limestone member (Foresi et al., 2014), likely indicating that a high productivity regime continued until ~17 Ma and the onset of the MCO. The return of phosphorite deposition in Malta during the interval coinciding with the MCO (Figure 3.7) (Föllmi et al., 2008; Baldassini & Di Stefano, 2017) indicates that oceanographic conditions favouring phosphorite deposition may have been restored in the central Mediterranean (Figure 3.9 c). One possible mechanism is that the glacio-eustatic sea-level rise associated with the MCO reconnected the Mesopotamian Seaway with the Indian Ocean

(Cornacchia et al., 2018), which facilitated periodic upwelling systems within the Mediterranean region (Figure 3.9 c) (de la Vara & Meijer, 2016). These mid-Miocene phosphatic intervals were most likely less active both temporally and spatially than the Late Oligocene to Early Miocene system, as suggested by the absence of hardgrounds and autochthonous phosphorites in Malta and Sicily during this second Miocene phase of phosphogenesis (Föllmi et al., 2008). The onset of the Blue Clay deposition following these phosphorites of the Upper Globigerina Limestone coincides with long term humid conditions over Africa and a permanent global cooling associated with the MMCT (John et al., 2003; Abels et al., 2005; Hilgen et al., 2009).

3.5 Conclusions

The Early Miocene records from the il-Blata section in the central Mediterranean Island of Malta indicate large regional climatic changes around the base of the Burdigalian (*c.* 19 Ma). A surge in sedimentation rate and aluminium normalised element proxies indicate a marked increase in humidity in the North African region following the Early Miocene restriction of the Mesopotamian Seaway. We suggest that tectonic closure of the Mesopotamian Seaway resulted in the advection of dense, saline waters into the Atlantic, favouring an enhanced Atlantic thermohaline circulation and altering sea surface temperature patterns. It is possible that consequent changes in ocean-land-atmosphere interactions over the Atlantic activated a humid climatic phase over North Africa, by enhancing the WAM. An alternative mechanism could be a tipping point response to the gradually warming global climate at this time. Regardless of the ultimate cause of the humid climate transition, it seems to have led to significant activation of drainage systems into the central Mediterranean. We suggest that the consequent surge in the delivery flux of terrigenous material, together with the shutting down of W-E upwelling systems, was an important factor in terminating Early Miocene phosphorite depositional systems in this region. Instead, the increased riverine fluxes may have promoted enhanced stratification near the Gulf of Sirte, leading to suboxic/anoxic conditions on the seafloor, and deposition of organic-rich laminated sediments. The high fluxes of terrigenous material in a warmer and wetter climate were

likely also associated with increased nutrient supply to the Mediterranean region. This enhanced nutrient supply is seen as the driver for enhanced biological productivity and deposition of silica rich sediments in the central Mediterranean, including the cherty mudstones of the il-Blata section.

The time interval between the first step restriction of the Mesopotamian Seaway (~ 20 Ma) and the final complete restriction (~14 Ma) was a time of large glacio-eustatic changes and there is a strong possibility of intermittent oceanic reconnection via the Mesopotamian Seaway influencing both the regional Mediterranean climate and the marine depositional environment. Further studies are needed to identify and temporally constrain these reconnection events and link them to changes in the hydrological cycle, and biogeochemical processes in the central Mediterranean. Nevertheless, this work highlights a new potential causal link between the tectonic closure of eastern Tethys and North African hydroclimate, with consequent feedbacks on regional carbon cycle processes.

Acknowledgements:

This work was funded by the ENDEAVOUR Scholarships Scheme (Group B) Malta, Cardiff University, and The Open University Geological Society – Ian Gass bursary (RZ) and NERC grant NE/P019102/1 (CHL). Support is given by Marie Skłodowska Curie Fellowship (101003394-RhodoMalta) (OMB). The Superintendence of Cultural Heritage Malta is thanked for granting permission to collect samples (SCH 213/16). Alexandra Nederbragt, Iain Macdonald and Anthony Oldroyd are thanked for laboratory assistance. John MacArthur is thanked for providing the LOWES-FIT 5 model and useful discussion. This manuscript was improved by the careful comments of two anonymous reviewers and the editor Ursula Röhl.

Open Research

This research used samples and data generated by the authors. All data presented in this study are given in Tables S1–S6 in Supporting Information **S1** and data is archived in PANGEA—Data Publisher for Earth & Environmental Sciences (Zammit, **2022**). Original εNd Carbonate data is available in the Supplementary Information at Bialik et al. (**2019**), it is reinterpreted in this study and is available in Table S2 in Supporting Information **S1** of the above-mentioned data archived in PANGEA and in Appendix 1.1 in this thesis.

Supporting information

https://agupubs.onlinelibrary.wiley.com/action/downloadSupplement?doi=10.1029%2F2022PA004414&file=2022PA004414-sup-0001-Supporting+Information+SI-S01.pdf

Data archive

https://doi.pangaea.de/10.1594/PANGAEA.947547

Chapter 4

Proto-Mediterranean oceanographic response following the Mid-Miocene expansion of the Antarctic Ice-Sheet.

Chapter 4 – Proto-Mediterranean oceanographic response following the Mid-Miocene expansion of the Antarctic Ice-Sheet.

4.1 Introduction

The Miocene era (20.03 Ma to 5.33 Ma) marks an important time in our understanding of climate evolution in an ice-house world (Steinthorsdottir et al., 2020). Following a time of elevated sea-levels and temperatures associated with the Miocene Climatic Optimum (MCO), the Middle Miocene climate transition (MMCT) is a very significant step in this process, with a large increase in Antarctic ice cover and associated global sea-level fall (Flower & Kennett, 1994). The MMCT is marked by a number of cooling steps that occur from ~ 14.6 Ma to 9.0 Ma (Holbourn et al., 2013) with the main cooling step occurring around the Langhian-Serravallian boundary (13.82 Ma), coinciding with the Mi-3b positive $\delta^{18}O$ excursion and closely associated with the CM-6 $\delta^{13}C$ positive excursion in the global isotope records (Abels et al., 2005; Hilgen et al., 2009; Mourik et al., 2011). It is a time of major changes in the global carbon cycle, with falling pCO_2 following the MCO (Foster et al., 2012). Several mechanisms have been proposed for the mechanism behind this CO_2 drawdown, from enhanced organic carbon burial (Vincent and Berger, 1985) to changes in the global balance of volcanism and chemical weathering (Foster et al., 2012). Orbitally paced variations in both $\delta^{18}O$ and $\delta^{13}C$ also point to feedbacks in the climate system (e.g., Sosdian et al., 2020), and these are discussed in more detail in Chapter 5. It has been suggested that the main Antarctic ice sheet expansion phase was facilitated by a rare congruence of orbital parameters (Abels et al., 2005) operating against this background of decreasing pCO_2, with changes in global oceanic circulation (Shevenell et al., 2004) and ice-albedo feedbacks helping to shift the Earth into a novel climate state (Shevenell et al., 2008).

The Global Boundary Stratotype Section and Point (GSSP) for the Langhian-Serravallian transition occurs at the Ras il-Pellegrin (RIP) section in Malta (Central Mediterranean) (Hilgen et al., 2009). It is dated at 13.82 Ma and coincides with the

initiation of the main phase of expansion of the Antarctic Ice sheet associated with the Middle Miocene Climate Transition. At Ras il-Pellegrin, this coincides with the transition from the Globigerina Limestone Formation to the Blue Clay Formation (Figure 4.1c), with the transition bed (TB) between the two formations correlatable with the positive excursion in the $\delta^{18}O$ records (Mi-3b) (Mourik et al., 2011). A number of studies have highlighted the suitability of this section in understanding the Mid-Miocene transition (Abels et al., 2005; Badger et al., 2013; Mourik et al., 2011). The main advantage of the Ras il-Pellegrin site is that it hosts well/excellently preserved foraminifera within a continuous sedimentary record making it ideal for producing astronomically-tuned geochemical records. The site has also proven to be well suited for other reasons. Being deposited on top of an isolated carbonate platform it is sufficiently removed from volcanic and tectonic sources making it ideal for the application of the εNd tracer to track water mass movements in oceanic basins (Kocsis et al., 2008; Bialik et al., 2019). Geochemical records generated from the RIP site and others sites on the Maltese Islands have been used to time constrain the water flow restriction through the Mesopotamian Sea-way during the Early and Middle Miocene (Bialik et al., 2019).

Being placed on the northern edge of the African shelf, and in proximity to now-extinct deltas in the Gulf of Sirte and the Gulf of Gabez (Hounslow et al., 2017), the RIP site is also sensitive to atmospheric and hydroclimatic changes over Western North Africa. Shifts in sedimentation rates, minerology and geochemical signatures over Malta have been related to hydroclimatic behavior over Western North Africa (John et al., 2003; Zammit et al., 2022). The onset of the Blue Clay formation closely correlates with a significant increase in terrigenous clay, sedimentation rate and elevated delivery of kaolinite into the central Mediterranean, suggesting a shift to a warm/humid climate over Western North Africa around the Middle Miocene (John et al., 2003). Modelling suggests that a closed Mesopotamian Gateway (such as that following the Mid-Miocene transition) enables close coupling of the Asian and African Monsoon systems (Fluteau et al., 1999) and on this premise one may assume that the African Monsoonal

climate was active around the same time as the Asian system. The Asian Monsoon system was weakly active from ~20 Ma to 12.9 Ma following which it strongly intensified (Betzler et al., 2016). Records from Malta suggest that a weak humid climate was present around the deposition of the Clay Rich Interval (~14 Ma) in the Upper Part of the Globigerina limestone and intensified around the onset of the Blue Clay (13.82 Ma) (Figure 4.1c). However, data for the onset of monsoonal climate over Western North Africa remains poor.

In order to investigate the regional and global implications of the MMCT and the final closure of the Mesopotamian Seaway, a record spanning from 13.7 Ma to 12.8 Ma from the RIP section is presented here. This high-resolution record spans a time during which the newly formed proto-Mediterranean region became thermally and materially isolated from the Indo-Pacific realm. Planktic and benthic foraminifera are used to produce a high resolution (~ 9000 kyr) stable isotope and trace metal (Mg/Ca) stratigraphy. These records are used to determine sea surface temperature (SST) and bottom water temperature (BWT) records. Combing the Mg/Ca-SST and $\delta^{18}O_p$ (planktic) allows for the determination of the $\delta^{18}O_{sw}$ of surface seawater, which reflects global ice-volume and local salinity. BWT and $\delta^{18}O_b$ (benthic) are used to produce a $\delta^{18}O_{sw}$ of bottom water which is dominated by the global ice volume signal. This allows for the generation of a $\Delta\delta^{18}O_{sw}$ from the same samples, which acts as a proxy for surface salinity. Absolute values of sea-surface salinity (SSS) were also produced by using the $\delta^{18}O_{sw}$ of surface waters allowing comparison with the $\Delta\delta^{18}O_{sw}$. These records therefore shed light on the details of the evolution of the proto-Mediterranean Sea in response to climatic (MMCT) and tectonic (closure of the Mesopotamian gateway) and allow speculation into possible climatic feedbacks associated with the formation of the Mediterranean realm.

4.2 Methodology

4.2.1 Foraminiferal geochemistry

A total of 84 samples previously obtained from the RIP section (Badger, 2010; Badger et al., 2013) were used to pick intact specimens of the planktic species *Trilobatus trilobus*. Around 60 individual clean specimens were picked by fine paint brush from each sample from the 250-355 µm size fraction. A sub-set of 32 samples was used to pick intact specimens of the benthic species *Heterolepa dutemplei* and *Uvigerina* spp. In general, 5 to 20 individual specimens were picked for these benthic species.

Trace element (Mg/Ca) and stable isotope ($\delta^{18}O$ and $\delta^{13}C$) records were produced from *Trilobatus trilobus*. Due to the low numbers of intact, clean benthic specimens it was not possible to produce the isotope and elemental record from the same species. *Heterolepa dutemplei* was used to produce a stable isotope record ($\delta^{18}O$ and $\delta^{13}C$) while *Uvigerina* spp. was used to produce a Mg/Ca record. All samples were cleaned prior to Mg/Ca analysis following the method of Boyle & Keigwin (1985) involving removal of clay minerals, removal of organic matter by oxidative cleaning method and dilute acid leach. A detailed methodology is presented in chapter 2, section 2.2.2.2. Long term precision for in-house carbonate standard is ≤ 0.04 ‰ (1 s.d.) for $\delta^{18}O$ and ≤ 0.03 ‰ (1 s.d.) for $\delta^{13}C$. Long-term precision (r.s.d.) for Mg/Ca is ≤ 1%

Microfossil preservation state (dissolution and recrystallisation) was assessed visually using the binocular microscope and also by means of Scanning Electron Microscope (SEM) images.

4.2.2 Age model - CenoGRID

A new age model for the Ras il-Pellegrin section was produced by tying points (table 4.1) from the benthic $\delta^{18}O_b$ stable isotope records of Mourik et. al. (2011) to the

Cenozoic Global Reference benthic foraminifer carbon and oxygen Isotope Dataset (CenoGRID) of Westerhold et al. (2020) (Figure 4.1a,b) (L.J. Lourens pers. comm. 2022). This new age model for the RIP section differs from the previously published models of Mourik et. al. (2011) and Badger et. al. (2013) in that it does not assume an astronomical (precession ~20 kyr) forcing frequency on the record. This allows for identifying the spectral component in the various proxies used in this study without running into circular arguments.

Section	Age (Ma) CenoGRID	height in section (m)	Magnetic polarity
MRSF	14.388	-25.75	
MRSF	14.306	-19.43	
MRSF	14.281	-17.53	
MRSF	14.212	-15.52	
MRSF	14.154	-13.12	
MRSF	14.112	-10.32	
MRSF	13.992	-7.21	
MRSF	13.905	-3.50	
MRSF	13.876	-1.90	
MRSF	13.842	-0.02	
RIP	13.728	5.10	
RIP	13.528	14.10	
RIP	13.426	17.20	
RIP	13.216	25.90	
RIP	**13.183**	26.47	C5Aan (average)
RIP	**13.032**	32.03	C5Ar.2r (average)
RIP	**12.887**	36.66	C5Ar.2n (average)

Table 4.1 Age model based on CenoGRID. Red data points in bold tied to magnetic polartity timescale while black data points tied to global benthic $\delta^{13}C$ of Westerhold et al., (2020). Point in red (height in section 25.90 m) is not specifically tied to the CenoGRID. MRSF – Marsalforn section, RIP – Ras il-Pellegrin section.

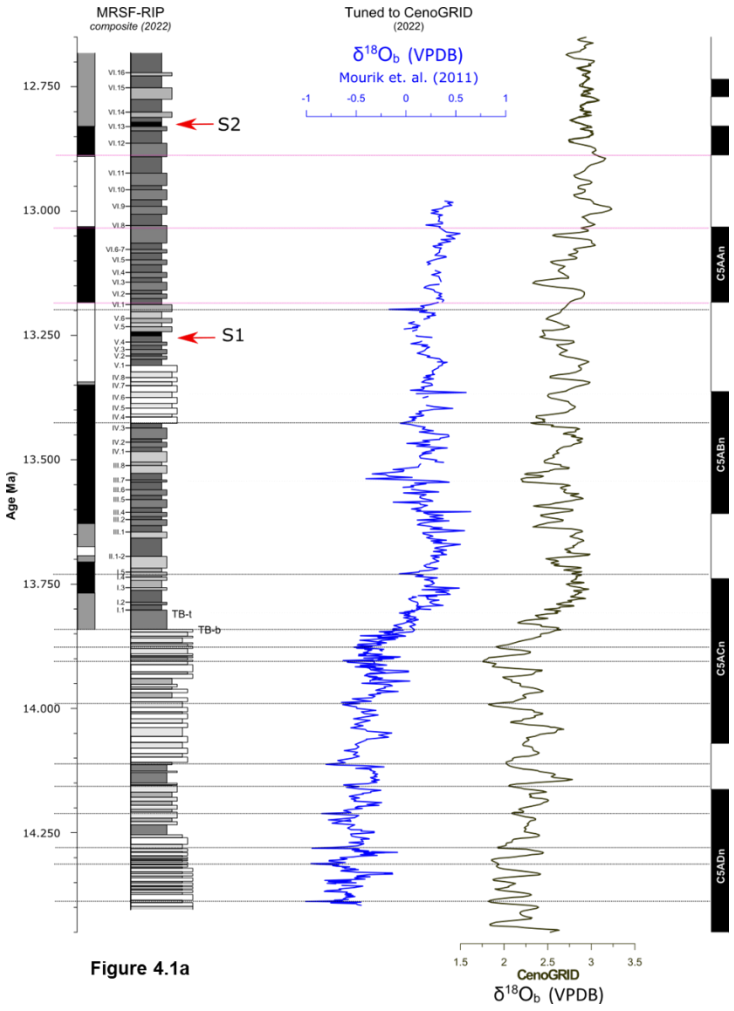

Figure 4.1a

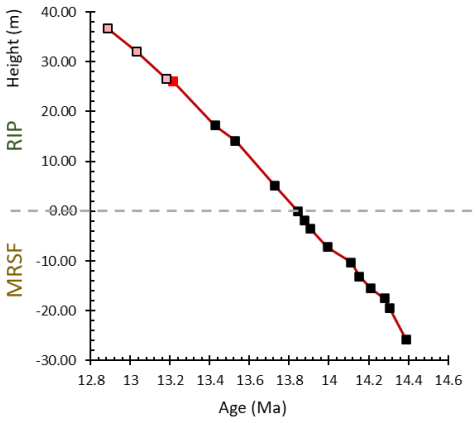

Figure 4.1b

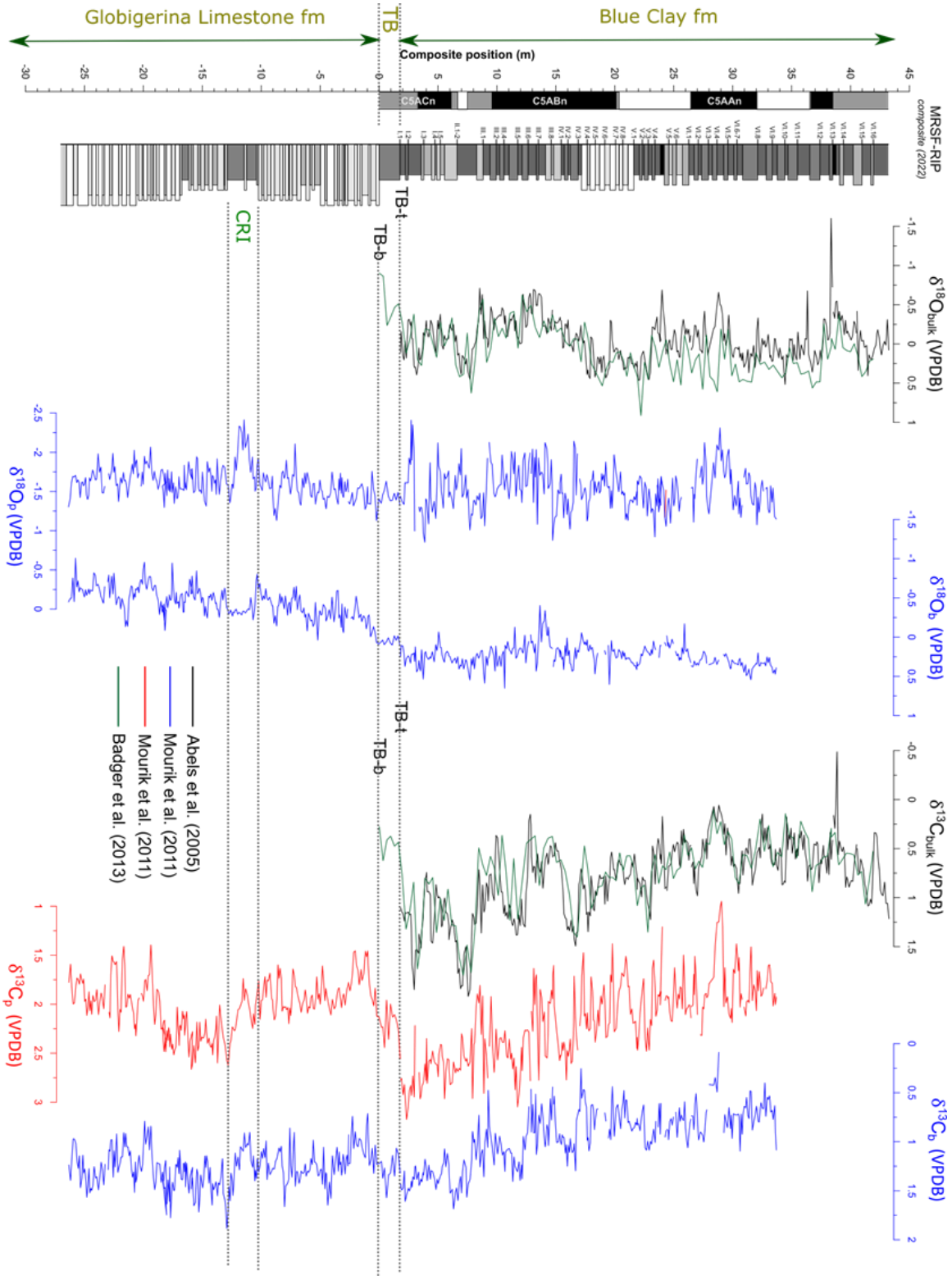
Globigerina Limestone fm
TB
Blue Clay fm
Composite position (m)
C5ACn
C5ABn
C5AAn
MRSF-RIP composite (2022)
CRI
TB-t
TB-b
δ18Obulk (VPDB)
δ18Op (VPDB)
δ18Ob (VPDB)
δ13Cbulk (VPDB)
δ13Cp (VPDB)
δ13Cb (VPDB)
Abels et al. (2005)
Mourik et al. (2011)
Mourik et al. (2011)
Badger et al. (2013)

Figure 4.1c

Figure 4.1 Composite lithostratigraphy and chronostratigraphy of the Middle Miocene Marsalforn (MRSF) and Ras il-Pellegrin (RIP) sections from Malta. (a) Benthic $\delta^{13}C$ record from Mourik et.al. (2011) with tie-points to the CenoGRID (Westerhold et al., 2020). Pink lines represent magnetostratigraphic tie points and black lines represent tie points to specific peaks in the $\delta^{13}C$ records. (b) Age model tie points with respect to height in the composite section with magnetostratigraphic tie points (pink) and tie points to $\delta^{13}C$ peaks (black). Red point not specific to CenoGRID. (c) All previously published stable isotope data plotted with respect to the lithology of the Composite section (Abels et al., 2005; Mourik et al., 2011; Badger et al., 2013). CRI – Clay rich interval (John et al., 2003), TB – transition bed between the Globigerina Limestone Formation and the Blue Clay formation (Mourik et al., 2011). TB-b – Base of transition bed, TB-t – Top of transition bed.

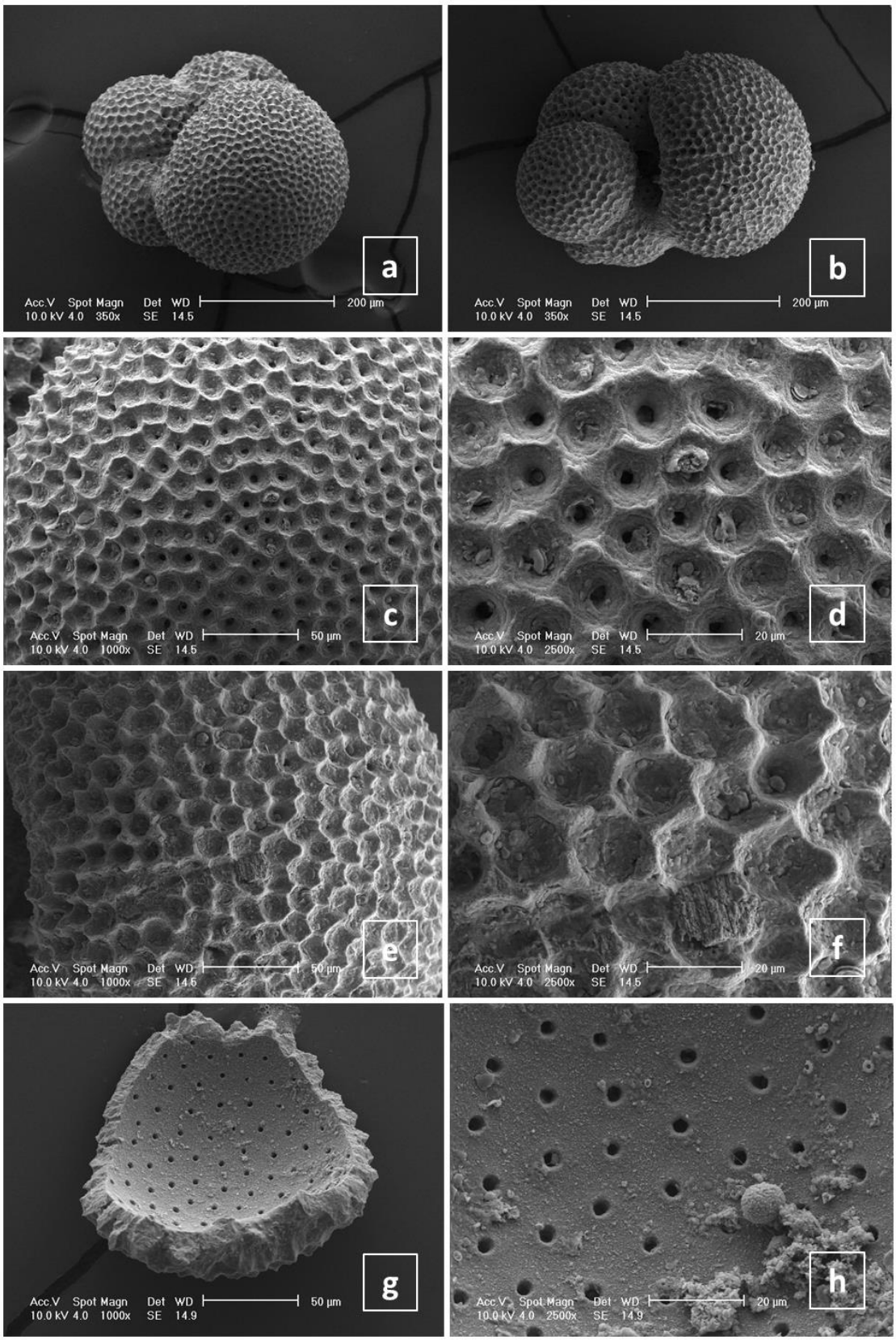
a
Acc.V Spot Magn Det WD 200 µm
10.0 kV 4.0 350x SE 14.5
b
Acc.V Spot Magn Det WD 200 µm
10.0 kV 4.0 350x SE 14.5
c
Acc.V Spot Magn Det WD 50 µm
10.0 kV 4.0 1000x SE 14.5
d
Acc.V Spot Magn Det WD 20 µm
10.0 kV 4.0 2500x SE 14.5
e
Acc.V Spot Magn Det WD 50 µm
10.0 kV 4.0 1000x SE 14.5
f
Acc.V Spot Magn Det WD 20 µm
10.0 kV 4.0 2500x SE 14.5
g
Acc.V Spot Magn Det WD 50 µm
10.0 kV 4.0 1000x SE 14.9
h
Acc.V Spot Magn Det WD 20 µm
10.0 kV 4.0 2500x SE 14.9

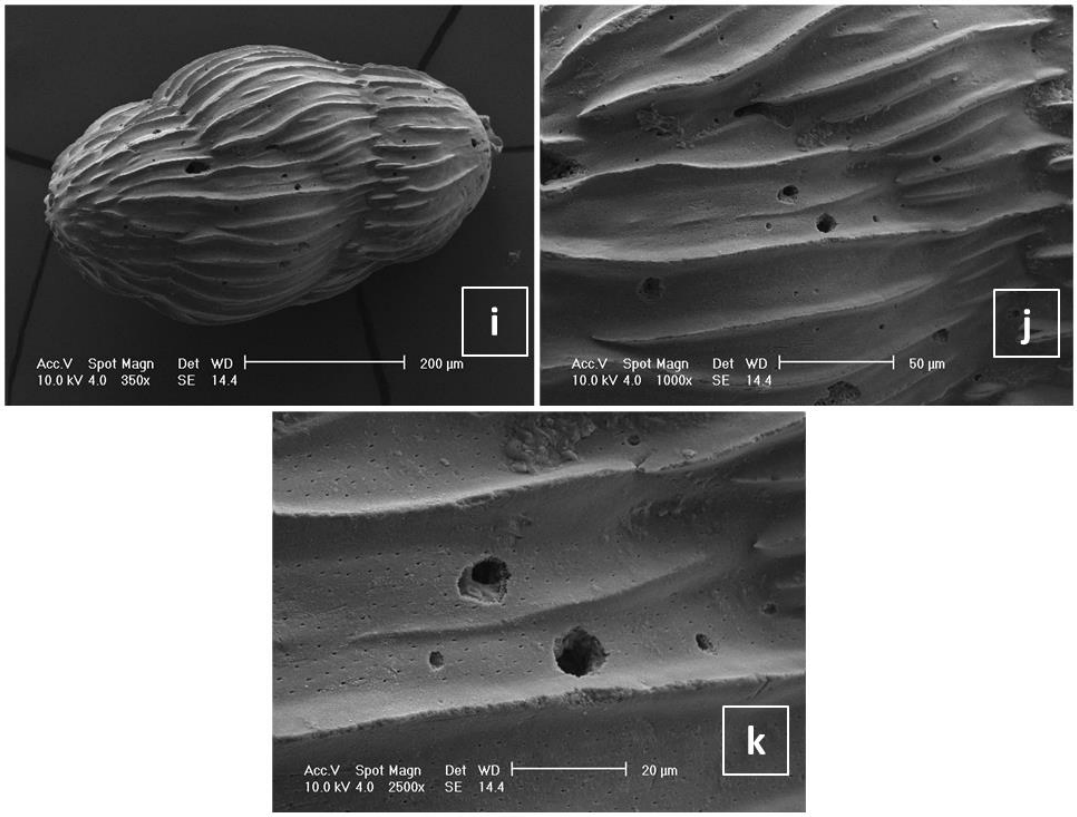

Figure 4.2 SEM images of microfossils (250-355 µm) from the Ras il-Pellegrin section, Blue Clay formation (Malta). (a) (b) Well preserved intact *Trilobatus trilobus* sample MT98 (13.053 Ma), clay rich lithology, (c)(d)(e)(f) primary pore structure clearly identifiable with characteristic hexagonal pore shape. Clay particles and nannofossils visible in some of the pores. (g) (h) interior chamber wall of *T. trilobus* fragment. Clear pore spaces and pore cross-section indicate lack of recrystallisation. (i) (j) (k) Infaunal benthic specimen of *Uvigerina* spp. sample MT116 (12.863 Ma), clay rich lithology. Well preserved specimen with no signs of recrystallisation or dissolution.

4.3 Results

4.3.1 Planktic and benthic microfossil preservation and potential for geochemical analysis

The lithology of the Ras il-Pellegrin section is known to be marly with a $CaCO_3$ content averaging 24% (Abels et al., 2005). The section is poorly consolidated and has been shown to be rich in planktic foraminifera (Mourik et al., 2011; Badger et al., 2013). Preservation of foraminifera microfossils is considered to be excellent, and this is confirmed through SEM analysis of *Trilobatus trilobus* and *Uvigerina* spp. (Figure 4.2). SEM Images show no evidence of post depositional recrystallisation or dissolution withfora and test walls in both planktic and benthic specimens being clearly defined (Figure 4.2 c,d,g,h,k).

4.3.2 The Ras il-Pellegrin stable isotope record.

The $\delta^{18}O$ record obtained from *Trilobatus trilobus* displays a gentle increasing trend towards heavier $\delta^{18}O$ from 13.7 to 12.9 Ma. Linear regression shows that the overall slope for this trend is ~0.8 ‰ Myr^{-1} (Figure 4.3a). High amplitude and high frequency variability is superimposed on this general trend. The amplitude of this variability tends to be higher during the initial part of the interval (~13.7 to ~13.4 Ma) with the lowest value being – 2.6 ‰ and highest value being – 0.6 ‰. This indicates that the early part of the interval tends to display a variability of around 1.5 to 2 ‰. The latter part of the interval (~13.4 to ~12.8 Ma) displays high frequency but lower amplitude variability than the initial part of the record. The amplitude variability (peak-to-peak) in this latter part of the interval is around 1 ‰.

The benthic $\delta^{18}O$ stable isotope record displays a generally gently sloping increase in $\delta^{18}O$ values from 13.7 Ma to 12.9 Ma. The rate of change obtained by linear regression is ~0.5 ‰ Myr^{-1} which is slightly less than that of the planktic oxygen isotope record (Figure 4.3b). The benthic $\delta^{18}O$ value increases by about 0.6 ‰ from a minimum value of 0.02 ‰ at 13.54 Ma to a maximum of 0.64 ‰ at 12.99 Ma during the whole interval. To summarize, the benthic $\delta^{18}O$ record is less variable than the planktic record but the

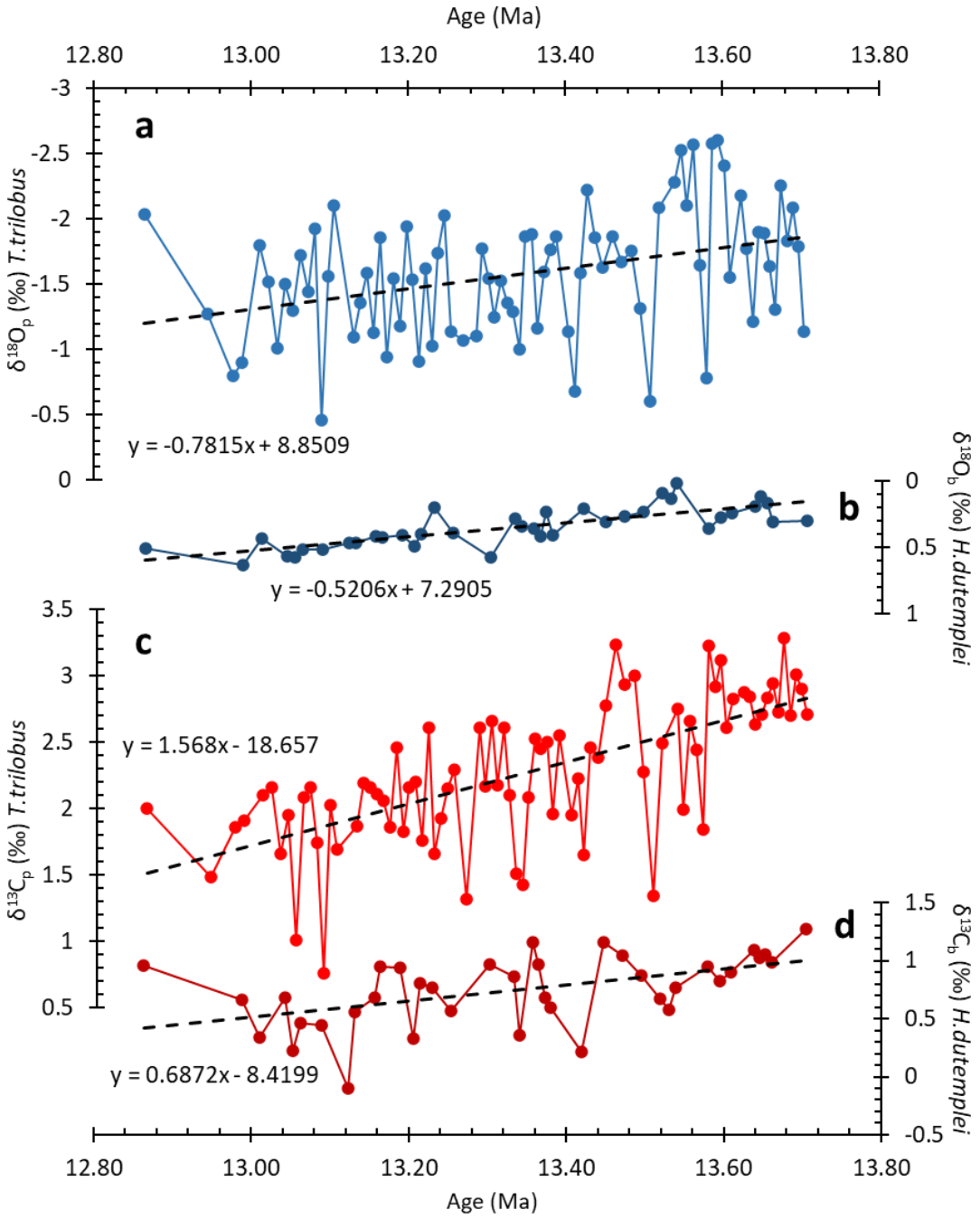

Figure 4.3 Planktic (*Trilobatus trilobus*) and benthic (*Heterolepa dutemplei*) $\delta^{18}O$ and $\delta^{13}C$ records from RIP section measured during this study. (a) (c) planktic stable isotope records, (b)(d) benthic stable isotope records. Linear regression indicates the overall trend for each of the stable isotope records.

two records show similar overall long-term trends with the planktic record displaying a slightly larger overall declining trend.

Both planktic and benthic $\delta^{13}C$ records demonstrate a trend towards lower values throughout the measured interval. The planktic record decreases at a rate of 1.6 ‰ Myr^{-1} while the rate of decrease for the benthic record is significantly lower at 0.7 ‰ Myr^{-1} (Figure 4.3c,d). The maximum value in the planktic record is 3.2 ‰ and the lowest is 0.76 ‰. Between 13.70 Ma and 13.58 Ma values are predominantly high with very little high frequency variability. The planktic $\delta^{13}C$ record tends to become more variable at high frequency from 13.58 Ma onwards with peak-to-peak amplitude variability of ~ 1 ‰ dominating the signal up to 13.27 Ma following which the high amplitude variability is less regular. The benthic $\delta^{13}C$ high frequency variability record is similar to the planktic record, but since this has a lower resolution than the planktic record many of the finer details that are present in the planktic record are not apparent. The maximum $\delta^{13}C$ value in the benthic record is 1.16 ‰ and the minimum is – 0.096 ‰ giving the Ras il-Pellegrin record a variability of ~1.1 ‰ through the interval.

4.3.3 The planktic and benthic Mg/Ca record, sea surface temperature (SST) and bottom water temperature (BWT) calculations.

The Mg/Ca ratio for the planktic species *Trilobatus trilobus* (Figure 4.4b) shows a general decrease from 13.70 Ma to 13.45 Ma, following which it remains steady until 13.28 Ma and gently increases thereafter. High frequency variability is observed throughout the whole interval. The maximum value is 5.9 mmol/mol while the minimum value is 3.5 mmol/mol. An Al/Ca threshold value of 200 µmol/mol was used to discard data points likely biased by residual clay material (Figure 4.4a). The degree of contamination following cleaning was also assessed by noting no significant correlation between Fe/Ca and Mg/Ca, Mn/Ca and Mg/Ca, and Al/Ca (below 200 µmol/mol threshold values) and Mg/Ca (Figure 4.5). This gives confidence in obtaining a reliable Mg/Ca palaeotemperature record.

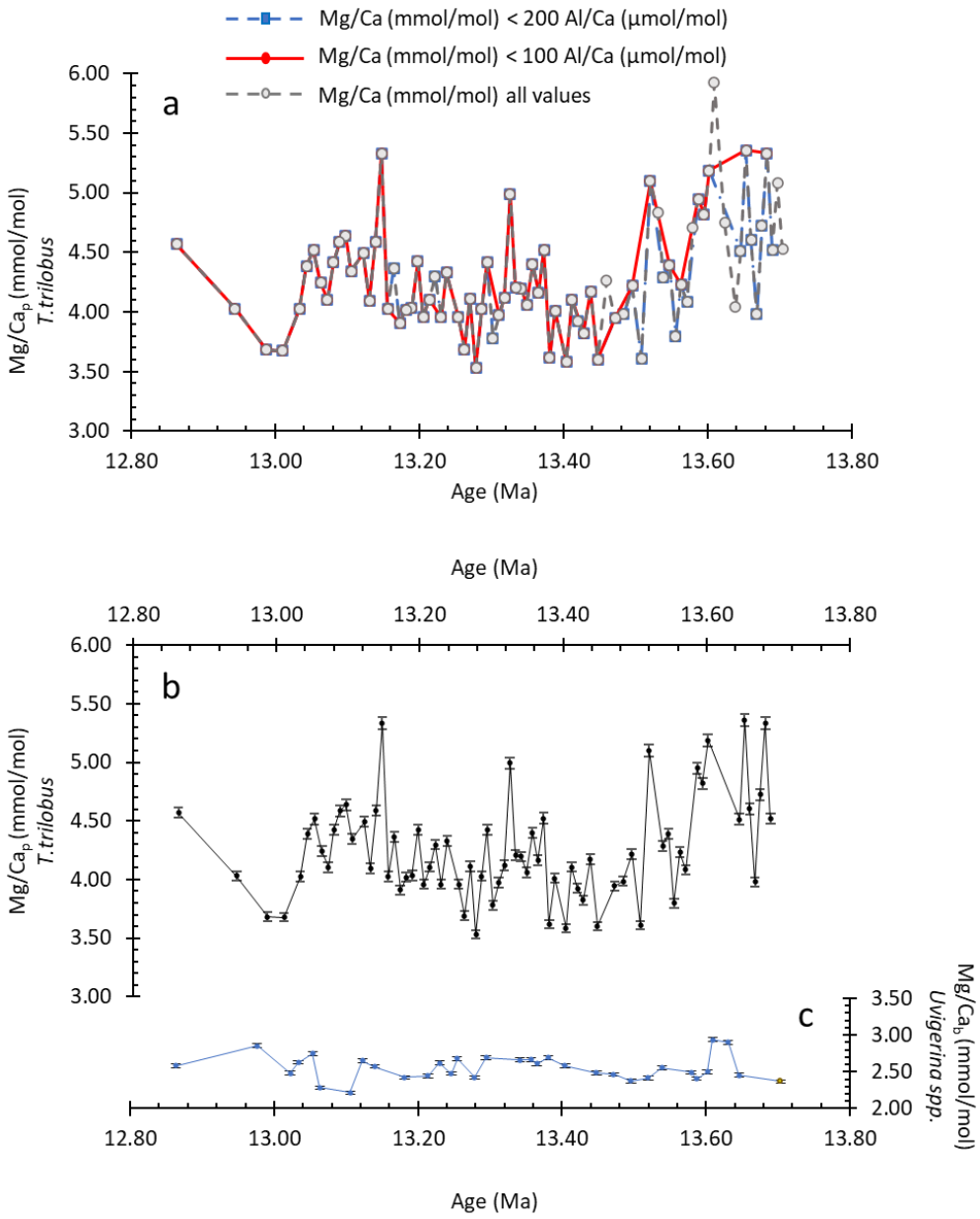

Figure 4.4 Planktic and benthic Mg/Ca from the Ras il-Pellegrin section. (a) Planktic Mg/Ca record indicating the full unscreened record (grey), the record where samples with Al/Ca > 200 µmol/mol have been removed (blue) and the record where samples with Al/Ca > 100 µmol/mol have been removed (red). (b) Planktic Mg/Ca record where samples with Al/Ca > 200 µmol/mol have been removed and (c) benthic Mg/Ca record (where the single sample with Al/Ca > 200 µmol/mol marked in yellow). Error bars indicate analytical error which for Mg/Ca is ≤ ±1%

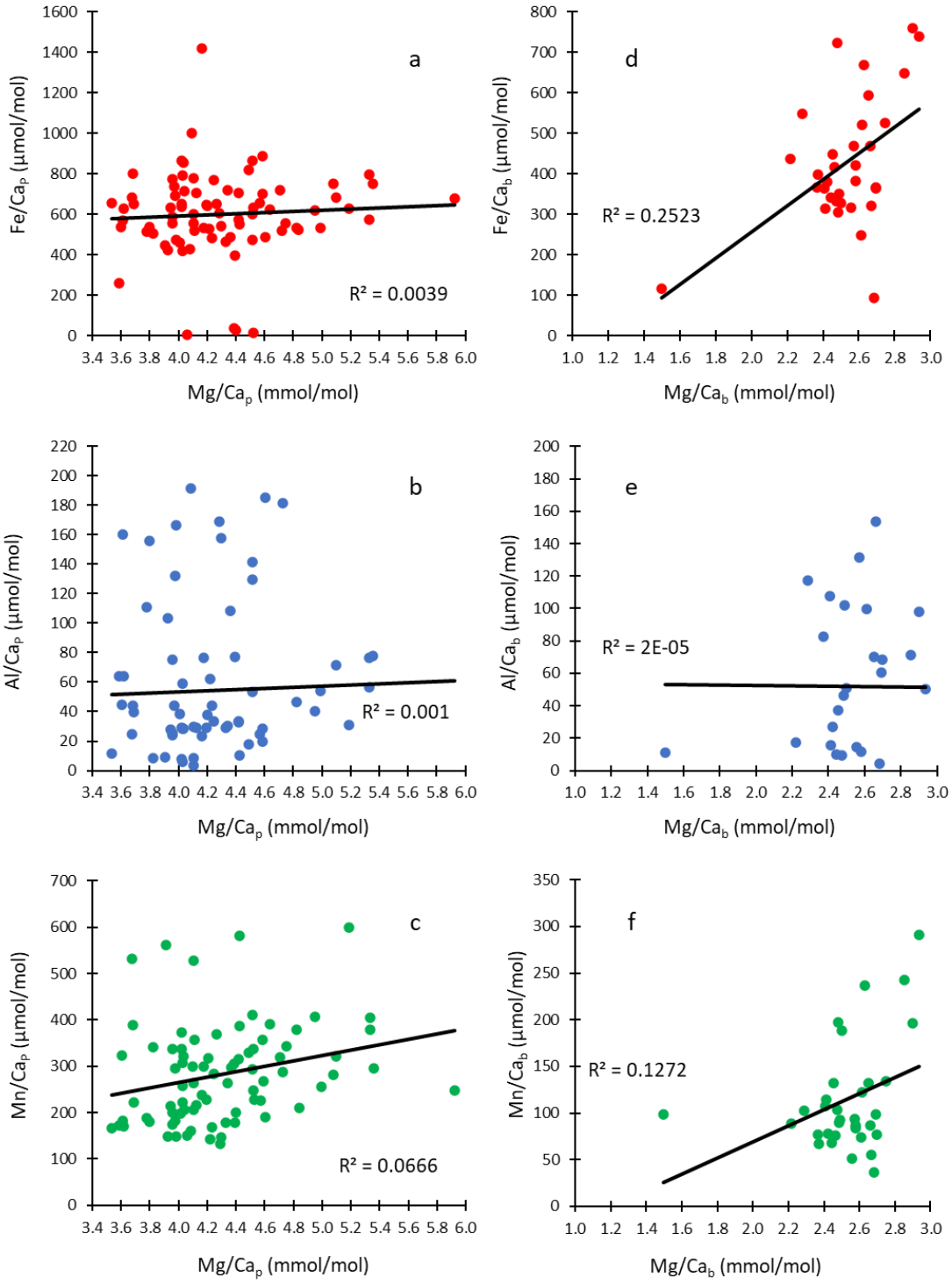

Figure 4.5 Correlations between possible contaminants for the Mg/Ca record. Fe/Ca, Al/Ca and Mn/Ca correlations with Mg/Ca (a)(b)(c) planktic record and (d)(e)(f) benthic record. No significant correlations are noted in either the planktic or the benthic record.

Sea-surface temperatures (SST) were calculated using a calibration for the modern day species *Trilobatus sacculifer* following (Sosdian et al., 2020; Sosdian & Lear, 2020) since the species *Trilobatus trilobus* is the morphotype for *T. sacculifer* (Spezzaferri et al., 2015). The Mg/Ca_F in the calcite shell of foraminifera is related to the sea-surface temperature, *T* by the equation:

$$\mathrm{Mg/Ca_F} = \left(\frac{\mathrm{Mg/Ca_{SW}}\ (t)}{\mathrm{Mg/Ca_{SW}}(0)}\right)^{C} Be^{AT} \quad (4.1)$$

where Mg/Ca_{SW} (*t*) represents the past seawater Mg/Ca ratio at age *t* and $Mg/Ca_{SW}(0)$ is the modern seawater Mg/Ca ratio of 5.2 mol/mol. The values of the constants are *A* = 0.09, *B* = 0.347, *C* = 0.41 (Evans & Mller, 2012). The value of Mg/Ca_{SW} (*t*) was calculated using equation 4.2 following Sosdian & Lear, (2020):

$$Mg/Ca_{SW}(t) = 5.3 - (0.153 \times t) + (0.00257 \times t^2) - (1.88 \times 10^{-5} \times t^3) + (4.85 \times 10^{-} \times t^4) \quad (4.2)$$

Using the $Mg/Ca_{SW}(t)$ values obtained from eq (4.2) and solving equation (4.1) the sea surface temperatures for the interval were calculated (Figure 4.6). Mg/Ca_{SW} does not vary significantly (from 3.6 mol/mol to 3.7 mol/mol) throughout the interval and therefore it impacts absolute temperature and salinity values but has no significant bearing on the temperature and salinity variations throughout the record. No correction for pH was conducted as it has been shown that *T. trilobus* Mg/Ca is insensitive to pH variability (Gray & Evans, 2019).

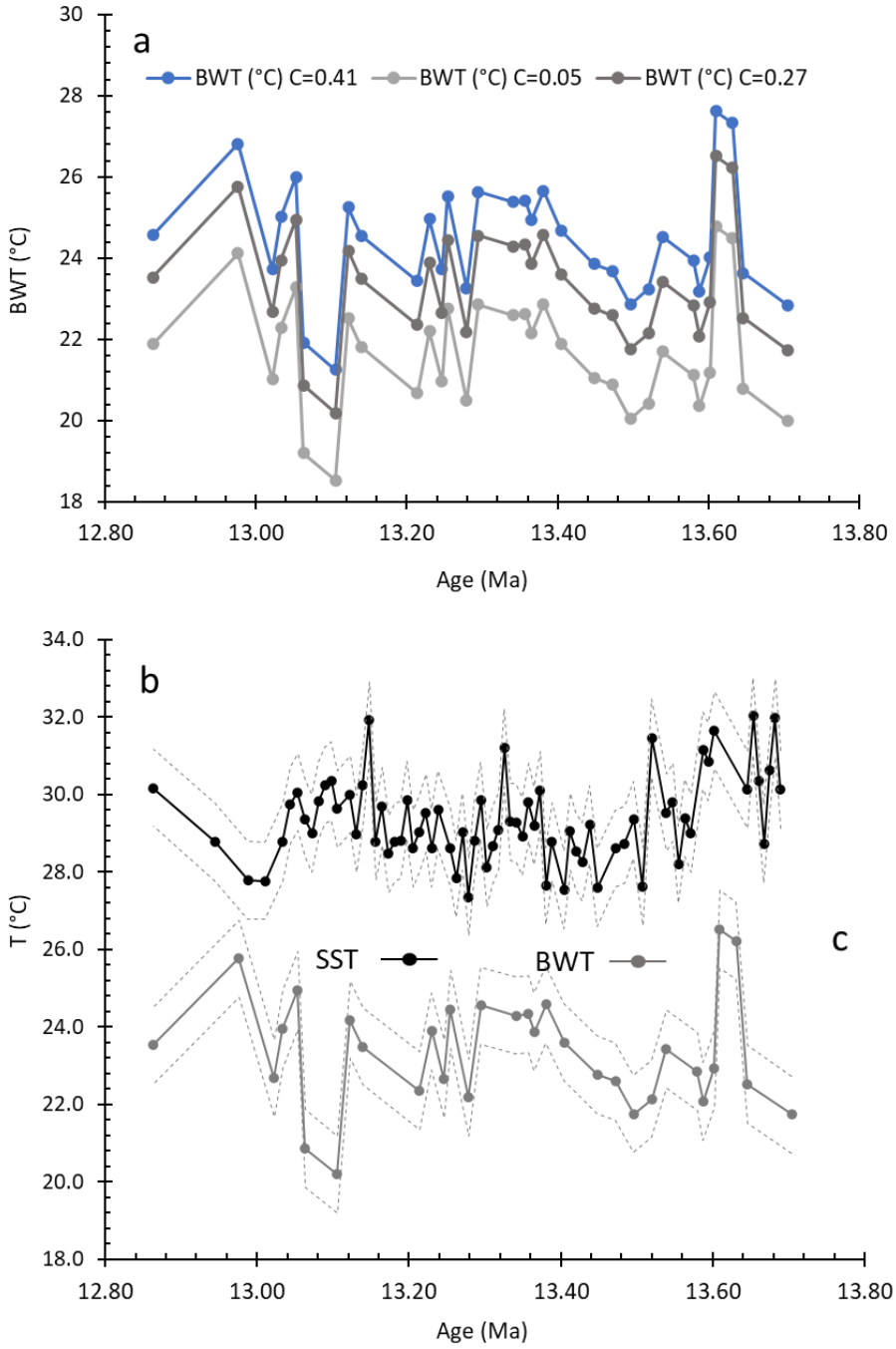

Figure 4.6 Mg/Ca SST and BWT records for the RIP section following the MMCT. (a) BWT obtained by three possible power constants. (b) SST record (c) BWT record using power constant C = 0.27. A sensitivity of ± 1° C applied in SST and BWT readings (dotted envelope). No salinity correction is applied as explained in text.

Salinity is expected to have a small effect on Mg/Ca and hence calculated SST. In order to avoid circular reasoning in the $\delta^{18}O_{sw}$ interpretations and salinity calculations, no salinity correction is applied to the Mg/Ca record. Instead, I evaluate the potential impact of this uncertainty by considering the sensitivity of the Mg/Ca to both temperature and salinity (Figure 4.7). Mg/Ca values increase with salinity by ~4.2%/PSU, whereas they increase with temperature by 10.5%/˚C (Gray & Evans 2019). Therefore, any real increase in sea surface salinity would tend to increase planktic Mg/Ca and lead to artificially high salinity reconstructions. The overall bias of these records is considered small relative to the signals reconstructed here, such that the reconstructed trends should be robust. Variations in the independent salinity proxy $\Delta\delta^{18}O_{sw}$ and calculated values in SSS will be compared to justify this approach (section 4.6.2).

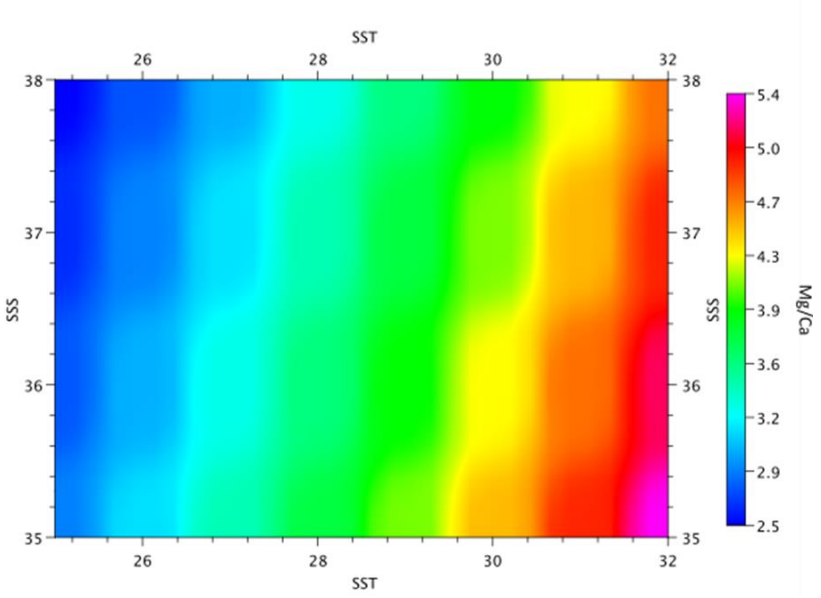

Figure 4.7 Sensitivity of foraminiferal Mg/Ca to Sea-Surface Salinity SSS and Sea-Surface Temperature SST (Gray & Evans, 2019)

Mg/Ca and other trace metal ratios were measured on benthic foraminifera from the genus *Uvigerina*. The Mg/Ca record displays minimal variation (Figure 4.4c). Correlation with the Al/Ca is not observed and only one Al/Ca value exceeds the 200 µmol/mol threshold. This sample was used in bottom water temperature (BWT) calculations since the Al/Ca is not excessively high (345 µmol/mol) and the Mg/Ca

value fits well in the general Mg/Ca trend for the RIP section. It is marked as a yellow data point in Figure 4.4c. Correlation with Fe/Ca and Mn/Ca is also low throughout the measured interval demonstrating effective cleaning procedure (Figure 4.5d,e,f). This allows for confident calculation of BWT. BWT were calculated using the equation:

$$\mathrm{Mg/Ca_F} = \left(\frac{\mathrm{Mg/Ca_{SW}}\ (t)}{\mathrm{Mg/Ca_{SW}}(0)}\right)^{C} Be^{AT} \tag{4.3}$$

Following (Elderfield et al., 2010 and Lear et al., 2015) where *T* is the BWT and *B* and *A* are constants. The values B = 0.98 and A = 0.045 were chosen for *Uvigerina* spp. specimens that have not been subjected to a reductive cleaning method (Elderfield et al., 2010). The power constant *C* is unknown for *Uvigerina* spp. Three different temperature calculations have been performed using *C* = 0.41 as for the planktic calculation, the power constant determined for the semi-infaunal species *O. umbonatus* by Lear et al., (2015) (*C* = 0.27), and a value of *C* = 0.05 to explore the possibility that *Uvigerina* spp. may have had an extremely low sensitivity to seawater Mg/Ca. BWT for the Ras il-Pellegrin section were compared with SST for the same section (Figure 4.6a), which suggests that the temperature data obtained with the power constant C = 0.27 is considered to yield the more likely absolute BWT values by considering the thermal gradient along the water column (Figure 4.6 b, c). Nevertheless, the uncertainty in the value of C does impact the absolute reconstructed SSTs. For context, a 1˚C temperature uncertainty in the *Uvigerina* spp. record will produce a ~0.25‰ uncertainty in reconstructed $\delta^{18}O_{sw}$.

Both the SST and BWT records display a rapid decline between 13.70 Ma and 13.50 Ma. Following this initial decline both records are rather steady until 13.28 Ma, following which there is an observable, gentle increase in both records. The maximum SST is 32°C at 13.65 Ma while the minimum SST is 27°C at 13.28 Ma. With regards to BWT the maximum value is 24°C at 13.61 Ma and the minimum BWT is 18°C at 13.11 Ma.

4.3.4 Surface and bottom water $\delta^{18}O_{SW}$ and sea surface salinity (SSS)

The $\delta^{18}O_{SW}$ obtained from planktic foraminifera represents a combined salinity and ice-volume signal while the benthic record is assumed to record the ice-volume signal exclusively. The relationship between $\delta^{18}O_{SW,}$ the planktic foraminiferal $\delta^{18}O_F$ and temperature, *T* (Erez & Luz, 1983) can be written as :

$$T = 17.0 - 4.52\,(\delta^{18}O_F - \delta^{18}O_{SW}) + 0.03\,(\delta^{18}O_F - \delta^{18}O_{SW})^2 \qquad (4.4)$$

The relationship between temperature *T*, $\delta^{18}O_{sw}$, and $\delta^{18}O_F$ for benthic foraminifera is given by equation (4.5). For *Uvigerina* spp*.*, the value of 0.47 ‰ is first subtracted from the $\delta^{18}O_F$ and then equation 4.5 is used to obtain $\delta^{18}O_{SW}$ (Marchitto et al., 2014).

$$(\delta^{18}O_F - \delta^{18}O_{SW} + 0.27) = -0.245T + 0.0011T^2 + 3.85 \qquad (4.5)$$

The average estimated $\delta^{18}O_{SW}$ for surface waters is 1.19 ‰ while that obtained from bottom waters is 1.77 ‰. The difference between the surface and bottom $\delta^{18}O_{SW}$ is expressed as $\Delta\delta^{18}O_{SW}$ and is considered to act as a proxy for the salinity at the surface. The $\Delta\delta^{18}O_{SW}$ was obtained by first linearly interpolating the surface $\delta^{18}O_{SW}$p and bottom $\delta^{18}O_{SW}$b data. The two interpolated records were subtracted from each other and a $\Delta\delta^{18}O_{SW}$ was obtained (Figure 4.8a).

Sea surface salinity was also determined by using the calculated $\delta^{18}O_{SW}$ of surface waters and applying the relationship between $\delta^{18}O_{SW}$ and SSS for the modern Mediterranean (Kontakiotis et al., 2022). Two possible relationships for Mediterranean surface waters can be applied, one with a slope of 0.25 ‰ /PSU and an intercept of – 8.2 (equation 4.6a) (Pierre, 1999) and the other with a slope of 0.28 ‰ /PSU and intercept – 9.24 (equation 4.6b) (LeGrande & Schmidt, 2006). Both yield very similar results, with the Pierre (1999) linear relation giving slightly higher SSS absolute values.

$$\delta^{18}O_{SW} = 0.25\,(SSS) - 8.2 \qquad (4.6a)$$

$$\delta^{18}O_{SW} = 0.28\,(SSS) - 9.24 \qquad (4.6b)$$

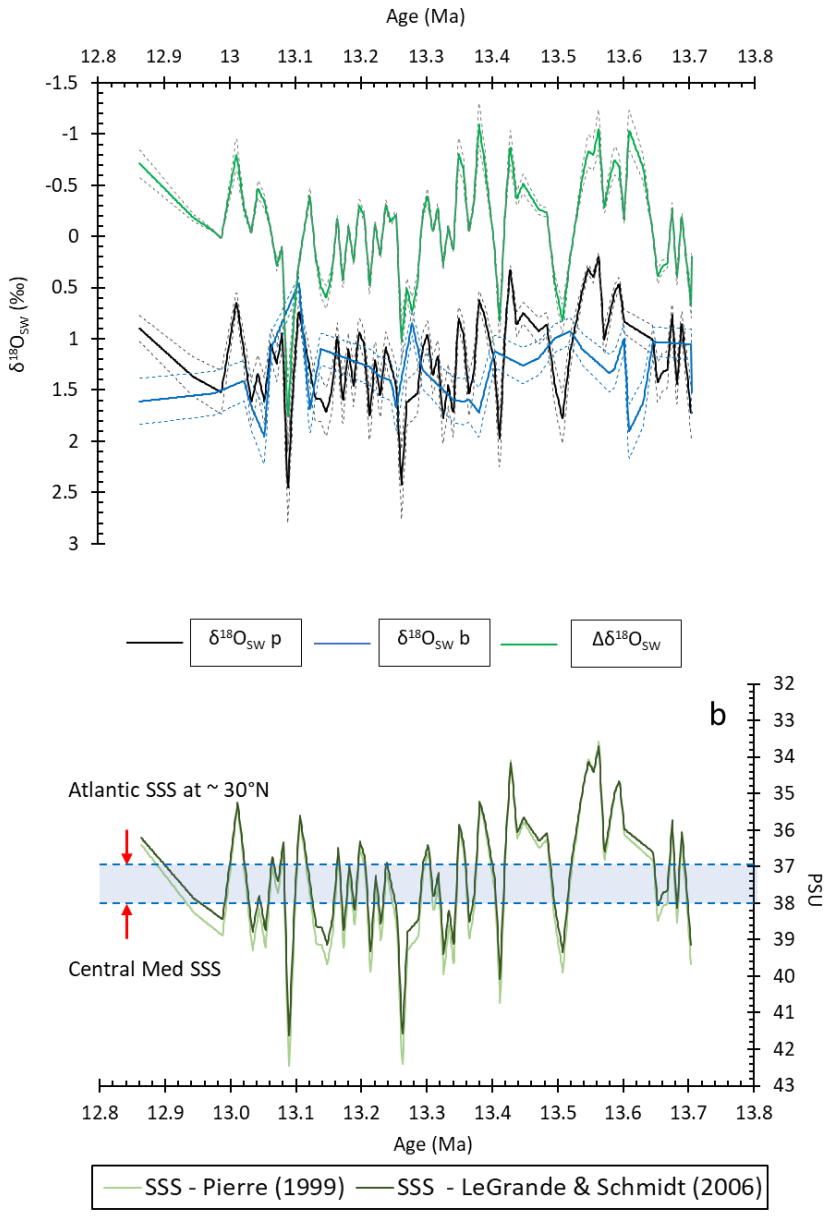

Figure 4.8 (a) Interpolated seawater stable oxygen isotope record**.** The $\delta^{18}O_{sw}$ p for the sea-surface (black) has high amplitude variability and acts as a combined proxy for both global ice-volume and local surface salinity. The bottom-water (~500 m) $\delta^{18}O_{sw}$ b (blue) excludes the local surface salinity, dotted lines indicate estimated error arising from temperature sensitivity of ±1 °C, this was estimated at around ±14%. The difference between the two $\Delta\delta^{18}$Osw (green) thus acts as a surface salinity proxy (propagated estimated uncertainty ±19%). (b) SSS salinity obtained by two possible linear relations. Light blue bar indicates modern day SSS range in the central Mediterranean and the Atlantic at 30°N and is used to identify times of high freshwater influx during the studied interval.

4.3.5 Spectral analysis

The planktic stable isotope record from Mourik et al., (2011), tuned to the new age model presented in this study, was subjected to spectral analysis. Spectral analysis was performed using Acycle software and applying a Blackman-Tukey power spectrum and Gaussian filtering (L.J. Lourens pers. comm., 2022). In general this reveals a planktic $\delta^{18}O$ dominated by a precessional signal and an obliquity signal shifted to ~48 kyr. The benthic $\delta^{18}O$ record is strongly dominated by long term trends.

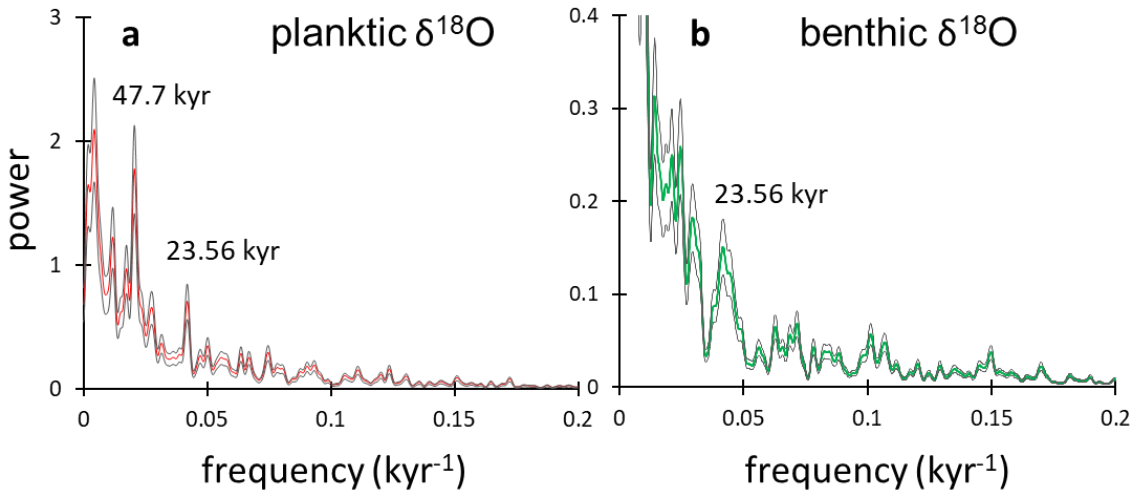

Figure 4.9 Power spectra for planktic (a) and benthic (b) $\delta^{18}O$ records with 20% Confidence intervals. Planktic record (a) shows a strong precession and obliquity control while the benthic record (b) is dominated by long-term trends.

4.4 Interpreting the Ras il-Pellegrin geochemical records

4.4.1 Foraminiferal preservation and integrity of geochemical records

It is important to consider post depositional preservation when interpreting geochemical records. Recrystallisation of planktic foraminifera tends to bias $\delta^{18}O$ and Mg/Ca to cooler and warmer temperatures respectively, whereas selective dissolution tends to bias both proxies to cooler temperatures (Pearson et al., 2001; Sexton et al.,

2006; Staudigel et al., 2022; Tripati et al., 2003). Preservation of both benthic and planktic species is considered to vary from good (Mourik et al., 2011) to excellent (Badger et al., 2013) for the Ras il-Pellegrin section with possible indications of dissolution in some samples from the Blue Clay and the Globigerina Limestone Formations, and calcite overgrowths in samples from the Globigerina Limestone Formation (Mourik et al., 2011). The clay-rich lithology is considered to inhibit recrystallisation of the foraminiferal fossil tests (Sexton & Wilson, 2009). The SEM images obtained during this study (Figure 4.2) indicate that any recrystallisation or dissolution effects were minimal, and that test preservation is generally excellent in the RIP section. Further SEM analysis of a larger number of specimens from different horizons within the section would be required to further validate this claim. Abundance of *Trilobatus trilobus* is also sufficiently high to enable selection of only those specimens that look well preserved (no indications of infills, overgrowths and staining in visual inspection). Benthic specimens were much less abundant, and care was taken to choose samples for stable isotope analysis (*H. dutemplei*) and trace metal analysis (*Uvigerina* spp.) which did not show significant indications of post depositional diagenesis. SEM images of *Uvigerina* spp. (Figure 4.2) indicate excellent preservation and no indication of recrystallisation or dissolution.

4.4.2 Paleoenvironment of the Central proto-Mediterranean from $\delta^{18}O$ and temperature records

The $\delta^{18}O$ records from RIP are interpreted in terms of factors that influence the $\delta^{18}O$ of planktic and benthic foraminifera. Foraminiferal $\delta^{18}O$ values incorporate a record of (i) global continental ice volume (ii) water temperature at the time and location of test formation (iii) evaporation and precipitation/runoff fluxes at the local site and (iv) possible post depositional diagenetic effects (Miller et al., 2005). Of these factors, the effects of evaporation and precipitation/runoff are highly unlikely to be preserved in the test of the epifaunal benthic species *Heterolepa dutemplei* as these effects are most significant in surface waters (Rohling, 2013). The species *Heterolepa dutemplei* is

considered to occupy the neritic, low-oxygen zone (Kováčvá et al., 2009) and the general interpretation of the depositional environment of the Blue Clay Formation supports this (Bellanca et al., 2002). The Blue Clay Formation has been estimated to have been deposited in a water depth of ~500 m in generally oxygen-poor conditions, based on benthic foraminifera and ostracod assemblages (Bellanca et al., 2002).

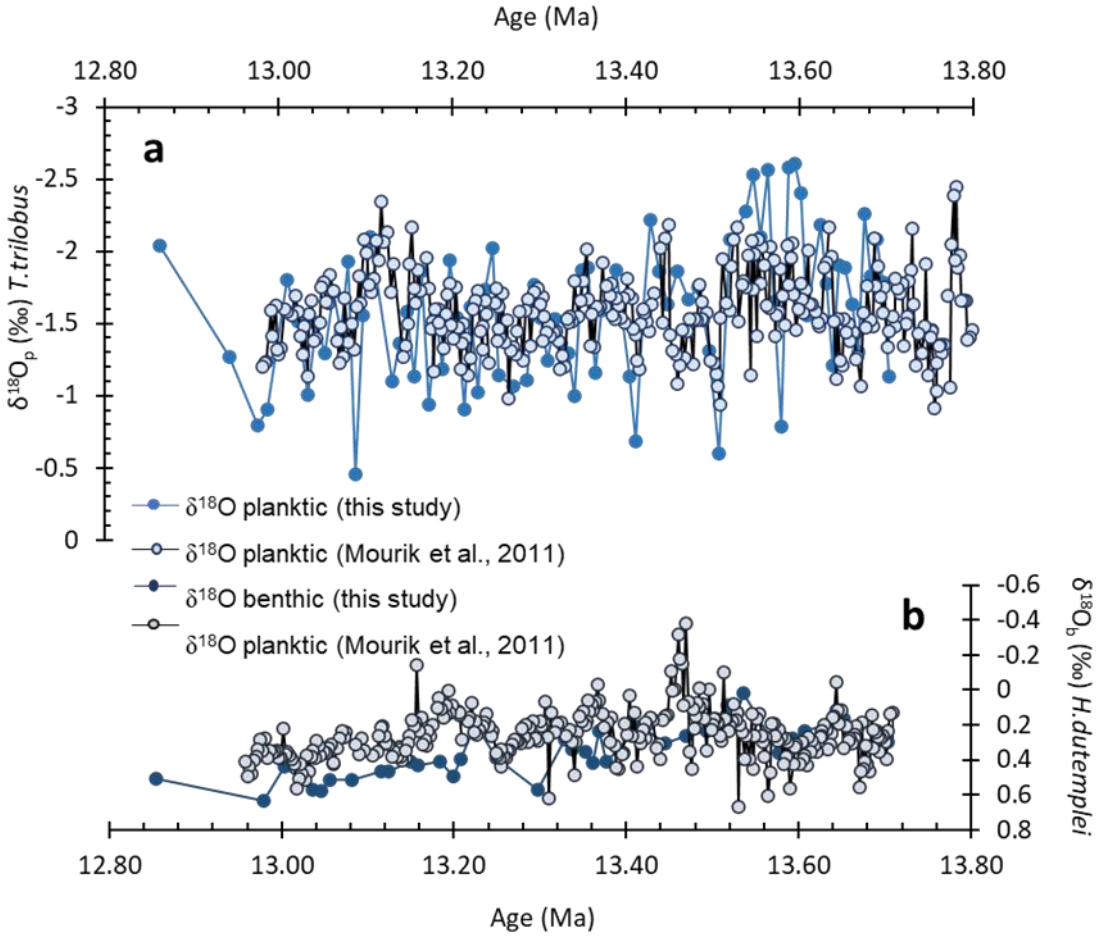

Figure 4.10 Planktic (a) and benthic (b) $\delta^{18}O$ records compiled during this study and compared with $\delta^{18}O$ for the same species as published in Mourik et al., (2011) and re-tuned to the age model developed during this study. Solid circles data from this study while open circles represent data originally published in Mourik et al., (2011).

When the Ras il-Pellegrin planktic and benthic records are compared it is clear that the planktic records presented here and in Mourik et al., (2011) (Figure 4.10a) have a

high-frequency, high-amplitude variability (2 to 1 ‰ change peak-to-peak). This high amplitude variability starts at 13.78 Ma just after the onset of the Blue Clay Formation, and persist for most of the Ras il-Pellegrin record (Figure 4.1c). This high-frequency variability is not evident in either the Ras il-Pellegrin benthic $\delta^{18}O$ (Mourik et al., 2011) (Figure 4.10b) record nor the Ras il-Pellegrin bulk isotope record (Abels et al., 2005) (Figure 4.1c) nor the fine fraction (<63 μm) bulk isotope record (Badger et al., 2013) (Figure 4.1c). It is also not represented in the global $\delta^{18}O$ benthic compilation (Westerhold et al., 2020) or in planktic $\delta^{18}O$ records from the Southern Ocean (Shevenell et al., 2004), Kerguelen Plateau-Southern Ocean (Majewski, 2010) and Indo-Pacific region (Sosdian & Lear, 2020). Therefore, as suggested in Mourik et al., (2011) the Ras il-Pellegrin planktic $\delta^{18}O$ record most likely demonstrates a strong, seasonal, evaporation-precipitation signal which reflects regional palaeoenvironmental processes. This seasonality signal is confirmed here by spectral analysis on the $\delta^{18}O$ data of Mourik et al., (2011) that has been re-calibrated to the CenoGRID and does not assume an orbital tuning (L.J. Lourens pers. comm. 2022) (Figure 4.9). This strong influx of fresh water into the system coinciding with the onset of the Blue Clay formation has previously been attributed to the intensification of humid climate over North Africa delivering clastic material (clay) and fresh water into the Central proto-Mediterranean (John et al., 2003). John et al. (2003) suggested that this overall intensification of humid climate was caused by the expansion of the Antarctic Ice-Sheet and the generation of a steep thermal gradient between the tropics and the South Pole with the ensuing northward shift of climate belts (John et al., 2003).

The calculated average SST is 29°C and the average BWT is 23°C, giving an average temperature difference between the water surface and the sea-floor of around 6.0 °C for the RIP section, although this value is dependent on assumed values for calibration constants (Section 4.3.3) (Figure 4.11). The average SST value is greater than the annually average mid-Miocene modeled SST of around 23 °C for the region (de la Vara & Meijer, 2016). Peak modern day SST around Malta have been recorded at 27.6 °C during July 2011 (Prendergast et al., 2013) and 28.2 °C during September

2012 and August 2013 (Deidun et al., 2016). The discrepancy between the Mg/Ca SST obtained from the RIP section and modelled values for the mid-Miocene could be explained by two possible factors. Firstly, it is possible that the SSTs obtained from planktic foraminifera *Trilobatus trilobus* are biased towards summer temperatures. The modern day planktic species *T. sacculifer* has maximum shell growth fluxes at temperatures greater than 25 °C that tends to occur towards the end of the summer season (Jonkers & Kučera, 2015). Therefore, it is reasonable to consider that SST obtained from Mg/Ca from *T. trilobus* may be biased towards late summer temperatures. Secondly, it is possible that the model underestimates the mid-Miocene warmth of the Mediterranean region.

The benthic $\delta^{18}O_{SW}$ record reflects changing global continental ice volume. Variability in the RIP benthic $\delta^{18}O_{SW}$ is low for most of the record with notable dips to lighter $\delta^{18}O_{SW}$ values at ~13.6 Ma (– 0.8 ‰), ~13.3 Ma (– 0.8 ‰) and ~13.1 Ma (–1.2 ‰) (Figure 4.12). These variations in the benthic $\delta^{18}O_{SW}$ are all on the order of 1 ‰ which for the Mediterranean is within the order of change expected during Pleistocene glacial-interglacial cycles (Paul et al., 2001). This may suggest retreat of the Antarctic Ice sheet during these three episodes. Such changes in Antarctic ice volume possibly had the effect of weakening the North African Monsoon by southward migration of the ITCZ. This could partly explain the close association of excess salinity following the negative oxygen isotope excursions in the benthic RIP record at ~ 13.3 Ma and ~ 13.1 Ma (Figure 4.12). With a weakening of the monsoonal rainfall and runoff, evaporation would have become the dominant control on surface waters giving rise to high salinity in the central proto-Mediterranean. This suggests that a close coupling between the waxing and waning of the Antarctic Ice Sheet and mid-latitude climate existed from ~13.5 Ma to ~ 12.8 Ma. (Figure 4.12)

It is also possible that part of the shift towards lighter benthic $\delta^{18}O_{SW}$ values during these three excursions resulted from the sinking of isotopically light water derived from freshening of the basin by precipitation and runoff. Modelling shows that such isotopically light waters can sink as far as 1000 m in the Western Mediterranean basin

by anti-estuarine circulation even during phases of stagnation such as sapropel deposition (Paul et al., 2001). This may suggest that at this time the Mediterranean basin started to undergo major changes in vertical water exchange.

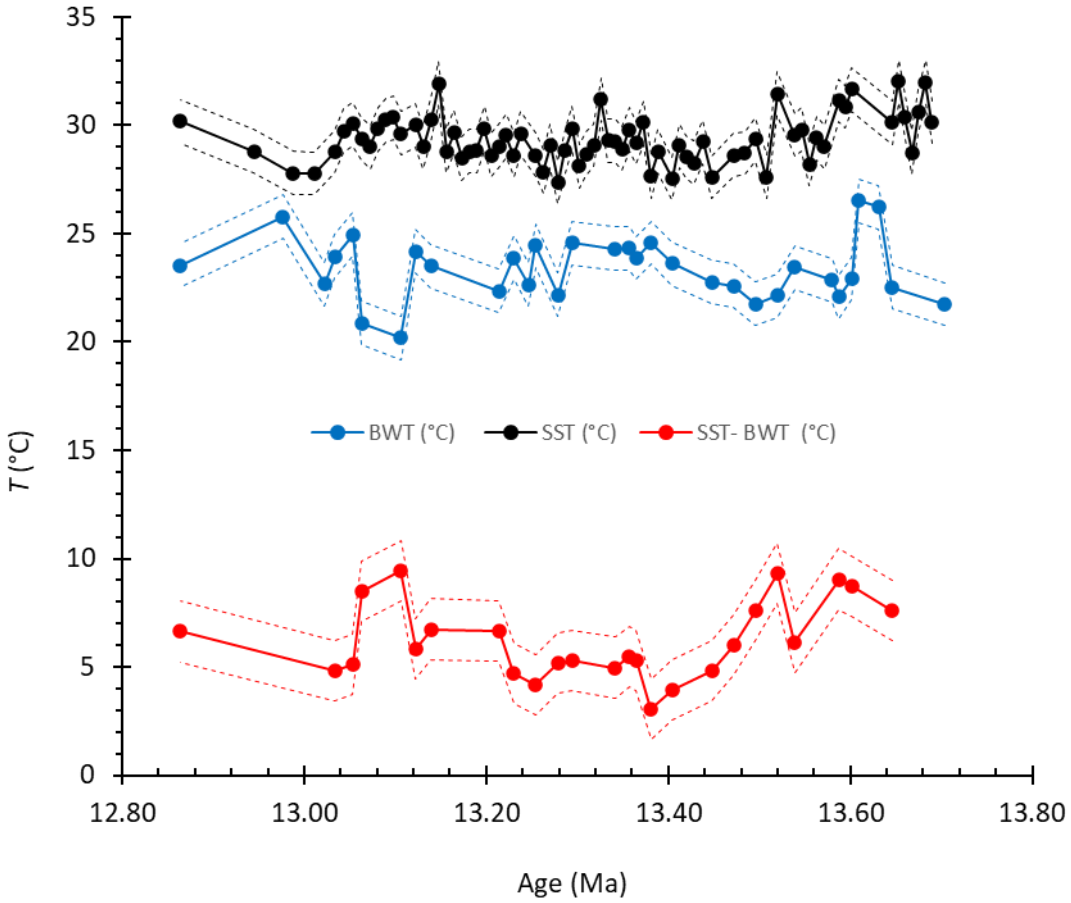

Figure 4.11 Difference between SST and BWT for the RIP section, dotted envelope indicates sensitivity of ±1 °C and propagated to ± 1.4 °C ($\delta(SST - BWT) = \sqrt{\delta(SST)^2 + \delta(BWT)^2}$) in the SST – BWT record. Average temperature difference ~6 °C

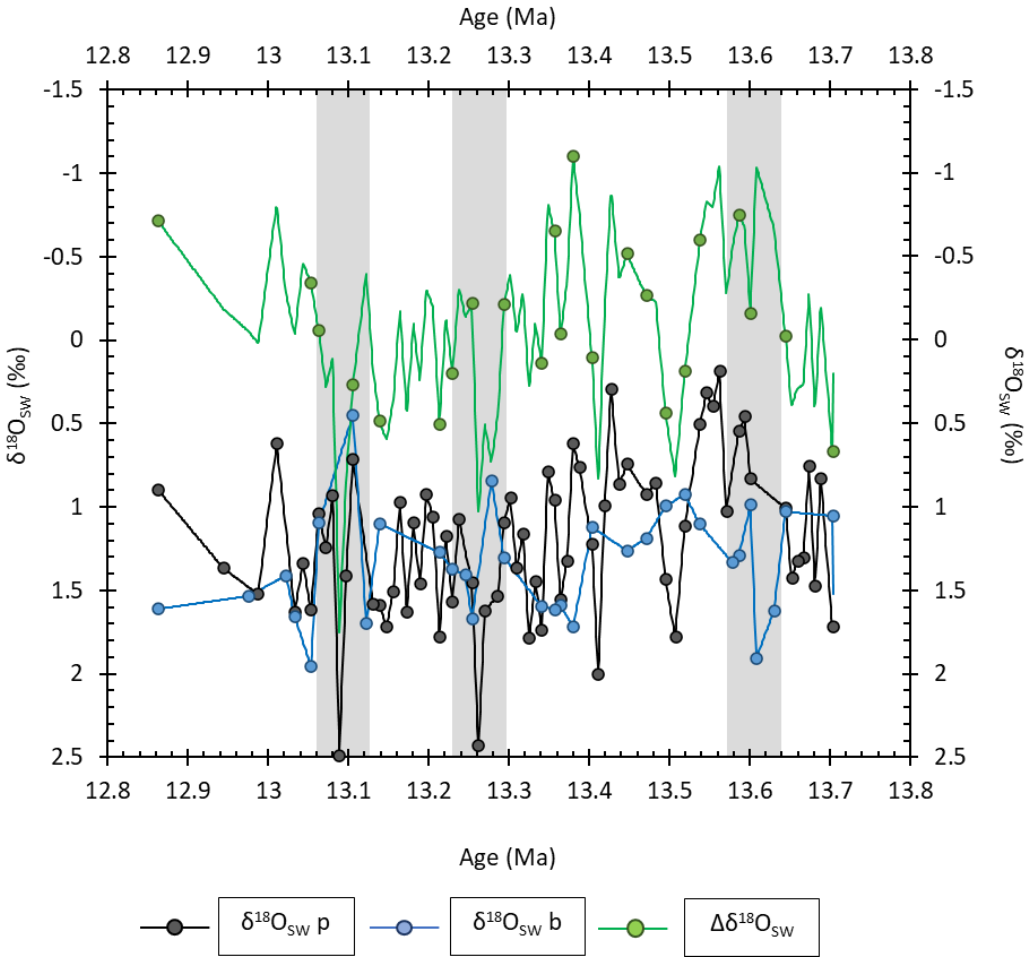

Figure 4.12 Surface water ($\delta^{18}O_{sw}p$) and bottom water ($\delta^{18}O_{sw}b$) stable oxygen isotope ratios measured data points shown as circles while solid lines represent linearly interpolated graphs. The difference between surface and bottom water stable oxygen isotopes ($\Delta\delta^{18}O_{sw}$) from data points (green circles) and from the interpolated graphs (green solid line). Grey bars indicate episodes of reduced $\delta^{18}O_{sw}b$ with the episodes at ~ 13.28 Ma and ~13.10 Ma coinciding with increased $\Delta\delta^{18}O_{sw}$ interpreted as an increase in surface salinity.

4.4.3 Central proto-Mediterranean salinity variability following the expansion of the Antarctic ice sheet

The difference between the $\delta^{18}O_{SW}$ obtained from the planktic and benthic records ($\Delta\delta^{18}O_{SW}$) represents the precipitation-evaporation component of the $\delta^{18}O$ planktic record and indicates the variations in salinity at the surface of the water. Reassuringly,

there is generally very good agreement with the variations in $\Delta\delta^{18}O_{SW}$ and calculated SSS (Figure 4.8). High amplitude variability is more prevalent in the older part of the record (~13.7Ma to ~13.32 Ma) with maximum changes in $\Delta\delta^{18}O_{SW}$ ~ 1.6 ‰. This maximum shift in $\Delta\delta^{18}O_{SW}$ is slightly higher than the measured shift in $\delta^{18}O_{SW}$ (~1.4 ‰) associated with outflow of the Niger River during the African humid period (14.8 Ka to 5.5. ka) (Demenocal et al., 2000). The determined SSS changes (max 5 PSU for the whole record)is overall lower than the changes in the late Miocene (Pre-Messinian Salinity crisis 7.2 Ma to 6.5 Ma) records from the Eastern Mediterranean (Greece) which exhibits a variability of 10 PSU at times (Kontakiotis et al., 2022). By comparing these SSS values with modern values for the central Mediterranean (~38 PSU) (Rohling et al., 2015) and the Atlantic at 30°N (~36.4 PSU) (Reverdin et al., 2007) it is possible to identify periods in the studied interval during which major input of fresh water occurred, superimposed on the precessional variability implied by the spectral analysis (Figure 4.8b). These periods of net input of fresh water occur in the earlier part of the record ~13.65 Ma to ~13.38 Ma and the final part ~13.10 Ma to ~12.98 Ma. Surface waters of the Central proto-Mediterranean tend to become saltier between ~ 13.34 Ma and ~13.12 Ma suggesting reduced influence of freshwater fluxes. Instances of very high salinity (~ 41 PSU) are recorded at 13.26 Ma and 13.09 Ma. The relation of the SSS variability (and the correlatable input of freshwater) with respect to local insolation and palaeoproductivity is further discussed in Chapter 5.

4.5 Global and Regional influences on the Central proto-Mediterranean temperature and salinity variability

The general trend in the SST and BWT records shows similarities with records from other locations. The initial part of the record shows a steep drop in both SST and BWT(Figure 4.6, 4.11) (~ 4°C in 200 kyr) following the Mi-3b oxygen isotope excursion (13.7 to 13.5 Ma), a trend that is somewhat also observed at Southern Ocean site 1172 (Kuhnert et al., 2009) and 1092 (Raitzsch et al., 2021). These trends tend to have good correlation with the pCO_2 records from the southern Ocean (Raitzsch et al., 2021) (Figure 4.13d,e).

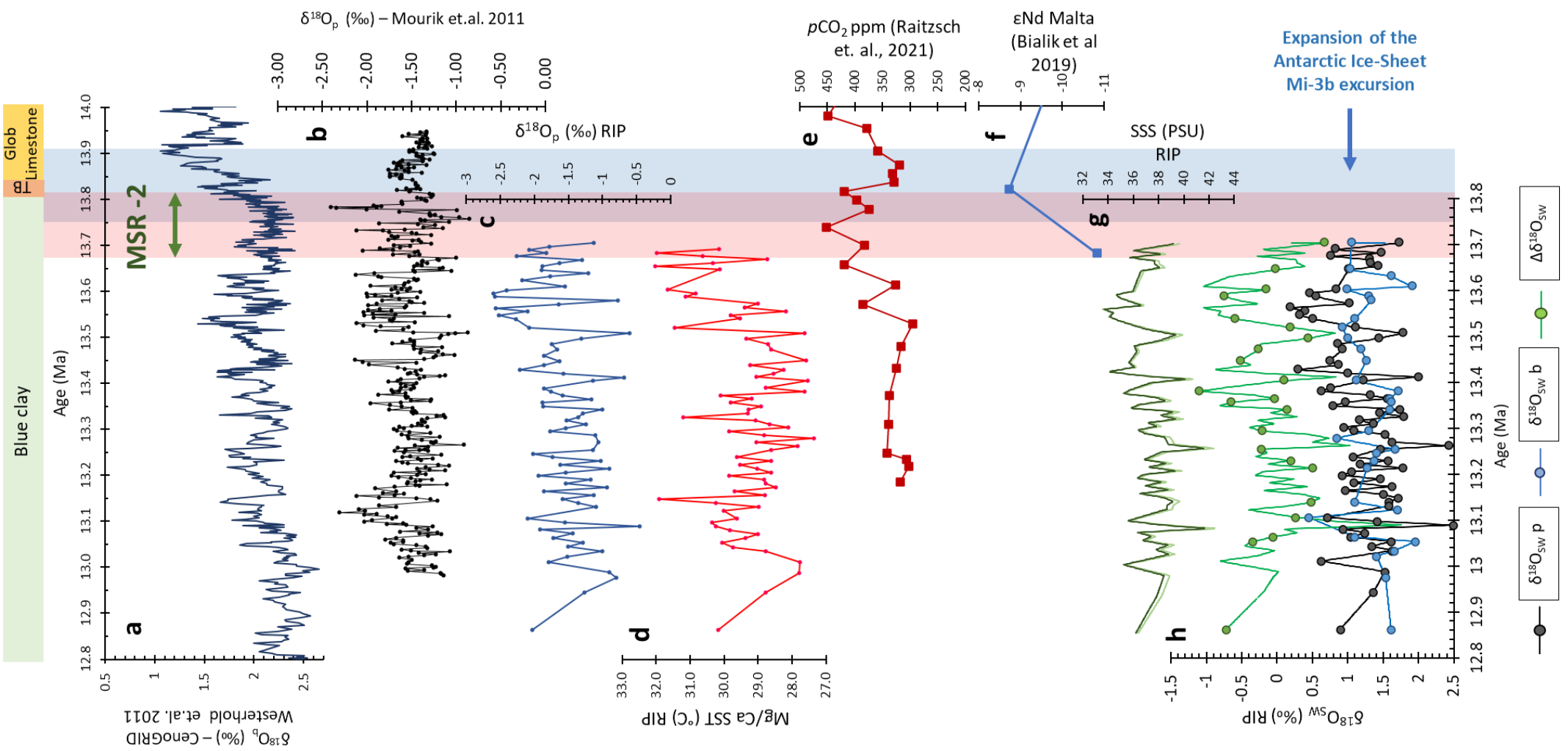
Glob
TB
Limestone
Blue clay
MSR -2
Age (Ma)
δ18Op (‰) – Mourik et.al. 2011
δ18Op (‰) RIP
pCO2 ppm (Raitzsch et. al., 2021)
εNd Malta (Bialik et al 2019)
SSS (PSU) RIP
Expansion of the Antarctic Ice-Sheet Mi-3b excursion
δ18Ob (‰) – CenoGRID Westerhold et.al. 2011
Mg/Ca SST (°C) RIP
δ18OSW (‰) RIP
δ18OSW p
δ18OSW b
ΔδδOSW
a
b
c
d
e
f
g
h

Figure 4.13 (a) Planktic $\delta^{18}O$ (*Trilobatus trilobus*) published in Mourik et.al. 2011 and re-tuned in this study. (b) Global benthic $\delta^{18}O$ compilation (Westerhold et al., 2020) with basic lithostratography of Malta in background (c) Planktic $\delta^{18}O$ (*Trilobatus trilobus*) (d) Mg/Ca sea-surface temperatures (e) Mid-Miocene atmospheric pCO_2 record (Raitzsch et al., 2021) (f) εNd data points from RIP marking the MSR-2 event (Bialik et al., 2019) (g) Sea-surface salinity (h) Seawater $\delta^{18}O$ for surface (blue) and bottom (~500 m) (dark grey) and difference in bottom and surface $\delta^{18}O$ values (green). All data in (c), (d), (f) and (g) from this study. Mesopotamian Seaway Restriction event 2 (MSR-2) represents the final and permanent closure of the Mesopotamian Seaway that connected the Indo-Pacific realm to the Atlantic realm via the Tethys Sea-way as identified in Bialik et. al. (2019).

However, owing to the higher resolution of the record presented here it impossible to make precise correlations. In the RIP record, this trend is reversed and a gentle rise in SST (~ 2 °C in 500 kyr) is observed from ~13.5 Ma to ~13.0 Ma. This trend is most likely also present in the BWT record (Figure 4.6b), but the lower resolution of this record does not allow the same confidence in interpretation as in the higher resolution SST record.

It has been shown that the intensification of the West African Monsoon system roughly coincided with the onset of the Blue Clay Formation (John et al., 2003) (Figure 4.13). The new ~9kyr resolution salinity-independent Mg/Ca SST record produced here allows for the first interpretation of the Mourick et al., (2011) planktic $\delta^{18}O$ record for the RIP section (Figure 4.13). The high amplitude variability in the Ras il-Pellegrin planktic $\delta^{18}O_{SW}$ and SSS records, that starts at 13.78 Ma, just after the onset of the Blue Clay Formation (Figure 4.1c, 4.13), confirms a strong local signal of varying influx of freshwater as suggested by Mourik et al., (2011). Such high amplitude variability as seen in the planktic but not in the benthic record can be explained by considering increased seasonal rainfall onto Western North Africa and subsequent run-off onto the central Mediterranean from active drainage systems in the Gulf of Sirte and the Gulf of Gabez (Hounslow et al., 2017).

4.6 The effect of the Middle Miocene closure of the Mesopotamian gateway on Antarctic ice sheet evolution and North African hydroclimate

The Middle Miocene expansion of the Antarctic Ice Sheet occurred in three steps (Holbourn et al., 2013) with the first step occurring ~14.6 Ma to 14.1 Ma and the larger second step starting at 13.82 Ma coinciding with the transition bed (TB) (Figure 4.13) that preceded the Blue Clay formation in Malta (Abels et al., 2005; Hilgen et al., 2009; Mourik et al., 2011; Badger et al., 2013; Holbourn et al., 2013; Raitzsch et al., 2021). Measurement of εNd tracer from RIP (Bialik et al., 2019) clearly shows that the Antarctic ice-sheet expansion and the ensuing sea-level drop (~ 50 m) (Miller et al., 2020) preceded the MSR-2 water flow restriction event (Figure 4.13f). Therefore, it can be concluded that this final disconnection between the Indo-Pacific realm in the East and the Proto-Mediterranean and Atlantic realm was driven by shoaling due to the eustatic drop associated with the expansion of the Antarctic ice sheet and not a result of tectonic movement.

4.6.1 Possible feedbacks on Antarctic cryospheric evolution

Fully coupled ocean-atmosphere general circulation models show that the MSR-2 event had important global climatic impact (Hamon et al., 2013). Models show that an open Mesopotamian gateway advects hot, dense Tethyan Intermediate Sea Water (TISW) into the Indian Ocean. The absence of TISW in the Indian Ocean has a tendency of generating a greater latitudinal density gradient which strengthens the Antarctic Circumpolar Current (ACC) (Hamon et al., 2013). The MSR-2 event would have also resulted in the advection of hot, dense Mediterranean intermediate waters into the Atlantic (de la Vara & Meijer, 2016) intensifying the Atlantic Meridional Overturning Circulation (AMOC) (Hamon et al., 2013). This can also enhance the ACC by generating a stronger latitudinal pressure gradient in the Atlantic Ocean. Therefore MSR-2 may have strengthened the ACC and thermally isolated Antarctica by influencing the dynamics of both the Indian and the Atlantic Oceans. This indicates that MSR-2 event may represent an important positive feedback in the Middle Miocene expansion of the Antarctic Icesheet. The εNd tracer data from RIP shows

unequivocally (Figure 4.13f) that the MMCT preceded the MSR-2 step restriction and therefore rules out the previously suggested (Woodruff & Savin, 1989; Flower & Kennett, 1994; Ramsay et al., 1998) possibility of low latitude gateway restriction being the main driver for the MMCT. Instead, modelling coupled with the refined age model for the RIP section provided in this study indicates that MSR-2 event may have provided an important positive feedback in sustaining the permanent growth of the Antarctic ice sheet by aiding the intensification of the ACC and keeping Antarctica thermally isolated from the world's oceans (de la Vara & Meijer, 2016; Hamon et al., 2013).

4.6.2 Onset of the West African Monsoon during the MMCT

Land-ocean interactions along the Atlantic coast of western North-Africa may also have played a part in the onset of monsoonal type climate as suggested in Zammit et. al., (2022). From a more regional perspective the data presented here indicates a strong, seasonal monsoonal type climate being established at 13.78 Ma. The large variations in SSS can be explained by considering large fluxes of fresh water from North Africa. These fluxes have good correspondences with precessional and obliquity cycles (Figure 4.9) suggesting seasonal control on the regional hydrologic cycle. Bottom water behavior follows long-term trends suggesting that the bottom waters of the partially enclosed proto-Mediterranean were still closely coupled with global changes in temperature. The effect of this new hydroclimatic regime on local regional productivity is explored in Chapter 5.

4.7 Conclusion

Coupled oxygen stable isotopes and Mg/Ca records from the Ras il-Pellegrin section in Malta have allowed for the determination of surface and bottom water temperatures in the central Mediterranean following the Middle Miocene expansion of the Antarctic Ice Sheet. The temperature and isotope records indicate that surface water conditions were influenced by the periodic influx of fresh water from North African river systems.

Spectral analysis also suggests a strong coupling between variability in planktic $\delta^{18}O$ record and precession and obliquity cycles. These geochemical records from the Ras il-Pellegrin section indicate that a monsoonal type climate was emplaced over western North Africa following the expansion of the Antarctic Ice-sheet at 13.82 Ma (Mi-3b oxygen isotope excursion). North African climate became wetter likely due to the northward migration of the ITCZ due to ensuing thermal gradient increase following Antarctic glaciation. The closure of the Mesopotamian Gateway into the Mediterranean was likely mediated by the sea-level drop associated with the Mi-3b excursion. In turn the changes in low-latitude ocean circulation induced by the closure of the gateway may have acted as positive feedback in the thermal isolation of Antarctica and further aided the intensification of the hydrological cycle over North Africa. This study indicates close coupling between cryosphere-atmosphere and ocean circulation following large scale expansion of Antarctic Ice Sheet during the Middle Miocene Climate Transition.

Chapter 5

Regional palaeoproductivity around the Mid-Miocene Climate transition and its influence on the global carbon cycle. A case study using foraminiferal B/Ca and Mn/Ca proxies from Malta.

Chapter 5 – Regional palaeoproductivity around the Mid-Miocene Climate transition and its influence on the global carbon cycle. A case study using foraminiferal B/Ca and Mn/Ca proxies from Malta.

5.1 Introduction

5.1.1 The global carbon cycle during the Middle Miocene

The Miocene climatic optimum (MCO) (~17 Ma to 14.7 Ma) represents a lengthy warm period of elevated atmospheric pCO_2 (Figure 5.1). Peak warmth occurs at ~15.6 Ma coinciding with negative excursion of ~0.8 ‰ in the global benthic $\delta^{13}C$ and $\delta^{18}O$ records (Holbourn et al., 2015). The MCO is associated with the Monterey Event (Flower & Kennett, 1993), a long term positive excursion in the global benthic $\delta^{13}C$ record referred to as the Monterey Carbon Isotope Excursion (MCIE) (Vincent & Berger, 1985). This coincides with deposition of the Monterey Formation in Southern California, an extensive organic carbon rich formation in which the Monterey $\delta^{13}C$ long-term positive excursion is expressed (Vincent & Berger, 1985). This excursion in the marine carbon isotope record has also been recorded in the pelagic records from the Central Mediterranean island of Malta (Jacobs et al., 1996). The MCO is followed by the Middle Miocene Climate Transition (MMCT) (~14.7 Ma to ~ 12.8 Ma), a step-wise transition into a colder climatic regime (Holbourn et al., 2013). The MMCT is associated with expansion of the Antarctic Ice Sheet and a decline in atmospheric pCO_2 levels (Foster et al., 2012). The largest positive oxygen isotope excursion of the MMCT (Mi-3b) ends at 13.82 Ma coinciding with the Langhian-Serravallian boundary (Figure 5.1) (Hilgen et al., 2009; Mourik et al., 2011). The GSSP for the base of the Serravallian is situated at Ras il-Pellegrin (RIP) in Malta and occurs in the transition bed (TB) between the Globigerina Limestone Formation and the Blue Clay Formation (Chapter 4, Figure 4.1) (Hilgen et al., 2009).

The MCIE was originally considered to represent a ~4 million year interval during which global temperature plummeted and Antarctic Ice Sheet expansion occurred (Vincent & Berger, 1985). In this scenario it was assumed that the extended positive $\delta^{13}C$ excursion was a response to enhanced productivity associated with global cooling. It was suggested that the increase in polar to low latitude thermal gradient

associated with expansion of the Antarctic Ice Sheet enhanced upwelling systems leading to enhanced productivity at low latitude coastal zones like the Monterey Formation (Vincent & Berger, 1985).

The general expression of the long term MCIE was originally viewed as the amalgamation of a series of positive $\delta^{13}C$ excursions termed CM (carbon maxima) events. Six CM events have been identified, some of which are further divided into different peaks (Figure 5.1) (Woodruff & Savin, 1991). In general, it has been assumed that these $\delta^{13}C$ peaks represent enhanced burial of organic carbon and drawdown of atmospheric CO_2 (Flower & Kennett, 1993; Vincent & Berger, 1985; Badger et al., 2013; Sosdian et al., 2020). Further evaluation revealed that some of these peaks are split into double-peaks and occur every ~400 kyr , indicating an astronomical pacing (long eccentricity cycle) on the Middle Miocene carbon cycle (Holbourn et al., 2007; Woodruff & Savin, 1991). However, the long-term MCIE has recently been reinterpreted to represent a carbon cycle perturbation driven by the ejection of CO_2 into the atmosphere during the formation of the Columbia River Flood Basalts (Sosdian et al., 2020). The MCIE extended $\delta^{13}C$ plateau was associated with an increase in surface water dissolved inorganic carbon (DIC) and global warming driven by the volcanic event (Sosdian et al., 2020). In this interpretation the CM-events superimposed on the long-term MCIE represent orbitally paced enhanced productivity events that occur during a time of global warming. These CM-events are therefore interpreted as negative feedback events which reduced atmospheric pCO_2 during the Middle Miocene warming and helped stabilize climate (Sosdian et al., 2020).

The final CM event (CM-6) of the MCIE occurs as a double peak (Diester-Haass et al., 2013). CM-6 has a longer duration and larger magnitude than the other carbon maxima, and occurs at a time when the warmth of the MCO is declining and the Antarctic Ice Sheet significantly expanded, as evidenced by the Mi-3b positive oxygen isotope excursion occurring just before the CM-6a $\delta^{13}C$ peak (Figure 5.1) (Badger et al., 2013). It has therefore been suggested that CM-6 represents a very different negative feedback in the climate system (Pagani et al., 1999).

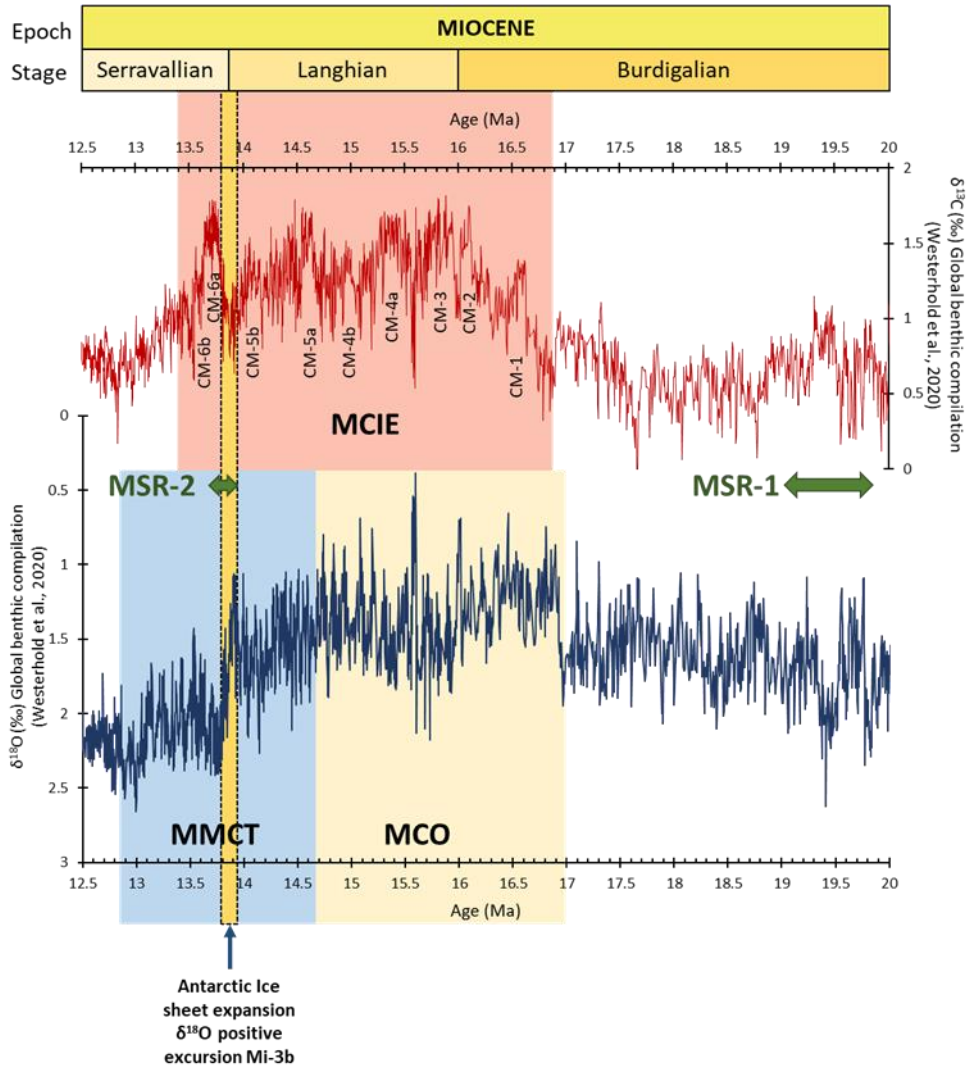

Figure 5.1 Early to Middle Miocene Global benthic stable isotope record (Westerhold et al., 2020). The Miocene Climatic Optimum (MCO) represents a long phase of global warmth. The extended positive excursion in the $\delta^{13}C$ record representing the Monterey Carbon Isotope Excursion (MCIE) is punctuated by six positive carbon maxima (CM) events. The CM-6 event occurs during the Mid-Miocene Climate Transition (MMCT) and is the largest positive $\delta^{13}C$ excursion. MSR-1 and MSR-2 (Mesopotamian Seaway Restriction events) represent Early and Middle Miocene events of restriction of water flow through the Mesopotamian Seaway respectively (Bialik et al., 2019).

The expansion of the Antarctic Ice Sheet associated with the Mi-3b excursion would have blanketed vast amounts of land area, reducing chemical weathering, and resulting in an increase in atmospheric pCO_2 (Pagani et al., 1999; Shevenell et al., 2008). This is similar to the mechanism proposed during the EOT (Oi-1 $\delta^{18}O$ excursion) Antarctic Ice Sheet expansion (Lear et al., 2004). However, using

foraminiferal $\delta^{11}B$ records from the RIP section in Malta, Badger et al., (2013) suggested that atmospheric pCO_2 declined following the Mi-3b $\delta^{18}O$ excursion, indicating that CM-6 was associated with decreasing, and not increasing, pCO_2. This led to the proposal that CM-6 actually represented a positive feedback in the climate system, with enhanced organic carbon burial linked with steep polar to low latitude gradients associated with the expansion of the Antarctic Icesheet (Badger et al., 2013).

Although it is well established that the long-term MCIE and CM events are global in extent, it is unclear whether the individual CM peaks represent global or regional productivity signals. Enhanced export productivity has not been clearly linked with the timing or amplitude of the $\delta^{13}C$ positive excursions at high productivity sites DSDP Site 588 (South Pacific), ODP Site 1171 (South Tasman Rise), or ODP Site 747 (Kerguelen Plateau) (Diester-Haass et al., 2013). This suggests that these CM events do not necessarily represent a global palaeoproductivity record and that enhanced palaeoproductivity during these events may have been localized in some regions more than others.

The final CM event, the double peaked CM-6, is particularly intriguing and occurs against a backdrop of increasing Antarctic ice cover (Raitzsch et al., 2021). The link between the final CM-6 and atmospheric pCO_2 drawdown is currently unclear. Only two high resolution atmospheric CO_2 records across the CM-6 excursion have been published, one from the RIP section in Malta and one from the Southern Ocean (ODP Site 1092) (Badger et al., 2013; Raitzsch et al., 2021). Although both records indicate a decline in atmospheric CO_2 associated with the MMCT prior to the onset of CM-6, the RIP record indicates declining pCO_2 during the CM-6 interval while Southern

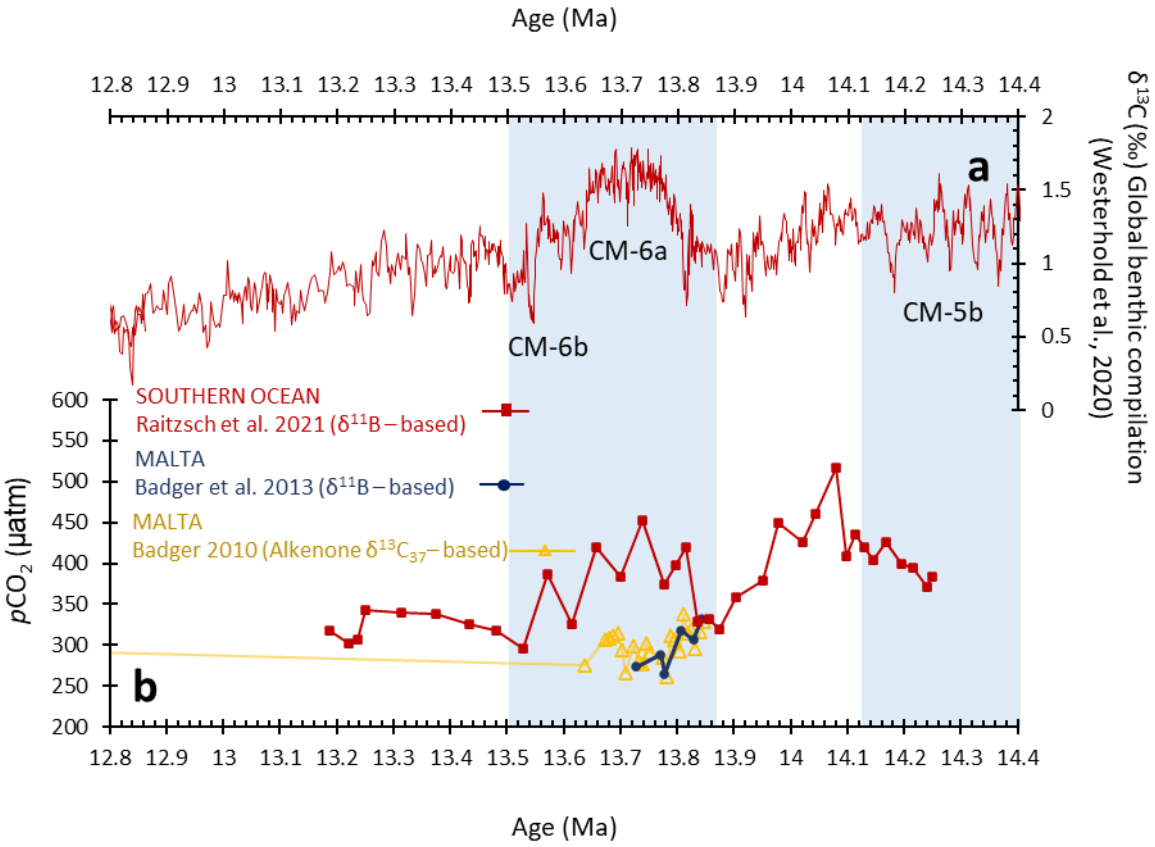

Figure 5.2 (a) CM – events 5b, 6a and 6b in the global benthic record of Westerhold et. al., (2020) $\delta^{13}C$ compared with (b) pCO_2 records from the RIP section (Badger et al., 2013) and from the Southern Ocean (Raitzsch et al., 2021). CO_2 records from Malta decrease during CM-6 (shaded box), while those from the Southern Ocean increase and correlate with the CM-6 event.

Ocean ODP Site 1092 shows a close correlation between the benthic $\delta^{13}C$ and a rise and decline in pCO_2 during CM-6 (Figure 5.2) (Badger et al., 2013; Raitzsch et al., 2021). This raises the possibility that surface waters at either RIP and/or ODP Site 1092 were not in equilibrium with the atmosphere, and that one or both sites recorded regional rather than global carbon cycle signals during the MMCT. For the case of Malta, one possible cause of disequilibrium between surface waters and the atmosphere could be enhanced surface productivity associated with increased runoff from North Africa (Bellanca et al., 2002; Mourik et al., 2011). For the Southern Ocean record (ODP Site 1092), surface water chemistry may have been impacted by the local migration of the polar front, although this is perhaps not supported by the accompanying rather low and constant opal and C_{org} accumulation (Raitzsch et al., 2021). Raitzsch et al., (2021) therefore propose that the transient pCO_2 increase

reconstructed at ODP Site 1092 reflects a global signal, caused by enhanced ocean ventilation essentially "burping" CO_2 from the deep ocean reservoir into the atmosphere. This mechanism would represent a negative feedback associated with the expansion of the Antarctic Ice Sheet, and furthermore implies that the RIP Malta pCO_2 record is dominated by a local/regional signal.

In order to investigate further the carbon cycle changes through the MMCT at Malta, high resolution (~9 kyr) foraminiferal isotope and trace metal records from the Marsalforn (MRSF) (Langhian) and the Ras il-Pellegrin (RIP) (Serravallian) sections are presented in this study. These records reveal orbitally paced variations in regional productivity that may contribute to the global $\delta^{13}C$ record. CM-6 was likely associated with drawdown of CO_2 through an enhanced biological pump, but the impact of this was likely outweighed by the improved ventilation of the deep ocean, which redistributed previously sequestered CO_2 to the atmosphere.

5.1.2 Carbon stable isotope systematics and insights from foraminiferal B/Ca and Mn/Ca

Foraminiferal stable isotope ratios of carbon ($\delta^{13}C$) can be useful indicators of carbon cycle dynamics and when combined with the B/Ca from the same samples allows for a more detailed interpretation (Mackensen & Schmiedl, 2019). The $\delta^{13}C$ record from planktic foraminifera is influenced by changes in the mean isotopic composition of dissolved inorganic carbon (DIC) of the oceans and local water masses (Rohling et al., 2004). The former is influenced by geological processes including volcanism, weathering, metamorphism and carbonate and organic carbon burial (e.g., Hilting et al., 2008; Shackleton, 1987). Seawater $\delta^{13}C$ values are also influenced by photosynthetic fractionation (the magnitude of which is in turn dependent on [CO_2]), vertical water mixing, the ratio of the flux of organic carbon to total carbon transferred from surface waters to the deep ocean, and air-sea gas exchange (Hilting et al., 2008). Furthermore, the measured $\delta^{13}C$ of planktic foraminiferal calcite is also species specific due to respiration and photosynthesis of host symbiotic algae (Zeebe et al., 1999). The surface water $\delta^{13}C$ during this study was measured from the planktic species *Trilobatus trilobus* which is the morphotype for the modern species *Trilobatus sacculifer*. In the case of *T. sacculifer,* the dependence on the symbiotic hosts for

nutrition is weak, and abundance of this planktic species likely reflects the species' ability to thrive on particulate organic matter (Scott, 2020). Calcification depth of *Trilobatus sacculifer* ranges from 20 to 75 m (Zhang et al., 2019) suggesting that the $\delta^{13}C$ record reflects water chemistry at these depths. The benthic $\delta^{13}C$ record for this study has been measured using the species *Heterolepa dutemplei* which is considered to be an epifaunal species (Kováčvá et al., 2009) suggesting that the $\delta^{13}C$ reflects the $\delta^{13}C$ of DIC of the bottom water mass, which in this case is at ~ 500 m (Bellanca et al., 2002). Planktic species tend to have relatively high $\delta^{13}C$ values due to the preferential incorporation of ^{12}C into organic matter by photosynthesizing organisms living in the photic zone. The biological pump shuttles this isotopically light carbon towards the seafloor, and subsequent remineralization of organic matter thus enriches deepwater DIC with ^{12}C. The biological pump therefore produces a "$\delta^{13}C$ gradient" from ^{12}C-depleted surface waters to ^{12}C-enriched deep waters (Broecker and Peng, 1982, Hilting et al., 2008). This vertical gradient of carbon stable isotopes is expressed as $\Delta\delta^{13}C$ ($\delta^{13}C_p - \delta^{13}C_b$) and can therefore be used to indicate the efficiency of the biological pump (Hilting et al., 2008). Biological pump efficiency can be defined as the ability of marine organisms to utilize phosphate and nitrogen in surface waters (Morée et al., 2021, Hilting et al., 2008). Therefore, calculated $\Delta\delta^{13}C$ values from Malta are used as a first order indication of local variations of biological pump efficiency during the MMCT.

The incorporation of B into foraminiferal calcite depends on seawater pH and the ratio of borate/dissolved inorganic carbon $[B(OH)_4^-]/[DIC]$ or the ratio of borate/bicarbonate $[B(OH)_4^-]/[HCO_3^-]$ (Allen et al., 2012; Haynes et al., 2019). The planktic B/Ca ratio is here used to discuss the carbonate system by using it to determine $[B(OH)_4^-]/[DIC]$ and in combination with the other proxies, infer changes in DIC. Previously published pH records for the RIP section spanning the CM-6 event (Badger et al., 2013) are combined with the B/Ca records to estimate DIC across the CM-6 event. Mn is a redox-sensitive element which is released in the form of Mn^{2+} from the sediment in low oxygen environments and adsorbed onto foraminiferal test as a coating (Wei et al., 2009). Planktic foraminiferal Mn/Ca is therefore used an indicator of seafloor redox conditions, which in this setting likely reflects the flux of organic matter to the seafloor.

Together, the $\Delta\delta^{13}C$, B/Ca and Mn/Ca records are interpreted in terms of export productivity and compared with records of global climate and regional hydrodynamics. The records support a local role for the Mediterranean region in drawing down CO_2 following the global cooling during the Middle Miocene Climate Transition. However, they also cast doubt on the interpretation of the Malta pCO_2 record as a global signal.

5.2 Methodology

Benthic and planktic foraminifera were picked from the Upper Globigerina Limestone member (UGLm) and the Blue Clay Formation (BCfm) sediments. The Upper Globigerina Limestone member outcrops in the Marsalforn Section (MRSF) (Island of Gozo) (Figure 4.1c) and was deposited during the Langhian (~14.4 Ma to ~ 13.8 Ma) and the section of the BCfm studied here was deposited during the Serravallian (~13.8 Ma to ~12.8 Ma). The MRSF samples were originally collected and used by Mourik et al., (2011) and are stored at the Faculty of Geosciences Utrecht University. The samples were dry sieved and foraminifera were picked from the 250-355 µm size fraction. 80 intact, well-preserved specimens of the planktic species *Trilobatus trilobus* were picked from 72 samples from this collection and used for trace metal analysis. The Blue Clay Formation samples were collected from the Ras il-Pellegrin section (Figure 4.1c) by Badger, (2010), Badger et al., (2013) and the samples are stored at the School of Earth and Environmental Sciences, Cardiff University. The planktic species *Trilobatus trilobus* was picked from the 250-355 µm size fraction of 84 samples from this collection. These were used to generate a stable isotope and a trace metal record. A total of 38 samples were used to pick specimens of the benthic species *Heterolepa dutemplei* for stable isotope analysis.

Approximately 3 to 4 whole specimens of benthic foraminifera and 5 to 7 whole specimens of planktic foraminifera from the RIP section were used to generate a stable $\delta^{18}O$ and $\delta^{13}C$ record at Cardiff University following the methods presented in Chapter 2 (section 2.2.2.1). Approximately 25-30 specimens of the planktic foraminifera were crushed and oxidatively cleaned for trace metal analysis at Cardiff University following the methods presented in Chapter 2 (section 2.2.2.2).

A new composite age model for the end-Langhian and the Serravallian of Malta was produced by Lucas J. Lourens (Utrecht University) by tying specific points on the

CenoGRID magnetic polarity timescale (L. Lourens pers. comm. 2022). This new age model does not assume orbital variability and therefore allows for spectral analysis of the various geochemical records. Details of the age model are presented in Chapter 4 (section 4.2.2).

One specimen from sample MT 1722 (14.292 Ma) of *Trilobatus trilobus* and one of *Uvigerina* spp. were analysed by SEM at Cardiff University to assess preservation of the calcite tests. These were compared with the SEM images obtained during this study from similar planktic and benthic specimens from the RIP section there were presented in Chapter 4 (section 4.3.1). (method in Chapter 2, section 2.2.2.3).

5.3 Results

5.3.1 Carbon stable isotope records

New planktic and benthic $\delta^{13}C$ records from the RIP section (13.8 Ma to 12.8 Ma) are presented in Figure 5.3b and Appendix 2.1, and compared with previously published RIP $\delta^{13}C$ data (Mourik et al., 2011) and the global benthic $\delta^{13}C$ compilation of Westerhold et al. (2020). In general, the previously published and new stable isotope data from the RIP section are in good agreement, which is reassuring as these samples were collected on different sampling campaigns (Badger et al., 2013; Mourik et al., 2011).

Both the benthic and the planktic $\delta^{13}C$ records demonstrate two intervals of elevated $\delta^{13}C$ which can be correlated with the global $\delta^{13}C$ compilation of Westerhold et al., (2020). The earliest interval (~14.32 Ma to ~14.14 Ma) can be correlated to the CM-5b $\delta^{13}C$ positive excursion and is more prominent in the planktic than the benthic record. The latter $\delta^{13}C$ excursion is also significantly more prominent in the planktic records and is correlatable with the CM-6a and CM-6b double peak $\delta^{13}C$ positive excursion. Following the CM-6 excursion both planktic and benthic records decrease steadily, with the planktic record demonstrating high-amplitude, high-frequency variability that is not observed in the benthic record.

5.3.2 Foraminiferal Mg/Ca, B/Ca, Mn/Ca, Sr/Ca and Ba/Ca records

The earlier (MRSF) Mg/Ca record has generally higher values than the RIP record with prominent intervals of very high Mg/Ca values (Figure 5.3c). Values vary between

~6 mmol/mol and ~8 mmol/mol from the base of the record to ~14.1 Ma, following which values exceed 8 mmol/mol and reach a maximum of ~ 11 mmol/mol. The Mg/Ca values decline after ~13.8 Ma and the subsequent (RIP) record oscillates around 4.5 mmol/mol for the rest of the studied section. The RIP Mg/Ca record is investigated in detail in Chapter 4.

During the Langhian (MRSF section) planktic B/Ca concentrations hover around 80 µmol/mol from ~14.3 Ma to ~ 14.0 Ma after which the values start to follow an increasing trend reaching a peak of ~116 µmol/mol at ~13.7 Ma. In the earlier part of the Serravallian (RIP section) (~13.80 Ma to ~13.45 Ma), the record is persistently high (~110 µmol/mol). Following this early interval of high B/Ca values, the record exhibits a phase (~13.45 Ma to ~ 13.20 Ma) of generally low values. The final part of the record, (~13.2 Ma to ~12.8 Ma) consists of high values oscillating between ~85 µmol/mol and ~110 µmol/mol (Figure 5.3d).

The planktic Mn/Ca record for the composite Malta section shows significant difference between the Langhian and the Serravallian interval. The older part of the record consists of generally lower values, around 100 µmol/mol while the younger record displays predominantly higher values that vary between 100 µmol/mol and 600 µmol/mol (Figure 5.3e). The Mn/Ca record displays high variability at high frequency following the Langhian-Serravallian boundary (13.8 Ma). In general, values oscillate between ~100 µmol/mol and ~ 380 µmol/mol for a large part of this interval (~13.8 Ma to ~13.2 Ma). The final part of the record (from ~13.2 Ma to ~12.9 Ma) displays an upward trend with values reaching around 500 µmol/mol. The high frequency, large amplitude variability is evident throughout the whole post Serravallian. For most of the record, the Mn/Ca data shows a remarkable similarity with the B/Ca data.

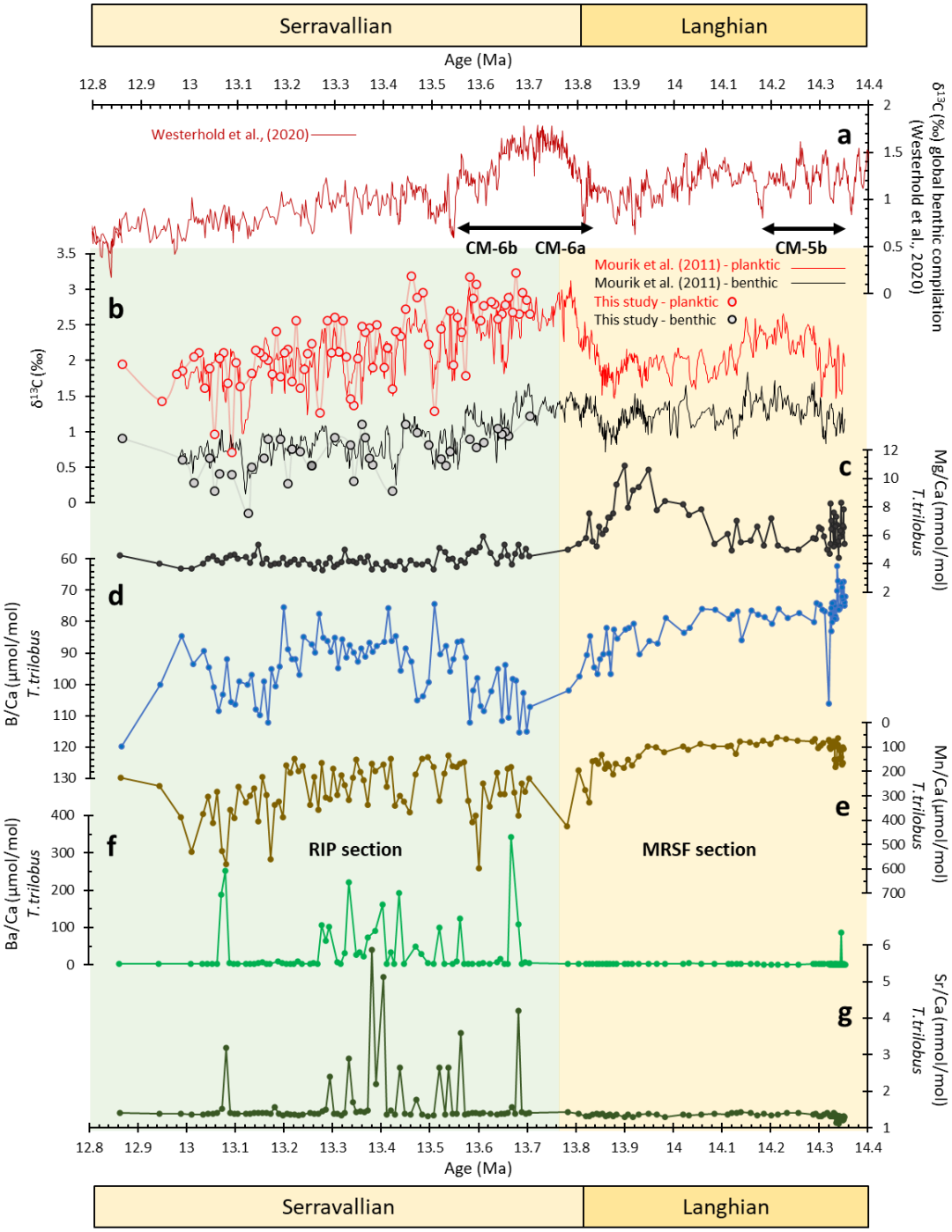

Figure 5.3 (a) Global benthic $\delta^{13}C$ compilation (Westerhold et al., 2020). (b) Previously published planktic and benthic $\delta^{13}C$ records from the Marsalforn (MRSF) and Ras il-Pellegrin (RIP) sections in Malta compared with newly obtained $\delta^{13}C$ records from RIP. Both the previously available data and the new data are plotted against the new age model for the MRSF and RIP composite section. (c) *T. trilobus* Mg/Ca (d) *T. trilobus* B/Ca (e) *T. trilobus* Mn/Ca (f) *T. trilobus* Ba/Ca (g) *T. trilobus* Sr/Ca. Yellow bar indicates samples from the MRSF section while green bar indicates samples from the RIP section.

The planktic Sr/Ca and Ba/Ca records (Figure 5.3 f,g) are mostly stable throughout the whole interval and do not display significant trends. However, both records exhibit very large positive short-term excursions from the mean. These positive excursions occur mostly during the earlier part of the RIP record and there is a good correspondence with very high Sr/Ca and very high Ba/Ca.

5.4 Microfossil preservation state and reliability of the B/Ca and Mn/Ca record

SEM images of foraminifera from the Globigerina Limestone Formation (MRSF section) and the Blue Clay formation (RIP section) demonstrate contrasting preservation state of microfossils. Although the clay-rich RIP section boasts exceptionally preserved benthic and planktic specimens (section 4.3.1, Figure 4.2, Figure 5.4), the same cannot be said about the foraminifera picked from the carbonate-rich MRSF section (Figure 5.4). Authigenic cements, partial destruction of the original pore spaces and minor to moderate recrystallisation of planktic test walls is revealed by SEM analysis (Figure 5.4). The extent to which these diagenetic changes may have impacted the various geochemical records is assessed below.

The first diagenetic process to consider is recrystallisation, a neomorphic process where thin films of fluid pass through the test facilitating the dissolution and reprecipitation of tiny biogenic crystallites eventually producing calcite crystals around 1-2µm diameter. Because this process occurs in the shallow sediment column it tends to bias planktic $\delta^{18}O$ towards colder values. However, recent modelling and high-resolution intra-test elemental mapping supports the suggestion that this process largely reshuffles metal cations through the calcite lattice, meaning that trace metal ratios (and $\delta^{13}C$) are more robust to recrystallisation than $\delta^{18}O$ (Staudigel et al., 2022).

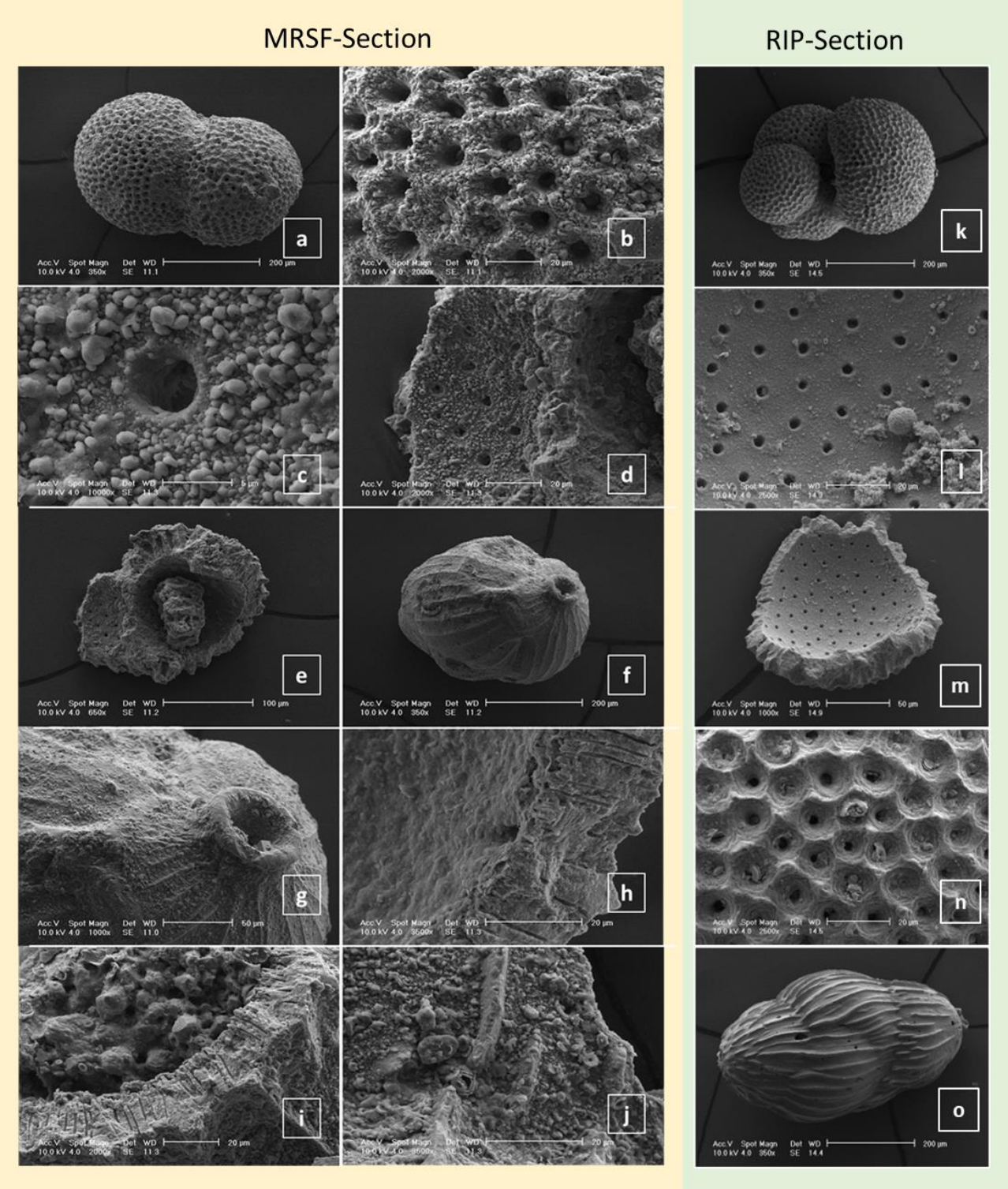
MRSF-Section
RIP-Section
a
b
c
d
e
f
g
h
i
j
k
l
m
n
o

Figure 5.4 Planktic and benthic individual specimens from sample MT 1722 from the MRSF section compared (yellow panel) with planktic and benthic specimens from the RIP section (green panel). MRSF section (a)(b) original hexagonal pore space in *T. trilobus* compromised by recrystallisation of test calcite (c) authigenic crystals visible on inner test wall of *T. trilobus* (d)(e) pores through *T. trilobus* test wall compromised by diagenetic processes (f)(g) authigenic crystal growth on exterior surface of Uvigerina spp. including a single prominent calcite crystal adhering to the aperture (h)(i) presence of straight-edged pores through *Uvigerina* spp. test wall demonstrate lack of wholesale recrystallisation in this benthic foraminifer (j) coccolith cements and authigenic overgrowths on the interior surface of *Uvigerina* spp. RIP section (k)(l)(m)(n) whole and interior and exterior fragments from *T. trilobus* showing excellent preservation of original test material. (o) excellently preserved whole specimen of *Uvigerina* spp .

Extensive recrystallisation will eventually impact calcite trace metal ratios, with equilibrium values dependent on partition coefficients and pore water concentrations. Advantage can be taken of the different behaviour of metal cation incorporation into calcite to assess the possibility that recrystallisation has impacted the trace metal records presented here. Specifically, severe recrystallisation would be expected to produce an inverse correlation between foraminiferal Mg/Ca and Sr/Ca (Baker et al., 1982; Lear et al., 2004). One complication of the foraminiferal Sr/Ca record presented here is that it contains unusual peaks that are not typically seen in deep sea settings (Figure 5.3g) (Lea and Boyle, 1991). The strong covariation with the Ba/Ca record suggests that these samples contain trace amounts of the mineral barite that was not removed during the cleaning process (Figure 5.3f). Therefore, the Ba/Ca record is first used to screen the Sr/Ca record, so it can be used to assess the potential impact of recrystallisation (Figure 5.5f).

Aside from a short interval near the base of the record (14.35 Ma to 14.33 Ma) there is no convincing anti-correlation between Mg/Ca and Sr/Ca, which would be expected if the records was dominated by a recrystallisation signal (Figure 5.5b,f). On the other hand, there is a close correspondence between Mg/Ca and Fe/Ca in the MRSF samples (Figure 5.6 a). This indicates the presence of a contaminant phase rich in both Fe and Mg.

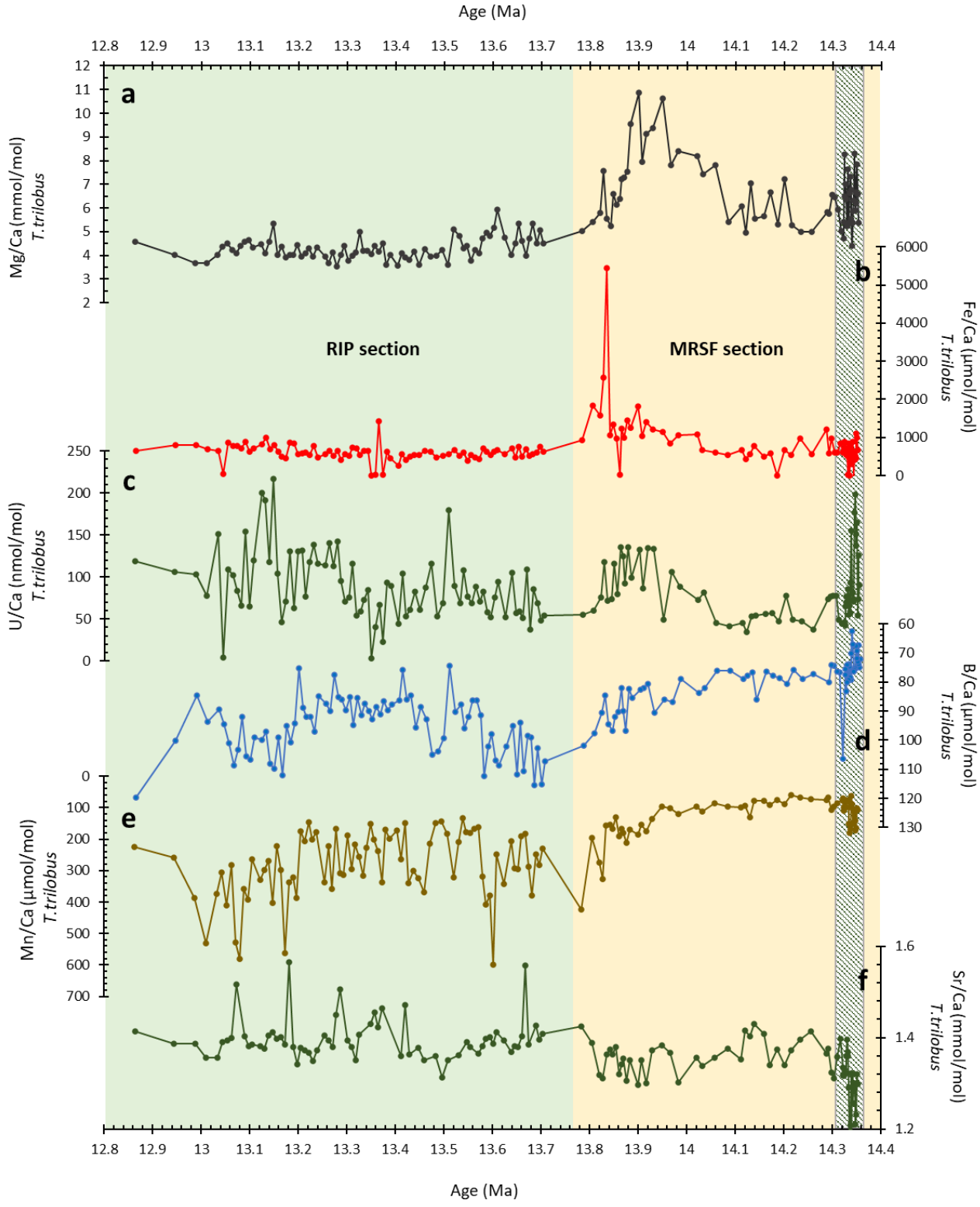
Age (Ma)
12.8 12.9 13 13.1 13.2 13.3 13.4 13.5 13.6 13.7 13.8 13.9 14 14.1 14.2 14.3 14.4
a
Mg/Ca (mmol/mol) T. trilobus
12 11 10 9 8 7 6 5 4 3 2
RIP section
MRSF section
b
Fe/Ca (µmol/mol) T. trilobus
6000 5000 4000 3000 2000 1000 0
c
U/Ca (nmol/mol) T. trilobus
250 200 150 100 50 0
d
B/Ca (µmol/mol) T. trilobus
60 70 80 90 100 110 120 130
e
Mn/Ca (µmol/mol) T. trilobus
0 100 200 300 400 500 600 700
f
Sr/Ca (mmol/mol) T. trilobus
1.6 1.4 1.2
Age (Ma)

Figure 5.5 Comparison of *T. trilobus* Mg/Ca, B/Ca, U/Ca, Fe/Ca and Sr/Ca in order to asses preservation of original geochemical signal. (a)(b)(c) Close correlation between Mg/Ca, Fe/Ca and U/Ca for most of the MRSF section indicates that contaminant phases rich in U and Fe exclude the possibility of using the Mg/Ca from the MRSF section to obtain a palaeotemperature record. No correlation is observed between B/Ca (d) and U/Ca (c) and Fe/Ca (b). There is also no correlation between Mn/Ca (e) and U/Ca (c) and Fe/Ca (b). Grey hatched bar indicates part of record likely impacted by recrystallisation.

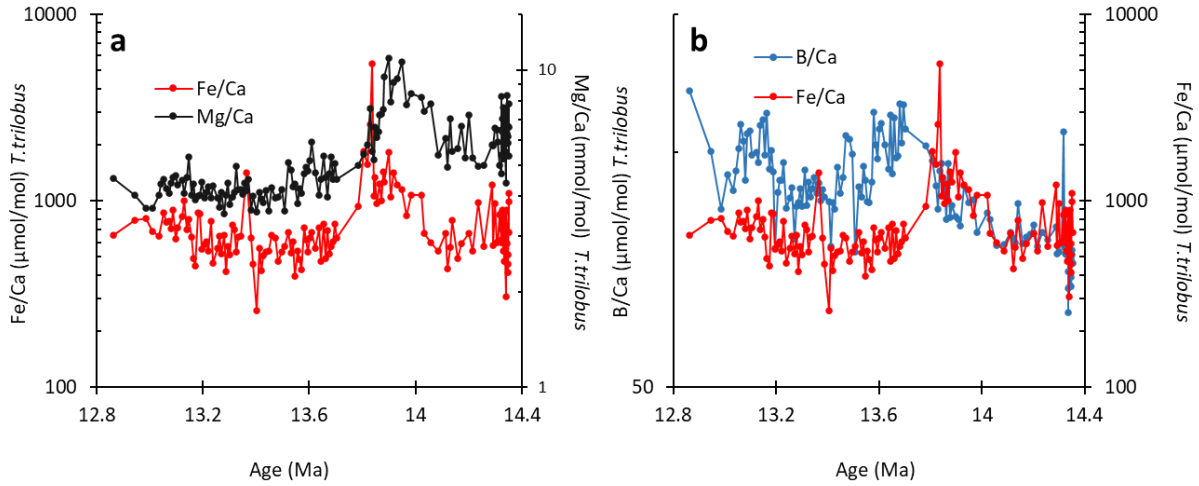

Figure 5.6 Assessing impact of Fe-related contamination. (a) Clear association between planktic foraminiferal Fe/Ca and Mg/Ca in the older (14.4 Ma to 13.8 Ma)(MRSF) part of the record indicating a contaminant phase containing both Fe and Mg, likely ankerite. (b) As expected, there is no clear co-variation between planktic Fe/Ca and B/Ca, suggesting that the B/Ca record is not impacted by the presence of ankerite.

This is consistent with an authigenic coating in the MRSF section that leads to elevated Fe/Ca and Mg/Ca but not Mn/Ca (Figure 5.5). The most likely type of coating would be from an iron-dolomite mineral such as ankerite, which has previously been documented in Maltese sections (John et al., 2003). Boron is not usually associated with Mn bearing minerals (Burdige, 1993). The significant co-variation throughout the Malta record between the planktic B/Ca and Mn/Ca (Figure 5.5) therefore instead likely indicates a common environmental mechanism. Benthic and planktic Mn/Ca show a similar trend suggesting that both are reflecting first order redox conditions at the sea-floor, with the generally higher planktic values due to the rougher, more porous

T.trilobus surface (Figure 5.7a). However, planktic and benthic B/Ca records have no identifiable covariation indicating that the planktic B/Ca data is indicative of sea-surface processes (Figure 5.7b).

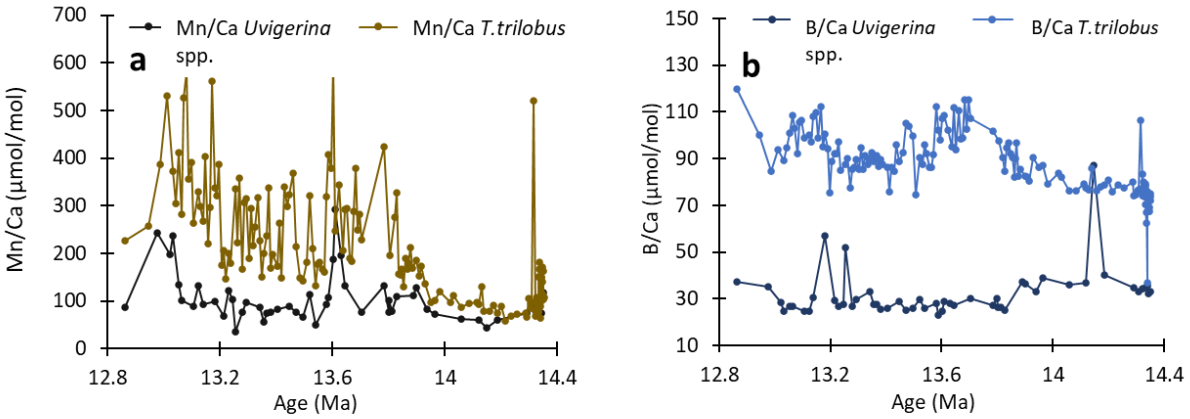

Figure 5.7 Comparison of B/Ca and Mn/Ca planktic and benthic records. (a) Planktic and benthic Mn/Ca records show close covariation for most of the studied interval (b) no identifiable covariation is observed in the B/Ca benthic and planktic records.

Therefore, for the interpretation of the geochemical records below all trace metal data from the compromised interval 14.35 Ma to 14.33 Ma (Figure 5.4), and all Mg/Ca data from the MRSF section are removed and the planktic B/Ca and Mn/Ca are considered to act as reliable proxies for sea surface carbonate chemistry and seafloor redox conditions respectively.

5.5 An enhanced biological pump in the Central proto-Mediterranean during the MMCT?

The composite Marsalforn and RIP Langhian-Serravallian record (Mourik et al., 2011; this study) displays similar trends in planktic and benthic $\delta^{13}C$ during the MMCT (Figure 5.8b). This similarity indicates that the trends in the $\delta^{13}C$ records represents whole ocean isotopic changes in the ocean reservoir (Flower & Kennett, 1994). However, the high frequency $\delta^{13}C$ variations in the planktic record from Malta are more amplified than in the benthic record (Figures 5.8b). Furthermore, the amplitude of the planktic $\delta^{13}C$ variations at Malta are also much larger than typical open ocean sites

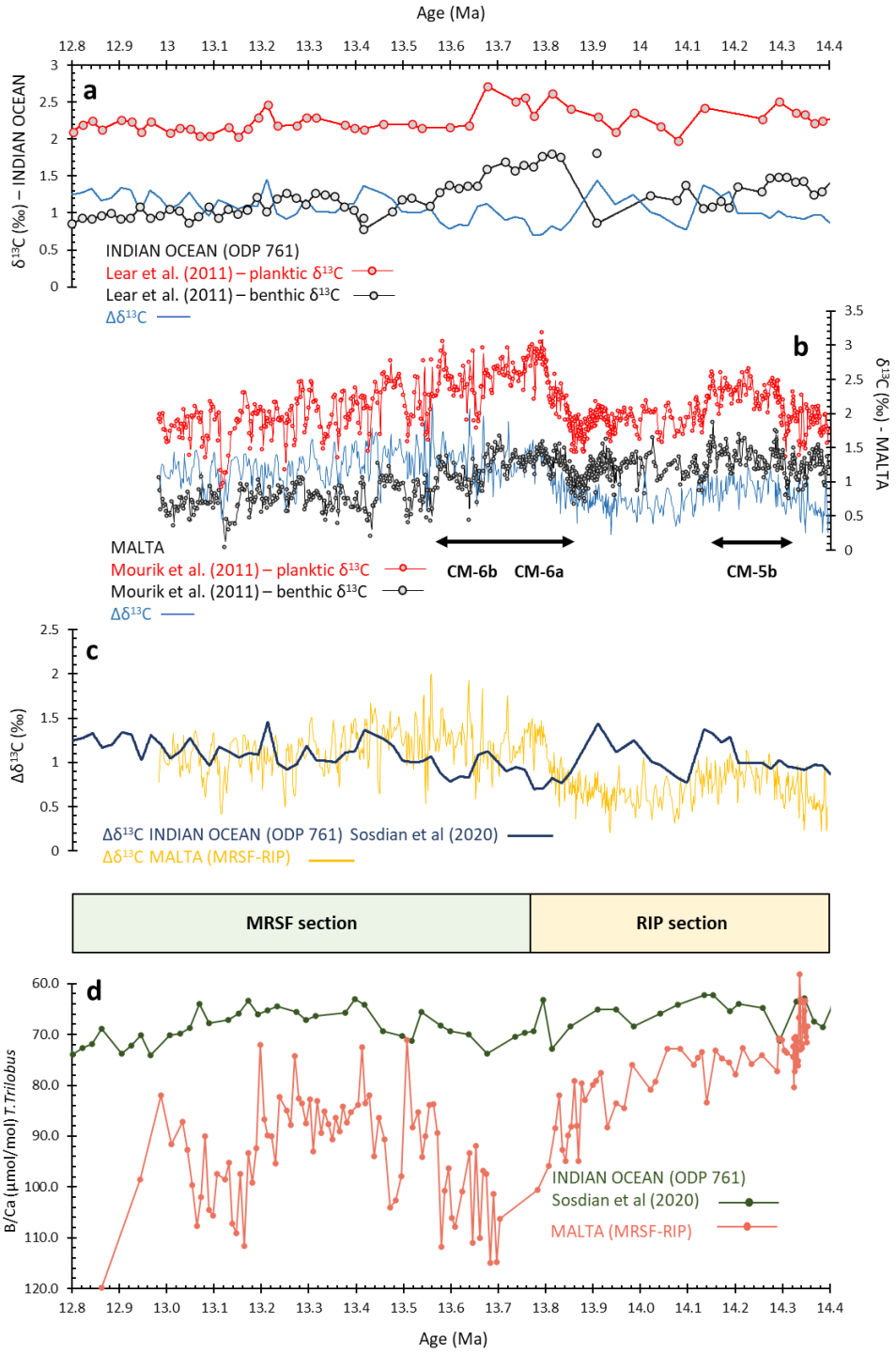

Figure 5.8 Comparison between shelf environment (Malta) with the open ocean (ODP 761). (a) (b) $\delta^{13}C$ and $\Delta\delta^{13}C$ records from ODP 761 and from Malta. (c) The $\delta^{13}C$ gradient ($\Delta\delta^{13}C$) from both sites acts as a proxy for export productivity and indicates significant differences between the two sites during the CM-6 event. (d) Difference in B/Ca during and following CM-6 between the two sites is clear.

such as ODP Site 761 (Figure 5.8a). For CM-6 in particular, it is difficult to explain the magnitude of the Malta planktic positive $\delta^{13}C$ shift through a reduction in air-sea gas exchange, when sea surface temperatures in this region were falling (Badger et al., 2013), and there is no evidence for cessation of significant upwelling. Therefore, the mostly likely explanation is that the amplified planktic $\delta^{13}C$ signal is reflecting a rapid increase in productivity in the central Mediterranean surface waters that starts at 13.86 Ma coinciding with the onset of CM-6. This assumption is examined below using $\Delta\delta^{13}C$ and Mn/Ca records.

The surface to seafloor $\delta^{13}C$ gradient ($\Delta\delta^{13}C$) is here used as a proxy for the efficiency of the biological pump (Hilting et al., 2008). At Malta, the $\Delta\delta^{13}C$ record increases by ~ 1.3 ‰ across the CM-6 interval and remains relatively high for the remaining studied interval suggesting an increase in biological pump efficiency (Figure 5.8b). $\delta^{13}C$ data from the Indian Ocean site ODP 761 (Lear et al., 2010) were also used to calculate $\Delta\delta^{13}C$ for this site (Figure 5.8a) using linear interpolation and subtracting the benthic $\delta^{13}C$ values from the planktic $\delta^{13}C$ values (Figure 5.8a). Unlike Malta, $\Delta\delta^{13}C$ at ODP Site 761 decreases across CM-6, because the planktic $\delta^{13}C$ signal is muted compared with the benthic signal at this open ocean site (Figure 5.8 a,b). Therefore, the increase in export productivity associated with CM-6 was certainly not global in extent.

The generally low Mn/Ca values (<100 µmol/mol) from the MRSF section suggest a lack of significant authigenic Mn-coatings (Figure 5.9) (Chen et al., 2017). The Mn/Ca values for the RIP section mostly exceed 100 µmol/mol, indicating that the Mn is present in coatings formed on the rough *T. trilobus* test in the sediment under low oxygen conditions when Mn^{+} becomes mobilised (Boyle, 1983). A low oxygen environment in the shallow subsurface is consistent with a highly active biological pump in the region.

Taken together, the evidence suggests that the high amplitude changes in planktic $\delta^{13}C$ in Malta reflect orbitally paced episodes of enhanced export productivity. In general, the amplitude of the planktic $\delta^{13}C$ high-frequency variability appears to increase after the MMCT (Figure 5.9) and the eccentricity pacing of this record (Mourik et al., 2011) suggests a regional, seasonal driver. It is therefore possible that the

intervals of intense export productivity in the Central proto-Mediterranean were driven by orbitally paced intervals of enhanced freshwater discharge and associated nutrient delivery following the Langhian-Serravallian transition and the closure of the Mesopotamian Gateway (MSR-2) (as discussed in Chapter 4). Below, I explore possible impacts on the carbon cycle through the planktic B/Ca proxy.

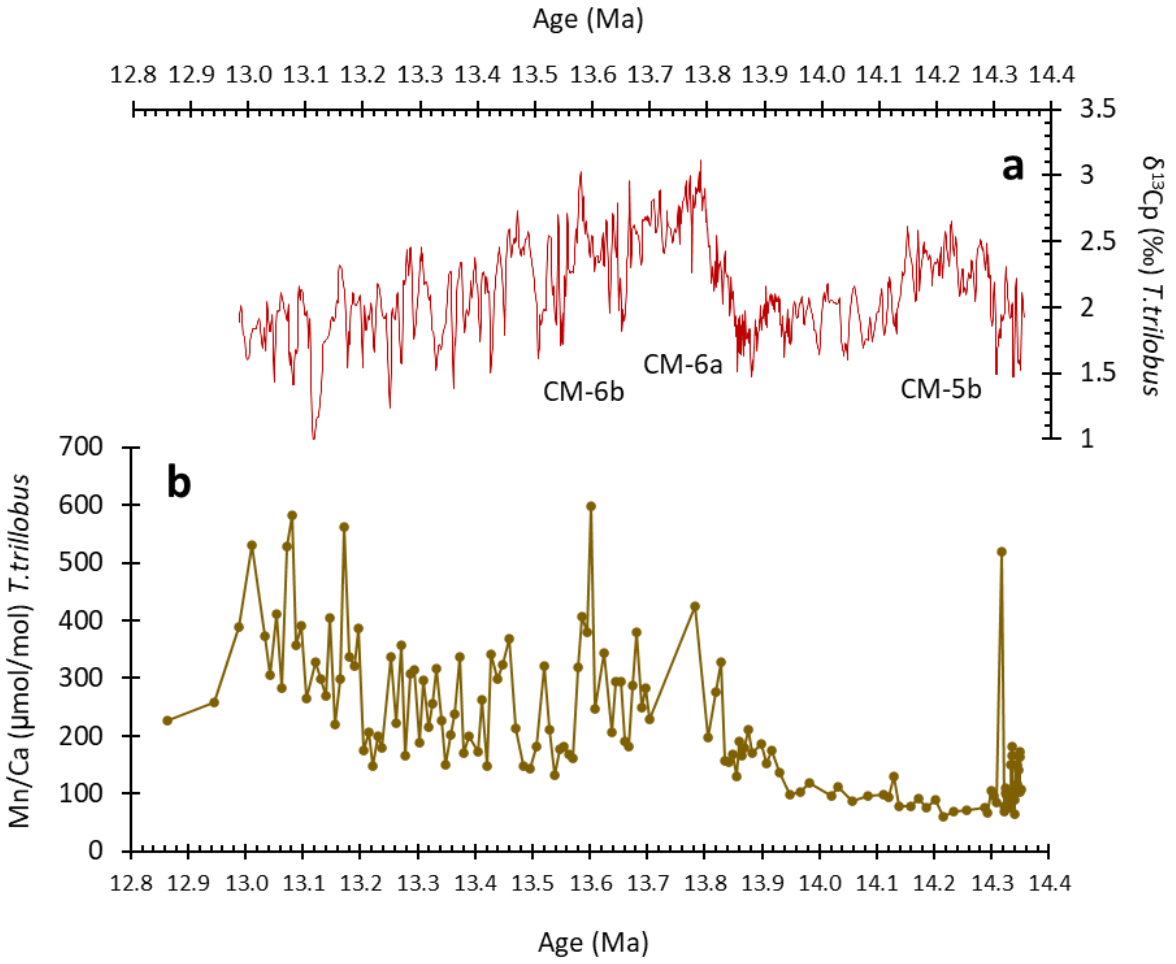

Figure 5.9 Planktic (a) $\delta^{13}C$ and (b) Mn/Ca from Malta. Mn/Ca increases during CM-6 indicating a close link between bottom water redox state and surface water productivity during the CM-6 event.

5.6 Impact of an enhanced biological pump on seawater carbonate chemistry in the proto-Mediterranean

To assess the possible impact of the enhanced biological pump on seawater carbonate chemistry the planktic B/Ca records from Malta (this study) are compared with those from ODP 761 (Sosdian et al., 2020). Both B/Ca records have been measured using the same planktic foraminiferal species, *T. trilobus*. This allows for comparison of the records without the influence of the variability that occurs between different species (Allen et al., 2012). Although the records from Malta are at a higher resolution, the records from ODP 761 are at sufficiently high resolution to enable a very good correlation between the two records (Figure 5.8c).

The planktic B/Ca record from Malta shows similar long-term trends as the record from ODP Site 761, but the long-term and the high frequency amplitude variability in the Malta record is much greater. In fact, the Indian Ocean record varies between 60 µmol/mol and 80 µmol/mol throughout the whole record while the central Mediterranean record displays a much larger variability of 60 µmol/mol to 120 µmol/mol (Figure 5.8c). This suggests that the Central proto-Mediterranean experienced a significant change in carbonate chemistry that is not observed at ODP Site 761. Below I explore this change, to determine whether it may have been the result of an enhanced biological pump in this region. Defining the oceanic carbonate system is a vital component in understanding palaeoclimate change, since the fluxes between the atmospheric and oceanic carbon reservoirs are fundamental in regulating atmospheric CO_2. The oceanic carbonate system is determined by the following co-varying parameters (Foster, 2008):

- pH
- concentration of dissolved carbon dioxide [CO_2]
- concentration of the bicarbonate ion $[HCO_3^-]$
- concentration of the carbonate ion $[CO_3^{2-}]$
- Total alkalinity
- Total dissolved inorganic carbon DIC (Which is the sum of the inorganic carbon species in the solution ($[CO_2] + [HCO_3^-] + [CO_3^{2-}]$)) (Bell et al., 2011)

The entire system can be described if two of these parameters are known. The pH of the system can be determined through the use of boron isotope ratios ($\delta^{11}B$) in foraminiferal calcite (Foster, 2008) while foraminiferal B/Ca can act as a proxy for the ratio of $[B(OH)_4^-]/[HCO_3^-]$ [borate]/[bicarbonate] and $[B(OH)_4^-]/[DIC]$ [borate]/[total dissolved inorganic carbon] (Allen et al., 2012). If the pH of the system is independently constrained it is therefore possible to use the B/Ca proxy to estimate variations in the concentration of dissolved inorganic carbon and borate ions in surface waters (Sosdian et al., 2020). However, before this approach can be applied, the influence of salinity and temperature on the B/Ca record needs to be assessed.

5.6.1 The effects of sea surface salinity on planktic foraminiferal B/Ca

In principle, the amount of boron incorporated in foraminiferal tests depends on the concentration of dissolved borate ions $[B(OH)_4^-]$ in surface waters which itself depends on total [B] and pH (Hemming & Hanson, 1992). Boron is incorporated in the foraminiferal calcite by the mechanism proposed by Hemming and Hanson (1992):

$$CaCO_3 + B(OH)_4^- \leftrightarrow Ca\,(HBO_3) + HCO_3^- + H_2O \tag{5.1}$$

The exchange distribution coefficient K_D for incorporation of boron into calcium carbonate (Foster, 2008) is:

$$K_D = \frac{[B/Ca]_{solid}}{[B(OH)_4^-/HCO_3^-]_{seawater}} \tag{5.2}$$

However, it is not straightforward to apply the B/Ca proxy in palaeoenvironments since it is unclear if other factors also affect the B/Ca value.

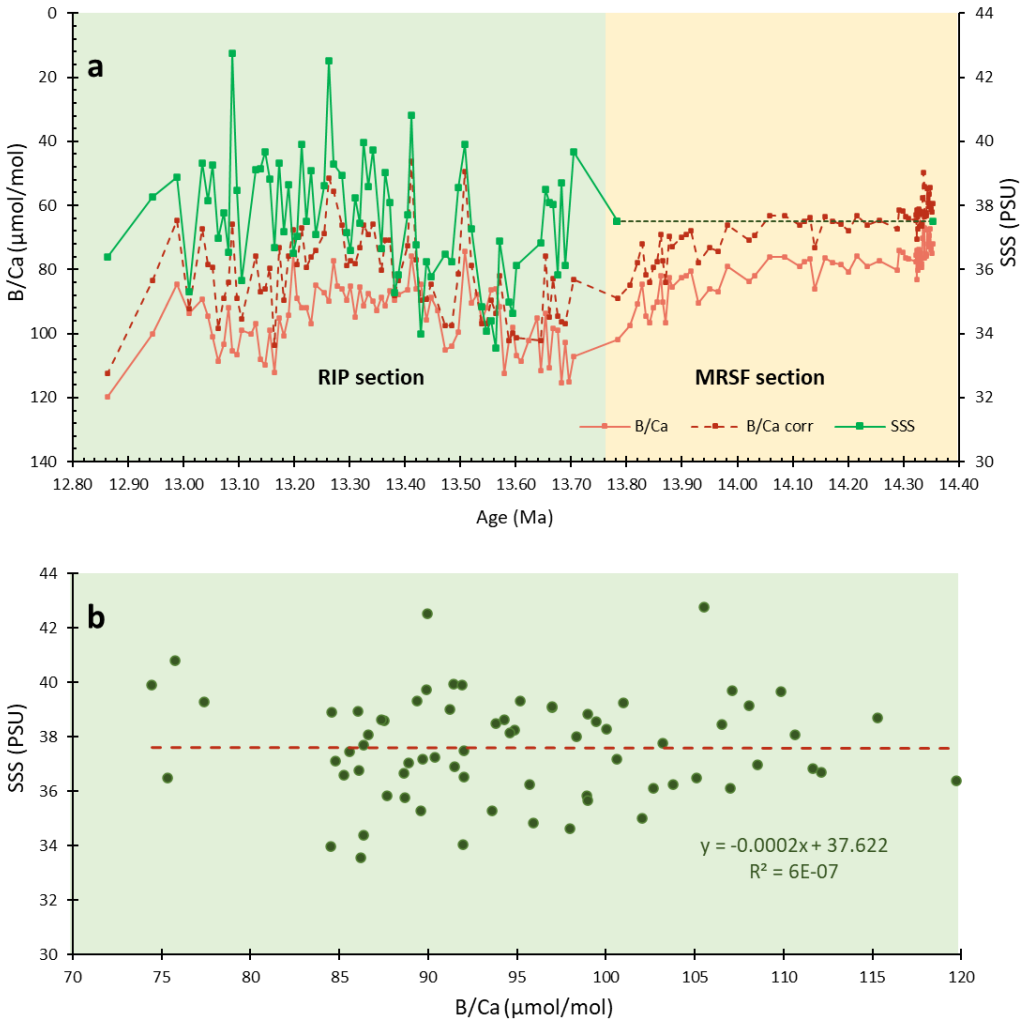

Figure 5.10 (a) Surface salinity (green), *T. trilobus* B/Ca (solid pink), and salinity-corrected B/Ca (dotted red) for the composite MRSF-RIP section (b) relationship between sea-surface salinity and planktic B/Ca for the RIP section. Salinity values for the older part (MRSF) of the section assumed at a constant 37.5 (PSU) using modelling data for the Central Mediterranean according to Hamon et al. (2013).

Culture experiments on *T. sacculifer* (for which *T. trilobus* is the morphotype (Spezzaferri et al., 2015)) have shown that there is no significant response to temperature, while increasing salinity tends to increase B/Ca (Allen et al., 2012). The relationship between B/Ca and salinity has been described using the linear equation 5.3 (Allen et al., 2012).

$$B/Ca = 5.10*(SSS) - 85.9 \qquad (R^2 = 0.96, p = 0.02) \tag{5.3}$$

The effect of salinity on the B/Ca can be corrected by normalizing the B/Ca values to a standard salinity of 35 PSU (e.g., Sosdian et al., 2020). Surface salinity values have been determined for the RIP section using a combination of planktic foraminiferal $\delta^{18}O$ and Mg/Ca SST (section 4.3.4). However, diagenetic coatings in the Langhian MRSF foraminifera (section 5.4) do not allow for a reliable Mg/Ca SST record to be obtained. Therefore, a salinity correction using calculated SSS values can only be applied on the Serravallian RIP record. For the MRSF section, reduced variability in the planktic $\delta^{18}O$ record implies relatively stable surface salinity and so a constant value of 37.5 PSU was used to correct the B/Ca. This value for salinity in the central Mediterranean is obtained from modelling studies for an open Mesopotamian Seaway during the Miocene (Hamon et al., 2013). It should be noted that the salinity correction is linear and therefore the absolute values of salinity are not important. The salinity corrected B/Ca record is determined using equation 5.4:

$$B/Ca_{corr} = 5.10\ (35\text{-}SSS) + B/Ca \tag{5.4}$$

Salinity corrected B/Ca for the composite MRSF-RIP section are shown in figure 5.10a. In general, the B/Ca record varies in an anticorrelation with the SSS record, with decrease in salinity accompanied by increases in B/Ca. No significant correlation in the RIP record between SSS and B/Ca is observed (Figure 5.10b). Increasing salinity would act to increase B/Ca (Allen et al., 2012), and so these observations imply that the primary variations are not driven by the observed salinity variations, and instead likely reflect changes in the carbonate system that are varying with the regional hydrologic changes. Indeed, while the salinity correction does not change the general trends in the B/Ca record, it acts to increase the amplitude of variability in the corrected record (Figure 5.7a).

5.6.2 Determination of $[\mathbf{B(OH)_4^-}]/[\mathbf{DIC}]$ and estimation of [DIC]

Following Sosdian et al., (2020), the linear relationship between salinity normalized foraminifera B/Ca and $[\mathrm{B(OH)_4^-}]/[\mathrm{DIC}]$ (equation 5.5) obtained from culture experiments on *T.sacculifer* (Allen et al., 2012) is used to calculate variations in $[\mathrm{B(OH)_4^-}]/[\mathrm{DIC}]$.

$$\mathrm{B/Ca_{foram}} = \frac{\mathrm{B/Ca_{sw}\ (t=t)}}{\mathrm{B/Ca_{sw}\ (t=0)}} \times \frac{[\mathrm{B(OH)_4^-}]}{(\mathrm{DIC})} 773 + 33 \qquad R^2 = 0.81$$

(5.5)

The ratio B/Ca_{sw} (t = t) represents the B/Ca ratio of seawater at the age of the sample while B/Ca_{sw} (t = 0) is the ratio for modern day seawater. The value of B/Ca_{sw} (t = t) between 14.35 Ma and 12.86 Ma varied from 70.01 µmol/mol to 68.98 µmol/mol (Sosdian et al., 2020) and B/Ca_{sw} (t = 0) is equal to 59.88 µmol/mol (Sosdian et al., 2020). These ratios have been calculated in Sosdian et al. (2020) from boron isotope modelling and fluid inclusion estimates (Horita et al., 2002; Lemarchand et al., 2002)

Age (Ma)	B/Ca_{sw} (Sosdian et al., 2020)	B_{tot} (µmol/kg) (Sosdian et al., 2020)	pH (Badger et al., 2013)
13.950	69.73	460.96	7.892
13.902	69.69	460.86	7.929
13.829	69.64	460.72	7.906
13.733	69.58	460.52	8.007
13.709	69.56	460.47	7.969
13.647	69.52	460.35	7.974

Table 5.1 pH values for Middle Miocene seawater obtained from $\delta^{11}B$ from the RIP section. (Badger et al., 2013).

The pH record from the RIP section (Badger et al., 2013) (table 5.1) is much lower resolution that the B/Ca record and therefore the estimated [DIC] will be of low

resolution and cannot be used to discuss the whole B/Ca record. To calculate DIC, the pH values are first used to determine the concentration of [H^+] ions (equation 5.6) , which is then used to calculate the borate ion concentration (equation 5.7) The DIC is then determined from the $[\mathrm{B(OH)_4^-}]/[\mathrm{DIC}]$ ratio (equation 5.5) (Figure 5.6).

$$\mathrm{pH} = -\log_{10}[\mathrm{H^+}] \tag{5.6}$$

$$\mathrm{B(OH)_4^-} = \frac{B_{TOT}}{\left(1 + \frac{\mathrm{H^+}}{K_B^*}\right)} \tag{5.7}$$

The stochiometric equilibrium constant for boric acid K_B^* has a value of 2.5 x 10^{-9} (Lemarchand et al., 2002).

5.6.3 The Mid-Miocene $[\mathbf{B(OH)_4^-}]/[\mathbf{DIC}]$, pH and DIC records

The B/Ca record for the whole composite section is plotted alongside the $[\mathrm{B(OH)_4^-}]/(\mathrm{DIC})$ (no units) calculated from both the salinity-corrected B/Ca and from the original B/Ca data (Figure 5.11 a,b). Both $[\mathrm{B(OH)_4^-}]/[\mathrm{DIC}]$ records co-vary with the B/Ca records, with stable values during the early part of the record and an increasing trend from ~14.0 Ma peaking during the CM-6 event. Lower values occur following the CM-6 plateau (~13.4 Ma to ~13.2 Ma) with an increase in $[\mathrm{B(OH)_4^-}]/[\mathrm{DIC}]$ during the final part of the record (~13.2 Ma to ~12.8 Ma).

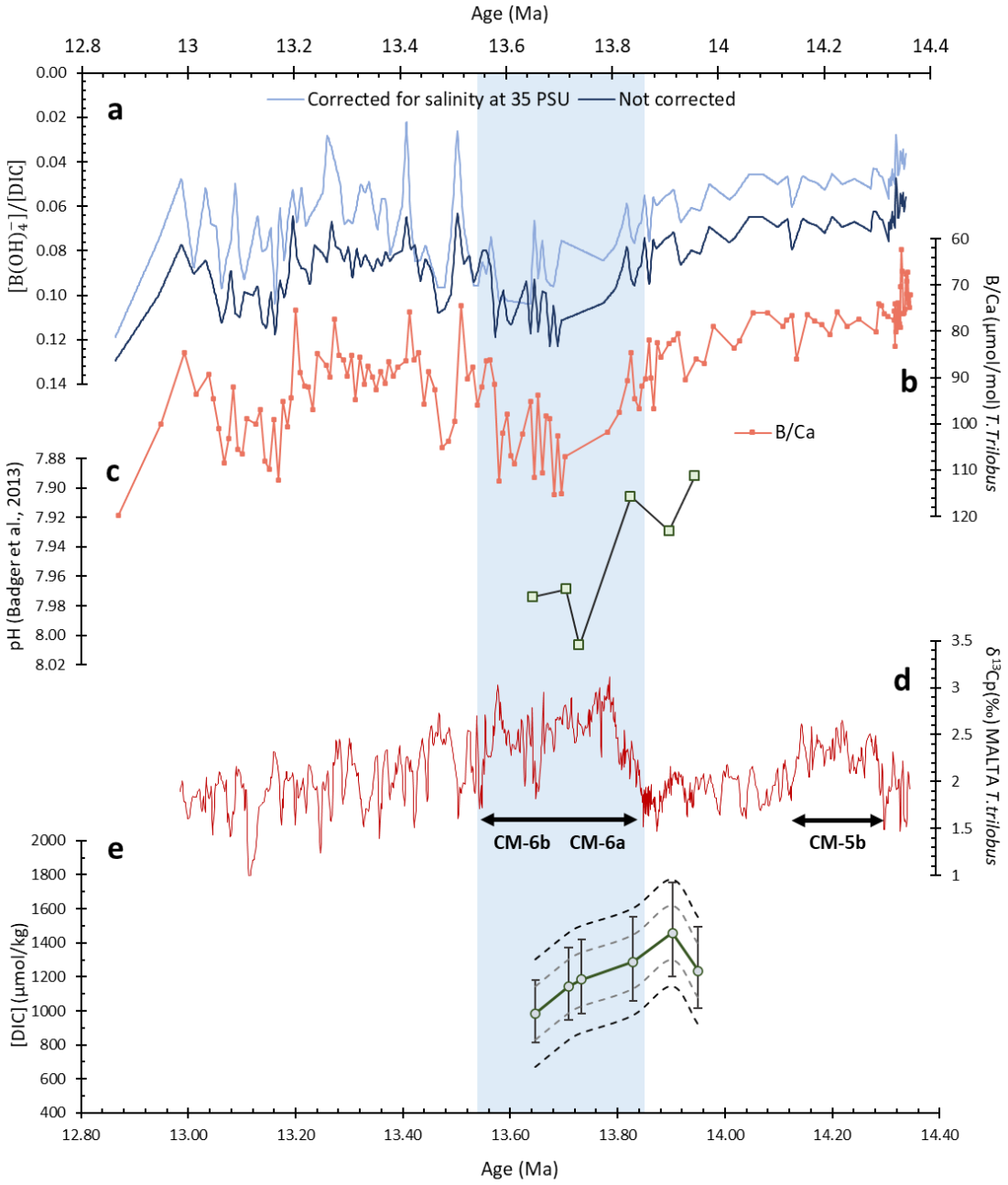

Figure 5.11 (a) $[B(OH)_4^-]/[DIC]$ obtained from linearly interpolated original planktic B/Ca data (dark blue) and salinity corrected B/Ca data (light blue) compared with (b) original planktic B/Ca (pink). (c) pH estimates from RIP (Badger et al.,2013) (d) Malta planktic $\delta^{13}C$ record displaying the CM-5b and the CM-6 double peak excursion and (e) estimated DIC, light grey dotted envelope represents ± 1 s.d, black dotted envelope represents ± 2 s.d assuming a normal distribution of data. Error bars obtained by considering a sensitivity of ± 0.1 on the pH values of Badger et al. (2013).

Amplitude variability at high frequency is observed during the Serravallian (RIP section). This amplitude variability is greatly accentuated in the record that is corrected for salinity indicating amplified increased [DIC] or a decrease in $[B(OH)_4^-]$ during episodes of high salinity.

Previously published pH records from the RIP section show a distinctive increase in pH coinciding with the onset of the CM-6 positive excursion (Badger et al., 2013) (Figure 5.11c, table 5.1) .The [DIC] estimated from the pH and B/Ca records also shows a significant declining trend change across CM-6, with a drop of ~ 750 µmol/kg (Figure 5.11e). The [DIC] record is plotted together with calculated ±1 s.d.

5.7 Biological production and carbon cycle during the Middle Miocene. The influence of high productivity regions.

Planktic foraminiferal B/Ca and hence reconstructed $[B(OH)_4^-]/[DIC]$ are persistently low during the earlier part of the record (MRSF data). Since the central Mediterranean pH record does not cover this earlier pre-CM-6 interval it is impossible to disentangle the [DIC] vs $[B(OH)_4^-]$ contributions. Persistently low Mn/Ca (~100 µmol/mol to 200 µmol/mol) from *T. trilobus* during this time suggests limited authigenic manganese coatings and a well oxygenated seafloor during this time (Figure 5.9). As discussed above, this is consistent with relatively low export productivity, which would tend to increase surface [DIC] and lower $[B(OH)_4^-]$, consistent with the record presented here (Figure 5.11). These records perhaps suggest that export productivity in the Central proto-Mediterranean during the CM-5b carbon maximum was not particularly different from the open ocean (Figure 5.8).

Planktic foraminiferal B/Ca and Mn/Ca gradually increase from ~14.1 Ma, in the interval immediately preceding the main ice growth episode of the MMCT. The pH data from the RIP section (Badger et al., 2013) allow for the determination of [DIC] during this phase and CM-6 (Figure 5.11). Declining [DIC] and increasing pH are consistent with a CO_2 mechanism for the MMCT, as previously suggested (e.g., Foster et al., 2012). Furthermore, our Mn/Ca and $\Delta\delta^{13}C$ records suggest this interval was

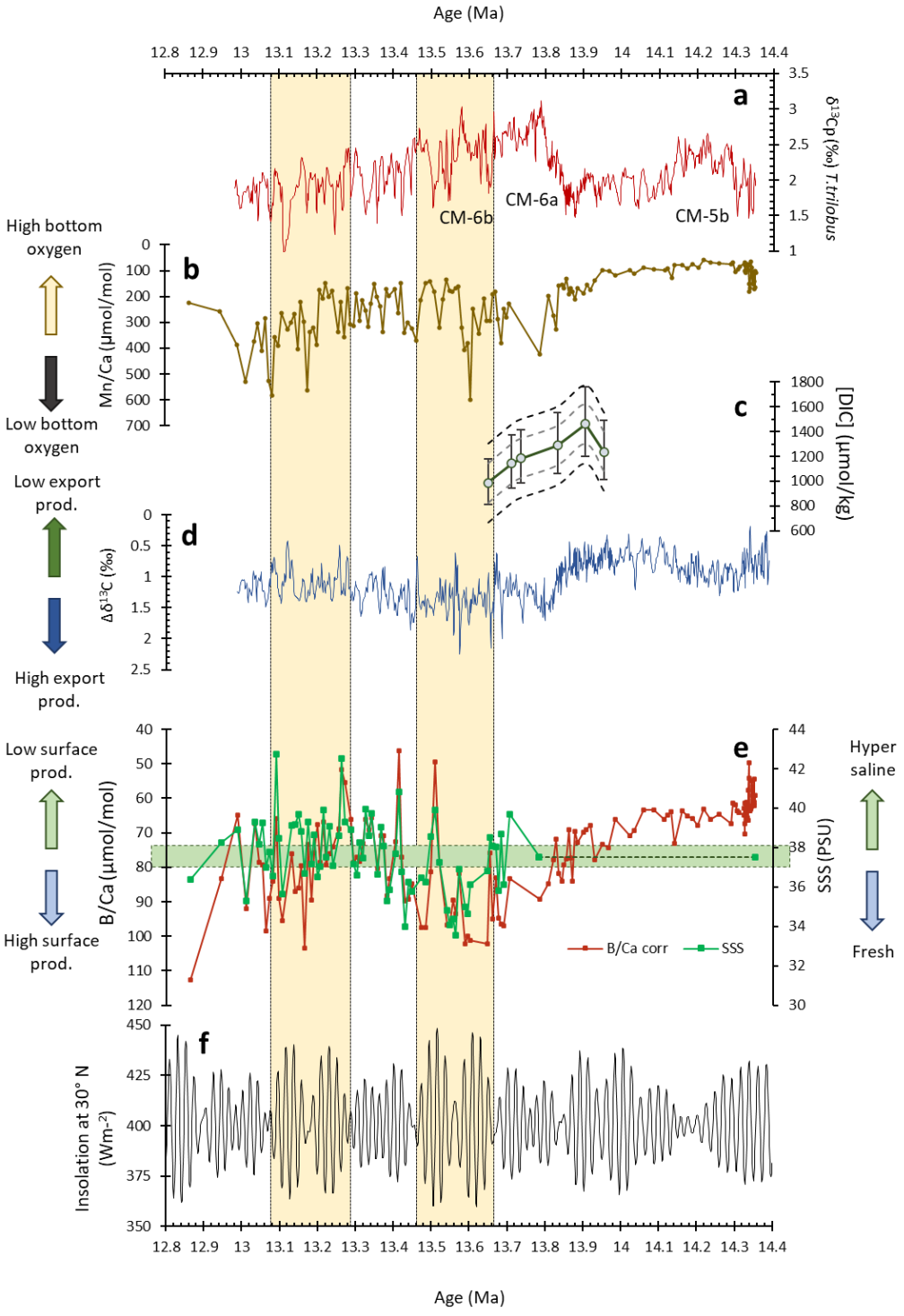

Figure 5.12 Proxy records from MRSF-RIP composite section plotted with the insolation at 30°N. Yellow bars indicate two phases of high insolation variability. High runoff (lowest SSS (e)) correlates with highest B/Ca, highest Mn/Ca (b) and highest export productivity ($\Delta\delta^{13}C$ proxy) (d) during the 1st phase of high insolation variability. The correlation between all the proxies and the $\Delta\delta^{13}C$ proxy is less evident during the 2nd phase of high insolation variability.

associated with enhanced export productivity in the Central proto-Mediterranean (Figure 5.12). A significant increase in export productivity in this region may therefore have contributed to the CO_2 decrease during the CM-6 event measured at the RIP site by Badger et al. (2013).

The decrease in [DIC] during the CM-6 event from the Malta record is around 750 µmol/kg.(Figure 5.12c) This value is an estimate since the calculations are not fully constrained due to low resolution and inherent uncertainties in the pH records and seawater composition. Nevertheless, this value is almost twice as much as the maximum value quoted for the drop in [DIC] during the MMCT for the open ocean site ODP 761, estimated at ~200 µmol/kg to ~400 µmol/kg (Sosdian et al., 2020). Both the [DIC] values from ODP 761 and Malta have been calculated using the same planktic species and the same salinity correction was applied indicating that comparisons between these two records are sufficiently robust to allow for discussion. Furthermore, the high salinity values in the partially enclosed Mediterranean may have possibly dampened these values. This points to significant differences in the carbonate chemistry across CM6 in the Central proto-Mediterranean and the open ocean. Reasons for this are explored below in section (5.7.1).

5.7.1 The influence of North African drainage systems on palaeoproductivity in the Central proto-Mediterranean

Lithological and mineralogical evidence indicates an extreme shift in sediment provenance and flux in the Central Mediterranean during the onset of Blue Clay deposition (John et al., 2003). The planktic $\delta^{18}O$ records (Mourik et al., 2011; this study) and calculated surface salinity values indicate an influx of fresh water into the central Mediterranean following the Antarctic Ice Sheet expansion from around 13.8 Ma (section 4.3.4). The orbital pacing strongly indicates a North African monsoonal mechanism, with possible positive feedback from closure of the Mesopotamian Seaway (MSR-2) (Figure 5.1) (Chapter 4; Zammit et al., 2022)

Enhanced hydrological activity favors chemical weathering with monsoon activity being the main factor that influences weathering at low latitudes in Asia (Clift & Plumb, 2008). Models indicate that orbital forcing by the 400 kyr eccentricity cycle is a

dominant control on weathering and river transport into the oceans (Ma et al., 2011). Orbitally controlled river nutrient delivery by river fluxes is considered to have a very important role in enhancing productivity and generating carbon burial (Ma et al., 2011). Thus, it can be reasonably assumed that the West African Monsoon had a significant effect on North African river systems and sedimentation and nutrient delivery into the Mediterranean. Therefore, productivity in the region was governed by short term precession cycles as well as the longer-term eccentricity modulated cycle (400 kyr), this is discussed further below.

High B/Ca, Mn/Ca and freshwater influx tends to occur during two phases of high insolation variability (yellow bars in Figure 5.12). The B/Ca records support a strong regional influence on surface productivity following the expansion of the Antarctic Icesheet at ~13.8 Ma. To further investigate this idea, it is important to relate the planktic B/Ca with the SSS records (Figure 5.12e). High salinity tends to increase foraminiferal B/Ca (Allen et al., 2012) but surface productivity is expected to increase during phases of low salinity when the influx of fresh water from North African deltas also delivers nutrients to surface waters. It can be argued that the high salinity in surface waters dampens the productivity signal in the foraminiferal B/Ca record (Figure 5.11a). Culture experiments indicate that $[\mathrm{B(OH)_4^-}]/[\mathrm{DIC}]$ varies by ~0.001 for a change in salinity of 1 PSU (Allen et al., 2012). Changes in the $[\mathrm{B(OH)_4^-}]/[\mathrm{DIC}]$ data for the RIP section can be as large as 0.06 in certain parts of the record particularly during the earliest (~13.66 Ma to ~13.46 Ma) and latest (~13.28 Ma to ~13.08 Ma) parts of the record (Figure 5.11a). These also correspond to the parts of the record with the largest swings in SSS and with lowest SSS values (and hence highest fluxes of fresh water and nutrients). Therefore, the surprisingly good correlation between B/Ca and reconstructed SSS most likely reflects a tight relationship between the hydrological and carbon cycles, rather than a salinity influence on the B/Ca proxy.

Therefore, enhanced export productivity in the Central proto-Mediterranean during CM-6 was likely caused by monsoonal activity in North Africa in a cooling world. This may explain why no strong, local productivity signals are observed during CM-5b, since there was limited monsoonal activity over North Africa in the warm world of the earliest part of the MMCT.

There are two phases of generally high planktic B/Ca, Mn/Ca for the RIP record. These intervals coincide with high amplitude insolation phases (yellow bars in Figure 5.12). During the 1st phase generally high $\Delta\delta^{13}C$, high B/Ca and elevated Mn/Ca are consistent with an efficient biological pump and highly productive waters. The presence of two distinct high productivity events being represented towards the earliest and latest parts of the RIP section was already suggested using bulk Ba/Ca records from the section by Bellanca et al., (2002) but accurate comparison with the results of this study are impossible due to different age models. Bellanca et al., (2002) suggested that two high-productivity events were driven by surface fertilization due to enhanced continental run-off and possible influence of upwelling systems (Bellanca et al., 2002). However, the lack of a strong peak in $\Delta\delta^{13}C$ during 2nd interval indicates that a different mechanism may be at play during this 2nd phase. The combined high B/Ca and low $\Delta\delta^{13}C$ may reflect high surface productivity via effective recycling of nutrients in the upper water column. Perhaps in this interval the poorly oxygenated conditions suggested by the Mn/Ca proxy reflect enhanced water column stratification and a reduction in bottom water ventilation. This interpretation could imply that the same level of export productivity and potential CO_2 drawdown was not achieved during the 2nd phase of favorable orbital parameters.

5.7.2 Implications for understanding the global carbon cycle during the MMCT

The geochemical records presented here suggest that the proto-Mediterranean had a highly dynamic carbon cycle. It is possible that during intervals of enhanced export productivity, surface waters pCO_2 was not in equilibrium with atmospheric pCO_2. Therefore, it is possible that the pCO_2 records from Malta published in Badger et al., (2013) do not represent atmospheric pCO_2. This allows for a re-evaluation of the CM-6 event in terms of drawdown of atmospheric CO_2 and climate feedbacks associated with growth of the Antarctic Ice Sheet. The Southern Ocean pCO_2 records from Raitzsch et al., (2021) (Figure 5.2b) can be interpreted to indicate either a local or a global signal. If the RIP records are interpreted to reflect regional behavior, then it is possible that the Southern Ocean record reflects a global increase in atmospheric pCO_2. This would imply that the CO_2 flux due to deep ocean ventilation was sufficiently large so as to overwhelm the CO_2 drawdown signal observed in Malta. The enhanced

ocean overturning following ice expansion therefore reflects a negative climate feedback, and may have also been responsible for the increase in atmospheric pCO_2 following the expansion of the Antarctic Ice Sheet at the Eocene-Oligocene transition (Pearson et al., 2009). The relatively stability of the Antarctic Ice Sheet through both transient increases in atmospheric pCO_2 confirms the predicted hysteresis effect (Pollard & DeConto, 2005).

5.8 Conclusion

The multiproxy approach using planktic foraminiferal B/Ca, Mn/Ca, and benthic and planktic foraminiferal $\delta^{13}C$ from the Central Mediterranean sediments of Malta highlights the differences in nutrient utilization and carbon cycle processes between the open ocean and low latitude shelf regions during the MMCT. The Central proto-Mediterranean experienced far higher export productivity than a site in the open ocean during the MMCT. High export productivity in the shelf environment represented by the MSRF and RIP sections in Malta was influenced by monsoonal activity and the ensuing surface run-off from Western North African river systems. The highly productive surface waters may have led to a disequilibrium between surface water dissolved CO_2 and atmospheric CO_2 in this region. Therefore, on this premise it is unreasonable to assume that the CO_2 record from Malta represents atmospheric pCO_2 during the CM-6 event. Currently, the only other high resolution pCO_2 record for the CM-6 event is from the Southern Ocean. Assuming this record is a better representation of atmospheric behavior during the MMCT it can be concluded that the Antarctic Ice Sheet expansion followed an interval of declining pCO_2 at a time when export productivity in the Central proto-Mediterranean was increasing, perhaps contributing to global drawdown of CO_2. Ice sheet expansion may have enhanced Southern Ocean bottom water formation, improving deep ocean ventilation and releasing CO_2 to the atmosphere, with implications for the stability of the Antarctic Ice Sheet. This study highlights the role of shallow water shelf environments in the carbon cycle during the MMCT. It also indicates the importance of gateway forcing, land-ocean teleconnections and weathering intensity at low latitudes as important mechanisms in global climate change.

Chapter 6

Synthesis – The pelagic deposits of the Maltese Islands as recorders of global carbon cycle dynamics

Chapter 6 - Synthesis – The pelagic deposits of the Maltese Islands as recorders of global carbon cycle dynamics

6.1 Climatic and oceanographic evolution during the Early to Middle Miocene, the records from Malta.

The mixed carbonate-siliciclastic shelf deposits of Malta have been widely used to reconstruct Late Oligocene to Late Miocene global and regional palaeoclimate and palaeoceanography. Many of the ideas presented in past studies are here confirmed or reinterpreted. New data and new ideas are also presented highlighting the validity of the Maltese deposits as a natural physical laboratory for the Miocene.

6.1.1 The Mesopotamian Gateway. The missing puzzle-piece in Miocene Antarctic cryospheric evolution?

The two-step (MSR-1 and MSR-2) Miocene closure of the Mesopotamian gateway determined from Maltese εNd records (Bialik et al., 2019) has been placed on an improved age model in this study (Figure 6.1). This has allowed for a more accurate correlation between the main changes in water flow through the Mesopotamian Seaway, the global stable isotope records of Westerhold et al. (2020), and the geochemical and lithological records from Malta. This has provided new insights into the possible effects that the changes in water circulation at low latitudes had on regional hydroclimate and Antarctic cryospheric evolution.

The main effect on regional climate related to the closure of the gateway seems to be a strong influence on hydroclimatic activity in North Africa. The records from Malta indicate a shift to a humid climate over western North Africa and increasing influence of river fluxes to Malta following each restriction event (MSR-1 and MSR-2) (Figure 6.1). Yet the two seawater restriction events happen against different global climatic backgrounds.

The timing of the Early Miocene restriction of the Mesopotamian Seaway (MSR-1) is better constrained by the new $^{87}Sr/^{86}Sr$ age model from the il-Blata site presented in Chapter 3 (Zammit et al., 2022). This has constrained the MSR-1 event to ~20.35 Ma to ~19.05 Ma, with further refinement at this site being impossible due to a large hiatus (Figure 6.1).

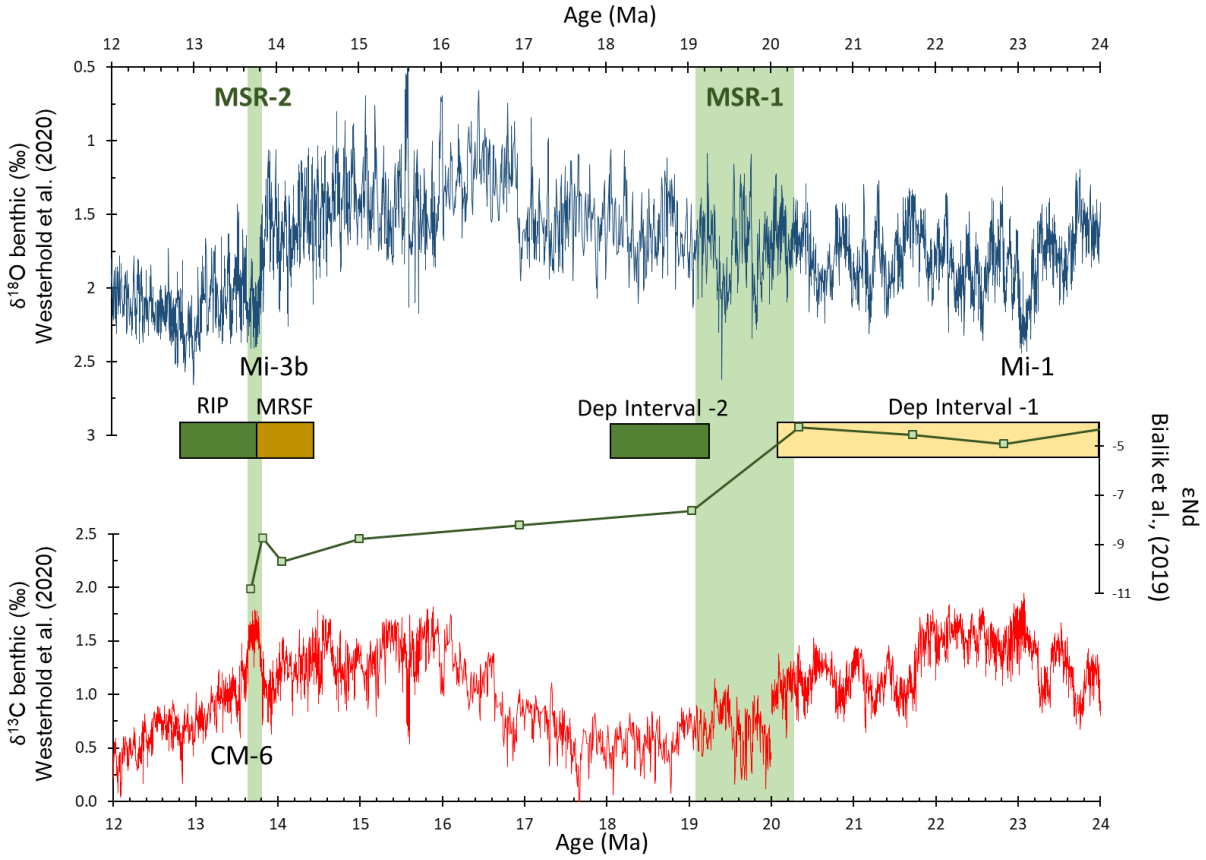

Figure 6.1 Main lithological deposits from Malta investigated during this study compared with global benthic stable isotope records from Westerhold et al., (2020) and the εNd records from Malta (Bialik et al., 2019). This shows that this important seaway restriction event coincided with two large positive excursions in the global $\delta^{18}O$ records of Westerhold et al., (2020).

It is possible that a eustatic mechanism may have amplified an ongoing tectonically driven seaway restriction. From a climate evolution perspective, MSR-1 happens towards the end of an Early Miocene cold-arid phase. Global climate subsequently enters a gently warming phase for reasons that are still unclear. The records from Malta show that the emplacement of a monsoonal-type climate over western North

Africa immediately followed, and hence was possibly caused by MSR-1. The diversion of warm intermediate waters into the Atlantic following the restriction in the Eastern Mediterranean may have energized the Atlantic Ocean at low latitudes with ensuing land-ocean teleconnections intensifying the hydrological cycle over North Africa. Chapter 3 proposes that il-Blata Depositional Interval 2 holds a record of this Early Miocene humid period over western North Africa. The sedimentary and geochemical records from the il-Blata Depositional Interval 2, indicates that this humid-warm climate existed at least until ~18.5 Ma. The termination of the phosphorites that were periodically deposited during Depositional Interval 1 suggests that the accompanying changes in the sedimentation rate and palaeoenvironment impacted the formation of these deposits.

The second and complete disconnection of water flow between the Indian Ocean and the Mediterranean (MSR-2) occurred during the MMCT and hence at a juncture between the warm world of the MCO and the colder world of the MMCT. A eustatic mechanism can be assumed to have caused the complete restriction of energy and water flow through the Mesopotamian gateway. Combining the new CenoGRID based age model for the Ras iI-Pellegrin section with the εNd data from Bialik et al., (2019) shows that the restriction was complete by 13.68 Ma (Figure 6.1). The main phase of Antarctic expansion (oxygen isotope excursion Mi-3b) had just occurred (13.82 Ma) excluding a causal mechanism for MSR-2 on Antarctic Ice-Sheet expansion. However, MSR-2 may have acted as an important positive feedback on Antarctic ice growth by enhancing the ACC and reducing heat transport from the low-latitudes to South Pole. The northward movement of the ITCZ due to strong atmospheric polar to low latitude thermal gradients is considered the main driver for the onset of an intense monsoonal climate over North Africa at this time (John et al., 2003). A land-ocean teleconnection mechanism similar to that following MSR-1 may also be considered here, possibly acting as a positive feedback in intensifying the West African Monsoon.

Both MSR-1 and MSR-2 may have acted to intensify hydrological activity over North Africa, however these two tectono-eustatic Miocene gateway restriction events cannot be considered primary climate drivers, since the variations in the Antarctic Ice Sheet

were likely controlled by other factors, predominantly atmospheric pCO_2. But for MSR-2 there is a strong case for considering the readjustment of the long-term ocean conveyor system as an important positive feedback in the thermal isolation of Antarctica.

It is intriguing to consider what may have been the effect on the evolution of the Antarctic ice sheet had MSR-1 acted to intensify the ACC. Presumably, reduced poleward heat transport would have facilitated ice expansion under appropriate boundary conditions. It is particularly intriguing that while a gradual warming trend is apparent in the interglacial benthic $\delta^{18}O$ values between 20Ma and 18Ma, the glacial cycle at 19.4Ma (which is associated with MSR-1), is unusually intense (Figure 6.1). Perhaps this unusually deep glacial cycle was aided by an intensified ACC, but fuller Antarctic glaciation was not supported by generally increasing atmospheric pCO_2. Clearly, higher resolution records of ocean circulation, pCO_2, and ice volume are needed to explore this robustly.

It would also be useful to extend and increase the resolution of the εNd record in Malta. This would include sections that span the time between MSR-1 and MSR-2. The il-Blata section could prove an ideal sampling location, although other sites containing the Upper Globigerina Limestone member and the Clay Rich Interval might prove more useful, including sites along the SW coast of Malta or Northern Gozo. These records could be coupled with records from Italy (e.g. Cornacchia et al., 2021) to further constrain the evolution of water flow through the Mesopotamian Gateway between ~19 Ma and ~14 Ma. It would also be of interest to measure εNd values within the younger parts of the RIP section, this would confirm that MSR-2 was indeed the final closure of the gateway.

6.1.2 Regional hydrodynamics and the carbon cycle

The short lived warm-humid interval that follows MSR-1 and recorded at il-Blata (~19.2 Ma to ~18.5 Ma) was also associated with a high-sedimentation rate and the eventual emplacement of chert deposits. It is possible that the high sedimentation rate, organic-rich deposits, and chert represent a high productivity interval induced by high river run-

off from North Africa. The termination of phosphorite deposition following MSR-1 may suggest changes in the operation of the carbon cycle, and further analysis of the extensive phosphorite beds of Malta is likely to yield useful information.

The mid-Miocene $\delta^{18}O$ records from Malta presented in Chapter 4 show that great variability in surface salinity occurred following the Mi-3b oxygen isotope excursion. These large changes in surface salinity indicate enhanced, astronomically-paced (precession and obliquity) hydrological activity over North Africa.

Investigation of the regional carbon cycle over Malta indicates that the hydrological activity that followed the expansion of the Antarctic ice sheet at ~13.8 Ma generated intense productivity in the surface waters of the Central Mediterranean (Chapter 5). Coupled with an efficient biological pump, this likely served as an important mechanism of drawing down atmospheric CO_2. However, comparison of $\delta^{13}C$ and B/Ca records from Malta with open ocean sites shows that this highly efficient biological pump was a regional phenomenon and that carbon cycle processes in the Central proto-Mediterranean were significantly different from the open ocean. This raises the possibility that the CO_2 record from Malta previously published in Badger et al., (2013) may reflect a regional rather than a global signal. This stresses the need for generating more palaeo-CO_2 records at high resolution from different sites. Ideally, sites chosen for *p*CO_2 reconstruction would allow for the distinction between global versus regional signals. Ideally, such work would include generating a longer-term, higher resolution CO_2 record using foraminifera from Malta using both alkenone and $\delta^{11}B$ proxies. This would allow identification of coupling and decoupling of the Central proto-Mediterranean CO_2 records with the global records, and help in further understanding the CM events, including the CM-6 event.

6.1.3 The foraminifera of Malta

It would be disingenuous to conclude this thesis without discussing the foraminifera of Malta. Although pristine benthic and planktic foraminifera provide extremely useful proxy data, one needs to carefully assess the suitability of terrestrial outcrops for

washing sediment and picking well-preserved foraminifera. For the case of the Maltese records this has proven to be as much a failure as a success.

Although many attempts were made to isolate foraminifera from the Early Miocene il-Blata records, this proved mostly a useless endeavor. Even though records exist of work that involved the extraction of foraminifera from the Lower Globigerina Limestone for taxonomic purposes (Foresi et al., 2007), I would assume that lithification processes are significantly advanced and the presence of diagenetic cements would render the foraminifera unsuitable for geochemical work. Well preserved foraminifera have been identified in Depositional Interval 2 of the il-Blata section, although these proved to be rather small in size. Although the presence of foraminifera tends to be low and foraminifera are absent in many horizons, future taxonomic studies from the il-Blata Depositional Interval -2 should not be excluded.

The foraminifera from the Middle Miocene sections (MRSF and RIP) are easy to obtain from the sediment and can occur in high abundances. The foraminifera from RIP demonstrate excellent preservation state, but future work should focus on generating SEM images from different horizons within the section to further validate this claim. The foraminifera from the MRSF section offer a conundrum. Although these foraminifera show signs of recrystallisation and contamination, this has not impaired the B/Ca and Mn/Ca records, yet Mg/Ca records from this section are mostly unusable for the generation of temperature records. Most likely these foraminifera are contaminated by the iron-dolomite mineral ankerite. Efforts should be made to study these foraminifera in detail and identify the diagenetic component that is raising the Mg/Ca and possibly identify methods to account for the Mg/Ca in the diagenetic coat and correct for this value. Alternatively, the foraminifera could be analysed by laser ablation ICP-MS to avoid the coating (Nairn et al., 2021). This would allow Mg/Ca temperature, and hence $\delta^{18}O_{sw}$, calculations for the MRSF section.

6.2 Conclusion

Overall, this study indicates that the two-step closure of the Mesopotamian Seaway during the Early and Middle Miocene played a significant contribution in the evolution of climate during the Miocene. The flow of water through the gateway was influenced by eustatic sea-level changes driven by the waxing and waning of the Antarctic Ice Sheet. In turn the re-adjusting of water circulation at low latitudes influenced the evolution of Miocene climate evolution. The new low latitude circulation system influenced regional hydrology over North Africa by intensifying the hydrological cycle. In turn intense run-off into the shallow waters of the Mediterranean influenced the carbon cycle by enhancing pCO_2 drawdown highlighting the importance of shallow water zones as important sites for carbon cycle processes.

References

Abels, H. A., Hilgen, F. J., Krijgsman, W., Kruk, R. W., Raffi, I., Turco, E., & Zachariasse, W. J. (2005). Long-period orbital control on middle Miocene global cooling: Integrated stratigraphy and astronomical tuning of the Blue Clay Formation on Malta. *Paleoceanography*. https://doi.org/10.1029/2004PA001129

Abreu, V. S., & Anderson, J. B. (1998). Glacial Eustasy During the Cenozoic: Sequence Stratigraphic Implications. *AAPG Bulletin*, *82*(7), 1385–1400. https://doi.org/10.1306/1D9BCA89-172D-11D7-8645000102C1865D

Allen, K. A., Onisch, H. ¨, Eggins, S. M., & Rosenthal, Y. (2012). Environmental controls on B/Ca in calcite tests of the tropical planktic foraminifer species *Globigerinoides ruber* and *Globigerinoides sacculifer*. https://doi.org/10.1016/j.epsl.2012.07.004

Alvarez, L. W., Alvarez, W., Asaro, F., & Michel, H. V. (1980). Extraterrestrial Cause for the Cretaceous-Tertiary Extinction - Experimental Results and Theoretical Interpretation. *Science*, *208*(4448), 1095–1108. https://doi.org/10.1126/science.208.4448.1095

Amorosi, A., Lucchi, F. R., & Tateo, F. (1995). The Lower Miocene siliceous zone: a marker in the palaeogeographic evolution of the northern Apennines. *Palaeogeography, Palaeoclimatology, Palaeoecology*, *118*(1–2), 131–149. https://doi.org/10.1016/0031-0182(94)00140-4

Auer, G., Piller, W. E., Reuter, M., & Harzhauser, M. (2015). *Correlating carbon and oxygen isotope events in early to middle Miocene shallow marine carbonates in the Mediterranean region using orbitally tuned chemostratigraphy and lithostratigraphy*. https://doi.org/10.1002/2014PA002716

Auer, G., Hauzenberger, C. A., Reuter, M., & Piller, W. E. (2016). Orbitally paced phosphogenesis in Mediterranean shallow marine carbonates during the middle Miocene Monterey event. *Geochemistry, Geophysics, Geosystems*, *17*(4), 1492–1510. https://doi.org/10.1002/2016GC006299

Badger, M. P. S., (2010). Middle Miocene carbon cycle dynamics : A multi-proxy approach. *Cardiff University PhD*, 221. https://doi.org/10.1017/S0016756809990227

Badger, M. P. S., Lear, C. H., Pancost, R. D., Foster, G. L., Bailey, T. R., Leng, M. J., & Abels, H. A. (2013). CO_2 drawdown following the middle Miocene expansion of the Antarctic Ice Sheet. *Paleoceanography*, *28*(1), 42–53. https://doi.org/10.1002/palo.20015

Baker, P. A., Gieskes, J. M., & Elderfield, H. (1982). Diagenesis of carbonates in deep-sea sediments; evidence from Sr/Ca ratios and interstitial dissolved Sr (super 2+) data. *Journal of Sedimentary Research*, *52*(1), 71–82. https://doi.org/10.1306/212F7EE1-2B24-11D7-8648000102C1865D

Baldassini, N., & Di Stefano, A. (2015). New insights on the Oligo-Miocene succession bearing phosphatic layers of the Maltese Archipelago. *Italian Journal of Geosciences*, *134*(2), 355–366. https://doi.org/10.3301/IJG.2014.52

Baldassini, N., & Di Stefano, A. (2017). Stratigraphic features of the Maltese Archipelago: a synthesis. *Natural Hazards*, *86*(September), 203–231. https://doi.org/10.1007/s11069-016-2334-9

Barron, E. J., & Peterson, W. H. (1989). Model Simulation of the Cretaceous Ocean Circulation. *New Series*, *244*(4905), 684–686.

Bell, R. J., Short, R. T., & Byrne, R. H. (2011). In situ determination of total dissolved inorganic carbon by underwater membrane introduction mass spectrometry. *Limnology and Oceanography: Methods*, *9*(4), 164–175. https://doi.org/10.4319/LOM.2011.9.164

Bellanca, A., Sgarrella, F., Neri, R., Russo, B., Sprovieri, M., Bonaduce, G., & Rocca, D. (2002). Evolution of the Mediterranean basin during the Late Langhian - Early Serravallian: An integrated paleoceanographic approach. *Rivista Italiana Di Paleontologia e Stratigrafia*, *108*(2), 223–239. https://doi.org/10.13130/2039-4942/5472

Ben Yahia, N., Sebei, A., Harris, C., Boussen, S., & Chaabani, F. (2019). Mineralogical and geochemical criteria to identify the origin and the depositional environment of the upper Numidian babouchite siliceous rocks, northwestern Tunisia. *Journal of African Earth Sciences*, *149*, 487–502. https://doi.org/10.1016/j.jafrearsci.2018.09.010

Berger, W. H., Kroenke, L. W., & Mayer, L. A. (1993). 22. Quaternary oxygen isotope record of pelagic foraminifers: site 806, ontong java plateau 1. *Scientific Results*, *130*.

Betzler, C., Eberli, G. P., Kroon, D., Wright, J. D., Swart, P. K., Nath, B. N., Alvarez-Zarikian, C. A., Alonso-Garciá, M., Bialik, O. M., Blättler, C. L., Guo, J. A., Haffen, S., Horozal, S., Inoue, M., Jovane, L., Lanci, L., Laya, J. C., Mee, A. L. H., Lüdmann, T., … Young, J. R. (2016). The abrupt onset of the modern South Asian Monsoon winds. *Scientific Reports*, *6*. https://doi.org/10.1038/srep29838

Bialik, O. M., Frank, M., Betzler, C., Zammit, R., & Waldmann, N. D. (2019). Two-step closure of the Miocene Indian Ocean Gateway to the Mediterranean. *Scientific Reports*, *9*(1), 8842. https://doi.org/10.1038/s41598-019-45308-7

Bialik, O. M., Reolid, J., Betzler, C., Eberli, G. P., & Waldmann, N. D. (2020). Source shifts to periplatform deposits during the early to middle Miocene in response to climatic and oceanographic forcing, Maldives, western Indian Ocean. *Palaeogeography, Palaeoclimatology, Palaeoecology*, *559*, 109969. https://doi.org/10.1016/J.PALAEO.2020.109969

Bialik, O. M., Zammit, R., & Micallef, A. (2021). Architecture and sequence stratigraphy of the Upper Coralline Limestone formation, Malta—Implications for Eastern Mediterranean restriction prior to the Messinian Salinity Crisis. *The Depositional Record*, *7*(2), 256–270. https://doi.org/10.1002/DEP2.138

Billups, K., Rickaby, R. E. M., & Schrag, D. P. (2004). Cenozoic pelagic Sr/Ca records: Exploring a link to paleoproductivity. *Paleoceanography*, *19*(3). https://doi.org/10.1029/2004PA001011

Boyle, E. A., & Keigwin, L. D. (1985). Comparison of Atlantic and Pacific paleochemical records for the last 215,000 years: changes in deep ocean circulation and chemical inventories. *Earth and Planetary Science Letters*, *76*(1–2), 135–150. https://doi.org/10.1016/0012-821X(85)90154-2

Boyle, Edward A. (1983). Manganese carbonate overgrowths on foraminifera tests. *Geochimica et Cosmochimica Acta*, *47*(10), 1815–1819. https://doi.org/10.1016/0016-7037(83)90029-7

Broecker, W.S. and Peng, T.H. (1982) Tracers in the Sea. Eldigio Press, 1-690.

Brown, E. T., Johnson, T. C., Scholz, C. A., Cohen, A. S., & King, J. W. (2007). Abrupt change in tropical African climate linked to the bipolar seesaw over the past 55,000 years. *Geophysical Research Letters*, *34*(20). https://doi.org/10.1029/2007GL031240

Burdige, D. J. (1993). The biogeochemistry of manganese and iron reduction in marine sediments. *Earth-Science Reuiews*, *35*, 249–284.

Carbone, S., Grasso, M., Lentini, F., & Pedley, H. M. (1987). The distribution and palaeoenvironment of early miocene phosphorites of southeast sicily and their relationships with the maltese phosphorites. *Palaeogeography, Palaeoclimatology, Palaeoecology*, *58*(1–2), 35–53. https://doi.org/10.1016/0031-0182(87)90004-6

Cao, W., Zahirovic, S., Flament, N., Williams, S., Golonka, J., Muller, R.D. (2017). Improving global paleogeography since the late Paleozoic using paleobiology, Biogeosciences, 14, 5425-5439

Chang, P., Zhang, R., Hazeleger, W., Wen, C., Wan, X., Link, J. I., Haarsma, R. J., Breugem, W.-P., & Seidel, H. (2008). *Oceanic link between abrupt changes in the North Atlantic Ocean and the African monsoon*. https://doi.org/10.1038/ngeo218

Chen, P., Yu, J., & Jin, Z. (2017). An evaluation of benthic foraminiferal U/Ca and U/Mn proxies for deep ocean carbonate chemistry and redox conditions. *Geochemistry, Geophysics, Geosystems*, *18*(2), 617–630. https://doi.org/10.1002/2016GC006730

Clift, P. D. (2010). Enhanced global continental erosion and exhumation driven by Oligo-Miocene climate change. *Geophysical Research Letters*, *37*, L09402. https://doi.org/10.1029/2010GL043067

Clift, P. D., & Plumb, R. A. (2008). The Asian monsoon: Causes, history and effects. *The Asian Monsoon: Causes, History and Effects*, 1–270. https://doi.org/10.1017/CBO9780511535833

Clift, P. D., Wan, S., & Blusztajn, J. (2014). Reconstructing chemical weathering, physical erosion and monsoon intensity since 25Ma in the northern South China Sea: A review of competing proxies. *Earth-Science Reviews*, *130*, 86–102. https://doi.org/10.1016/J.EARSCIREV.2014.01.002

Cohen, A. S., Coe, A. L., & Kemp, D. B. (2007). The late Palaeocene-Early Eocene and Toarcian (Early Jurassic) carbon isotope excursions: a comparison of their time scales, associated environmental changes, causes and consequences. *Journal of the Geological Society*, *164*, 1093–1108.

Cornacchia, I., Agostini, S., & Brandano, M. (2018). Miocene Oceanographic Evolution Based on the Sr and Nd Isotope Record of the Central Mediterranean. *Paleoceanography and Paleoclimatology*, *33*(1), 31–47. https://doi.org/10.1002/2017PA003198

Cornacchia, Irene, Brandano, M., & Agostini, S. (2021). Miocene paleoceanographic evolution of the Mediterranean area and carbonate production changes: A review. *Earth-Science Reviews*, 103785. https://doi.org/10.1016/J.EARSCIREV.2021.103785

Cramer, B. S., Miller, K. G., Barrett, P. J., & Wright, J. D. (2011). Late Cretaceous-Neogene trends in deep ocean temperature and continental ice volume: Reconciling records of benthic foraminiferal geochemistry (δ18O and Mg/Ca) with sea level history. *Journal of Geophysical Research: Oceans*, *116*(12). https://doi.org/10.1029/2011JC007255

Cramer, B. S., Toggweiler, J. R., Wright, J. D., Katz, M. E., & Miller, K. G. (2009). Ocean overturning since the Late Cretaceous: Inferences from a new benthic foraminiferal isotope compilation. *Paleoceanography*, *24*(4). https://doi.org/10.1029/2008PA001683

Dart, C. J., Bosence, D. W. J., & McClay, K. R. (1993). Stratigraphy and structure of the Maltese graben system. *Journal of the Geological Society*, *150*(6), 1153–1166. https://doi.org/10.1144/GSJGS.150.6.1153

de la Vara, A., & Meijer, P. (2016). Response of Mediterranean circulation to Miocene shoaling and closure of the Indian Gateway: A model study. *Palaeogeography, Palaeoclimatology, Palaeoecology*, *442*, 96–109. https://doi.org/10.1016/J.PALAEO.2015.11.002

De Vleeschouwer, D., Vahlenkamp, M., Crucifix, M., & Pälike, H. (2017). Alternating Southern and Northern Hemisphere climate response to astronomical forcing during the past 35 m.y. *Geology*, *45*(4), 375–378. https://doi.org/10.1130/G38663.1

Deidun, A., Gauci, A., Azzopardi, J., Cutajar, D., Farrugia, H., & Drago, A. (2016). Which is the best predictor of sea temperature: satellite, model or data logger values? a case study from the Maltese Islands (Central Mediterranean). *Journal of Coastal Research*, *1*(75), 627–631. https://doi.org/10.2112/SI75-126.1/29488/WHICH-IS-THE-BEST-PREDICTOR-OF-SEA-TEMPERATURE

Demenocal, P., Ortiz, J., Guilderson, T., Adkins, J., Sarnthein, M., Baker, L., & Yarusinsky, M. (2000). Abrupt onset and termination of the African Humid Period:: rapid climate responses to gradual insolation forcing. *Quaternary Science Reviews*, *19*(1–5), 347–361. https://doi.org/10.1016/S0277-3791(99)00081-5

Diester-Haass, L., Billups, K., Gröcke, D. R., François, L., Lefebvre, V., & Emeis, K. C. (2009). Mid-Miocene paleoproductivity in the Atlantic Ocean and implications for the global carbon cycle. *Paleoceanography*, *24*(1), https://doi.org/10.1029/2008PA001605

Diester-Haass, L., Billups, K., Jacquemin, I., Emeis, K. C., Lefebvre, V., & François, L. (2013). Paleoproductivity during the middle Miocene carbon isotope events: A data-model approach. *Paleoceanography*, *28*(2), 334–346. https://doi.org/10.1002/palo.20033

Drury, A. J., Liebrand, D., Westerhold, T., Beddow, H. M., Hodell, D. A., Rohlfs, N., Wilkens, R. H., Lyle, M., Bell, D. B., Kroon, D., Pälike, H., & Lourens, L. J. (2021). Climate, cryosphere and carbon cycle controls on Southeast Atlantic orbital-scale carbonate deposition since the Oligocene (30–0 Ma). *Climate of the Past*, *17*(5), 2091–2117. https://doi.org/10.5194/CP-17-2091-2021

Elderfield, H., Greaves, M., Barker, S., Hall, I. R., Tripati, A., Ferretti, P., Crowhurst, S., Booth, L., & Daunt, C. (2010). A record of bottom water temperature and seawater δ18O for the Southern Ocean over the past 440 kyr based on Mg/Ca of benthic foraminiferal *Uvigerina* spp. *Quaternary Science Reviews*, *29*(1–2), 160–169. https://doi.org/10.1016/J.QUASCIREV.2009.07.013

Erez, J., & Luz, B. (1983). Experimental paleotemperature equation for planktonic foraminifera. *Geochimica et Cosmochimica Acta*, *47*(6), 1025–1031. https://doi.org/10.1016/0016-7037(83)90232-6

Essid, J., Saidi, R., Ahmed, A. H., Felhi, M., Fattah, N., & Tlili, A. (2019). Characterization, nomenclature and factors controlling the stability of quartz and opal-CT of Burdigalian and Ypresian siliceous rocks from Tunisia. *Journal of African Earth Sciences*, *155*, 151–160. https://doi.org/10.1016/j.jafrearsci.2019.04.018

Evans, D., & Mller, W. (2012). Deep time foraminifera Mg/Ca paleothermometry: Nonlinear correction for secular change in seawater Mg/Ca. *Paleoceanography*, *27*(4). https://doi.org/10.1029/2012PA002315

Fabbrini, A., Baldassini, N., Caricchi, C., Foresi, L. M., Sagnotti, L., Dinarés-Turell, J., Di Stefano, A., Lirer, F., Menichetti, M., Winkler, A., & Distefano, S. (2019). In search of the Burdigalian GSSP: New evidence from the Contessa Section (Italy). *Italian Journal of Geosciences*, *138*(2), 274–295. https://doi.org/10.3301/IJG.2019.07

Filippidi, A., & Lange, G. J. De. (2019). Eastern Mediterranean Deep Water Formation During Sapropel S1: A Reconstruction Using Geochemical Records Along a Bathymetric Transect in the Adriatic Outflow Region. *Paleoceanography and Paleoclimatology*, *34*(3), 409–429. https://doi.org/10.1029/2018PA003459

Flower, B., & Kennett, J. (1993). Relations between Monterey Formation deposition and Middle Miocene global cooling - Naples-Beach section, California. *Geology*, *21*(10), 877–880. https://doi.org/10.1130/0091-7613(1993)0212.3.CO2

Flower, B. P., & Kennett, J. P. (1994). The middle Miocene climatic transition: East Antarctic ice sheet development, deep ocean circulation and global carbon cycling. *Palaeogeography, Palaeoclimatology, Palaeoecology*, *108*(3–4), 537–555. https://doi.org/10.1016/0031-0182(94)90251-8

Fluteau, F., Ramstein, G., & Besse, J. (1999). Simulating the evolution of the Asian and African monsoons during the past 30 Myr using an atmospheric general circulation model. *Journal of Geophysical Research Atmospheres*, *104*(D10), 11995–12018. https://doi.org/10.1029/1999JD900048

Föllmi, K. B. (1996). The phosphorus cycle, phosphogenesis and marine phosphate-rich deposits. *Earth-Science Reviews*, *40*(1–2). https://doi.org/10.1016/0012-8252(95)00049-6

Föllmi, K. B., Gertsch, B., Renevey, J. P., De Kaenel, E., & Stille, P. (2008). Stratigraphy and sedimentology of phosphate-rich sediments in Malta and south-eastern Sicily (latest Oligocene to early Late Miocene). *Sedimentology*. https://doi.org/10.1111/j.1365-3091.2007.00935.x

Föllmi, K. B., Schöllhorn, I., Ulianov, A., Adatte, T., Spangenberg, J. E., de Kaenel, E., Gertsch, B., Schwennicke, T., Ledesma, M. C., Grimm, K. A., & Garrison, R. E. (2019). Phosphogenesis during the Cenozoic transition from greenhouse to icehouse conditions: Upper Oligocene to lower Miocene siliceous, phosphate, and organic-rich sediments near La Purísima, Baja California Sur, Mexico. *The Depositional Record*, *5*(1), 23–52. https://doi.org/10.1002/dep2.52

Foresi, L.M., Baldassini, N., Sagnotti, L., Lirer, F., Di Stefano, A., Caricchi, C., Verducci, M., Salvatorini, G., & Mazzei, R. (2014). Integrated stratigraphy of the St. Thomas section (Malta Island): A reference section for the lower Burdigalian of the Mediterranean Region. *Marine Micropaleontology*. https://doi.org/10.1016/j.marmicro.2014.06.004

Foresi, L. M., Mazzei, R., Salvatorini, G., Donia, F., Foresi, L. M., Mazzei, R., & Salvatorini, G. (2007). *Biostratigraphy and chronostratigraphy of the Maltese Lower Globigerina Limestone Member (Globigerina Limestone Formation): new preliminary data based on calcareous plankton*. *46*(15), 175–181.

Foresi, L. M., Verducci, M., Baldassini, N., Lirer, F., Mazzei, R., Gianfranco, S., Ferraro, L., & Da Prato, S. (n.d.). Integrated stratigraphy of St. Peter's Pool section (Malta): new age for the Upper Globigerina Limestone member and progress towards the Langhian GSSP.

Foster, G. L. (2008). Seawater pH, pCO2 and [CO2-3] variations in the Caribbean Sea over the last 130 kyr: A boron isotope and B/Ca study of planktic foraminifera. *Earth and Planetary Science Letters*, *271*(1–4), 254–266. https://doi.org/10.1016/J.EPSL.2008.04.015

Foster, Gavin L., Lear, C. H., & Rae, J. W. B. (2012). The evolution of pCO2, ice volume and climate during the middle Miocene. *Earth and Planetary Science Letters*, *341–344*, 243–254. https://doi.org/10.1016/J.EPSL.2012.06.007

Gatt, P. A., & Gluyas, J. G. (2012). Climatic controls on facies in Palaeogene Mediterranean subtropical carbonate platforms. *Petroleum Geoscience*, *18*(3), 355–367. https://doi.org/10.1144/1354-079311-032

González, F. J., Somoza, L., Hein, J. R., Medialdea, T., León, R., Urgorri, V., Reyes, J., & Martín-Rubí, J. A. (2016). Phosphorites, Co-rich Mn nodules, and Fe-Mn crusts from Galicia Bank, NE Atlantic: Reflections of Cenozoic tectonics and paleoceanography. *Geochemistry, Geophysics, Geosystems*, *17*(2), 346–374. https://doi.org/10.1002/2015GC005861

Govin, A., Holzwarth, U., Heslop, D., Keeling, L. F., Zabel, M., Mulitza, S., Collins, J. A., Chiessi, C. M., Govin, A., Holzwarth, U., Heslop, D., Keeling, L. F., Zabel, M., Mulitza, S., Collins, J. A., & Chiessi, C. M. (2012). Distribution of major elements in Atlantic surface sediments (36°N–49°S): Imprint of terrigenous input and continental weathering. *Geochemistry, Geophysics, Geosystems*, *13*(1). https://doi.org/10.1029/2011GC003785

Gradstein, F. M., Ogg, J. G. (James G., Schmitz, M. D., & Ogg, G. (2020). *Geologic time scale 2020* https://doi.org/10.1016/C2020-1-02369-3

Gradstein, Felix M., Ogg, J. G., & Hilgen, F. J. (2012). On The Geologic Time Scale. *Newsletters on Stratigraphy*, *45*(2), 171–188. https://doi.org/10.1127/0078-0421/2012/0020

Gray, W. R., & Evans, D. (2019). Nonthermal Influences on Mg/Ca in Planktonic Foraminifera: A Review of Culture Studies and Application to the Last Glacial Maximum. *Paleoceanography and Paleoclimatology*, *34*(3), 306–315. https://doi.org/10.1029/2018PA003517

Gruszczynski, M., Marshall, J. D., Goldring, R., Coleman, M. L., Malkowski, K., Gazdzicka, E., Semil, J., & Gatt, P. (2008). Hiatal surfaces from the Miocene Globigerina Limestone Formation of Malta: Biostratigraphy, sedimentology, trace fossils and early diagenesis. *Palaeogeography Palaeoclimatology Palaeoecology*, *270*(3–4), 239–251. https://doi.org/10.1016/j.palaeo.2008.01.035

Hamon, N., Sepulchre, P., Lefebvre, V., & Ramstein, G. (2013). Climate of the Past The role of eastern Tethys seaway closure in the Middle Miocene Climatic Transition (ca. 14 Ma). *Clim. Past*, *9*, 2687–2702. https://doi.org/10.5194/cp-9-2687-2013

Haynes, L. L., Hönisch, B., Holland, K., Rosenthal, Y., & Eggins, S. M. (2019). Evaluating the planktic foraminiferal B/Ca proxy for application to deep time paleoceanography. *Earth and Planetary Science Letters*, *528*, 115824. https://doi.org/10.1016/J.EPSL.2019.115824

Heggie, D. T., Skyring, G. W., O'Brien, G. W., Reimers, C., Herczeg, A., Moriarty, D. J. W., Burnett, W. C., & Milnes, A. R. (1990). Organic carbon cycling and modern phosphorite formation on the East Australian continental margin: an overview. *Geological Society, London, Special Publications*, *52*(1), 87–117. https://doi.org/10.1144/GSL.SP.1990.052.01.07

Hemming, N. G., & Hanson, G. N. (1992). Boron isotopic composition and concentration in modern marine carbonates. *Geochimica et Cosmochimica Acta*, *56*(1), 537–543. https://doi.org/10.1016/0016-7037(92)90151-8

Hennekam, R., Donders, T. H., Zwiep, K., & de Lange, G. J. (2015). Integral view of Holocene precipitation and vegetation changes in the Nile catchment area as inferred from its delta sediments. *Quaternary Science Reviews*, *130*, 189–199.

Hilgen, FJ, Abels, HA, Iaccarino, S, Krijgsman, W, Raffi, I, Sprovieri, R, Turco, E, Zachariasse, W. (2009). The Global Stratotype Section and Point (GSSP) of the Serravallian Stage (Middle Miocene). *EPISODES*, *32*(3), 152–166.

Hilting, A. K., Kump, L. R., & Bralower, T. J. (2008). Variations in the oceanic vertical carbon isotope gradient and their implications for the Paleocene-Eocene biological pump. *Paleoceanography*, *23*(3). https://doi.org/10.1029/2007PA001458

Holbourn, A., Kuhnt, W., Clemens, S., Prell, W., & Andersen, N. (2013). Middle to late Miocene stepwise climate cooling: Evidence from a high-resolution deep water isotope curve spanning 8 million years. *Paleoceanography*, *28*(4), 688–699. https://doi.org/10.1002/2013PA002538

Holbourn, A., Kuhnt, W., Kochhann, K. G. D., Andersen, N., & Sebastian Meier, K. J. (2015). Global perturbation of the carbon cycle at the onset of the Miocene Climatic Optimum. *Geology*, *43*(2), 123–126. https://doi.org/10.1130/G36317.1

Holbourn, A., Kuhnt, W., Lyle, M., Schneider, L., Romero, O., & Andersen, N. (2014). Middle Miocene climate cooling linked to intensification of eastern equatorial Pacific upwelling. *Geology*, *42*(1), 19–22. https://doi.org/10.1130/G34890.1

Holbourn, A., Kuhnt, W., Schulz, M., Flores, J.-A., & Andersen, N. (2007). *Orbitally-paced climate evolution during the middle Miocene "Monterey" carbon-isotope excursion*. https://doi.org/10.1016/j.epsl.2007.07.026

Hopcroft, P. O., & Valdes, P. J. (2021). Paleoclimate-conditioning reveals a North Africa land–atmosphere tipping point. *Proceedings of the National Academy of Sciences*, *118*(45), e2108783118. https://doi.org/10.1073/PNAS.2108783118

Horita, J., Zimmermann, H., & Holland, H. D. (2002). Chemical evolution of seawater during the Phanerozoic: Implications from the record of marine evaporites. *Geochimica et Cosmochimica Acta*, *66*(21), 3733–3756. https://doi.org/10.1016/S0016-7037(01)00884-5

Hounslow, M. W., White, H. E., Drake, N. A., Salem, M. J., El-Hawat, A., McLaren, S. J., Karloukovski, V., Noble, S. R., & Hlal, O. (2017). Miocene humid intervals and establishment of drainage networks by 23 Ma in the central Sahara, southern Libya. *Gondwana Research*, *45*, 118–137. https://doi.org/10.1016/J.GR.2016.11.008

Iaccarino, S. M., Di Stefano, A., Foresi, L. M., Turco, E., Baldassini, N., Cascella, A., Da Prato, S., Ferraro, L., Gennari, R., Hilgen, F. J., Lirer, F., Maniscalco, R., Mazzei, R., Riforgiato, F., Russo, B., Sagnotti, L., Salvatorini, G., Speranza, F., & Verducci, M. (2011). High-resolution integrated stratigraphy of the upper Burdigalian-lower Langhian in the Mediterranean: the Langhian historical stratotype and new candidate sections for defining its GSSP. *Stratigraphy*, *8*(2–3), 199–215.

Jacobs, E., Weissert, H., Shields, G., & Stille, P. (1996). The monterey event in the Mediterranean: A record from shelf sediments of Malta. *Paleoceanography*, *11*(6). https://doi.org/10.1029/96PA02230

Jicha, B. R., Scholl, D. W., & Rea, D. K. (2009). Circum-Pacific arc flare-ups and global cooling near the Eocene-Oligocene boundary. *Geology*, *37*(4), 303–306. https://doi.org/10.1130/G25392A.1

John, C. M., Mutti, M., & Adatte, T. (2003). Mixed carbonate-siliciclastic record on the North African margin (Malta) - coupling of weathering processes and mid Miocene climate. *Geological Society of America Bulletin*, *115*(2), 217–229. https://doi.org/10.1130/0016-7606(2003)115<0217:MCSROT>2.0.CO;2

Jonkers, L., & Kučera, M. (2015). Global analysis of seasonality in the shell flux of extant planktonic Foraminifera. *Biogeosciences*, *12*(7), 2207–2226. https://doi.org/10.5194/BG-12-2207-2015

Kasbohm, J., & Schoene, B. (2018). Rapid eruption of the Columbia River flood basalt and correlation with the mid-Miocene climate optimum. *Science Advances*, *4*(9). https://doi.org/10.1126/SCIADV.AAT8223

Kocsis, L., Vennemann, T. W., Fontignie, D., Baumgartner, C., Montanari, A., & Jelen, B. (2008). Oceanographic and climatic evolution of the Miocene Mediterranean deduced from Nd, Sr, C, and O isotope compositions of marine fossils and sediments. *Paleoceanography*, *23*(4). https://doi.org/10.1029/2007PA001540

Kontakiotis, G., Butiseacă, G. A., Antonarakou, A., Agiadi, K., Zarkogiannis, S. D., Krsnik, E., Besiou, E., Zachariasse, W. J., Lourens, L., Thivaiou, D., Koskeridou, E., Moissette, P., Mulch, A., Karakitsios, V., & Vasiliev, I. (2022). Hypersalinity accompanies tectonic restriction in the eastern Mediterranean prior to the Messinian Salinity Crisis. *Palaeogeography, Palaeoclimatology, Palaeoecology*, *592*. https://doi.org/10.1016/J.PALAEO.2022.110903

Kováčvá, P., Emmanuel, L., Hudáčková, N., & Renard, M. (2009). Central paratethys paleoenvironment during the Badenian (Middle Miocene): Evidence from foraminifera and stable isotope (δ13C and δ18O) study in the Vienna Basin (Slovakia). *International Journal of Earth Sciences*, *98*(5), 1109–1127. https://doi.org/10.1007/S00531-008-0307-2/FIGURES/8

Krijgsman, W., Hilgen, F. J., Raffi, I., Sierro, F. J., & Wilsonk, D. S. (1999). *Chronology, causes and progression of the Messinian salinity crisis*. www.nature.com

Krom, M. D., Michard, A., Cliff, R. A., & Strohle, K. (1999). Sources of sediment to the Ionian Sea and western Levantine basin of the Eastern Mediterranean during S-1 sapropel times. *Marine Geology*, *160*(1–2), 45–61.

Kuhnert, H., Bickert, T., & Paulsen, H. (2009). Southern Ocean frontal system changes precede Antarctic ice sheet growth during the middle Miocene. *Earth and Planetary Science Letters*, *284*(3–4), 630–638. https://doi.org/10.1016/J.EPSL.2009.05.030

Kumar Warrier, A., & Shankar, R. (2009). *Geochemical evidence for the use of magnetic susceptibility as a paleorainfall proxy in the tropics*. https://doi.org/10.1016/j.chemgeo.2009.05.023

Kylander, M. E., Ampel, L., Wohlfarth, B., & Veres, D. (2011). High-resolution X-ray fluorescence core scanning analysis of Les Echets (France) sedimentary sequence: new insights from chemical proxies. *Journal of Quaternary Science*, *26*(1), 109–117. https://doi.org/10.1002/JQS.1438

Latimer, J. C., & Murray, R. W. (2007). Productivity records from the Southern Ocean and the equatorial Pacific Ocean: Testing the glacial Shelf-Nutrient Hypothesis. *Deep Sea Research Part II: Topical Studies in Oceanography*, *54*(21–22), 2443–2452. https://doi.org/10.1016/J.DSR2.2007.07.021

Lear, C. H., Rosenthal, Y., Coxall, H. K., & Wilson, P. A. (2004). Late Eocene to early Miocene ice sheet dynamics and the global carbon cycle. *Paleoceanography*, *19*(4), PA4015. https://doi.org/10.1029/2004PA001039

Lear, C.H., Coxall, H. K., Foster, G. L., Lunt, D. J., Mawbey, E. M., Rosenthal, Y., Sosdian, S. M., Thomas, E., & Wilson, P. A. (2015a). Neogene ice volume and ocean temperatures: Insights from infaunal foraminiferal Mg/Ca paleothermometry. *Paleoceanography*, *30*(11), 1437–1454. https://doi.org/10.1002/2015PA002833

Lear, C. H., Mawbey, E. M., & Rosenthal, Y. (2010). Cenozoic benthic foraminiferal Mg/Ca and Li/Ca records: Toward unlocking temperatures and saturation states. *Paleoceanography*, *25*(4). https://doi.org/10.1029/2009PA001880

LeGrande, A. N., & Schmidt, G. A. (2006). Global gridded data set of the oxygen isotopic composition in seawater. *Geophysical Research Letters*, *33*(12), 12604. https://doi.org/10.1029/2006GL026011

Lemarchand, D., Gaillardet, J., Lewin, A., & Allègre, C. J. (2002). Boron isotope systematics in large rivers: implications for the marine boron budget and paleo-pH reconstruction over the Cenozoic. *Chemical Geology*, *190*(1–4), 123–140. https://doi.org/10.1016/S0009-2541(02)00114-6

Lewis, L., & Christensen, A. M. (2016). Effects of Aluminum Foil Packaging on Elemental Analysis of Bone. *Journal of Forensic Sciences*, *61*(2), 439–441. https://doi.org/10.1111/1556-4029.12994

Liebrand, D., Lourens, L. J., Hodell, D. A., de Boer, B., van de Wal, R. S. W., & Paelike, H. (2011). Antarctic ice sheet and oceanographic response to eccentricity forcing during the early Miocene. *Climate of the Past*, *7*(3), 869–880. https://doi.org/10.5194/cp-7-869-2011

Lirer, F., Foresi, L. M., Iaccarino, S. M., Salvatorini, G., Turco, E., Cosentino, C., Sierro, F. J., & Caruso, A. (2019). Mediterranean Neogene planktonic foraminifer biozonation and biochronology. *Earth-Science Reviews*, *196*, 102869. https://doi.org/10.1016/J.EARSCIREV.2019.05.013

Lourens, L. J., Wehausen, R., & Brumsack, H. J. (2001). Geological constraints on tidal dissipation and dynamical ellipticity of the Earth over the past three million years. *Nature 2001 409:6823*, *409*(6823), 1029–1033. https://doi.org/10.1038/35059062

Lourens, L.J., (2022) CenoGRID age model for the Marsalfron and Ras il-Pellegrin Sections (Malta). Personal communication.

Ma, W., Tian, J., Li, Q., & Wang, P. (2011). Simulation of long eccentricity (400-kyr) cycle in ocean carbon reservoir during Miocene Climate Optimum: Weathering and nutrient response to orbital change. *Geophysical Research Letters*, *38*(10). https://doi.org/10.1029/2011GL047680

Mackensen, A., & Schmiedl, G. (2019). Stable carbon isotopes in paleoceanography: atmosphere, oceans, and sediments. *Earth-Science Reviews*, *197*, 102893. https://doi.org/10.1016/j.earscirev.2019.102893

Majewski, W. (2010). Planktonic foraminiferal response to Middle Miocene cooling in the Southern Ocean (ODP Site 747, Kerguelen Plateau). *Acta Palaeontologica Polonica*, *55*(3), 541–560. https://doi.org/10.4202/app.2009.0088

Marchitto, T. M., Curry, W. B., Lynch-Stieglitz, J., Bryan, S. P., Cobb, K. M., & Lund, D. C. (2014). Improved oxygen isotope temperature calibrations for cosmopolitan benthic foraminifera. *Geochimica et Cosmochimica Acta*, *130*, 1–11. https://doi.org/10.1016/J.GCA.2013.12.034

Martín-Puertas, C., Jiménez-Espejo, F., Martínez-Ruiz, F., Nieto-Moreno, V., Rodrigo, M., Mata, M. P., & Valero-Garcés, B. L. (2010). Late Holocene climate variability in the southwestern Mediterranean region: An integrated marine and terrestrial geochemical approach. *Climate of the Past*, *6*(6), 807–816. https://doi.org/10.5194/CP-6-807-2010

Martinez-Ruiz, F., Kastner, M., Gallego-Torres, D., Rodrigo-Gámiz, M., Nieto-Moreno, V., & Ortega-Huertas, M. (2015). Paleoclimate and paleoceanography over the past 20,000yr in the Mediterranean Sea Basins as indicated by sediment elemental proxies. *Quaternary Science Reviews*, *107*, 25–46.

Mawbey, E. M., & Lear, C. H. (2013). Carbon cycle feedbacks during the oligocene-miocene transient glaciation. *Geology*, *41*(9), 963–966. https://doi.org/10.1130/G34422.1

Mcarthur, J. M., Howarth, R. J., & Bailey, T. R. (2001). Strontium Isotope Stratigraphy: LOWESS Version 3: Best Fit to the Marine Sr-Isotope Curve for 0-509 Ma and Accompanying Look-up Table for Deriving Numerical Age. *The Journal of Geology*, *109*, 155–170.

McArthur, J. M., Howarth, R. J., & Shields, G. A. (2012). Strontium Isotope Stratigraphy. *The Geologic Time Scale 2012*, 127–144. https://doi.org/10.1016/B978-0-444-59425-9.00007-X

Miller, K. G., Browning, J. V., Schmelz, W. J., Kopp, R. E., Mountain, G. S., & Wright, J. D. (2020). Cenozoic sea-level and cryospheric evolution from deep-sea geochemical and continental margin records. *Science Advances*, *6*(20), eaaz1346. https://doi.org/10.1126/sciadv.aaz1346

Miller, K. G., Kominz, M. A., Browning, J. V., Wright, J. D., Mountain, G. S., Katz, M. E., Sugarman, P. J., Cramer, B. S., Christie-Blick, N., & Pekar, S. F. (2005). The phanerozoic record of global sea-level change. *Science*, *310*(5752), 1293–1298. https://doi.org/10.1126/SCIENCE.1116412/SUPPL_FILE/MILLER_SOM.PDF

Miller, K. G., Wright, J. D., & Fairbanks, R. G. (1991). Unlocking the Ice House - Oligocene-Miocene Oxygen Isotopes, Eustasy, and Margin Erosion. *Journal of Geophysical Research-Solid Earth and Planets*, *96*(B4), 6829–6848. https://doi.org/10.1029/90JB02015

Morée, A. L., Schwinger, J., Ninnemann, U. S., Jeltsch-Thömmes, A., Bethke, I., & Heinze, C. (2021). Evaluating the biological pump efficiency of the Last Glacial Maximum ocean using δ13C. *Climate of the Past*, *17*(2), 753–774. https://doi.org/10.5194/CP-17-753-2021

Mourik, A. A., Abels, H. A., Hilgen, F. J., Di Stefano, A., & Zachariasse, W. J. (2011). Improved astronomical age constraints for the middle Miocene climate transition based on high-resolution stable isotope records from the central Mediterranean Maltese Islands. *Paleoceanography*, *26*(1). https://doi.org/10.1029/2010PA001981

Mudelsee, M., Bickert, T., Lear, C. H., & Lohmann, G. (2014). Cenozoic climate changes: A review based on time series analysis of marine benthic δ 18 O records. *Reviews of Geophysics*, *52*(3), 333–374. https://doi.org/10.1002/2013RG000440

Mutti, M., John, C. M., & Knoerich, A. C. (2006). Chemostratigraphy in Miocene heterozoan carbonate settings: applications, limitations and perspectives. *Geological Society, London, Special Publications*, *255*(1), 307–322. https://doi.org/10.1144/GSL.SP.2006.255.01.18

Muttoni, G., & Kent, D. V. (2007). *Widespread formation of cherts during the early Eocene climate optimum*. *253*(3–4), 348–362. https://doi.org/10.7916/D8S75RVS

Nairn, M. G., Lear, C. H., Sosdian, S. M., Bailey, T. R., & Beavington-Penney, S. (2021). Tropical Sea Surface Temperatures Following the Middle Miocene Climate Transition From Laser-Ablation ICP-MS Analysis of Glassy Foraminifera. *Paleoceanography and Paleoclimatology*, *36*(3), e2020PA004165. https://doi.org/10.1029/2020PA004165

Naish, T. R., Woolfe, K. J., Barrett, P. J., Wilson, G. S., Atkins, C., Bohaty, S. M., Bucker, C. J., Claps, M., Davey, F. J., Dunbar, G. B., Dunn, A. G., Fielding, C. R., Florindo, F., Hannah, M. J., Harwood, D. M., Henrys, S. A., Krissek, L. A., Lavelle, M., van der Meer, J., … Wonik, T. (2001). Orbitally induced oscillations in the East Antarctic ice sheet at the Oligocene/Miocene boundary. *Nature*, *413*(6857), 719–723. https://doi.org/10.1038/35099534

Oehlert, A. M., & Swart, P. K. (2014). ARTICLE Interpreting carbonate and organic carbon isotope covariance in the sedimentary record. *Nature Communications*. https://doi.org/10.1038/ncomms5672

Ortega-Ariza, D., Franseen, E. K., Santos-Mercado, H., Ramírez-Martínez, W. R., & Core-Suárez, E. E. (2015). Strontium Isotope Stratigraphy for Oligocene-Miocene Carbonate Systems in Puerto Rico and the Dominican Republic: Implications for Caribbean Processes Affecting Depositional History. *Https://Doi.Org/10.1086/683335*, *123*(6), 539–560. https://doi.org/10.1086/683335

Pagani, M., Arthur, M. A., & Freeman, K. H. (1999). Miocene evolution of atmospheric carbon dioxide. *PALEOCEANOGRAPHY*, *14*(3), 273–292. https://doi.org/10.1029/1999PA900006

Passier, H. F., & de Lange, G. J. (1998). 20. Sedimentary sulfur and iron chemistry in relation to the formation of Eastern Mediterranean sapropels 1. *Scientific Results*, *160*.

Paul, H. A., Bernasconi, S. M., Schmid, D. W., & Mckenzie, J. A. (2001). *Oxygen isotopic composition of the Mediterranean Sea since the Last Glacial Maximum: constraints from pore water analyses*. Retrieved August 18, 2022, from www.elsevier.com/locate/epsl

Pearson, P. N., Ditchfield, P. W., Singano, J., Harcourt-Brown, K. G., Nicholas, C. J., Olsson, R. K., Shackleton, N. J., & Hall, M. A. (2001). Warm tropical sea surface temperatures in the Late Cretaceous and Eocene epochs. *Nature 2001 413:6855*, *413*(6855), 481–487. https://doi.org/10.1038/35097000

Pearson, P. N., Foster, G. L., & Wade, B. S. (2009). Atmospheric carbon dioxide through the Eocene-Oligocene climate transition. *Nature*, *461*(7267), 1110-U204. https://doi.org/10.1038/nature08447

Pedley, H. M., & Bennett, S. M. (1985). Phosphorites, hardgrounds and syndepositional solution subsidence: A palaeoenvironmental model from the miocene of the Maltese Islands. In *Sedimentary Geology*. https://doi.org/10.1016/0037-0738(85)90022-3

Pedley, H. M., House, M. R., & Waugh, B. (1976). The geology of Malta and Gozo. *Proceedings of the Geologists' Association*, *87*(3), 325–341. https://doi.org/10.1016/S0016-7878(76)80005-3

Pedley, H.M., 1978. "A new lithostratigraphical and palaeoenvironmental interpretation for the coralline limestone formations (Miocene) of the Maltese Islands". Overseas Geol. and Miner. Resour., No. 54, p.1-17.

Penman, D. E., Keller, A., D'haenens, S., Turner, S. K., & Hull, P. M. (2019). Atlantic Deep-Sea Cherts Associated With Eocene Hyperthermal Events. *Paleoceanography and Paleoclimatology*, *34*(2), 287–299. https://doi.org/10.1029/2018PA003503

Pierre, C. (1999). The oxygen and carbon isotope distribution in the Mediterranean water masses. *Marine Geology*, *153*(1–4), 41–55. https://doi.org/10.1016/S0025-3227(98)00090-5

Pollard, D., & DeConto, R. M. (2005). Hysteresis in cenozoic antarctic ice-sheet variations. *Global and Planetary Change*, *45*(1–3), 9–21. https://doi.org/10.1016/j.gloplacha.2004.09.011

Potter, P. E., & Szatmari, P. (2009). Global Miocene tectonics and the modern world. *Earth-Science Reviews*, *96*(4), 279–295. https://doi.org/10.1016/J.EARSCIREV.2009.07.003

Prendergast, A. L., Azzopardi, M., O'Connell, T. C., Hunt, C., Barker, G., & Stevens, R. E. (2013). Oxygen isotopes from *Phorcus* (*Osilinus*) *turbinatus* shells as a proxy for sea surface temperature in the central Mediterranean: A case study from Malta. *Chemical Geology*, *345*, 77–86. https://doi.org/10.1016/J.CHEMGEO.2013.02.026

Raitzsch, M., Bijma, J., Bickert, T., Schulz, M., Holbourn, A., & Kučera, M. (2021). Atmospheric carbon dioxide variations across the middle Miocene climate transition. *Climate of the Past*, *17*(2), 703–719. https://doi.org/10.5194/CP-17-703-2021

Ramsay, A. T. S., Smart, C. W., & Zachos, J. C. (1998). A model of early to middle Miocene deep ocean circulation for the Atlantic and Indian Oceans. *Geological Society Special Publication*, *131*, 55–70. https://doi.org/10.1144/GSL.SP.1998.131.01.04

Renard, M. (1986). Pelagic carbonate chemostratigraphy (Sr, Mg, 18O, 13C). *Marine Micropaleontology*, *10*(1–3), 117–164. https://doi.org/10.1016/0377-8398(86)90027-7

Reolid, J., & Betzler, C. (2019). The ichnology of carbonate drifts. *Sedimentology*, *66*(4), 1427–1448. https://doi.org/10.1111/SED.12563

Reverdin, G., Kestenare, E., Frankignoul, C., & Delcroix, T. (2007). Surface salinity in the Atlantic Ocean (30°S–50°N). *Progress in Oceanography*, *73*(3–4), 311–340. https://doi.org/10.1016/J.POCEAN.2006.11.004

Riahi, S., Soussi, M., & Ben Ismail Lattrache, K. (2015). Age, internal stratigraphic architecture and structural style of the oligocene-miocene numidian formation of northern Tunisia. *Annales Societatis Geologorum Poloniae*, *85*(2), 345–370. https://doi.org/10.14241/ASGP.2015.009

Rogerson, M., Rohling, E. J., & Weaver, P. P. E. (2006). Promotion of meridional overturning by Mediterranean-derived salt during the last deglaciation. *Paleoceanography*, *21*(4). https://doi.org/10.1029/2006PA001306

Rögl, F. (1999). Mediterranean and Paratethys. Facts and hypotheses of an Oligocene to Miocene paleogeography *(short overview)*. Geologica Carpathica *50 (4)*, 339–349.

Rohling, E. J. (2013). *Oxygen Isotope Composition of Seawater*. Encyclopedia of Quaternary Science vol 2, 915-922

Rohling, E. J., Marino, G., & Grant, K. M. (2015). Mediterranean climate and oceanography, and the periodic development of anoxic events (sapropels). *Earth-Science Reviews*, *143*, 62–97. https://doi.org/10.1016/J.EARSCIREV.2015.01.008

Rohling, E. J., Sprovieri, M., Cane, T., Casford, J. S. L., Cooke, S., Bouloubassi, I., Emeis, K. C., Schiebel, R., Rogerson, M., Hayes, A., Jorissen, F. J., & Kroon, D. (2004). Reconstructing past planktic foraminiferal habitats using stable isotope data: A case history for Mediterranean sapropel S5. *Marine Micropaleontology*, *50*(1–2), 89–123.

Russo, B., Ferraro, L., Correggia, C., Alberico, I., Foresi, L. M., Vallefuoco, M., & Lirer, F. (2021). Deep-water paleoenvironmental changes based on early-middle Miocene benthic foraminifera from Malta Island (central Mediterranean). *Palaeogeography, Palaeoclimatology, Palaeoecology*, 110722. https://doi.org/10.1016/J.PALAEO.2021.110722

Savrda, C. E., & Bottjer, D. J. (1989). Trace-fossil model for reconstructing oxygenation histories of ancient marine bottom waters: Application to upper cretaceous niobrara formation, Colorado. *Palaeogeography, Palaeoclimatology, Palaeoecology*, *74*(1–2), 49–74. https://doi.org/10.1016/0031-0182(89)90019-9

Scher, H. D., & Martin, E. E. (2008). Oligocene deep water export from the North Atlantic and the development of the Antarctic Circumpolar Current examined with neodymium isotopes. *Paleoceanography*, *23*(1). https://doi.org/10.1029/2006PA001400

Schöllhorn, I., Houben, A., Gertsch, B., Adatte, T., Alexey, U., de Kaenel, E., Spangenberg, J. E., Janssen, N., Schwennicke, T., & Föllmi, K. B. (2019). Enhanced upwelling and phosphorite formation in the northeastern Pacific during the late Oligocene: Depositional mechanisms, environmental conditions, and the impact of glacio-eustacy. *GSA Bulletin*, *132*(3–4), 687–709. https://doi.org/10.1130/B32061.1

Scott, G. H. (2020). *Zooplankters in an oligotrophic ocean: contrasts in the niches of Globigerinoides ruber and Trilobatus sacculifer (Foraminifera: Globigerinida) in the South Pacific*. https://doi.org/10.1080/11956860.2020.1793561

Sexton, P. F., Wilson, P. A., Pearson, P. N., Sexton, P. F., Wilson, P. A., & Pearson, P. N. (2006). Microstructural and geochemical perspectives on planktic foraminiferal preservation: “Glassy” versus “Frosty.” *Geochemistry, Geophysics, Geosystems*, *7*(12). https://doi.org/10.1029/2006GC001291

Sexton, P. F., & Wilson, P. A. (2009). Preservation of benthic foraminifera and reliability of deep-sea temperature records: Importance of sedimentation rates, lithology, and the need to examine test wall structure. *Paleoceanography*, *24*(2). https://doi.org/10.1029/2008PA001650

Shackleton, N. J. (1987). The carbon isotope record of the Cenozoic: history of organic carbon burial and of oxygen in the ocean and atmosphere. *Geological Society, London, Special Publications*, *26*, 423–434. https://doi.org/10.1144/GSL.SP.1987.026.01.27

Shevenell, A. E., Kennett, J. P., & Lea, D. W. (2004). Middle Miocene Southern Ocean cooling and antarctic cryosphere expansion. *Science*, *305*(5691), 1766–1770. https://doi.org/10.1126/SCIENCE.1100061/SUPPL_FILE/SHEVENELL_SOM.PDF

Shevenell, A. E., Kennett, J. P., & Lea, D. W. (2008). Middle Miocene ice sheet dynamics, deep-sea temperatures, and carbon cycling: A Southern Ocean perspective. *Geochemistry, Geophysics, Geosystems*, *9*(2). https://doi.org/10.1029/2007GC001736

Sibert, E. C., & Rubin, L. D. (2020). *An early Miocene extinction in pelagic sharks*. https://doi.org/10.5061/dryad

Sosdian, S. M., Babila, T. L., Greenop, R., Foster, G. L., & Lear, C. H. (2020). Ocean Carbon Storage across the middle Miocene: a new interpretation for the Monterey Event. *Nature Communications*, *11*(1), 134. https://doi.org/10.1038/s41467-019-13792-0

Sosdian, S. M., & Lear, C. H. (2020). Initiation of the Western Pacific Warm Pool at the Middle Miocene Climate Transition? *Paleoceanography and Paleoclimatology*, *35*(12), e2020PA003920. https://doi.org/10.1029/2020PA003920

Spezzaferri, S., Kucera, M., Pearson, P. N., Wade, B. S., Rappo, S., Poole, C. R., Morard, R., & Stalder, C. (2015). Fossil and Genetic Evidence for the Polyphyletic Nature of the Planktonic Foraminifera "*Globigerinoides*", and Description of the New Genus *Trilobatus*. *PLOS ONE*, *10*(5), e0128108. https://doi.org/10.1371/JOURNAL.PONE.0128108

Staudigel, P. T., John, E. H., Buse, B., Pearson, P. N., & Lear, C. H. (2022). Apparent preservation of primary foraminiferal Mg/Ca ratios and Mg-banding in recrystallized foraminifera. *Geology*, *50*(7), 760–764. https://doi.org/10.1130/G49984.1

Steininger, F. F., Aubry, M. P., Berggren, W. A., Biolzi, M., Borsetti, A. M., Cartlidge, J. E., Cati, F., Corfield, R., Gelati, R., Iaccarino, S., Napoleone, C., Ottner, F., Rogl, F., Roetzel, R., Spezzaferri, S., Tateo, F., Villa, G., & Zvenboom, D. (1997). The Global Stratotype Section and Point (GSSP) for the base of the Neogene. *Episodes*, *20*(1).

Steinthorsdottir, M., Coxall, H. K., De Boer, A. M., Huber, M., Barbolini, N., Bradshaw, C. D., Burls, N. J., Feakins, S. J., Gasson, E., Henderiks, J., Holbourn, A. E., Kiel, S., Kohn, M. J., Knorr, G., Kürschner, W. M., Lear, C. H., Liebrand, D., Lunt, D. J., Mörs, T., … Strömberg, C. A. E. (2020). *The Miocene: The Future of the Past Citation: Special Section: The Miocene: The Future of the Past Paleoceanography and Paleoclimatology*. https://doi.org/10.1029/2020PA004037

Sun, J., Sheykh, M., Ahmadi, N., Cao, M., Zhang, Z., Tian, S., Sha, J., Jian, Z., Windley, B. F., & Talebian, M. (2021). Permanent closure of the Tethyan Seaway in the northwestern Iranian Plateau driven by cyclic sea-level fluctuations in the late Middle Miocene. *Palaeogeography, Palaeoclimatology, Palaeoecology*, *564*, 110172. https://doi.org/10.1016/J.PALAEO.2020.110172

Thomas, E. (2008). Descent into the Icehouse. *Geology*, *36*(2), 191–192. https://doi.org/10.1130/focus022008.1 ER

Tripati, A. K., Delaney, M. L., Zachos, J. C., Anderson, L. D., Kelly, D. C., Elderfield, H., Tripati, C. :, Delaney, M. L., Zachos, J. C., Anderson, L. D., Kelly, D. C., & Elderfield, H. (2003). Tropical sea-surface temperature reconstruction for the early Paleogene using Mg/Ca ratios of planktonic foraminifera. *Paleoceanography*, *18*(4), 1101. https://doi.org/10.1029/2003PA000937

Vincent, E., & Berger, W. H. (1985). Carbon Dioxide and Polar Cooling in the Miocene: The Monterey Hypothesis. *The Carbon Cycle and Atmospheric CO*, 455–468. https://doi.org/10.1029/GM032P0455

Wade, B. S., Pearson, P. N., Berggren, W. A., & Pälike, H. (2011). Earth-Science Reviews Review and revision of Cenozoic tropical planktonic foraminiferal biostratigraphy and calibration to the geomagnetic polarity and astronomical time scale. *Earth Science Reviews*, *104*(1–3), 111–142. https://doi.org/10.1016/j.earscirev.2010.09.003

Wei, G.-J., Zou, L., Deng, W.-F., Li, X.-H., Liu, Y., & Chen, J.-F. (2009). Mn/Ca ratio in planktonic foraminifer from ODP Site 1144, the northern South China Sea: A possible paleoclimate indicator. *Geochemical Journal*, *43*.

Westerhold, T., Marwan, N., Drury, A. J., Liebrand, D., Agnini, C., Anagnostou, E., Barnet, J. S. K., Bohaty, S. M., De Vleeschouwer, D., Florindo, F., Frederichs, T., Hodell, D. A., Holbourn, A. E., Kroon, D., Lauretano, V., Littler, K., Lourens, L. J., Lyle, M., Pälike, H., … Zachos, J. C. (2020). An astronomically dated record of Earth's climate and its predictability over the last 66 million years. *Science (New York, N.Y.)*, *369*(6509), 1383–1388. https://doi.org/10.1126/SCIENCE.ABA6853

Woodruff, F., & Savin, S. M. (1989). Miocene deepwater oceanography. *Paleoceanography*, *4*(1), 87–140. https://doi.org/10.1029/PA004I001P00087

Woodruff, F., & Savin, S. (1991). Mid-Miocene isotope stratigraphy in the deep sea: High-resolution correlations, paleoclimatic cycles, and sediment preservation. *Paleoceanography*, *6*(6), 755–806. https://doi.org/10.1029/91PA02561

Wu, J., Böning, P., Pahnke, K., Tachikawa, K., & de Lange, G. J. (2016). Unraveling North-African riverine and eolian contributions to central Mediterranean sediments during Holocene sapropel S1 formation. *Quaternary Science Reviews*, *152*, 31–48. https://doi.org/10.1016/J.QUASCIREV.2016.09.029

Wu, J., Liu, Z., Stuut, J. B. W., Zhao, Y., Schirone, A., & de Lange, G. J. (2017). North-African paleodrainage discharges to the central Mediterranean during the last 18,000 years: A multiproxy characterization. *Quaternary Science Reviews*, *163*, 95–113. https://doi.org/10.1016/J.QUASCIREV.2017.03.015

Zabel, M., Schneider, R. R., Wagner, T., Adegbie, A. T., De Vries, U., & Kolonic, S. (2001). Late Quaternary Climate Changes in Central Africa as Inferred from Terrigenous Input to the Niger Fan. *Quaternary Research*, *56*(2), 207–217. https://doi.org/10.1006/QRES.2001.2261

Zachos, J., Pagani, M., Sloan, L., Thomas, E., & Billups, K. (2001). Trends, rhythms, and aberrations in global climate 65 Ma to present. *Science*, *292*(5517), 686–693.

Zammit, R., Lear, C. H., Samankassou, E., Lourens, L. J., Micallef, A., Pearson, P. N., & Bialik, O. M. (2022). Early Miocene Intensification of the North African Hydrological Cycle: Multi-Proxy Evidence From the Shelf Carbonates of Malta. *Paleoceanography and Paleoclimatology*, *37*(9). https://doi.org/10.1029/2022PA004414

Zeebe, R. E., Bijma, J., & Wolf-Gladrow, D. A. (1999). A diffusion-reaction model of carbon isotope fractionation in foraminifera. *Marine Chemistry*, *64*, 199–227.

Zhang, P., Zuraida, R., Rosenthal, Y., Holbourn, A., Kuhnt, W., & Xu, J. (2019). Geochemical characteristics from tests of four modern planktonic foraminiferal species in the Indonesian Throughflow region and their implications. *Geoscience Frontiers*, *10*(2), 505–516. https://doi.org/10.1016/J.GSF.2018.01.011

Appendices

Appendix 1 – Data for chapter 3

Appendix 1.1 Sr-isotope age model data for the il-Blata section

	Height [m]	Sample no.	Sed package	$^{87}Sr/^{86}Sr$	Minimum Age [Ma]	Mean Age [Ma]	Maximum Age [Ma]
Depositional Interval 1	1.80	LG10	I	0.708218	23.62	23.76	23.94
Depositional Interval 1	2.90	MG02	II	0.708209	23.77	23.93	24.09
Depositional Interval 1	6.10	MG20	II	0.708255	22.87	23.04	23.21
Depositional Interval 1	7.40	MG29	III	0.708273	22.53	22.68	22.84
Depositional Interval 1	7.90	MG32	III	0.708291	22.19	22.33	22.47
Depositional Interval 1	10.00	MG42	III	0.708335	21.45	21.58	21.71
Depositional Interval 1	10.95	MG47	III	0.708402	20.18	20.35	20.54
Depositional Interval 2	11.80	MG51	IV	0.708479	19.03	19.12	19.22
Depositional Interval 2	14.00	MG56	IV	0.70848	19.02	19.06	19.22
Depositional Interval 2	16.00	MG63	V	0.708485	18.95	19.05	19.15
Depositional Interval 2	21.00	MG76	VI	0.708512	18.63	18.72	18.80
Depositional Interval 2	22.60	MG81	VI	0.708508	18.67	18.77	18.86
Depositional Interval 2	24.00	MG88	VI	0.708515	18.59	18.68	18.77
Depositional Interval 2	25.00	MG94	VII	0.708503	18.73	18.83	18.92
Depositional Interval 2	25.50	MC01	VII	0.708492	18.87	18.96	19.06
Depositional Interval 2	31.10	MC15	VII	0.708512	18.63	18.72	18.80

Height [m]	Min $^{87}Sr/^{86}Sr$	Mean $^{87}Sr/^{86}Sr$	Max $^{87}Sr/^{86}Sr$	1 s.d.
1.80	0.708214	0.708218	0.708222	4E-06
2.90	0.708207	0.708209	0.708211	2E-06
6.10	0.708253	0.708255	0.708257	2E-06
7.40	0.708270	0.708273	0.708276	3E-06
7.90	0.708289	0.708291	0.708293	2E-06
10.00	0.708332	0.708335	0.708338	3E-06
10.95	0.708399	0.708402	0.708405	3E-06
11.80	0.708477	0.708479	0.708481	2E-06
14.00	0.708478	0.70848	0.708482	2E-06
16.00	0.708482	0.708485	0.708488	3E-06
21.00	0.708510	0.708512	0.708514	2E-06
22.60	0.708506	0.708508	0.70851	2E-06
24.00	0.708513	0.708515	0.708517	2E-06
25.00	0.708501	0.708503	0.708505	2E-06
25.50	0.708490	0.708492	0.708494	2E-06
31.10	0.708510	0.708512	0.708514	2E-06

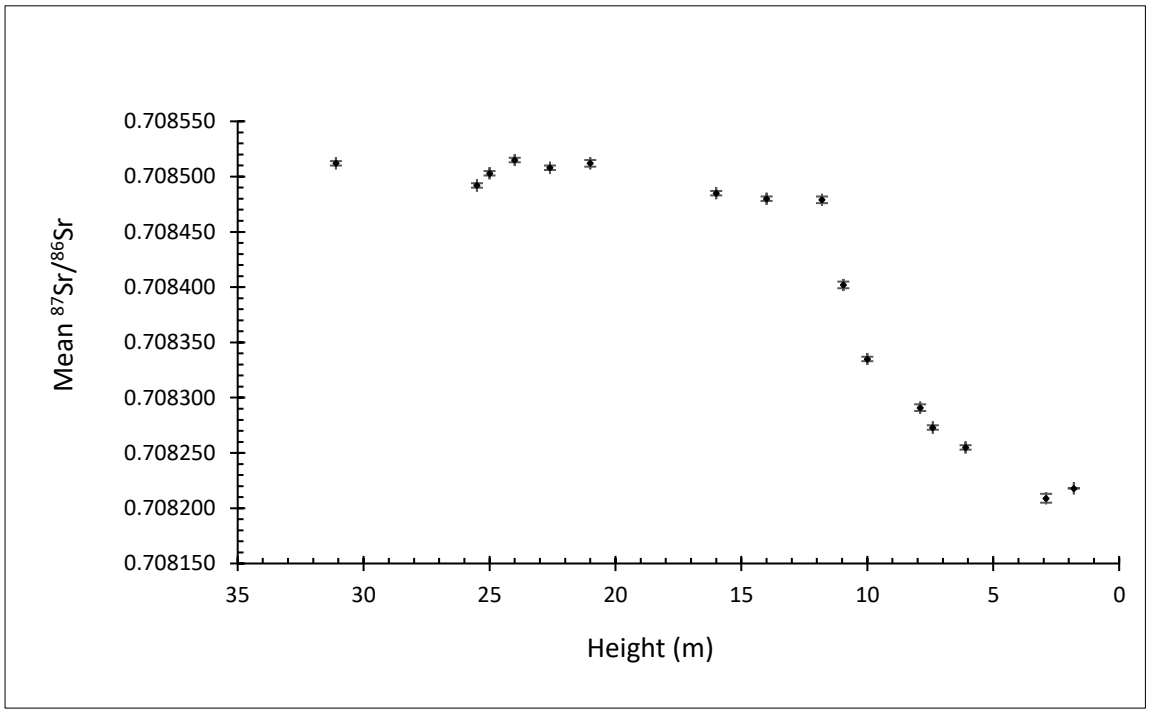

Figure 1.1.1 Original $^{87}Sr/^{86}Sr$ data used to generate the age model for the il-Blata section.

Appendix 1.2 εNd data from Malta as published in Bialik et al., (2019) and retuned during this study

Height [m]	Age [Ma]	εNd Bialik et. al 2019	1 s.d.
1.80	24.40	-5.05	0.26
2.90	24.04	-4.3	0.09
6.50	22.84	-4.9	0.08
9.80	21.73	-4.55	0.08
10.95	20.35	-4.23	0.15
16.00	19.05	-7.64	0.15
Different sites	16.95	-8.23	0.13
Different sites	15.00	-8.78	0.15
Different sites	14.06	-9.72	0.08
Different sites	13.82	-8.73	0.09
Different sites	13.68	-10.82	0.09

Green shaded points from the il-Blata section. The other points are from Ras il-Pellegrin and the closely related Gnejna Bay section

Appendix 1.3 % carbonate content from bulk sample from the il-Blata section

Sample no.	Height [m]	Age [Ma]	$CaCO_3$ [%]	1 s.d.
LG 01	0.00	25.0095		
LG02	0.20	24.9427	79.84	1.60
LG03	0.40	24.8758	89.15	1.78
LG04	0.60	24.8090		
LG05	0.80	24.7422	67	1.34
LG06	1.00	24.6753	75.07	1.50
LG08	1.40	24.5416	66.17	1.32
LG10	1.80	24.4079	72.51	1.45
MG01	2.70	24.1071	72.05	1.44
MG02	2.90	24.0403	75.5	1.51
MG03	3.00	24.0069	79.12	1.58
MG04	3.20	23.9400	77.25	1.55
MG05	3.40	23.8732		
MG06	3.60	23.8064		
MG07	3.80	23.7395		
MG08	4.00	23.6727		
MG09	4.20	23.6058		
MG10	4.40	23.5390		
MG11	4.80	23.4053		
MG12	5.00	23.2716		
MG13	5.20	23.2716	74.31	1.49
MG14	5.40	23.2048	82.15	1.64
MG15	5.60	23.1379		0.00
MG16	5.80	23.0711	75.45	1.51
MG17	5.90	23.0377	72.4	1.45
MG18	6.00	23.0042	76.06	1.52
MG19	6.10	22.9708	75.02	1.50
MG20	6.20	22.9374		
MG21	6.30	22.9040		
MG22	6.40	22.8706		
MG23	6.50	22.8371	78.19	1.56
MG24	6.60	22.8037	77.48	1.55
MG25	6.80	22.7369	76.84	1.54
MG26	7.00	22.6700	70.6	1.41
MG27	7.20	22.6032	79.64	1.59
MG28	7.40	22.5363	78.09	1.56
MG29	7.50	22.5029	74.79	1.50
MG30	7.70	22.4361	81.99	1.64
MG31	7.90	22.3692	80.21	1.60
MG32	8.20	22.2690	65.97	1.32
MG33	8.40	22.2021	77.91	1.56

MG34	8.60	22.1353	78.66	1.57
MG35	8.80	22.0684	80.55	1.61
MG36	9.00	22.0016	76.96	1.54
MG37	9.20	21.9348	75.88	1.52
MG38	9.40	21.8679	78.18	1.56
MG39	9.60	21.8011	76.23	1.52
MG40	9.80	21.7342	77.81	1.56
MG41	10.00	21.6198	79.98	1.60
MG42	10.20	21.3452	76.46	1.53
MG43	10.40	21.0707	81.46	1.63
MG44	10.60	20.7962	72.24	1.44
MG45	10.80	20.5216	70.27	1.41
MG46	10.95	20.3157	80.69	1.61
MG47	11.00	20.2471	83.38	1.67
MG48	11.20	19.9725	86.01	1.72
MG49	11.70	19.2862	76.04	1.52
MG50	11.80	19.1489	75.08	1.50
MG51	12.60	19.0377	58.93	1.18
MG52	13.00	19.0292	64.33	1.29
MG53	13.30	19.0227	64.03	1.28
MG54	13.60	19.0163	57.29	1.15
MG55	14.00	19.0078	65.69	1.31
MG56	14.30	19.0013	65.16	1.30
MG57	14.60	18.9949	64.14	1.28
MG58	14.80	18.9906	58.28	1.17
MG59	15.10	18.9842	59.04	1.18
MG60	15.30	18.9799	68.91	1.38
MG61	15.60	18.9735	71.29	1.43
MG62	16.00	18.9649	68.35	1.37
MG63	16.50	18.9542	68.04	1.36
MG64	17.00	18.9435	71.92	1.44
MG65	17.40	18.9349	75.14	1.50
MG66	17.60	18.9306	69.2	1.38
MG67	18.00	18.9221	67.78	1.36
MG68	18.40	18.9135	74.03	1.48
MG69	18.60	18.9092	75.38	1.51
MG70	19.00	18.9006	65.7	1.31
MG71	19.40	18.8921	73.85	1.48
MG72	19.60	18.8878	54.22	1.08
MG73	20.00	18.8792	71.08	1.42
MG74	20.50	18.8685		
MG75	21.00	18.8578		
MG76	21.50	18.8471	73.56	1.47
MG77	22.10	18.8342		
MG78	22.20	18.8321		
MG79	22.40	18.8278		

MG80	22.60	18.8235		
MG81	22.80	18.8192		
MG82	23.00	18.8150	62.9	1.26
MG83	23.20	18.8107		
MG84	23.40	18.8064		
MG85	23.60	18.8021		
MG86	23.80	18.7978	62.84	1.26
MG87	24.00	18.7935		
MG88	24.20	18.7893		
MG89	24.40	18.7850		
MG90	24.50	18.7828	59.72	1.19
MG91	24.60	18.7807		0.00
MG92	24.80	18.7764	69.87	1.40
MG93	25.00	18.7721		
MG94	25.10	18.7700	65.26	1.31
MG95	25.50	18.7614		
MC01	25.90	18.7528	51.29	1.03
MC02	26.30	18.7443		
MC03	26.70	18.7357		
MC04	27.10	18.7271		
MC05	27.50	18.7186		
MC06	28.30	18.7014	69.93	1.40
MC08	28.70	18.6929	31.95	0.64
MC09	29.10	18.6843	42.8	0.86
MC10	29.50	18.6757	52.26	1.05
MC11	30.30	18.6586		
MC13	31.10	18.6414	54.06	1.08

Appendix 1.4 $\delta^{13}C$ and $\delta^{18}O$ from bulk sample from the il-Blata section

	Height [m]	Age [Ma]	$\delta^{13}C$ ‰(VPDB)	1 s.d	$\delta^{18}O$ ‰(VPDB)	1 s.d
LG 01	0.00	25.00953	0.463	0.082	-0.694	0.059
LG 02	0.20	24.94268	0.195	0.036	-1.198	0.051
LG 03	0.40	24.87584	0.385	0.062	-0.735	0.085
LG 04	0.60	24.809	0.374	0.055	-0.873	0.093
LG 05	0.80	24.74215	0.352	0.077	-0.77	0.071
LG 06	1.00	24.67531	0.318	0.069	-1.209	0.067
LG 07	1.20	24.60847	0.335	0.095	-1.121	0.046
LG 08	1.40	24.54163	0.249	0.092	-1.577	0.09
LG 09	1.60	24.47478	0.36	0.04	-1.544	0.071
LG 10	1.80	24.40794	0.218	0.086	-1.592	0.078
MG 01	2.70	24.10715	0.121	0.044	-0.73	0.077
MG 02	2.90	24.04031	0.242	0.07	-0.431	0.051
MG 03	3.00	24.00688	0.158	0.088	-0.395	0.149
MG 04	3.20	23.94004	0.21	0.079	-0.416	0.076
MG 05	3.40	23.8732	0.273	0.077	-0.256	0.071
MG 06	3.60	23.80636	0.084	0.079	-0.306	0.072
MG 07	3.80	23.73951	0.159	0.077	-0.355	0.038
MG 08	4.00	23.67267	0.185	0.07	-0.218	0.055
MG 09	4.20	23.60583	0.15	0.046	-0.335	0.072
MG 10	4.40	23.53899	0.113	0.059	-0.344	0.088
MG 11	4.80	23.4053	0.068	0.066	-0.381	0.046
MG 12	4.90	23.37188	0.138	0.065	-0.273	0.072
MG 13	5.00	23.33846	0.129	0.076	-0.264	0.098
MG 14	5.20	23.27162	0.18	0.09	-0.208	0.118
MG 15	5.40	23.20477	0.164	0.069	-0.285	0.062
MG 16	5.60	23.13793	0.01	0.047	-0.34	0.073
MG 17	5.80	23.07109	-0.002	0.071	-0.309	0.072
MG 18	5.90	23.03767	0.002	0.076	-0.376	0.053
MG 19	6.00	23.00424	0.112	0.093	-0.354	0.065
MG 20	6.10	22.97082	0.099	0.039	-0.379	0.09
MG 21	6.20	22.9374	0.013	0.062	-0.333	0.07
MG 22	6.30	22.90398	-0.088	0.041	-0.379	0.08
MG 23	6.40	22.87056	0.046	0.063	-0.445	0.045
MG 24	6.50	22.83714	0.193	0.081	-0.37	0.069
MG 25	6.60	22.80372	0.239	0.083	-0.442	0.088
MG 26	6.80	22.73687	0.099	0.039	-0.431	0.051
MG 27	7.00	22.67003	0.12	0.094	-0.243	0.107
MG 28	7.20	22.60319	0.072	0.068	-0.27	0.057
MG 29	7.40	22.53635	-0.081	0.079	-0.245	0.115
MG 30	7.50	22.50292	-0.209	0.075	-0.352	0.095
MG30.1	7.60	22.4695	-0.15	0.051	-0.31	0.076
MG 31	7.70	22.43608	-0.51	0.081	-0.197	0.073
MG31.1	7.80	22.40266	-0.49	0.103	-0.197	0.1

MG 32	7.90	22.36924	-0.302	0.032	-0.549	0.084
MG32.1	8.00	22.33582	-0.174	0.088	-0.397	0.118
MG 33	8.20	22.26897	-0.189	0.067	-0.238	0.067
MG 34	8.40	22.20213	-0.124	0.073	-0.268	0.076
MG 35	8.60	22.13529	-0.144	0.065	-0.194	0.066
MG 36	8.80	22.06845	-0.188	0.078	-0.229	0.061
MG 37	9.00	22.0016	-0.269	0.082	-0.279	0.068
MG 38	9.20	21.93476	-0.16	0.092	-0.148	0.081
MG 39	9.40	21.86792	-0.238	0.046	-0.211	0.051
MG 40	9.60	21.80108	-0.202	0.064	-0.111	0.068
MG 41	9.80	21.73423	-0.212	0.102	-0.163	0.054
MG 42	10.00	21.61977	-0.331	0.063	-0.314	0.068
MG42.1	10.10	21.4825	0.014	0.064	0.013	0.077
MG 43	10.20	21.34523	0.074	0.121	0.15	0.091
MG43.1	10.30	21.20796	0.006	0.072	0.079	0.057
MG 44	10.40	21.07069	-0.119	0.054	-0.092	0.092
MG44.1	10.50	20.93342	-0.01	0.038	-0.054	0.085
MG 45	10.60	20.79616	-0.111	0.082	-0.257	0.077
MG45.1	10.70	20.65889	-0.257	0.097	-0.332	0.081
MG 46	10.80	20.52162	-0.285	0.087	-0.493	0.088
MG47	10.95	20.31572	-0.176	0.099	-0.52	0.083
MG48	11.00	20.24708	-0.135	0.081	-0.242	0.123
MG49	11.20	19.97255	0.2	0.098	0.077	0.107
MG50	11.70	19.2862	0.064	0.105	-0.23	0.101
MG51	11.80	19.14894	-0.073	0.08	-0.427	0.107
MG52	12.60	19.03774	-0.083	0.115	-0.353	0.122
MG53	13.00	19.02918	-0.025	0.113	-0.23	0.096
MG54	13.30	19.02275	-0.099	0.073	-0.285	0.092
MG55	13.60	19.01632	-0.117	0.06	-0.34	0.079
MG56	14.00	19.00775	-0.014	0.074	-0.299	0.069
MG57	14.30	19.00133	-0.135	0.047	-0.354	0.089
MG58	14.60	18.9949	-0.044	0.067	-0.293	0.089
MG59	14.80	18.99062	-0.331	0.102	-0.467	0.049
MG60	15.10	18.98419	-0.116	0.053	-0.31	0.055
MG61	15.30	18.97991	-0.193	0.051	-0.331	0.05
MG62	15.60	18.97348	-0.242	0.1	-0.562	0.103
MG63	16.00	18.96491	-0.342	0.068	-0.607	0.082
MG64	16.50	18.9542	-0.263	0.112	-0.538	0.116
MG65	17.00	18.94349	-0.221	0.043	-0.525	0.078
MG66	17.40	18.93492	-0.378	0.123	-0.498	0.076
MG67	17.60	18.93064	-0.276	0.111	-0.446	0.065
MG68	18.00	18.92207	-0.25	0.093	-0.284	0.1
MG69	18.40	18.9135	-0.477	0.044	-0.367	0.102
MG70	18.60	18.90922	-0.347	0.116	-0.224	0.097
MG71	19.00	18.90065	-0.279	0.091	-0.365	0.059
MG72	19.40	18.89208	-0.313	0.085	-0.113	0.059

MG73	19.60	18.88779	-0.384	0.047	-0.378	0.044
MG74	20.00	18.87923	-0.511	0.055	-0.252	0.046
MG75	20.50	18.86851	-0.555	0.084	-0.223	0.053
MG76	21.00	18.8578	-0.58	0.099	-0.396	0.116
MG77	21.50	18.84709	-0.576	0.074	-0.303	0.097
MG78	22.10	18.83424	-0.677	0.064	-0.204	0.089
MG79	22.20	18.8321	-0.774	0.054	-0.062	0.058
MG80	22.40	18.82781	-0.785	0.062	-0.174	0.068
MG81	22.60	18.82353	-0.742	0.046	-0.111	0.059
MG82	22.80	18.81925	-0.829	0.104	-0.013	0.109
MG83	23.00	18.81496	-0.816	0.051	-0.089	0.053
MG84	23.20	18.81068	-0.738	0.106	-0.119	0.084
MG85	23.40	18.80639	-0.723	0.056	-0.045	0.085
MG86	23.60	18.80211	-0.745	0.1	-0.102	0.095
MG87	23.80	18.79782	-0.591	0.084	-0.114	0.075
MG88	24.00	18.79354	-0.654	0.091	-0.123	0.107
MG89	24.20	18.78925	-0.596	0.072	0.009	0.067
MG90	24.40	18.78497	-0.527	0.057	0.045	0.072
MG91	24.50	18.78283	-0.474	0.064	0.039	0.063
MG92	24.60	18.78069	-0.45	0.067	0.088	0.073
MG93	24.80	18.7764	-0.386	0.06	0.089	0.077
MG94	25.00	18.77212	-0.291	0.063	0.103	0.077
MG95	25.10	18.76998	-0.245	0.084	-0.306	0.077
MC01	25.50	18.76141	-0.117	0.063	0.053	0.059
MC02	25.90	18.75284	0	0.041	-0.034	0.074
MC03	26.30	18.74427	0.099	0.066	0.099	0.048
MC04	26.70	18.7357	0.158	0.058	0.052	0.082
MC05	27.10	18.72713	0.086	0.052	0.001	0.065
MC06	27.50	18.71856	0.17	0.077	0.215	0.071
MC07	27.90	18.71	0.161	0.068	0.081	0.107
MC08	28.30	18.70143	0.426	0.033	0.288	0.093
MC09	28.70	18.69286	0.142	0.067	0.067	0.055
MC10	29.10	18.68429	0.1	0.101	0.043	0.086
MC11	29.50	18.67572	0.119	0.063	0.189	0.095
MC12	29.90	18.66715	0.268	0.051	0.319	0.084
MC13	30.30	18.65858	0.056	0.063	0.129	0.082
MC14	30.70	18.65001	0.168	0.063	0.334	0.066
MC15	31.10	18.64145	0.257	0.085	0.405	0.062

Appendix 1.5 % Major and minor element content in bulk sediment from the il-Blata section

Height [m]	Age [Ma]	Ca [%]	Ca +/-	Sr [%]	Sr +/-	S [%]	S +/-	Al [%]	Al +/-	Ti [%]	Ti +/-	K [%]	K +/-	Zr	Zr +/-	Si [%]	Si +/-
0.00	25.0095	29.95	0.3900	0.0489	0.0013	0.0889	0.0040	0.7300	0.0700	0.1501	0.0378	0.2815	0.0056	0.0052	0.0007	3.4000	0.0600
0.20	24.9427	39.42	0.3900	0.0487	0.0011	<LOD	0.0123	1.3100	0.0700	<LOD	0.0214	0.3336	0.0051	0.0041	0.0006	4.9400	0.0600
0.40	24.8758	36.67	0.3900	0.0483	0.0012	<LOD	0.0134	1.0500	0.0700	<LOD	0.0222	0.3115	0.0051	0.0044	0.0006	4.3200	0.0600
0.60	24.8090	36.47	0.3600	0.0455	0.0010	0.0320	0.0030	1.3800	0.0700	0.1201	0.0309	0.3429	0.0051	0.0066	0.0006	5.3500	0.0600
0.80	24.7422	36.61	0.3900	0.0526	0.0012	<LOD	0.0135	1.3200	0.0700	0.1908	0.0375	0.3424	0.0055	0.0076	0.0007	5.4100	0.0700
1.00	24.6753	38.80	0.3900	0.0433	0.0011	<LOD	0.0125	1.1800	0.0700	0.1617	0.0346	0.2979	0.0048	0.0063	0.0006	5.1600	0.0600
1.40	24.5416	39.11	0.4100	0.0383	0.0010	0.0558	0.0033	0.9600	0.0700	<LOD	0.0207	0.2072	0.0042	0.0045	0.0006	3.8600	0.0500
1.80	24.4079	39.83	0.4200	0.0274	0.0009	0.0453	0.0032	0.6800	0.0600	0.1235	0.0336	0.1580	0.0037	0.0039	0.0005	3.0288	0.0436
2.70	24.1071	35.24	0.3700	0.0519	0.0012	0.1300	0.0038	0.9300	0.0700	0.1526	0.0345	0.2796	0.0048	0.0042	0.0006	4.4200	0.0600
2.90	24.0403	39.40	0.4000	0.0485	0.0011	0.0261	0.0031	0.9600	0.0700	0.1115	0.0326	0.3048	0.0049	0.0060	0.0006	4.6300	0.0600
3.00	24.0069	34.55	0.4700	0.0461	0.0014	<LOD	0.0178	0.5700	0.0800	<LOD	0.0289	0.3222	0.0064	0.0048	0.0007	3.7300	0.0600
3.20	23.9400	38.43	0.4000	0.0539	0.0012	<LOD	0.0130	0.9300	0.0700	0.1982	0.0369	0.3819	0.0056	0.0046	0.0006	4.3100	0.0600
3.40	23.8732	37.44	0.4200	0.0575	0.0013	<LOD	0.0139	0.6900	0.0700	0.1048	0.0341	0.3106	0.0053	0.0063	0.0007	3.9400	0.0600
3.60	23.8064	33.83	0.4000	0.0531	0.0013	0.0587	0.0035	0.6200	0.0700	0.1530	0.0365	0.2393	0.0047	0.0057	0.0007	3.5800	0.0500
3.80	23.7395	35.49	0.3800	0.0625	0.0014	0.0142	0.0031	0.9900	0.0700	0.1535	0.0348	0.3711	0.0057	0.0056	0.0006	4.5200	0.0600
4.00	23.6727	36.01	0.4000	0.0556	0.0013	0.0923	0.0036	0.6600	0.0700	<LOD	0.0214	0.2566	0.0046	0.0033	0.0006	3.6000	0.0500
4.20	23.6058	35.94	0.4000	0.0608	0.0014	0.0705	0.0035	0.9000	0.0700	<LOD	0.0225	0.3125	0.0052	0.0056	0.0007	4.1200	0.0600
4.40	23.5390	33.19	0.4200	0.0583	0.0014	0.0986	0.0040	0.7800	0.0700	0.1464	0.0381	0.2764	0.0054	0.0060	0.0007	3.8700	0.0600
4.80	23.4053	35.56	0.3700	0.0528	0.0012	0.0481	0.0031	0.8600	0.0600	<LOD	0.0216	0.2855	0.0047	0.0043	0.0006	4.0700	0.0500
5.00	23.2716	36.21	0.3800	0.0527	0.0012	0.0462	0.0031	0.8100	0.0600	0.1078	0.0313	0.2990	0.0048	0.0050	0.0006	4.1800	0.0500
5.20	23.2716	35.36	0.3700	0.0519	0.0012	0.0717	0.0033	0.7300	0.0600	0.1246	0.0328	0.2810	0.0048	0.0052	0.0006	3.9000	0.0500
5.40	23.2048	33.95	0.3800	0.0539	0.0012	0.0744	0.0034	0.7600	0.0600	0.1636	0.0349	0.2686	0.0048	0.0046	0.0006	3.8900	0.0500
5.60	23.1379	35.21	0.3700	0.0540	0.0012	0.2229	0.0045	0.7600	0.0600	0.1126	0.0311	0.2340	0.0043	0.0056	0.0006	3.8900	0.0500
5.80	23.0711	35.51	0.3700	0.0544	0.0012	0.0616	0.0032	0.8800	0.0600	0.1069	0.0312	0.2971	0.0049	0.0047	0.0006	4.2600	0.0600
5.90	23.0377	35.97	0.3700	0.0545	0.0012	0.0786	0.0034	0.9900	0.0700	0.1080	0.0317	0.3073	0.0050	0.0057	0.0006	4.3600	0.0600

6.00	23.0042	36.64	0.3800	0.0542	0.0012	0.0465	0.0032	0.9600	0.0700	0.1614	0.0340	0.3107	0.0050	0.0062	0.0006	4.1800	0.0500
6.10	22.9708	36.08	0.3800	0.0590	0.0013	0.0354	0.0031	0.9000	0.0700	<LOD	0.0216	0.3136	0.0050	0.0044	0.0006	4.0500	0.0500
6.20	22.9374	35.25	0.3800	0.0516	0.0012	0.0475	0.0032	0.7300	0.0600	0.1254	0.0327	0.2866	0.0049	0.0039	0.0006	4.0700	0.0500
6.30	22.9040	36.97	0.3800	0.0536	0.0012	0.0406	0.0031	0.6900	0.0600	0.1531	0.0345	0.3057	0.0049	0.0047	0.0006	3.9000	0.0500
6.40	22.8706	38.40	0.4100	0.0549	0.0013	0.0147	0.0031	0.7200	0.0700	0.1004	0.0331	0.3362	0.0054	0.0047	0.0006	3.8600	0.0500
6.50	22.8371	32.87	0.3500	0.0575	0.0013	0.0172	0.0032	1.3900	0.0700	0.1150	0.0321	0.3827	0.0058	0.0066	0.0006	5.9700	0.0700
6.60	22.8037	37.64	0.4000	0.0529	0.0012	0.0307	0.0032	0.7100	0.0700	0.1207	0.0334	0.3017	0.0050	0.0032	0.0006	3.6800	0.0500
6.80	22.7369	37.41	0.3900	0.0509	0.0012	0.0394	0.0032	0.7000	0.0600	<LOD	0.0209	0.2993	0.0050	0.0047	0.0006	3.9700	0.0500
7.00	22.6700	35.14	0.3800	0.0511	0.0012	0.0517	0.0033	0.6700	0.0600	<LOD	0.0216	0.2506	0.0046	0.0036	0.0006	3.5069	0.0491
7.20	22.6032	40.64	0.3900	0.0502	0.0011	0.0614	0.0032	0.8800	0.0600	<LOD	0.0190	0.2699	0.0045	0.0050	0.0006	4.3200	0.0500
7.40	22.5363	37.08	0.3900	0.0463	0.0011	0.0752	0.0034	0.7000	0.0600	0.1274	0.0331	0.2496	0.0045	0.0046	0.0006	3.6632	0.0500
7.50	22.5029	33.84	0.3900	0.0749	0.0016	0.1938	0.0046	0.5900	0.0700	0.1130	0.0344	0.2563	0.0049	0.0038	0.0007	3.2773	0.0490
7.70	22.4361	35.98	0.3800	0.0600	0.0013	0.0257	0.0031	0.7700	0.0600	<LOD	0.0218	0.2800	0.0048	0.0037	0.0006	3.8200	0.0500
7.90	22.3692	37.85	0.4000	0.0692	0.0014	0.0348	0.0031	0.7100	0.0600	<LOD	0.0205	0.2161	0.0042	0.0041	0.0006	3.0534	0.0435
8.20	22.2690	35.93	0.3900	0.0669	0.0014	0.0248	0.0031	0.6400	0.0600	0.1426	0.0337	0.2531	0.0046	0.0032	0.0006	3.4770	0.0485
8.40	22.2021	35.40	0.3900	0.0679	0.0014	0.0288	0.0031	0.5900	0.0600	<LOD	0.0221	0.2515	0.0046	0.0036	0.0006	3.5400	0.0500
8.60	22.1353	34.85	0.3800	0.0656	0.0014	0.0301	0.0031	0.7900	0.0600	0.1036	0.0312	0.2398	0.0045	0.0033	0.0006	3.4666	0.0484
8.80	22.0684	36.08	0.3800	0.0700	0.0014	0.0364	0.0031	0.7600	0.0600	<LOD	0.0214	0.2518	0.0045	0.0026	0.0006	3.8700	0.0500
9.00	22.0016	36.65	0.3800	0.0677	0.0014	0.0355	0.0031	0.9200	0.0600	0.1113	0.0317	0.2765	0.0047	0.0037	0.0006	4.0800	0.0500
9.20	21.9348	36.50	0.3800	0.0684	0.0014	0.0284	0.0031	0.9300	0.0700	<LOD	0.0222	0.2739	0.0047	0.0034	0.0006	4.0700	0.0500
9.40	21.8679	37.05	0.3900	0.0665	0.0014	0.0263	0.0031	0.8100	0.0700	0.1349	0.0337	0.2549	0.0046	0.0038	0.0006	3.8400	0.0500
9.60	21.8011	37.95	0.3900	0.0652	0.0014	0.0249	0.0031	0.8500	0.0600	<LOD	0.0214	0.2517	0.0045	0.0045	0.0006	3.9400	0.0500
9.80	21.7342	36.58	0.3900	0.0615	0.0013	0.0123	0.0030	0.7200	0.0600	<LOD	0.0216	0.2372	0.0044	0.0041	0.0006	3.7400	0.0500
10.00	21.6198	33.92	0.3700	0.0764	0.0015	0.0377	0.0032	0.8400	0.0600	0.1340	0.0335	0.2819	0.0049	0.0034	0.0006	3.9800	0.0500
10.20	21.3452	33.84	0.3800	0.0702	0.0015	0.0275	0.0032	0.8000	0.0700	<LOD	0.0236	0.3165	0.0053	0.0033	0.0006	3.9300	0.0600
10.40	21.0707	36.78	0.4000	0.0658	0.0014	<LOD	0.0139	0.8000	0.0700	0.1078	0.0330	0.2697	0.0048	0.0020	0.0006	3.4029	0.0486
10.60	20.7962	38.74	0.4100	0.0586	0.0013	0.0183	0.0030	0.5400	0.0600	0.1031	0.0319	0.1837	0.0039	0.0027	0.0006	2.8665	0.0415
10.80	20.5216	42.48	0.4300	0.0498	0.0012	0.0294	0.0030	0.4600	0.0600	0.1213	0.0331	0.1010	0.0033	0.0021	0.0006	2.1316	0.0338
10.95	20.3157	35.16	0.4100	0.0524	0.0013	0.0540	0.0034	0.5500	0.0700	0.1137	0.0343	0.1923	0.0043	0.0025	0.0006	2.8188	0.0445
11.00	20.2471	30.45	0.4100	0.0756	0.0018	0.0217	0.0037	0.6200	0.0700	<LOD	0.0274	0.2427	0.0053	0.0031	0.0007	3.6700	0.0600

11.20	19.9725	35.32	0.3700	0.0624	0.0013	0.0886	0.0035	0.8200	0.0600	<LOD	0.0216	0.2941	0.0048	0.0024	0.0006	4.0000	0.0500
11.70	19.2862	31.03	0.3600	0.0766	0.0016	0.0291	0.0034	0.7900	0.0700	<LOD	0.0251	0.2747	0.0051	0.0033	0.0007	6.2100	0.0800
11.80	19.1489	32.19	0.3300	0.0754	0.0014	0.0227	0.0032	0.9200	0.0600	<LOD	0.0233	0.2846	0.0048	0.0042	0.0006	7.0700	0.0800
12.60	19.0377	30.86	0.3100	0.0700	0.0013	0.0230	0.0032	0.8600	0.0600	<LOD	0.0237	0.2977	0.0049	0.0046	0.0006	9.4000	0.1000
13.00	19.0292	31.75	0.3500	0.0738	0.0015	0.1188	0.0039	0.9600	0.0700	0.1274	0.0328	0.3012	0.0051	0.0020	0.0006	5.7800	0.0700
13.30	19.0227	31.92	0.3500	0.0735	0.0015	0.1114	0.0038	0.9800	0.0700	<LOD	0.0244	0.2905	0.0051	0.0046	0.0006	5.5700	0.0700
13.60	19.0163	30.77	0.3300	0.0719	0.0014	0.0984	0.0036	0.9400	0.0600	0.1253	0.0314	0.2562	0.0046	0.0037	0.0006	5.5700	0.0700
14.00	19.0078	30.28	0.3300	0.0719	0.0014	0.0495	0.0033	0.9500	0.0600	0.0946	0.0305	0.2577	0.0047	0.0032	0.0006	5.5700	0.0700
14.30	19.0013	29.51	0.3300	0.0671	0.0014	0.1721	0.0042	0.9000	0.0600	<LOD	0.0246	0.2306	0.0045	0.0040	0.0006	4.9600	0.0700
14.60	18.9949	34.26	0.3500	0.0710	0.0014	0.0766	0.0034	1.2000	0.0700	0.1177	0.0314	0.2647	0.0046	0.0072	0.0007	5.5100	0.0700
14.80	18.9906	31.63	0.3500	0.0686	0.0014	0.1213	0.0038	0.7600	0.0600	0.0934	0.0308	0.2210	0.0044	0.0037	0.0006	4.6800	0.0600
15.10	18.9842	31.05	0.3400	0.0641	0.0013	0.1213	0.0038	1.0400	0.0700	<LOD	0.0239	0.2120	0.0043	0.0045	0.0006	4.9500	0.0600
15.30	18.9799	33.74	0.3400	0.0664	0.0013	0.1188	0.0037	1.2100	0.0600	<LOD	0.0226	0.2447	0.0044	0.0080	0.0006	5.8000	0.0700
15.60	18.9735	34.70	0.3900	0.0650	0.0014	0.0417	0.0033	0.6700	0.0600	<LOD	0.0220	0.1902	0.0042	0.0033	0.0006	4.2800	0.0600
16.00	18.9649	36.48	0.3500	0.0616	0.0012	0.0634	0.0032	0.9200	0.0600	<LOD	0.0198	0.2221	0.0041	0.0032	0.0006	4.7400	0.0600
16.50	18.9542	35.61	0.3500	0.0675	0.0013	0.0736	0.0034	1.1000	0.0600	<LOD	0.0214	0.3853	0.0055	0.0039	0.0006	5.6100	0.0700
17.00	18.9435	32.87	0.3400	0.0717	0.0014	0.0668	0.0033	1.0700	0.0600	0.0953	0.0297	0.3202	0.0050	0.0028	0.0006	5.1700	0.0600
17.40	18.9349	36.64	0.3600	0.0701	0.0014	0.0546	0.0032	1.0100	0.0600	<LOD	0.0202	0.2544	0.0044	0.0022	0.0006	4.6200	0.0600
17.60	18.9306	36.93	0.3700	0.0703	0.0014	0.0643	0.0033	0.9200	0.0600	<LOD	0.0206	0.3038	0.0049	0.0031	0.0006	4.8300	0.0600
18.00	18.9221	34.16	0.3400	0.0811	0.0015	0.0710	0.0033	1.2000	0.0600	<LOD	0.0221	0.3055	0.0048	0.0027	0.0006	5.8800	0.0700
18.40	18.9135	33.50	0.3800	0.0702	0.0015	0.0458	0.0034	0.8300	0.0700	0.1056	0.0332	0.2395	0.0047	0.0050	0.0007	4.5200	0.0600
18.60	18.9092	37.34	0.3800	0.0770	0.0015	0.0566	0.0033	0.9600	0.0600	0.1632	0.0346	0.2391	0.0044	0.0039	0.0006	4.5700	0.0600
19.00	18.9006	33.08	0.3400	0.0773	0.0015	0.0390	0.0032	1.2700	0.0700	0.1224	0.0317	0.5426	0.0071	0.0043	0.0006	6.1800	0.0700
19.40	18.8921	31.66	0.3300	0.0809	0.0015	0.0422	0.0033	1.5600	0.0700	<LOD	0.0260	0.5014	0.0068	0.0039	0.0006	6.9300	0.0800
19.60	18.8878	36.06	0.3600	0.0726	0.0014	0.2065	0.0044	1.2400	0.0700	0.1221	0.0318	0.3841	0.0055	0.0032	0.0006	5.5200	0.0700
20.00	18.8792	37.36	0.3800	0.0684	0.0014	0.2433	0.0047	0.9900	0.0700	<LOD	0.0215	0.2932	0.0049	0.0029	0.0006	4.3700	0.0600
20.50	18.8685	36.52	0.3700	0.0664	0.0013	0.3569	0.0057	0.9500	0.0600	<LOD	0.0211	0.2963	0.0048	0.0037	0.0006	4.3100	0.0600
21.00	18.8578	33.72	0.3500	0.0719	0.0014	0.1847	0.0042	0.9700	0.0600	0.1207	0.0313	0.3067	0.0049	0.0049	0.0006	4.4800	0.0600
21.50	18.8471	37.91	0.3800	0.0855	0.0016	0.1717	0.0040	0.9000	0.0600	0.1371	0.0329	0.2762	0.0046	0.0029	0.0006	4.4300	0.0600
22.10	18.8342	33.34	0.3300	0.0811	0.0015	0.3726	0.0057	0.6800	0.0600	0.1021	0.0296	0.2390	0.0044	0.0032	0.0006	5.8800	0.0700

22.20	18.8321	33.79	0.3400	0.0677	0.0013	0.7103	0.0088	0.7900	0.0600	<LOD	0.0215	0.2294	0.0042	0.0023	0.0006	5.8200	0.0700
22.40	18.8278	35.05	0.3500	0.0723	0.0014	0.2671	0.0048	0.9300	0.0600	0.1089	0.0304	0.2721	0.0046	0.0028	0.0006	6.4600	0.0700
22.60	18.8235	34.86	0.3500	0.0744	0.0014	0.2382	0.0046	0.9500	0.0600	<LOD	0.0220	0.2873	0.0047	0.0023	0.0006	6.3900	0.0700
22.80	18.8192	32.66	0.3300	0.0730	0.0014	0.1730	0.0041	1.0600	0.0600	0.1075	0.0301	0.2489	0.0045	0.0022	0.0006	6.5700	0.0800
23.00	18.8150	32.55	0.3300	0.0714	0.0014	0.1767	0.0041	0.9600	0.0600	<LOD	0.0229	0.2635	0.0046	0.0027	0.0006	6.1400	0.0700
23.20	18.8107	33.19	0.3300	0.0719	0.0014	0.1709	0.0040	0.8700	0.0600	<LOD	0.0227	0.2554	0.0045	0.0020	0.0006	6.1000	0.0700
23.40	18.8064	33.19	0.3400	0.0727	0.0014	0.2056	0.0043	0.9500	0.0600	<LOD	0.0227	0.2692	0.0046	0.0031	0.0006	5.8800	0.0700
23.60	18.8021	32.45	0.3300	0.0700	0.0014	0.1589	0.0040	0.8800	0.0600	<LOD	0.0228	0.2585	0.0046	0.0032	0.0006	6.3400	0.0700
23.80	18.7978	32.06	0.3200	0.0703	0.0013	0.1948	0.0043	0.8900	0.0600	<LOD	0.0226	0.2248	0.0043	0.0021	0.0006	6.6900	0.0800
24.00	18.7935	30.76	0.3200	0.0723	0.0014	0.1828	0.0041	0.9100	0.0600	0.1110	0.0294	0.2512	0.0044	0.0018	0.0006	5.6500	0.0700
24.20	18.7893	32.40	0.3300	0.0774	0.0014	0.3157	0.0053	1.1100	0.0600	<LOD	0.0234	0.3019	0.0049	0.0019	0.0006	5.6600	0.0700
24.40	18.7850	30.69	0.3200	0.0751	0.0014	0.3321	0.0054	1.2100	0.0600	0.0995	0.0290	0.2704	0.0046	0.0031	0.0006	5.4200	0.0700
24.50	18.7828	34.49	0.3600	0.0775	0.0015	0.2412	0.0047	1.3400	0.0700	<LOD	0.0232	0.3665	0.0055	0.0034	0.0006	6.1800	0.0700
24.60	18.7807	31.74	0.3300	0.0765	0.0014	0.0348	0.0031	1.1400	0.0600	0.1530	0.0321	0.3153	0.0050	0.0030	0.0006	5.9600	0.0700
24.80	18.7764	31.01	0.3200	0.0725	0.0014	0.0298	0.0030	0.9600	0.0600	0.1059	0.0295	0.3144	0.0050	0.0031	0.0006	5.3700	0.0700
25.00	18.7721	33.46	0.3600	0.0706	0.0014	0.0564	0.0032	1.1100	0.0600	<LOD	0.0226	0.3348	0.0053	0.0026	0.0006	5.3900	0.0700
25.10	18.7700	27.29	0.2600	0.0586	0.0012	0.0816	0.0037	0.6600	0.0600	<LOD	0.0248	0.1558	0.0040	0.0022	0.0005	12.6100	0.1300
25.50	18.7614	29.40	0.2800	0.0607	0.0012	0.1317	0.0039	0.9400	0.0600	<LOD	0.0248	0.2795	0.0047	0.0030	0.0005	11.3400	0.1200
25.90	18.7528	31.00	0.3000	0.0672	0.0013	0.1041	0.0036	1.1200	0.0600	0.0983	0.0290	0.2524	0.0045	0.0035	0.0006	9.8800	0.1000
26.30	18.7443	31.48	0.3100	0.0709	0.0013	0.1635	0.0041	1.2200	0.0600	0.1271	0.0307	0.3355	0.0052	0.0034	0.0006	8.5700	0.0900
26.70	18.7357	30.21	0.2900	0.0645	0.0013	0.1967	0.0044	1.1100	0.0600	0.0869	0.0289	0.2797	0.0048	0.0027	0.0006	10.8200	0.1100
27.10	18.7271	30.09	0.2900	0.0660	0.0013	0.1508	0.0040	0.9800	0.0600	0.1149	0.0299	0.2849	0.0048	0.0026	0.0006	11.0500	0.1200
27.50	18.7186	31.23	0.3200	0.0687	0.0013	0.3066	0.0054	1.4200	0.0700	0.1014	0.0296	0.3381	0.0053	0.0030	0.0006	9.9100	0.1100
28.30	18.7014	22.36	0.2000	0.0494	0.0010	0.2119	0.0046	0.8900	0.0600	<LOD	0.0277	0.1671	0.0040	0.0034	0.0005	19.8300	0.1900
28.70	18.6929	28.30	0.2700	0.0631	0.0012	0.1447	0.0039	1.1500	0.0600	0.1032	0.0285	0.3057	0.0049	0.0032	0.0005	10.9400	0.1100
29.10	18.6843	30.41	0.2900	0.0649	0.0012	0.1713	0.0041	1.1200	0.0600	0.0979	0.0294	0.2729	0.0046	0.0030	0.0006	10.0800	0.1100
29.50	18.6757	32.85	0.3300	0.0745	0.0014	0.2162	0.0045	1.1100	0.0600	0.1012	0.0299	0.3390	0.0052	0.0029	0.0006	7.5500	0.0800
30.30	18.6586	28.91	0.2700	0.0653	0.0012	0.0630	0.0035	0.8200	0.0600	<LOD	0.0248	0.1933	0.0041	<LOD	0.0481	12.6800	0.1300
31.10	18.6414	33.38	0.3300	0.0729	0.0014	0.0752	0.0034	1.1700	0.0600	<LOD	0.0236	0.4131	0.0058	0.0019	0.0006	7.3900	0.0800

Appendix 1.6 Major and minor element concentration (Ca, Sr, S) and major element ratios from bulk sediment from the il-Blata section

Height [m]	Age [Ma]	Ca [mmol/g]	Sr [µmol/g]	S [µmol/g]	Sr/Ca [mmol/mol]	Ti/Al [mmol/mol]	K/Al [mol/mol]	Zr/Al [mmol/mol]	Si/Ti [mol/mol]
0.00	25.0095	7.4729	5.5809	27.7249	0.7468	115.9016	266.1126	2.1069	38.6058
0.20	24.9427	9.8358	5.5581		0.5651		175.7376	0.9257	
0.40	24.8758	9.1497	5.5124		0.6025		204.7286	1.2394	
0.60	24.8090	9.0998	5.1929	9.9797	0.5707	49.0564	171.4740	1.4146	75.9215
0.80	24.7422	9.1347	6.0032		0.6572	81.4772	179.0068	1.7029	48.3251
1.00	24.6753	9.6811	4.9418		0.5105	77.2431	174.2201	1.5791	54.3868
1.40	24.5416	9.7585	4.3711	17.4022	0.4479		148.9458	1.3864	
1.80	24.4079	9.9381	3.1271	14.1276	0.3147	102.3740	160.3460	1.6963	41.7982
2.70	24.1071	8.7929	5.9233	40.5426	0.6736	92.4918	207.4742	1.3357	49.3653
2.90	24.0403	9.8308	5.5353	8.1397	0.5631	65.4689	219.1056	1.8486	70.7718
3.00	24.0069	8.6207	5.2614		0.6103		390.0861	2.4907	
3.20	23.9400	9.5888	6.1516		0.6415	120.1302	283.3848	1.4630	37.0619
3.40	23.8732	9.3418	6.5624		0.7025	85.6138	310.6434	2.7005	64.0751
3.60	23.8064	8.4410	6.0603	18.3066	0.7180	139.1013	266.3550	2.7192	39.8791
3.80	23.7395	8.8552	7.1331	4.4285	0.8055	87.3986	258.6816	1.6731	50.1862
4.00	23.6727	8.9850	6.3456	28.7853	0.7062		268.3012	1.4789	
4.20	23.6058	8.9675	6.9391	21.9866	0.7738		239.6168	1.8404	
4.40	23.5390	8.2814	6.6537	30.7500	0.8035	105.7981	244.5419	2.2752	45.0530
4.80	23.4053	8.8727	6.0260	15.0008	0.6792		229.0960	1.4789	
5.00	23.2716	9.0349	6.0146	14.4082	0.6657	75.0180	254.7393	1.8258	66.0863
5.20	23.2716	8.8228	5.9233	22.3608	0.6714	96.2114	265.6399	2.1069	53.3458
5.40	23.2048	8.4710	6.1516	23.2029	0.7262	121.3392	243.8946	1.7902	40.5248
5.60	23.1379	8.7854	6.1630	69.5150	0.7015	83.5134	212.4771	2.1794	58.8797
5.80	23.0711	8.8602	6.2086	19.2110	0.7007	68.4741	232.9860	1.5797	67.9182

5.90	23.0377	8.9750	6.2200	24.5127	0.6930	61.4922	214.2087	1.7029	68.8045
6.00	23.0042	9.1422	6.1858	14.5018	0.6766	94.7685	223.3469	1.9102	44.1394
6.10	22.9708	9.0024	6.7336	11.0401	0.7480		240.4603	1.4460	
6.20	22.9374	8.7953	5.8891	14.8137	0.6696	96.8292	270.9338	1.5802	55.3160
6.30	22.9040	9.2245	6.1173	12.6618	0.6632	125.0713	305.7428	2.0147	43.4154
6.40	22.8706	9.5813	6.2657	4.5844	0.6539	78.6018	322.2367	1.9307	65.5251
6.50	22.8371	8.2015	6.5624	5.3641	0.8001	46.6353	190.0000	1.4044	88.4770
6.60	22.8037	9.3917	6.0374	9.5743	0.6428	95.8253	293.2424	1.3331	51.9630
6.80	22.7369	9.3343	5.8092	12.2875	0.6223		295.0655	1.9859	
7.00	22.6700	8.7679	5.8320	16.1235	0.6652		258.1167	1.5892	
7.20	22.6032	10.1402	5.7293	19.1486	0.5650		211.6557	1.6805	
7.40	22.5363	9.2520	5.2842	23.4524	0.5711	102.5895	246.0687	1.9437	49.0055
7.50	22.5029	8.4435	8.5483	60.4397	1.0124	107.9588	299.7826	1.9050	49.4301
7.70	22.4361	8.9775	6.8478	8.0150	0.7628		250.9442	1.4212	
7.90	22.3692	9.4441	7.8977	10.8530	0.8363		210.0420	1.7080	
8.20	22.2690	8.9650	7.6352	7.7343	0.8517	125.5946	272.9116	1.4789	41.5565
8.40	22.2021	8.8328	7.7494	8.9818	0.8773		294.1683	1.8047	
8.60	22.1353	8.6955	7.4869	9.3872	0.8610	73.9204	209.4749	1.2355	57.0293
8.80	22.0684	9.0024	7.9890	11.3519	0.8874		228.6399	1.0119	
9.00	22.0016	9.1447	7.7265	11.0713	0.8449	68.1928	207.4040	1.1895	62.4768
9.20	21.9348	9.1072	7.8064	8.8570	0.8572		203.2445	1.0813	
9.40	21.8679	9.2445	7.5896	8.2021	0.8210	93.8768	217.1674	1.3876	48.5147
9.60	21.8011	9.4690	7.4412	7.7655	0.7858		204.3498	1.5659	
9.80	21.7342	9.1272	7.0189	3.8360	0.7690		227.3485	1.6843	
10.00	21.6198	8.4635	8.7195	11.7574	1.0302	89.9201	231.5931	1.1972	50.6212
10.20	21.3452	8.4435	8.0119	8.5763	0.9489		273.0194	1.2201	
10.40	21.0707	9.1771	7.5097		0.8183	75.9557	232.6488	0.7394	53.8003
10.60	20.7962	9.6662	6.6880	5.7072	0.6919	107.6208	234.7606	1.4789	47.3857
10.80	20.5216	10.5993	5.6836	9.1689	0.5362	148.6396	151.5212	1.3503	29.9501
10.95	20.3157	8.7729	5.9804	16.8408	0.6817	116.5277	241.2828	1.3444	42.2530

11.00	20.2471	7.5977	8.6282	6.7675	1.1356		270.1394	1.4789	
11.20	19.9725	8.8128	7.1217	27.6314	0.8081		247.5090	0.8657	
11.70	19.2862	7.7424	8.7423	9.0753	1.1291		239.9614	1.2355	
11.80	19.1489	8.0318	8.6053	7.0794	1.0714		213.4799	1.3503	
12.60	19.0377	7.7000	7.9890	7.1729	1.0375		238.8857	1.5820	
13.00	19.0292	7.9221	8.4227	37.0497	1.0632	74.8048	216.5178	0.6162	77.3237
13.30	19.0227	7.9645	8.3885	34.7419	1.0532		204.5643	1.3883	
13.60	19.0163	7.6775	8.2059	30.6877	1.0688	75.1371	188.0880	1.1642	75.7632
14.00	19.0078	7.5553	8.2059	15.4374	1.0861	56.1305	187.1978	0.9963	100.3502
14.30	19.0013	7.3631	7.6581	53.6722	1.0401		176.8181	1.3145	
14.60	18.9949	8.5483	8.1032	23.8890	0.9479	55.2875	152.2238	1.7746	79.7865
14.80	18.9906	7.8921	7.8293	37.8294	0.9920	69.2731	200.6728	1.4399	85.3990
15.10	18.9842	7.7474	7.3157	37.8294	0.9443		140.6735	1.2798	
15.30	18.9799	8.4186	7.5782	37.0497	0.9002		139.5592	1.9555	
15.60	18.9735	8.6581	7.4184	13.0048	0.8568		195.9050	1.4568	
16.00	18.9649	9.1023	7.0304	19.7723	0.7724		166.5983	1.0288	
16.50	18.9542	8.8852	7.7037	22.9534	0.8670		241.7220	1.0486	
17.00	18.9435	8.2015	8.1831	20.8327	0.9978	50.2043	206.5130	0.7740	92.4595
17.40	18.9349	9.1422	8.0005	17.0279	0.8751		173.8223	0.6443	
17.60	18.9306	9.2145	8.0233	20.0530	0.8707		227.8819	0.9966	
18.00	18.9221	8.5234	9.2559	22.1425	1.0859		175.6871	0.6655	
18.40	18.9135	8.3587	8.0119	14.2835	0.9585	71.7162	199.1303	1.7818	72.9505
18.60	18.9092	9.3168	8.7879	17.6516	0.9432	95.8253	171.8772	1.2016	47.7255
19.00	18.9006	8.2539	8.8222	12.1628	1.0689	54.3262	294.8397	1.0014	86.0520
19.40	18.8921	7.8996	9.2331	13.1608	1.1688		221.8041	0.7394	
19.60	18.8878	8.9975	8.2858	64.4004	0.9209	55.5042	213.7630	0.7633	77.0509
20.00	18.8792	9.3218	7.8064	75.8771	0.8374		204.3801	0.8664	
20.50	18.8685	9.1122	7.5782	111.3052	0.8316		215.2375	1.1520	
21.00	18.8578	8.4136	8.2059	57.6017	0.9753	70.1402	218.1986	1.4941	63.2594
21.50	18.8471	9.4591	9.7580	53.5475	1.0316	85.8670	211.7829	0.9530	55.0707

22.10	18.8342	8.3188	9.2559	116.2015	1.1126	84.6347	242.5486	1.3919	98.1535
22.20	18.8321	8.4311	7.7265	221.5188	0.9164		200.3900	0.8611	
22.40	18.8278	8.7454	8.2515	83.2995	0.9435	66.0049	201.9089	0.8905	101.1018
22.60	18.8235	8.6980	8.4912	74.2866	0.9762		208.6997	0.7161	
22.80	18.8192	8.1491	8.3314	53.9529	1.0224	57.1655	162.0425	0.6139	104.1624
23.00	18.8150	8.1217	8.1488	55.1068	1.0033		189.4171	0.8319	
23.20	18.8107	8.2814	8.2059	53.2980	0.9909		202.5869	0.6799	
23.40	18.8064	8.2814	8.2972	64.1198	1.0019		195.5516	0.9652	
23.60	18.8021	8.0967	7.9890	49.5556	0.9867		202.7158	1.0755	
23.80	18.7978	7.9994	8.0233	60.7516	1.0030		174.3075	0.6979	
24.00	18.7935	7.6750	8.2515	57.0092	1.0751	68.7564	190.4970	0.5850	86.7520
24.20	18.7893	8.0842	8.8336	98.4563	1.0927		187.6938	0.5063	
24.40	18.7850	7.6576	8.5711	103.5709	1.1193	46.3521	154.2166	0.7578	92.8390
24.50	18.7828	8.6057	8.8450	75.2222	1.0278		188.7465	0.7505	
24.60	18.7807	7.9196	8.7309	10.8530	1.1024	75.6516	190.8662	0.7784	66.3909
24.80	18.7764	7.7374	8.2744	9.2936	1.0694	62.1808	226.0066	0.9551	86.4236
25.00	18.7721	8.3487	8.0575	17.5893	0.9651		208.1480	0.6928	
25.10	18.7700	6.8092	6.6880	25.4483	0.9822		162.9046	0.9859	
25.50	18.7614	7.3357	6.9276	41.0728	0.9444		205.1936	0.9440	
25.90	18.7528	7.7349	7.6695	32.4653	0.9915	49.4729	155.5182	0.9243	171.3000
26.30	18.7443	7.8547	8.0918	50.9902	1.0302	58.7242	189.7765	0.8243	114.9183
26.70	18.7357	7.5378	7.3613	61.3441	0.9766	44.1294	173.8919	0.7194	212.2079
27.10	18.7271	7.5079	7.5325	47.0295	1.0033	66.0884	200.6209	0.7847	163.9065
27.50	18.7186	7.7923	7.8407	95.6183	1.0062	40.2514	164.3110	0.6249	166.5673
28.30	18.7014	5.5791	5.6380	66.0845	1.0106		129.5676	1.1299	
28.70	18.6929	7.0612	7.2016	45.1271	1.0199	50.5840	183.4457	0.8230	180.6723
29.10	18.6843	7.5877	7.4070	53.4227	0.9762	49.2715	168.1494	0.7922	175.4817
29.50	18.6757	8.1965	8.5026	67.4255	1.0373	51.3912	210.7592	0.7727	127.1512
30.30	18.6586	7.2134	7.4526	19.6476	1.0332		162.6776		
31.10	18.6414	8.3288	8.3200	23.4524	0.9990		243.6571	0.4803	

Appendix 2 – Data for chapter 4

Appendix 2.1 Planktic and benthic $\delta^{18}O$ and $\delta^{13}C$ from the Ras il-Pellegrin section. The planktic record was produced using 5 to 7 specimens of *Trilobatus trilobus* and the benthic record was produced using 3 to 4 specimens of *Heterolepa dutemplei*.

Sample no	Height in Section (m) (Badger et al., 2013)	Age (Ma) Lourens 2022	$\delta^{13}C_p$ ‰(VPDB)	$\delta^{18}O_p$ ‰(VPDB)	$\delta^{13}C_b$ ‰(VPDB)	$\delta^{18}O_b$ ‰(VPDB)
MT20	6.65	13.703943	2.706	-1.136	1.27	0.296
MT21	7.00	13.696743	2.901	-1.788		
MT22	7.35	13.689544	3.005	-2.083		
MT23	7.70	13.682345	2.697	-1.828		
MT24	8.05	13.675042	3.278	-2.258		
MT25	8.40	13.667716	2.727	-1.305		
MT26	8.75	13.660391	2.937	-1.633	0.99	0.307
MT27	9.10	13.653066	2.832	-1.887	1.052	0.165
MT28	9.45	13.645741	2.703	-1.9	1.022	0.118
MT29	9.80	13.638416	2.628	-1.211	1.096	0.19
MT30	10.15	13.631091	2.843	-1.776		
MT31	10.50	13.623765	2.872	-2.182		
MT33	11.20	13.609115	2.823	-1.556	0.904	0.237
MT34	11.55	13.601790	2.609	-2.405		
MT35	11.90	13.594465	3.119	-2.606	0.829	0.273
MT36	12.25	13.587139	2.919	-2.578		
MT37	12.60	13.579359	3.221	-0.782	0.95	0.36
MT38	12.95	13.571236	1.841	-1.647		
MT39	13.30	13.563114	2.443	-2.568		
MT40	13.65	13.554992	2.655	-2.1		
MT41	14.00	13.546869	1.991	-2.528		
MT42	14.35	13.538747	2.745	-2.278	0.772	0.018
MT43	14.70	13.530624			0.575	0.132
MT44	15.05	13.519860	2.492	-2.082	0.668	0.087
MT45	15.40	13.507833	1.342	-0.6		
MT46	15.75	13.495807	2.273	-1.312	0.871	0.235
MT47	16.10	13.483781	2.997	-1.752		
MT48	16.45	13.471754	2.932	-1.667	1.042	0.263
MT49	16.80	13.459728	3.234	-1.863		
MT50	17.15	13.447764	2.772	-1.629	1.155	0.303
MT51	17.50	13.437923	2.385	-1.859		
MT52	17.85	13.428081	2.46	-2.217		
MT53	18.20	13.419818	1.651	-1.582	0.219	0.208
MT54	18.55	13.411977	2.225	-0.681		
MT55	18.90	13.404137	1.951	-1.137		
MT57	19.60	13.388456	2.551	-1.868		
MT58	19.95	13.380615	1.956	-1.763	0.593	0.41
MT59	20.30	13.372775	2.502	-1.592	0.683	0.234

MT60	20.65	13.364934	2.445	-1.162	0.972	0.419
MT61	21.00	13.357094	2.527	-1.886	1.16	0.353
MT62	21.35	13.349253	2.079	-1.869		
MT63	21.70	13.341413	1.422	-1	0.36	0.342
MT64	22.05	13.333572	1.51	-1.292	0.862	0.286
MT65	22.40	13.325732	2.1	-1.359		
MT66	22.75	13.317891	2.608	-1.53		
MT67	23.10	13.310051	2.176	-1.244		
MT68-	23.45	13.302210	2.654	-1.54	0.965	0.571
MT69	23.80	13.294370	2.164	-1.768		
MT70	24.15	13.286530	2.607	-1.107		
MT71	24.50	13.278585				
MT72	24.85	13.270484	1.316	-1.066		
MT73	25.20	13.262384				
MT74	25.55	13.254283	2.287	-1.141	0.569	0.389
MT75	25.90	13.246182	2.149	-2.025		
MT76	26.25	13.238082	1.928	-1.735		
MT77	26.60	13.229981	1.66	-1.025	0.77	0.195
MT78	26.95	13.221880	2.606	-1.617		
MT79	27.30	13.213779	1.759	-0.908	0.809	0.395
MT80	27.65	13.205679	2.203	-1.538	0.329	0.49
MT81	28.00	13.197578	2.159	-1.938		
MT82	28.35	13.189477	1.82	-1.181	0.944	0.411
MT83	28.70	13.181318	2.459	-1.541		
MT84	29.05	13.172926	1.856	-0.941		
MT85	29.40	13.164533	2.058	-1.858	0.947	0.427
MT86	29.75	13.156140	2.107	-1.131	0.679	0.412
MT87	30.10	13.147748	2.158	-1.583		
MT88	30.45	13.139355	2.19	-1.36		
MT89	30.80	13.130962	1.869	-1.098	0.558	0.468
MT90	31.15	13.122570			-0.096	0.468
MT92	31.85	13.105785	1.688	-2.101		
MT93	32.20	13.097392	2.02	-1.557		
MT94	32.55	13.088999	0.759	-0.456	0.446	0.512
MT95	32.90	13.080607	1.738	-1.925		
MT96	33.25	13.072214	2.155	-1.438		
MT97	33.60	13.063370	2.083	-1.72	0.465	0.513
MT98	33.95	13.053397	1.012	-1.296	0.226	0.577
MT99	34.30	13.043423	1.946	-1.504	0.68	0.57
MT100	34.65	13.033450	1.66	-1.01		
MT101	35.00	13.022171	2.157	-1.518		
MT102	35.35	13.010670	2.098	-1.798	0.338	0.436
MT104	36.05	12.987669	1.911	-0.903	0.66	0.636
MT105	36.40	12.976168	1.859	-0.796		
MT108	37.45	12.944426	1.482	-1.272		
MT116	40.25	12.863462	1.995	-2.037	0.96	0.505

Appendix 2.2 Trace element ratios from planktic species *Trilobatus trilobus* from the Ras il-Pellegrin section. Analysis was conducted using 25 to 30 individual specimens.

Sample no	Height in Section (m) (Badger et al., 2013)	Age (Ma) Lourens 2022	Mg/Ca (mmol/mol)	Li/Ca (µmol/mol)	Sr/Ca (mmol/mol)	Cd/Ca (µmol/mol)	U/Ca (nmol/mol)	Al/Ca (µmol/mol)	Mn/Ca (µmol/mol)	B/Ca (µmol/mol)	Ba/Ca (µmol/mol)	Fe/Ca (µmol/mol)
MT20	6.65	13.703943	4.525	14.713	1.408	0.064	53.617	308.996	228.789	107.115	4.483	633.979
MT21	7.00	13.696743	5.079	14.889	1.395	0.077	48.283	545.192	281.754	115.035	8.177	752.681
MT22	7.35	13.689544	4.518	13.179	1.426	0.063	68.922	129.354	248.658	102.648	2.749	602.19
MT23	7.70	13.682345	5.333	13.108	4.201	0.071	85.695	76.452	379.705	115.303	108.97	572.849
MT24	8.05	13.675042	4.724	12.288	1.385	0.05	37.342	181.563	287.344	98.923		518.951
MT25	8.40	13.667716	3.979	12.71	1.558	0.068	108.525	132.042	182.661	98.337	341.372	691.506
MT26	8.75	13.660391	4.604	15.755	1.403	0.065	51.577	185.06	190.259	110.647	3.455	489.169
MT27	9.10	13.653066	5.358	13.018	1.379	0.034	59.253	77.857	294.873	93.8	2.813	749.997
MT28	9.45	13.645741	4.514	12.733	1.382	0.066	56.586	141.208	293.184	111.635	16.94	475.852
MT29	9.80	13.638416	4.042	11.504	1.369	0.081	105.334	413.54	206.111	95.179	6.682	714.214
MT30	10.15	13.631091										
MT31	10.50	13.623765	4.749	14.03	1.394	0.057	51.888	311.148	343.433	102.175	2.995	557.232
MT33	11.20	13.609115	5.924	13.518	1.413	0.064	94.157	1388.513	247.787	108.627	4.844	676.33
MT34	11.55	13.60179	5.187	13.251	1.386	0.052	75.764	31.129	598.654	106.986	2.76	630.187
MT35	11.90	13.594465	4.821	13.002	1.401	0.063	51.822	46.264	379.498	97.997		533.087
MT36	12.25	13.587139	4.95	13.148	1.398	0.054	57.806	40.012	406.808	102.05	2.767	621.2
MT37	12.60	13.579359	4.708	13.174	1.382	0.067	82.334	442.663	319.498	112.298	2.355	719.236
MT38	12.95	13.571236	4.083	12.512	1.365	0.061	70.896	191.307	161.266	91.508	2.427	427.754
MT39	13.30	13.563114	4.232	12.374	3.599	0.051	88.768	44.122	167.291	86.197	123.637	483.02
MT40	13.65	13.554992	3.797	12.5	1.38	0.044	68.389	155.734	180.998	86.375	10.198	538.255

MT41	14.00	13.546869	4.391	12.713	1.39	0.048	76.982	77.166	178.143	91.983	2.628	395.912
MT42	14.35	13.538747	4.288	13.155	2.652	0.061	108.258	168.757	133.001	95.941		605.5
MT43	14.70	13.530624	4.839	11.983	1.361	0.046	69.212	294.887	210.208	87.695	3.81	524.444
MT44	15.05	13.51986	5.099	13.016	2.643	0.047	89.294	71.632	320.59	90.368	100.082	680.613
MT45	15.40	13.507833	3.609	11.439	1.35	0.044	179.728	160.355	182.175	74.437	3.367	571.195
MT46	15.75	13.495807	4.218	12.491	1.313	0.026	68.642	62.299	142.78	99.445	5.818	529.616
MT47	16.10	13.483781	3.983	12.805	1.36	0.042	53.398	166.554	147.857	103.784	28.572	472.666
MT48	16.45	13.471754	3.946	13.384	1.76	0.077	116.115	27.878	213.439	105.082	48.233	633.787
MT49	16.80	13.459728	4.264	12.62	1.351	0.063	87.527	322.586	369.17	92.658		651.758
MT50	17.15	13.447764	3.602	12.465	1.377	0.081	60.737	44.435	323.569	88.676	2.403	538.434
MT51	17.50	13.437923	4.174	12.677	2.635	0.118	82.752	76.312	299.492	95.726	192.566	535.209
MT52	17.85	13.428081	3.824	12.395	1.363	0.049	60.852	8.525	340.493	84.522	2.824	505.692
MT53	18.20	13.419818	3.925	12.036	1.471	0.096	53.553	103.533	148.865	86.081	32.783	421.789
MT54	18.55	13.411977	4.107	11.661	1.36	0.054	104.241	8.199	263.534	75.748	3.406	557.952
MT55	18.90	13.404137	3.585	11.845	5.118	0.052	44.706	64.12	172.606	86.345	160.485	259.074
MT57	19.60	13.388456	4.011	12.193	2.187	0.069	89.396	38.677	198.91	87.673	91.003	459.44
MT58	19.95	13.380615	3.62	12.706	5.876	0.078	93.333	64.267	169.683	89.604		629.73
MT59	20.30	13.372775	4.523	12.678	1.465	0.032	22.575	-9.165	337.594	86.631	72.852	13.807
MT60	20.65	13.364934	4.163	13.345	1.423	0.058	66.883	23.39	236.887	91.217	23.528	1417.912
MT61	21.00	13.357094	4.4	13.337	1.454	0.049	40.128	-28.567	200.811	88.656	33.615	30.457
MT62	21.35	13.349253	4.061	12.743	1.43	0.04	2.727	-16.006	150.744	92.708	27.026	8.601
MT63	21.70	13.341413	4.195	12.593	1.708	0.045	84.096	29.295	226.891	89.878		648.497
MT64	22.05	13.333572	4.204	12.515	2.887	0.036	72.517	37.624	317.355	87.514	220.713	642.375
MT65	22.40	13.325732	4.992	12.754	1.406	0.031	58.73	53.877	255.59	91.419	31.187	533.559
MT66	22.75	13.317891	4.122	12.826	1.35	0.037	53.673	29.118	215.709	85.571	2.714	704.35
MT67	23.10	13.310051	3.974	13.035	1.379	0.041	116.131	44.277	295.433	94.834	6.464	739.396
MT68-	23.45	13.30221	3.78	12.386	1.395	0.069	76.059	110.872	188.998	85.258		516.018
MT69	23.80	13.29437	4.421	13.01	2.398	0.078	70.537	33.408	314.5	89.675	101.434	573.035

MT70	24.15	13.28653	4.028	12.754	1.506	0.063	94.788	6.031	307.136	86.072	64.838	418.657
MT71	24.50	13.278585	3.534	12.723	1.449	0.112	142.604	11.694	166.352	85.228	107.25	653.95
MT72	24.85	13.270484	4.112	12.223	1.379	0.056	112.955	-0.798	357.79	77.393	3.526	519.194
MT73	25.20	13.262384	3.689	13.144	1.394	0.083	140.767	39.979	221.732	89.934	4.005	648.999
MT74	25.55	13.254283	3.957	12.93	1.404	0.087	113.806	23.831	336.318	87.357	3.474	556.613
MT75	25.90	13.246182										
MT76	26.25	13.238082	4.33	12.297	1.372	0.054	116.1	29.141	178.563	84.802	2.933	466.177
MT77	26.60	13.229981	3.957	12.622	1.349	0.085	138.528	25.058	200.099	96.98	10.165	775.678
MT78	26.95	13.22188	4.298	12.067	1.367	0.044	117.658	157.729	147.134	92.016	3.13	541.12
MT79	27.30	13.213779	4.107	12.699	1.372	0.06	76.747	29.553	206.513	91.919	2.722	601.773
MT80	27.65	13.205679	3.957	12.967	1.378	0.088	131.893	75.027	174.542	88.91	2.529	585.592
MT81	28.00	13.197578	4.427	12.117	1.342	0.048	130.708	10.393	387.178	75.358	4.798	552.476
MT82	28.35	13.189477	4.033	12.754	1.38	0.047	63.237	28.259	322.11	94.285	9.361	853.191
MT83	28.70	13.181318	4.02	14.314	1.565	0.071	130.862	28.987	337.574	100.598		865.974
MT84	29.05	13.172926	3.91	13.593	1.385	0.045	71.096	9.017	561.499	95.187	3.247	445.841
MT85	29.40	13.164533	4.364	13.647	1.401	0.052	46.551	108.565	297.527	112.114	3.301	489.74
MT86	29.75	13.15614	4.025	13.764	1.398	0.051	103.795	28.2	220.913	98.985	6.784	637.959
MT87	30.10	13.147748	5.333	13.625	1.413	0.084	216.913	56.511	403.932	109.83	4.995	796.802
MT88	30.45	13.139355	4.588	13.734	1.405	0.084	118.042	19.43	268.316	108.051	2.894	700.82
MT89	30.80	13.130962	4.096	13.413	1.376	0.058	191.487	-2.139	299.087	96.969	2.641	998.437
MT90	31.15	13.12257	4.492	13.385	1.382	0.061	200.173	17.709	328.377	99.986	2.949	820.999
MT92	31.85	13.105785	4.342	13.46	1.385	0.06	120.057	30.099	264.591	98.96	3.149	721.331
MT93	32.20	13.097392	4.638	13.251	1.382	0.033	64.592	-18.159	391.16	106.541	3.044	622.569
MT94	32.55	13.088999	4.585	13.842	1.403	0.057	154.494	28.193	356.991	105.509	5.298	888.081
MT95	32.90	13.080607	4.422	13.164	3.188	0.064	65.749	32.825	581.491	91.993	251.729	706.593
MT96	33.25	13.072214	4.104	13.125	1.516	0.058	83.081	3.781	527.604	103.204	188.168	779.946
MT97	33.60	13.06337	4.245	13.499	1.399	0.062	101.926	33.493	282.77	108.514	2.738	771.134
MT98	33.95	13.053397	4.516	12.901	1.394	0.045	108.748	53.383	411.307	100.997	3.038	864.522

MT99	34.30	13.043423	4.386	13.069	1.391	0.035	4.204	-9.474	304.994	94.613	2.81	37.428
MT100	34.65	13.03345	4.024	12.506	1.356	0.049	151.022	8.042	373.388	89.39	2.754	648.936
MT101	35.00	13.022171										
MT102	35.35	13.01067	3.676	12.57	1.356	0.047	77.168	24.536	531.283	93.582	2.484	683.731
MT104	36.05	12.987669	3.682	12.661	1.387	0.042	103.241	44.106	387.885	84.591		800.83
MT105	36.40	12.976168										
MT108	37.45	12.944426	4.03	13.133	1.387	0.046	105.931	59.022	258.016	100.05	2.754	789.733
MT116	40.25	12.863462	4.57	15.283	1.414	0.055	119.122	24.824	225.796	119.725	2.792	654.095

Appendix 2.3 Trace element ratios from benthic species *Uvigerina* spp. from the Ras il-Pellegrin section. Analysis was conducted using 10 to 15 individual specimens.

Sample no	Height in Section (m) (Badger et al., 2013)	Age (Ma) Lourens 2022	Mg/Ca (mmol/mol)	Li/Ca (µmol/mol)	Sr/Ca (mmol/mol)	Cd/Ca (µmol/mol)	U/Ca (nmol/mol)	Al/Ca (µmol/mol)	Mn/Ca (µmol/mol)	B/Ca (µmol/mol)	Ba/Ca (µmol/mol)	Fe/Ca (µmol/mol)
MT20	6.65	13.703943	2.367	11.433	1.234	0.082	21.607	334.598	76.546	30.067	3.643	367.718
MT21	7.00	13.696743										
MT22	7.35	13.689544										
MT23	7.70	13.682345										
MT24	8.05	13.675042										
MT25	8.40	13.667716										
MT26	8.75	13.660391										
MT27	9.10	13.653066										
MT28	9.45	13.645741	2.454	11.852	1.212	0.094	37.758	37.335	131.626	27.358	32.856	447.867
MT29	9.80	13.638416										
MT30	10.15	13.631091	2.899	12.424	2.552	0.147	141.05	98.077	196.104	28.046	36.522	759.84
MT31	10.50	13.623765										
MT33	11.20	13.609115	2.937	12.002	1.156	0.123	136.003	50.447	291.475	28.787	2.817	740.191
MT34	11.55	13.60179	2.499	11.817	1.178	0.074	24.025	50.857	188.299	24.618	4.195	328.899
MT35	11.90	13.594465										
MT36	12.25	13.587139	2.406	11.45	1.195	0.067	17.515	107.593	107.47	22.953	3.303	364.135
MT37	12.60	13.579359	2.491	11.777	1.167	0.082	26.003	101.93	92.655	28.271	2.956	349.876
MT38	12.95	13.571236										
MT39	13.30	13.563114										
MT40	13.65	13.554992										

MT41	14.00	13.546869										
MT42	14.35	13.538747	2.557	11.465	1.168	0.07	33.339	14.33	50.744	25.9	3.025	316.101
MT43	14.70	13.530624										
MT44	15.05	13.51986	2.414	11.773	1.191	0.066	40.199	15.534	114.052	29.604	3.648	314.224
MT45	15.40	13.507833										
MT46	15.75	13.495807	2.373	11.942	1.226	0.064	24.243	82.782	66.825	25.802	3.732	397.689
MT47	16.10	13.483781										
MT48	16.45	13.471754	2.464	11.731	1.203	0.077	34.571		76.288	25.326	3.626	417.503
MT49	16.80	13.459728										
MT50	17.15	13.447764	2.484	11.75	1.196	0.085	19.255	46.54	89.6	28.807	3.248	304.955
MT51	17.50	13.437923										
MT52	17.85	13.428081										
MT53	18.20	13.419818										
MT54	18.55	13.411977										
MT55	18.90	13.404137	2.58	11.247	1.209	0.088	41.709	11.731	83.477	26.178	4.137	381.882
MT57	19.60	13.388456										
MT58	19.95	13.380615	2.696	11.715	1.55	0.107	42.131	68.228	76.969	25.643	128.331	367.076
MT59	20.30	13.372775										
MT60	20.65	13.364934	2.611	11.627	1.233	0.069	16.265	99.454	73.898	27.503	33.858	248.746
MT61	21.00	13.357094	2.667	12.257	1.2	0.069	20.287		55.501	27.588	3.656	320.74
MT62	21.35	13.349253										
MT63	21.70	13.341413	2.663	12.078	1.295	0.086	30.935	153.446	86.617	33.279	7.425	468.323
MT64	22.05	13.333572										
MT65	22.40	13.325732										
MT66	22.75	13.317891										
MT67	23.10	13.310051										
MT68-	23.45	13.30221										
MT69	23.80	13.29437	2.694	11.91	1.19	0.095	27.885	60.711	98.189	29.69	3.956	363.665

MT70	24.15	13.28653										
MT71	24.50	13.278585	2.422	10.939	1.175	0.148	57.261	27.061	77.402	26.77	16.775	379.887
MT72	24.85	13.270484										
MT73	25.20	13.262384										
MT74	25.55	13.254283	2.683	8.382	1.202	2.804	9.84	4.06	36.513	51.793	2.744	94.365
MT75	25.90	13.246182	2.475	11.087	1.171	0.076	34.435	9.133	103.714	27.668	3.366	333.611
MT76	26.25	13.238082										
MT77	26.60	13.229981	2.617	11.237	1.187	0.1	80.91		122.706	26.907	5.005	520.64
MT78	26.95	13.22188										
MT79	27.30	13.213779	2.443	11.342	1.194	0.096	25.557	9.956	68.455	29.488	4.833	342.076
MT80	27.65	13.205679										
MT81	28.00	13.197578										
MT82	28.35	13.189477										
MT83	28.70	13.181318	1.497	10.256	2.204	1.408	2.943	11.2	99.044	56.876	294.203	116.993
MT84	29.05	13.172926										
MT85	29.40	13.164533										
MT86	29.75	13.15614										
MT87	30.10	13.147748										
MT88	30.45	13.139355	2.572	12.099	1.204	0.105	55.052	131.333	94.061	30.382	4.656	468.308
MT89	30.80	13.130962										
MT90	31.15	13.12257	2.653	11.581	1.17	0.098	72.194	70.088	132.331	24.561	2.859	593.969
MT92	31.85	13.105785	2.217	10.88	1.188	0.082	53.861	17.2	88.303	24.625	3.54	437.221
MT93	32.20	13.097392										
MT94	32.55	13.088999										
MT95	32.90	13.080607										
MT96	33.25	13.072214										
MT97	33.60	13.06337	2.287	10.667	1.183	0.085	48.021	117.257	102.224	26.895	2.99	548.462
MT98	33.95	13.053397	2.747	11.816	1.199	0.06	33.448		134.199	26.62	3.459	525.279

MT99	34.30	13.043423										
MT100	34.65	13.03345	2.628	11.68	1.172	0.083	162.209		237.039	24.736	3.233	669.14
MT101	35.00	13.022171	2.481	10.952	1.174	0.116	83.373		197.132	28.648	2.937	724.41
MT102	35.35	13.01067										
MT104	36.05	12.987669										
MT105	36.40	12.976168	2.852	11.986	1.204	0.078	67.241	71.355	242.266	35.062	3.35	648.952
MT108	37.45	12.944426										
MT116	40.25	12.863462	2.581	11.658	1.185	0.077	34.927		86.343	37.292	2.824	420.947

Appendix 2.4 Bottom water temperature (BWT) from benthic Mg/Ca, sea surface temperature from planktic Mg/Ca and difference between surface and boom temperatures. Ras il-Pellegrin section. Surface ($\delta^{18}O_{sw}$ p) boom ($\delta^{18}O_{sw}$ b) water $\delta^{18}O$ and vertical gradient ($\Delta\delta^{18}O_{sw}$) . Sea surface salinity (SSS) calculated using two different calibrations.

Sample no	Height in Section (m) (Badger et al., 2013)	Age (Ma) Lourens 2022	SST (°C)	BWT (°C) (C=0.27)	SST-BWT (°C)	$\delta^{18}O_{sw}$ p	$\delta^{18}O_{sw}$ b	$\Delta\delta^{18}O_{sw}$	SSS calibration from Pierre (1999)	SSS calibration from LeGrande & Schmidt (2006)
MT20	6.65	13.703943	30.16	21.741	8.418	1.721	1.053	0.669	39.685	39.147
MT21	7.00	13.696743								
MT22	7.35	13.689544	30.142			0.828			36.113	35.958
MT23	7.70	13.682345	31.982			1.474			38.698	38.266
MT24	8.05	13.675042	30.634			0.758			35.834	35.709
MT25	8.40	13.667716	28.727			1.305			38.02	37.661
MT26	8.75	13.660391	30.348			1.323			38.091	37.724
MT27	9.10	13.653066	32.032			1.427			38.507	38.095
MT28	9.45	13.645741	30.126	22.526	7.6	1.009	1.029	-0.02	36.836	36.604
MT29	9.80	13.638416								
MT30	10.15	13.631091		26.231			1.62			
MT31	10.50	13.623765								
MT33	11.20	13.609115		26.516			1.91			
MT34	11.55	13.60179	31.665	22.926	8.739	0.832	0.989	-0.156	36.129	35.972
MT35	11.90	13.594465	30.851			0.459			34.634	34.638
MT36	12.25	13.587139	31.144	22.086	9.059	0.549	1.294	-0.745	34.996	34.961
MT37	12.60	13.579359		22.851			1.334			
MT38	12.95	13.571236	29.002			1.024			36.896	36.657
MT39	13.30	13.563114	29.4			0.188			33.553	33.672
MT40	13.65	13.554992	28.193			0.398			34.394	34.423

MT41	14.00	13.546869	29.809			0.316			34.063	34.128
MT42	14.35	13.538747	29.542	23.428	6.115	0.509	1.104	-0.595	34.837	34.819
MT43	14.70	13.530624								
MT44	15.05	13.51986	31.465	22.149	9.316	1.115	0.924	0.191	37.259	36.981
MT45	15.40	13.507833	27.624			1.778			39.911	39.349
MT46	15.75	13.495807	29.354	21.761	7.594	1.436	0.995	0.441	38.545	38.129
MT47	16.10	13.483781	28.716			0.86			36.24	36.072
MT48	16.45	13.471754	28.611	22.596	6.015	0.923	1.187	-0.264	36.492	36.296
MT49	16.80	13.459728								
MT50	17.15	13.447764	27.596	22.768	4.828	0.744	1.261	-0.517	35.777	35.658
MT51	17.50	13.437923	29.232			0.865			36.258	36.088
MT52	17.85	13.428081	28.258			0.298			33.994	34.066
MT53	18.20	13.419818	28.547			0.995			36.782	36.555
MT54	18.55	13.411977	29.048			2.004			40.816	40.157
MT55	18.90	13.404137	27.538	23.608	3.931	1.225	1.121	0.104	37.699	37.374
MT57	19.60	13.388456	28.785			0.761			35.844	35.718
MT58	19.95	13.380615	27.642	24.581	3.062	0.622	1.718	-1.096	35.287	35.221
MT59	20.30	13.372775	30.116			1.322			38.086	37.72
MT60	20.65	13.364934	29.193	23.87	5.323	1.555	1.59	-0.035	39.02	38.553
MT61	21.00	13.357094	29.809	24.335	5.473	0.963	1.614	-0.651	36.65	36.438
MT62	21.35	13.349253	28.916			0.789			35.957	35.819
MT63	21.70	13.341413	29.275	24.299	4.976	1.735	1.596	0.139	39.741	39.197
MT64	22.05	13.333572	29.3			1.449			38.594	38.173
MT65	22.40	13.325732	31.207			1.788			39.951	39.385
MT66	22.75	13.317891	29.079			1.164			37.455	37.156
MT67	23.10	13.310051	28.67			1.363			38.25	37.866
MT68-	23.45	13.30221	28.113			0.948			36.59	36.384
MT69	23.80	13.29437	29.853	24.551	5.302	1.092	1.302	-0.21	37.166	36.898

MT70	24.15	13.28653	28.818			1.532			38.927	38.47
MT71	24.50	13.278585	27.362	22.183	5.179		0.844	-0.844		
MT72	24.85	13.270484	29.045			1.622			39.287	38.792
MT73	25.20	13.262384	27.839			2.43			42.52	41.678
MT74	25.55	13.254283	28.618	24.452	4.165	1.456	1.672	-0.216	38.623	38.199
MT75	25.90	13.246182		22.656			1.406			
MT76	26.25	13.238082	29.617			1.076			37.103	36.842
MT77	26.60	13.229981	28.615	23.893	4.722	1.572	1.371	0.201	39.087	38.614
MT78	26.95	13.22188	29.532			1.176			37.503	37.199
MT79	27.30	13.213779	29.025	22.363	6.662	1.777	1.274	0.503	39.907	39.346
MT80	27.65	13.205679	28.611			1.058			37.034	36.78
MT81	28.00	13.197578	29.858			0.925			36.5	36.304
MT82	28.35	13.189477	28.82			1.461			38.643	38.217
MT83	28.70	13.181318	28.785			1.093			37.173	36.905
MT84	29.05	13.172926	28.473			1.627			39.308	38.811
MT85	29.40	13.164533	29.695			0.971			36.684	36.468
MT86	29.75	13.15614	28.796			1.506			38.825	38.38
MT87	30.10	13.147748	31.92			1.719			39.678	39.141
MT88	30.45	13.139355	30.248	23.496	6.752	1.587	1.099	0.488	39.15	38.67
MT89	30.80	13.130962	28.986			1.581			39.122	38.645
MT90	31.15	13.12257	30.009	24.186	5.824		1.7			
MT92	31.85	13.105785	29.631	20.195	9.436	0.716	0.449	0.267	35.664	35.557
MT93	32.20	13.097392	30.363			1.416			38.464	38.057
MT94	32.55	13.088999	30.234			2.49			42.76	41.893
MT95	32.90	13.080607	29.832			0.935			36.541	36.341
MT96	33.25	13.072214	29.002			1.245			37.782	37.448
MT97	33.60	13.06337	29.374	20.871	8.504	1.043	1.097	-0.054	36.973	36.726
MT98	33.95	13.053397	30.062	24.948	5.115	1.614	1.955	-0.34	39.257	38.765

MT99	34.30	13.043423	29.736			1.337			38.148	37.775
MT100	34.65	13.03345	28.778	23.957	4.82	1.627	1.658		39.306	38.809
MT101	35.00	13.022171		22.674			1.41			
MT102	35.35	13.01067	27.771		27.771	0.624			35.294	35.227
MT104	36.05	12.987669	27.786		27.786	1.522			38.889	38.437
MT105	36.40	12.976168		25.77	-25.77		1.533			
MT108	37.45	12.944426	28.784			1.368			38.273	37.886
MT116	40.25	12.863462	30.171	23.53	6.641	0.901	1.611	-0.71	36.404	36.218

Appendix 3 – Data for chapter 5

Appendix 3.1 Stable isotope data from the composite Marsalforn (MRSF) and Ras il-Pellegrin (RIP) sections. Planktic data from *Trilobatus trilobus*, benthic data from *Heterolepa dutemplei* Data previously published in Abels et al., (2005) and Mourik et al., (2011) and retuned in this study according to the CenoGRID age model by Lucas Lourens (2022). $\Delta\delta^{13}C$ vertical gradient calculated during this study

Sample no	Height in section (m) (Composite) Lourens 2022	Section	Age (Ma) Lourens 2022	$\delta^{13}C$ (bulk) (Abels et al. 2005)	$\delta^{13}O$ (bulk) (Abels et al. 2005)	$\delta^{13}C_p$ ‰(VPDB) (Mourik et al., 2011)	$\delta^{18}O_p$ ‰(VPDB) (Mourik et al., 2011)	$\delta^{13}C_b$ ‰(VPDB) (Mourik et al., 2011)	$\delta^{18}O_b$ ‰(VPDB) (Mourik et al., 2011)	$\Delta\delta^{13}C_p$ ‰(VPDB)
MT 1950	-26.35	MRSF	14.395783			1.78	-1.30	1.24	-0.45	0.54
MT 1949	-26.21	MRSF	14.393937			1.59	-1.41	1.39	-0.49	0.20
MT 1948	-26.10	MRSF	14.392594			1.83	-1.61	1.18	-0.49	0.66
MT 1947	-25.99	MRSF	14.391084			2.00	-1.69	0.97	-0.75	1.03
MT 1946	-25.87	MRSF	14.389574			1.99	-1.68	0.97	-0.45	1.01
MT 1945	-25.75	MRSF	14.388063			1.81	-1.71	1.02	-1.01	0.80
MT 1944	-25.65	MRSF	14.386721			1.73	-1.61	1.20	-0.64	0.53
MT 1943	-25.55	MRSF	14.385378			1.75	-1.65	1.27	-0.72	0.48
MT 1942	-25.46	MRSF	14.384204			1.80	-1.61	1.14	-0.58	0.65
MT 1941	-25.37	MRSF	14.383029			1.69	-1.42	1.47	-0.63	0.22
MT 1940	-25.25	MRSF	14.381519			1.76	-1.61	1.37	-0.61	0.38
MT 1939	-25.16	MRSF	14.380344			1.79	-1.62	1.14	-0.61	0.65
MT 1938	-25.10	MRSF	14.379505			1.74	-1.57	1.32	-0.56	0.42
MT 1937	-25.00	MRSF	14.37833			1.97	-1.59	1.28	-0.51	0.69
MT 1936	-24.90	MRSF	14.376988			1.95	-1.68	1.40	-0.60	0.55
MT 1935	-24.82	MRSF	14.375981			2.11	-1.45	1.57	-0.53	0.55
MT 1934	-24.73	MRSF	14.374806			2.03	-1.40	1.44	-0.57	0.58
MT 1933	-24.64	MRSF	14.373632			1.87	-1.45	1.27	-0.61	0.60
MT 1932	-24.58	MRSF	14.372793			2.07	-1.67	1.52	-0.55	0.54
MT 1931	-24.49	MRSF	14.371618			1.97	-1.63	1.48	-0.60	0.49

MT 1930	-24.41	MRSF	14.370611			2.10	-1.67	1.50	-0.59	0.61
MT 1929	-24.31	MRSF	14.369268			1.91	-1.77	1.45	-0.59	0.46
MT 1928	-24.20	MRSF	14.367926			1.97	-1.73	1.25	-0.82	0.72
MT 1927	-24.09	MRSF	14.366416			1.96	-1.65	1.37	-0.79	0.59
MT 1926	-23.98	MRSF	14.365073			1.85	-1.65	1.36	-0.65	0.49
MT 1925	-23.84	MRSF	14.363227			2.11	-1.98	1.49	-0.67	0.61
MT 1924	-23.72	MRSF	14.361717			1.98	-1.74	1.36	-0.61	0.61
MT 1923	-23.61	MRSF	14.360207			1.89	-1.81	1.21	-0.52	0.68
MT 1922	-23.50	MRSF	14.358864			1.94	-1.49	1.28	-0.48	0.66
MT 1921	-23.39	MRSF	14.357354			2.05	-1.48	1.44	-0.43	0.61
MT 1920	-23.28	MRSF	14.356011			1.80	-1.56	1.23	-0.64	0.57
MT 1674	-23.01	MRSF	14.352487					1.28	-0.71	
MT 1675	-22.94	MRSF	14.35148			2.08	-1.73	1.08	-0.79	1.00
MT 1676	-22.86	MRSF	14.350474			2.14	-1.65	1.10	-0.50	1.04
MT 1677	-22.79	MRSF	14.349635			1.70	-1.69	0.98	-0.60	0.72
MT 1678	-22.69	MRSF	14.348292			1.51	-1.76	0.98	-0.78	0.53
MT 1679	-22.59	MRSF	14.34695			1.56	-1.98	1.36	-0.55	0.20
MT 1680	-22.51	MRSF	14.345943			1.57	-1.74	1.09	-0.81	0.48
MT 1681	-22.43	MRSF	14.344936			1.60	-1.82	1.26	-0.67	0.34
MT 1682	-22.30	MRSF	14.343258			1.56	-1.57	0.92	-0.41	0.64
MT 1683	-22.19	MRSF	14.341747			2.05	-1.60	1.31	-0.49	0.74
MT 1684	-22.11	MRSF	14.34074			2.28	-1.37	1.27	-0.52	1.01
MT 1685	-22.00	MRSF	14.339398			2.05	-1.56	1.22	-0.49	0.83
MT 1686	-21.93	MRSF	14.338391			2.08	-1.67	1.16	-0.36	0.92
MT 1687	-21.81	MRSF	14.336881			1.55	-1.60	1.16	-0.49	0.40
MT 1688	-21.69	MRSF	14.335371			1.41	-1.74	0.91	-0.42	0.50
MT 1689	-21.60	MRSF	14.334196			1.61	-1.63	1.05	-0.37	0.55
MT 1690	-21.53	MRSF	14.333189			2.03	-1.64	0.92	-0.13	1.11
MT 1691	-21.44	MRSF	14.332014			2.02	-1.58	1.05	-0.21	0.97
MT 1692	-21.33	MRSF	14.330672			1.90	-1.42	1.05	-0.14	0.84

MT 1693	-21.23	MRSF	14.329329			1.94	-1.56	1.14	-0.49	0.79
MT 1694	-21.14	MRSF	14.328155			1.90	-1.66	1.09	-0.55	0.81
MT 1695	-21.03	MRSF	14.326812			1.98	-1.76	1.28	-0.65	0.70
MT 1696	-20.94	MRSF	14.325637			2.05	-1.85	1.36	-0.64	0.68
MT 1697	-20.85	MRSF	14.324463			2.09	-1.72	1.31	-0.48	0.78
MT 1698	-20.78	MRSF	14.323456			2.25	-2.02	1.52	-0.56	0.73
MT 1699	-20.70	MRSF	14.322449			2.20	-1.80	1.21	-0.51	1.00
MT 1700	-20.66	MRSF	14.321946			2.32	-1.86	1.41	-0.62	0.91
MT 1701	-20.57	MRSF	14.320771			2.15	-1.90	1.36	-0.60	0.79
MT 1702	-20.48	MRSF	14.319596			1.96	-1.67	1.22	-0.64	0.74
MT 1703	-20.39	MRSF	14.318422			1.94	-1.73	1.14	-0.57	0.80
MT 1704	-20.30	MRSF	14.317247					1.25	-0.70	
MT 1705	-20.19	MRSF	14.315904			1.89	-1.57	1.30	-0.74	0.59
MT 1706	-20.09	MRSF	14.314562			1.92	-1.75	1.23	-0.67	0.69
MT 1707	-20.01	MRSF	14.313555			1.97	-1.59	1.04	-0.86	0.93
MT 1708	-19.91	MRSF	14.312212			1.77	-1.95	0.79	-0.95	0.98
MT 1709	-19.83	MRSF	14.311206			1.75	-1.85	1.02	-0.69	0.72
MT 1710	-19.71	MRSF	14.309695			1.86	-1.88	0.95	-0.61	0.91
MT 1711	-19.61	MRSF	14.308353			1.71	-1.84	0.85	-0.71	0.86
MT 1712	-19.51	MRSF	14.30701			1.70	-1.79	1.08	-0.77	0.62
MT 1713	-19.39	MRSF	14.305493			1.39	-2.06	0.84	-0.77	0.55
MT 1714	-19.29	MRSF	14.304132			1.65	-1.75	1.15	-0.63	0.50
MT 1715	-19.17	MRSF	14.3026			2.00	-1.64	1.37	-0.59	0.63
MT 1716	-19.07	MRSF	14.301238			2.21	-1.76	1.49	-0.66	0.72
MT 1717	-18.98	MRSF	14.300047			2.11	-1.67	1.42	-0.66	0.69
MT 1718	-18.87	MRSF	14.298686			1.85	-1.64	1.21	-0.54	0.63
MT 1719	-18.74	MRSF	14.296984			1.87	-1.52	1.22	-0.47	0.65
MT 1720	-18.63	MRSF	14.295452			1.97	-1.61	1.23	-0.29	0.75
MT 1721	-18.51	MRSF	14.293921			2.25	-1.76	1.41	-0.46	0.84
MT 1722	-18.40	MRSF	14.292389			2.24	-1.78	1.31	-0.32	0.93

MT 1723	-18.38	MRSF	14.290857			2.48	-1.71	1.48	-0.42	1.01
MT 1724	-18.31	MRSF	14.289496			2.37	-1.60	1.47	-0.09	0.91
MT 1725	-18.28	MRSF	14.287964			2.39	-1.62	1.75	-0.34	0.64
MT 1726	-18.23	MRSF	14.292219			2.23	-1.57	1.38	-0.40	0.84
MT 1727	-18.18	MRSF	14.291198			2.18	-1.49	1.40	-0.34	0.78
MT 1728	-18.14	MRSF	14.290177			2.16	-1.29	1.26	-0.22	0.90
MT 1729	-18.06	MRSF	14.288985			2.49	-1.73	1.19	-0.40	1.29
MT 1730	-18.02	MRSF	14.287454			2.27	-1.44	1.63	-0.52	0.63
MT 1731	-17.94	MRSF	14.286433			2.37	-1.77	1.39	-0.37	0.98
MT 1732	-17.88	MRSF	14.285582			2.24	-1.54	1.48	-0.44	0.76
MT 1733	-17.83	MRSF	14.284901			2.28	-1.51	1.61	-0.49	0.67
MT 1734	-17.80	MRSF	14.284561			2.44	-1.66	1.26	-0.54	1.18
MT 1735	-17.72	MRSF	14.28354			2.31	-1.49	1.78	-0.48	0.53
MT 1736	-17.66	MRSF	14.282689			2.41	-1.59	1.60	-0.47	0.81
MT 1737	-17.61	MRSF	14.282008			2.46	-1.75	1.48	-0.51	0.97
MT 1738	-17.55	MRSF	14.281327			2.41	-1.49	1.41	-0.94	0.99
MT 1739	-17.45	MRSF	14.278302			2.52	-1.61	1.50	-0.61	1.02
MT 1740	-17.39	MRSF	14.276082			2.48	-1.35	1.49	-0.48	0.98
MT 1741	-17.27	MRSF	14.272086			2.44	-1.56	1.23	-0.42	1.20
MT 1742	-17.21	MRSF	14.269866			2.27	-1.50	1.23	-0.57	1.04
MT 1743	-17.15	MRSF	14.26809			2.03	-1.41	1.26	-0.43	0.77
MT 1744	-17.08	MRSF	14.265426			2.23	-1.43	1.16	-0.44	1.07
MT 1745	-17.01	MRSF	14.263206			2.32	-1.55	1.31	-0.45	1.02
MT 1746	-16.99	MRSF	14.262318			2.42	-1.69	1.33	-0.37	1.09
MT 1747	-16.95	MRSF	14.260986			2.22	-1.61	1.09	-0.40	1.14
MT 1748	-16.88	MRSF	14.258766			2.22	-1.53	1.22	-0.50	1.00
MT 1749	-16.82	MRSF	14.256546			2.27	-1.54	1.38	-0.54	0.88
MT 1750	-16.70	MRSF	14.25255			2.07	-1.53	1.39	-0.56	0.68
MT 1751	-16.62	MRSF	14.249886			2.15	-1.53	1.22	-0.32	0.93
MT 1752	-16.56	MRSF	14.247666			2.11	-1.51	1.22	-0.32	0.89

MT 1753	-16.53	MRSF	14.246778			2.32	-1.83	1.31	-0.45	1.01
MT 1754	-16.46	MRSF	14.244114			2.22	-1.54	1.20	-0.44	1.01
MT 1755	-16.44	MRSF	14.24367			2.16	-1.61	1.46	-0.55	0.70
MT 1756	-16.35	MRSF	14.240562			2.07	-1.52	1.22	-0.59	0.85
MT 1757	-16.16	MRSF	14.233902			2.54	-1.88	1.52	-0.52	1.01
MT 1758	-16.07	MRSF	14.230794			2.38	-1.74	1.36	-0.74	1.02
MT 1759	-15.96	MRSF	14.22369			2.28	-1.66	1.26	-0.56	1.02
MT 1760	-15.87	MRSF	14.227242			2.66	-1.78	1.48	-0.55	1.18
MT 1761	-15.86	MRSF	14.224134			2.61	-1.79	1.37	-0.78	1.25
MT 1762	-15.74	MRSF	14.219694			2.42	-1.48	1.65	-0.52	0.77
MT 1763	-15.61	MRSF	14.215254			2.60	-1.51	1.62	-0.47	0.98
MT 1764	-15.49	MRSF	14.211165			2.18	-1.94	1.28	-0.85	0.90
MT 1765	-15.41	MRSF	14.20929			2.47	-1.92	1.33	-0.55	1.14
MT 1766	-15.32	MRSF	14.207102			2.42	-1.55	1.72	-0.59	0.71
MT 1767	-15.25	MRSF	14.205539			2.18	-1.50	1.60	-0.63	0.58
MT 1768	-15.16	MRSF	14.203351			2.38	-1.52	1.34	-0.57	1.04
MT 1769	-15.07	MRSF	14.201163			2.33	-1.47	1.41	-0.44	0.92
MT 1770	-14.99	MRSF	14.199288			2.34	-1.75	1.47	-0.51	0.87
MT 1771	-14.90	MRSF	14.1971			2.34	-1.57	1.39	-0.48	0.96
MT 1772	-14.81	MRSF	14.194912			2.29	-1.38	1.15	-0.27	1.15
MT 1773	-14.74	MRSF	14.193036			2.15	-1.34	1.26	-0.39	0.89
MT 1774	-14.67	MRSF	14.191474			2.28	-1.31	1.14	-0.32	1.14
MT 1775	-14.58	MRSF	14.189286			2.40	-1.88	1.20	-0.24	1.20
MT 1776	-14.46	MRSF	14.186473			2.35	-1.74	1.42	-0.52	0.92
MT 1777	-14.37	MRSF	14.184285			2.42	-1.80	1.26	-0.50	1.16
MT 1778	-14.27	MRSF	14.181784			2.44	-1.71	1.52	-0.55	0.92
MT 1779	-14.19	MRSF	14.179909			2.40	-1.50	1.65	-0.47	0.75
MT 1780	-14.14	MRSF	14.178658			2.52	-1.70	1.43	-0.50	1.09
MT 1781	-14.06	MRSF	14.176783			2.37	-1.69	1.49	-0.57	0.88
MT 1782	-13.97	MRSF	14.174595			2.34	-1.60	1.46	-0.51	0.87

MT 1783	-13.87	MRSF	14.172094			2.25	-1.65	1.41	-0.43	0.84
MT 1784	-13.82	MRSF	14.170844			2.12	-1.46	1.46	-0.44	0.66
MT 1785	-13.74	MRSF	14.168969			2.60	-1.92	1.55	-0.35	1.05
MT 1786	-13.66	MRSF	14.167093			2.37	-1.69	1.42	-0.35	0.95
MT 1787	-13.56	MRSF	14.164593			2.01	-1.46	1.44	-0.25	0.57
MT 1788	-13.44	MRSF	14.16178			2.14	-1.64	1.36	-0.47	0.78
MT 1789	-13.31	MRSF	14.158654			2.28	-1.79	1.17	-0.60	1.11
MT 1790	-13.25	MRSF	14.157091			2.34	-1.83	1.53	-0.47	0.81
MT 1791	-13.11	MRSF	14.153785			2.41	-1.81	1.60	-0.63	0.81
MT 1792	-13.04	MRSF	14.152815			2.47	-1.73	1.67	-0.55	0.80
MT 1793	-12.95	MRSF	14.151457			2.57	-1.59	1.88	-0.38	0.69
MT 1794	-12.83	MRSF	14.149711			2.62	-1.59	1.68	-0.35	0.94
MT 1795	-12.76	MRSF	14.148546			2.54	-1.52	1.46	-0.29	1.08
MT 1796	-12.67	MRSF	14.147188			2.40	-1.35	1.60	-0.31	0.79
MT 1797	-12.59	MRSF	14.146024			2.37	-1.41	1.32	-0.35	1.05
MT 1798	-12.48	MRSF	14.144472			2.23	-1.59	1.40	-0.29	0.83
MT 1799	-12.43	MRSF	14.143696			2.24	-1.59	1.55	-0.27	0.69
MT 1800	-12.38	MRSF	14.14292			2.25	-1.54	1.48	-0.32	0.78
MT 1801	-12.29	MRSF	14.141562			2.27	-1.72	1.25	-0.31	1.02
MT 1802	-12.23	MRSF	14.140592			2.26	-1.94	1.11	-0.34	1.14
MT 1803	-12.12	MRSF	14.13904			2.17	-1.77	1.25	-0.36	0.92
MT 1804	-11.99	MRSF	14.1371			2.06	-2.00	1.16	-0.29	0.90
MT 1805	-11.88	MRSF	14.135354			2.05	-2.33	1.29	-0.32	0.76
MT 1806	-11.79	MRSF	14.133996			2.01	-2.32	1.05	-0.31	0.96
MT 1807	-11.66	MRSF	14.132056			1.97	-2.25	1.08	-0.29	0.89
MT 1808	-11.55	MRSF	14.130504			1.74	-2.03	1.10	-0.33	0.64
MT 1809	-11.45	MRSF	14.128952			1.96	-2.41	0.91	-0.33	1.05
MT 1810	-11.35	MRSF	14.1274			1.84	-2.06	1.06	-0.31	0.78
MT 1811	-11.19	MRSF	14.125072			1.91	-2.15	1.02	-0.34	0.89
MT 1812	-11.11	MRSF	14.123908			1.98	-2.23	1.03	-0.36	0.95

MT 1813	-11.00	MRSF	14.122162			2.05	-1.90	0.90	-0.35	1.15
MT 1814	-10.89	MRSF	14.12061			2.15	-1.74	1.20	-0.50	0.95
MT 1815	-10.75	MRSF	14.118475			2.25	-1.94	1.26	-0.35	0.99
MT 1816	-10.69	MRSF	14.117505			2.10	-1.66	1.14	-0.22	0.95
MT 1817	-10.56	MRSF	14.115565			2.21	-1.68	1.40	-0.36	0.81
MT 1818	-10.52	MRSF	14.114983			2.01	-1.50	1.29	-0.42	0.72
MT 1819	-10.43	MRSF	14.113625			1.94	-1.54	1.38	-0.72	0.56
MT 1820	-10.35	MRSF	14.112461			1.86	-1.83	1.17	-0.80	0.69
MT 1821	-10.25	MRSF	14.109194			1.77	-1.92	1.31	-0.61	0.46
MT 1822	-10.13	MRSF	14.104703			2.15	-1.60	1.24	-0.69	0.91
MT 1823	-10.01	MRSF	14.100211			1.96	-1.55	1.10	-0.54	0.86
MT 1824	-9.91	MRSF	14.096219			1.96	-1.51	1.17	-0.47	0.78
MT 1825	-9.82	MRSF	14.092725			1.83	-1.74	1.07	-0.53	0.76
MT 1826	-9.70	MRSF	14.088234			1.72	-1.66	1.16	-0.49	0.56
MT 1827	-9.61	MRSF	14.08474			1.93	-1.62	0.99	-0.62	0.94
MT 1828	-9.52	MRSF	14.081247			1.75	-1.71	1.39	-0.50	0.37
MT 1829	-9.42	MRSF	14.077255			1.76	-1.65	1.22	-0.47	0.54
MT 1830	-9.29	MRSF	14.072264			1.68	-1.53	1.34	-0.51	0.35
MT 1831	-9.13	MRSF	14.066275			1.94	-1.54	1.30	-0.43	0.64
MT 1832	-9.06	MRSF	14.063281			1.96	-1.69	1.27	-0.40	0.69
MT 1833	-9.02	MRSF	14.061784			2.05	-1.48	1.27	-0.40	0.77
MT 1834	-8.92	MRSF	14.057792			2.16	-1.19	1.28	-0.18	0.88
MT 1835	-8.81	MRSF	14.053799			2.12	-1.28	1.20	-0.27	0.92
MT 1836	-8.70	MRSF	14.049308			1.94	-1.13	1.17	-0.14	0.77
MT 1837	-8.60	MRSF	14.045814			1.60	-1.29	1.12	-0.39	0.48
MT 1838	-8.51	MRSF	14.042321			1.74	-1.45	1.06	-0.41	0.67
MT 1839	-8.42	MRSF	14.038828			1.63	-1.58	1.10	-0.55	0.53
MT 1840	-8.32	MRSF	14.034835			1.73	-1.54	1.05	-0.43	0.69
MT 1841	-8.24	MRSF	14.031841			2.07	-1.74	1.25	-0.52	0.82
MT 1842	-8.14	MRSF	14.027848			2.02	-1.76	1.32	-0.45	0.71

MT 1843	-8.05	MRSF	14.024355			2.03	-1.66	1.66	-0.36	0.37
MT 1844	-7.96	MRSF	14.020862			2.03	-1.71	1.45	-0.53	0.58
MT 1845	-7.87	MRSF	14.017368			2.06	-1.90	1.44	-0.43	0.62
MT 1846	-7.76	MRSF	14.013376			2.03	-1.66	1.42	-0.28	0.62
MT 1847	-7.69	MRSF	14.010382			2.20	-1.68	1.38	-0.42	0.82
MT 1848	-7.60	MRSF	14.006888			2.04	-1.56	0.86	-0.45	1.18
MT 1849	-7.52	MRSF	14.003894			2.12	-1.46	1.24	-0.30	0.87
MT 1850	-7.41	MRSF	13.999901			1.92	-1.58	1.36	-0.50	0.56
MT 1851	-7.34	MRSF	13.996907			1.64	-1.71	1.13	-0.50	0.51
MT 1852	-7.22	MRSF	13.992416			1.71	-1.69	0.91	-0.64	0.80
MT 1853	-7.13	MRSF	13.99013			1.82	-2.11	1.46	-0.46	0.36
MT 1854	-7.03	MRSF	13.987703			1.83	-1.69	1.30	-0.65	0.53
MT 1855	-6.94	MRSF	13.98558			1.90	-1.51	1.31	-0.35	0.59
MT 1856	-6.81	MRSF	13.982547			1.97	-1.48	1.43	-0.48	0.54
MT 1857	-6.73	MRSF	13.980727			2.00	-1.36	1.38	-0.54	0.62
MT 1858	-6.64	MRSF	13.978604			2.08	-1.32	1.30	-0.34	0.78
MT 1859	-6.50	MRSF	13.975268			1.99	-1.67	1.33	-0.31	0.66
MT 1860	-6.39	MRSF	13.972841			1.96	-1.55	1.31	-0.37	0.64
MT 1861	-6.29	MRSF	13.970415			1.85	-1.73	1.23	-0.26	0.63
MT 1862	-6.21	MRSF	13.968595			1.93	-1.60	1.35	-0.29	0.58
MT 1863	-6.10	MRSF	13.965866			2.09	-1.74	1.30	-0.08	0.79
MT 1864	-5.99	MRSF	13.963439			2.02	-1.66	1.31	-0.30	0.71
MT 1865	-5.89	MRSF	13.961013			2.04	-1.59	1.28	-0.26	0.76
MT 1866	-5.80	MRSF	13.95889			1.93	-1.44	1.17	-0.21	0.76
MT 1867	-5.69	MRSF	13.956463			1.91	-1.42	1.23	-0.22	0.67
MT 1868	-5.60	MRSF	13.95434			2.04	-1.60	0.98	-0.14	1.06
MT 1869	-5.50	MRSF	13.951914			2.05	-1.60	1.21	-0.17	0.84
MT 1870	-5.40	MRSF	13.949487			1.94	-1.34	1.21	-0.44	0.73
MT 1871	-5.31	MRSF	13.947364			1.72	-1.43	1.24	-0.20	0.48
MT 1872	-5.20	MRSF	13.944938			1.95	-1.49	1.35	0.04	0.60

MT 1873	-5.11	MRSF	13.942815			1.89	-1.48	1.34	-0.26	0.55
MT 1874	-5.02	MRSF	13.940692			2.00	-1.64	1.29	-0.34	0.71
MT 1875	-4.92	MRSF	13.938265			1.81	-1.52	1.28	-0.28	0.53
MT 1876	-4.83	MRSF	13.936142			1.61	-1.50	1.44	-0.30	0.17
MT 1877	-4.74	MRSF	13.934019			1.75	-1.40	1.06	-0.42	0.69
MT 1878	-4.62	MRSF	13.931289			1.97	-1.41	1.48	-0.39	0.48
MT 1879	-4.54	MRSF	13.92935			1.84	-1.32	1.32	-0.36	0.52
MT 1880	-4.50	MRSF	13.928354			1.88	-1.28	1.33	-0.21	0.55
MT 1881	-4.38	MRSF	13.925699			1.96	-1.44	1.65	-0.26	0.31
MT 1882	-4.24	MRSF	13.92238			2.04	-1.42	1.41	-0.35	0.63
MT 1883	-4.11	MRSF	13.919393			2.11	-1.48	1.58	-0.23	0.53
MT 1884	-3.99	MRSF	13.916406			1.95	-1.74	1.14	-0.51	0.81
MT 1885	-3.83	MRSF	13.912756			2.05	-1.52	1.34	-0.19	0.71
MT 1886	-3.72	MRSF	13.910189			2.02	-1.53	1.19	-0.31	0.84
MT 1887	-3.60	MRSF	13.907238			1.91	-1.41	1.06	-0.59	0.85
MT 1888	-3.48	MRSF	13.904656			1.84	-1.34	1.30	-0.59	0.54
MT 1889	-3.40	MRSF	13.903205			1.83	-1.66	1.10	-0.24	0.73
MT 1890	-3.34	MRSF	13.902168			1.91	-1.52	1.23	-0.28	0.67
MT 1891	-3.28	MRSF	13.900924			1.96	-1.73	1.21	-0.25	0.76
MT 1892	-3.21	MRSF	13.899679			2.03	-1.47	1.34	-0.12	0.69
MT 1893	-3.15	MRSF	13.898643			1.97	-1.67	1.29	-0.42	0.67
MT 1894	-3.08	MRSF	13.897398			1.92	-1.44	1.13	-0.10	0.79
MT 1895	-3.02	MRSF	13.896362			1.89	-1.42	1.17	-0.06	0.72
MT 1896	-2.91	MRSF	13.894288			2.01	-1.62	1.33	-0.38	0.68
MT 1897	-2.83	MRSF	13.892837			1.92	-1.50	1.18	-0.29	0.74
MT 1898	-2.74	MRSF	13.891178			1.84	-1.55	1.14	-0.24	0.70
MT 1899	-2.67	MRSF	13.889933			1.81	-1.65	1.25	-0.36	0.56
MT 1900	-2.61	MRSF	13.888689			1.78	-1.49	0.93		0.85
MT 1951	-2.60	MRSF	13.888897			1.78	-1.37	1.22	-0.39	0.56
MT 1952	-2.49	MRSF	13.886616			1.86	-1.34	1.22		0.64

MT 1953	-2.37	MRSF	13.884542			1.78	-1.41	0.93	-0.24	0.86
MT 1954	-2.28	MRSF	13.882883			1.68	-1.49	0.74	-0.26	0.94
MT 1955	-2.18	MRSF	13.881017			1.47	-1.31	1.07	-0.22	0.40
MT 1955A	-2.05	MRSF	13.878661			1.46	-1.37	0.90	-0.38	0.56
MT 1956	-1.94	MRSF	13.876794			1.60	-1.40	1.03	-0.52	0.58
MT 1957	-1.82	MRSF	13.874463			1.65	-1.54	1.05	-0.39	0.60
MT 1958	-1.70	MRSF	13.872367			1.80	-1.54	0.97	-0.25	0.83
MT 1959	-1.56	MRSF	13.869806			1.65	-1.57	0.99	-0.29	0.66
MT 1960	-1.47	MRSF	13.868176			1.76	-1.60	1.06	-0.20	0.70
MT 1961	-1.33	MRSF	13.865614			1.69	-1.52	1.13	-0.27	0.56
MT 1962	-1.18	MRSF	13.863052			1.46	-1.27	1.16	-0.24	0.30
MT 1962A	-1.08	MRSF	13.861189			1.52	-1.32	0.82	-0.11	0.69
MT 1963	-0.98	MRSF	13.859326			1.46	-1.56	0.71	-0.18	0.74
MT 1964	-0.95	MRSF	13.858861			1.59	-1.34	0.91	-0.26	0.68
MT 1964A	-0.85	MRSF	13.856938			1.80	-1.35	1.24	-0.28	0.55
MT 1965	-0.72	MRSF	13.854678			1.92	-1.34	1.18	0.00	0.73
MT 1965A	-0.60	MRSF	13.852419			1.95	-1.76	1.07	-0.06	0.89
MT 1966	-0.47	MRSF	13.850159			2.02	-1.53	1.32	-0.13	0.69
MT 1966A	-0.35	MRSF	13.847899			1.84	-1.45	1.03	-0.07	0.80
MT 1967	-0.22	MRSF	13.845639			2.12	-1.13	1.23	0.07	0.89
MT 1968	-0.02	MRSF	13.842088			2.13	-1.41	1.22	0.09	0.91
MT 1969	0.18	MRSF	13.837514			2.24	-1.35	1.20	0.06	1.03
MT 1970	0.30	MRSF	13.834852			2.23	-1.45	1.37	0.04	0.86
MT 1971	0.44	MRSF	13.831809			2.44	-1.51	1.27	0.10	1.17
MT 1972	0.61	MRSF	13.828006			1.96	-1.63	1.57	0.06	0.39
MT 1973	0.78	MRSF	13.824203			2.36	-1.44	1.34	0.01	1.02
MT 1974	0.95	MRSF	13.8204			2.00	-1.38	1.32	0.07	0.68

MT 1975	1.12	MRSF	13.816597			2.13	-1.38	1.14	0.10	0.99
MT 1976	1.29	MRSF	13.812793			2.11	-1.48	1.35	-0.02	0.76
MT 1976A	1.45	MRSF	13.809371			2.16	-1.39	1.06	0.04	1.10
MT 1977	1.60	MRSF	13.805948			2.26	-1.49	1.13	-0.02	1.13
MT 1978	1.77	MRSF	13.802145			2.55	-1.32	1.32	0.11	1.23
MT 1979	1.84	MRSF	13.800678			2.58	-1.27	1.32	0.13	1.26
MT 1980	1.91	MRSF	13.798918			2.63	-1.33	1.30	0.14	1.34
MT 1981	2.00	MRSF	13.797012			2.69	-1.43	1.32	0.12	1.37
MT 1982	2.07	MRSF	13.795546			2.82	-1.67	1.47	0.18	1.34
MT 1983	2.13	MRSF	13.794079			2.79	-1.67	1.27	0.11	1.52
MT 1984	2.20	MRSF	13.792613			2.72	-1.61	1.47	0.11	1.24
MT 1985	2.29	MRSF	13.790652			2.90	-1.80	1.42	0.12	1.49
MT 1986	2.45	MRSF	13.78701			2.80	-1.61	1.56	0.12	1.23
MT 1987	2.61	MRSF	13.783367			2.91	-2.03	1.43	0.06	1.48
MT 1988	2.78	MRSF	13.779724			2.80	-2.07	1.52	0.03	1.28
MT 1989	2.94	MRSF	13.776081			2.89	-2.29	1.32	0.10	1.56
MT 1990	2.97	MRSF	13.77542			2.37	-1.46	1.13	0.06	1.24
MT 1560	-5.24	RIP	13.945803	0.429	-0.596	1.71	-1.34	0.83	-0.36	0.87
MT 1561	-5.15	RIP	13.943693	0.45	-0.547	1.72	-1.41	0.83	-0.36	0.88
MT 1562	-5.05	RIP	13.941348	0.541	-0.56	1.74	-1.34	0.96	-0.28	0.78
MT 1563	-4.96	RIP	13.939237	0.617	-0.456	1.80	-1.54	1.12	-0.24	0.68
MT 1564	-4.86	RIP	13.936892	0.627	-0.646	1.82	-1.34	1.04	-0.37	0.78
MT 1565	-4.75	RIP	13.934313	0.512	-0.7	1.66	-1.61	1.33	-0.40	0.33
MT 1566	-4.62	RIP	13.931264	0.532	-0.553	1.72	-1.38	1.33	-0.40	0.39
MT 1567	-4.54	RIP	13.929388	0.566	-0.443	1.90	-1.32	1.11	-0.24	0.79
MT 1568	-4.43	RIP	13.926809	0.648	-0.488	2.07	-1.40	1.22	0.02	0.85
MT 1569	-4.34	RIP	13.924698	0.637	-0.521	2.08	-1.38	1.22	0.02	0.86
MT 1570	-4.24	RIP	13.922353	0.701	-0.471	1.92	-1.32	1.18	-0.29	0.75
MT 1571	-4.22	RIP	13.921884	0.663	-0.649	2.04	-1.44	1.29	-0.36	0.75

MT 1572	-4.10	RIP	13.91907	0.714	-0.504	1.94	-1.31	1.44	-0.37	0.50
MT 1573	-4.03	RIP	13.917429	0.612	-0.729	2.06	-1.42	1.28	-0.39	0.78
MT 1574	-4.01	RIP	13.91696	0.73	-0.538			1.42	-0.31	
MT 1575	-3.93	RIP	13.915084	0.797	-0.777	2.12	-1.34	1.41	-0.34	0.72
MT 1576	-3.84	RIP	13.912973	0.772	-0.574	1.96	-1.27	1.23	-0.46	0.73
MT 1577	-3.76	RIP	13.911097	0.705	-0.685	2.13	-1.42	1.36	-0.30	0.77
MT 1578	-3.68	RIP	13.909221	0.653	-0.707	2.11	-1.36	1.11	-0.32	1.00
MT 1579	-3.60	RIP	13.907345	0.728	-0.675	1.99	-1.33	1.26	-0.31	0.73
MT 1580	-3.52	RIP	13.905469	0.694	-0.557	2.06	-1.48	1.14	-0.33	0.93
MT 1581	-3.43	RIP	13.903731	0.694	-0.664	2.18	-1.52	0.87	-0.63	1.31
MT 1582	-3.33	RIP	13.901919	0.655	-0.582	1.93	-1.48	1.05	-0.33	0.88
MT 1583	-3.25	RIP	13.900469	0.629	-0.686	1.90	-1.53			1.90
MT 1584	-3.13	RIP	13.898294	0.717	-0.598	1.89	-1.44	1.22	-0.23	0.68
MT 1585	-3.06	RIP	13.897025	0.687	-0.615	1.95	-1.25	1.08	-0.26	0.86
MT 1586	-2.98	RIP	13.895575	0.628	-0.488	1.81	-1.24	1.17	-0.19	0.64
MT 1587	-2.90	RIP	13.894125	0.576	-0.54	2.06	-1.38	1.39	-0.48	0.67
MT 1588	-2.82	RIP	13.892675	0.589	-0.633	1.82	-1.45	1.25	-0.40	0.57
MT 1589	-2.74	RIP	13.891225	0.586	-0.536	1.95	-1.43	1.08	-0.47	0.87
MT 1590	-2.65	RIP	13.889594	0.499	-0.518			1.09	-0.36	
MT 1591	-2.55	RIP	13.887781	0.499	-0.383	1.65	-1.39	1.15	-0.43	0.50
MT 1592	-2.45	RIP	13.885969	0.503	-0.37	1.86	-1.37	1.15	-0.38	0.71
MT 1593	-2.37	RIP	13.884519	0.467	-0.443	1.88	-1.30	0.94	-0.38	0.95
MT 1594	-2.28	RIP	13.882888	0.464	-0.29	1.93	-1.60	1.11	-0.35	0.82
MT 1595	-2.19	RIP	13.881256	0.38	-0.378	1.71	-1.38	0.97	-0.41	0.74
MT 1596	-2.13	RIP	13.880169	0.354	-0.675	1.60	-1.38	0.79	-0.33	0.80
MT 1597	-2.06	RIP	13.8789	0.37	-0.553	1.60	-1.63	1.00	-0.50	0.60
MT 1598	-1.99	RIP	13.877631	0.394	-0.742	1.50	-1.70	0.86	-0.48	0.64
MT 1599	-1.89	RIP	13.875819	0.508	-0.536	1.86	-1.66	1.10	-0.34	0.76
MT 1600	-1.79	RIP	13.874011	0.353	-0.734	1.88	-1.54	1.03	-0.34	0.86
MT 1601	-1.72	RIP	13.872745	0.404	-0.553	1.71	-1.33	0.83	-0.49	0.87

MT 1602	-1.63	RIP	13.871117	0.259	-0.585	1.82	-1.62	0.79	-0.48	1.03
MT 1603	-1.55	RIP	13.86967	0.295	-0.8	1.76	-1.67	0.99	-0.35	0.77
MT 1604	-1.45	RIP	13.867862	0.305	-0.597	1.99	-1.62	0.94	-0.25	1.04
MT 1605	-1.36	RIP	13.866234	0.533	-0.653	1.82	-1.47	1.10	-0.27	0.71
MT 1606	-1.28	RIP	13.864787	0.499	-0.648	1.93	-1.54	1.10	-0.35	0.83
MT 1607	-1.18	RIP	13.862979	0.535	-0.515	1.94	-1.67	1.07	-0.46	0.87
MT 1608	-1.11	RIP	13.861713	0.435	-0.498	1.97	-1.76	1.09	-0.35	0.88
MT 1609	-0.99	RIP	13.859543	0.608	-0.739	1.90	-1.58	1.19	-0.23	0.71
MT 1610	-0.89	RIP	13.857734	0.533	-0.385	1.95	-1.54	1.00	-0.08	0.95
MT 1611	-0.83	RIP	13.856649	0.264	-0.38	1.86	-1.53	0.90	-0.28	0.96
MT 1612	-0.75	RIP	13.855202	0.203	-0.427	1.56	-1.39	0.89	-0.25	0.67
MT 1613	-0.67	RIP	13.853755	0.087	-0.488	1.48	-1.74	0.87	-0.46	0.61
MT 1614	-0.59	RIP	13.852309	0.2	-0.584	1.76	-1.67	0.96	-0.07	0.80
MT 1615	-0.50	RIP	13.850681	0.3	-0.495	1.81	-1.62	1.07	-0.16	0.74
MT 1616	-0.42	RIP	13.849234	0.379	-0.501	1.86	-1.75	1.17	-0.22	0.69
MT 1617	-0.31	RIP	13.847245	0.419	-0.519	2.02	-1.74	0.99	-0.13	1.03
MT 1618	-0.22	RIP	13.845617	0.425	-0.562	1.92	-1.61	1.06	-0.27	0.86
MT 1619	-0.16	RIP	13.844532	0.496	-0.605	2.08	-1.63	1.17	-0.12	0.91
MT 1620	-0.10	RIP	13.843447	0.431	-0.768	2.07	-1.62	1.25	-0.13	0.82
MT 1621	-0.07	RIP	13.842904	0.697	-0.569	2.27	-1.63	1.23	-0.03	1.04
MT 1622	0.00	RIP	13.841555	0.56	-0.6			1.24	-0.14	
MT 1623	0.08	RIP	13.839773	0.483	-0.414	1.92	-1.49	1.32	-0.13	0.60
MT 1624	0.15	RIP	13.838215	0.388	-0.287			1.52	-0.04	
MT 1625	0.26	RIP	13.835766	0.369	-0.46			1.39	-0.08	
MT 1626	0.37	RIP	13.833316	0.484	-0.422	2.28	-1.46	1.29	-0.12	0.99
MT 1627	0.54	RIP	13.829531	0.462	-0.366	2.32	-1.45	1.26	-0.03	1.05
MT 1628	0.67	RIP	13.826637	0.498	-0.325	2.21	-1.43	1.31	0.01	0.90
MT 1629	0.79	RIP	13.823965	0.516	-0.375			1.45	0.08	
MT 1630	0.90	RIP	13.821516	0.443	-0.247	2.31	-1.45	1.51	0.12	0.80
MT 1631	0.94	RIP	13.820625	0.428	-0.242	2.33	-1.56	1.32	0.10	1.00

MT 1632	1.00	RIP	13.819289	0.472	-0.31	2.28	-1.40	1.55	0.02	0.73
MT 1633	1.08	RIP	13.817508	0.629	-0.278	2.57	-1.66	1.33	-0.02	1.24
MT 1634	1.15	RIP	13.815949	0.691	-0.441	2.37	-1.52	1.47	0.03	0.90
MT 1635	1.25	RIP	13.813723	0.367	-0.57	2.19	-1.53	1.10	0.04	1.09
MT 1636	1.42	RIP	13.809938	0.381	-0.436	2.37	-1.30	1.26	0.00	1.11
MT 1637	1.50	RIP	13.808156	0.387	-0.353	2.20	-1.27	1.28	-0.07	0.93
MT 1639	1.62	RIP	13.805484	0.623	-0.365	2.47	-1.26	1.38	0.09	1.09
MT 1638	1.77	RIP	13.802145	0.75	-0.176	2.46	-1.28	1.38	0.06	1.08
MT 1101	1.82	RIP	13.801031	1.106	0.106	2.78	-1.44	1.43	0.25	1.34
MT 1102	1.88	RIP	13.799695	1.134	-0.158	2.75	-1.40	1.49	0.11	1.26
MT 1103	2.02	RIP	13.796578	1.168	0.151	2.92	-1.35	1.48	0.11	1.45
MT 1104	2.12	RIP	13.794352	1.24	0.204	2.82	-1.33	1.30	0.21	1.52
MT 1105	2.19	RIP	13.792793	1.155	-0.035	2.94	-1.61	1.61	0.37	1.33
MT 1106	2.31	RIP	13.790121	1.158	0.181	3.18	-1.61	1.54	0.27	1.63
MT 1107	2.46	RIP	13.786781	1.148	-0.304	3.04	-1.61	1.48	0.24	1.57
MT 1108	2.55	RIP	13.784777	1.177	-0.314	2.88	-1.93	1.50	0.25	1.38
MT 1109	2.67	RIP	13.782105	1.167	-0.237	2.83	-1.84	1.46	0.33	1.37
MT 1110	2.72	RIP	13.780992	1.325	-0.284	2.93	-2.41	1.40	0.25	1.53
MT 1111	2.77	RIP	13.779879	1.686	-0.073	2.87	-1.90	1.46	0.21	1.41
MT 1112	2.85	RIP	13.778098	1.758	-0.065	2.73	-2.35	1.36	0.22	1.37
MT 1113	2.96	RIP	13.775648	1.939	0.276	2.95	-2.01	1.38	0.20	1.56
MT 1114	3.02	RIP	13.774313	1.678	0.301	2.22	-0.99	1.25	0.31	0.96
MT 1115	3.07	RIP	13.773199	1.537	0.294			1.25	0.12	
MT 1116	3.18	RIP	13.77075	1.529	0.395	3.01	-1.64	1.38	0.44	1.62
MT 1117	3.33	RIP	13.76741	1.568	0.26			1.31	0.40	
MT 1118	3.38	RIP	13.766297	1.371	0.052	2.70	-1.30	1.45	0.30	1.25
MT 1119	3.46	RIP	13.764516	1.431	0.206	2.97	-1.24	1.42	0.39	1.55
MT 1120	3.53	RIP	13.762957	1.516	0.193	2.93	-1.30	1.38	0.43	1.55
MT 1121	3.61	RIP	13.761176	1.33	0.134	2.83	-1.29	1.41	0.16	1.43

MT 1122	3.71	RIP	13.758949	1.213	0.048	2.81	-1.17	1.32	0.45	1.49
MT 1123	3.75	RIP	13.758059	1.096	-0.145	2.79	-0.97	1.34	0.53	1.45
MT 1124	3.88	RIP	13.755164	0.801	-0.098	2.61	-0.85	1.18	0.20	1.43
MT 1125	3.96	RIP	13.753383	0.791	-0.221	2.78	-1.40	1.25	0.18	1.53
MT 1126	4.01	RIP	13.75227	0.742	-0.298	2.35	-1.39	1.30	0.23	1.05
MT 1127	4.06	RIP	13.751156	0.941	-0.158	2.81	-1.35	1.40	0.26	1.41
MT 1128	4.20	RIP	13.748039	0.938	-0.087	2.58	-1.08	1.24	0.28	1.34
MT 1129	4.33	RIP	13.745145	0.972	-0.206	2.56	-1.87	1.38	0.25	1.18
MT 1130	4.38	RIP	13.744031	1.443	-0.303	2.61	-1.43	1.29	0.27	1.31
MT 1131	4.52	RIP	13.740914	1.464	-0.24	2.48	-1.23	1.30	0.19	1.17
MT 1132	4.68	RIP	13.737352	1.186	-0.027	2.59	-1.37	1.37	0.31	1.22
MT 1133	4.81	RIP	13.734457	0.867	0.113	2.61	-1.15	1.49	0.10	1.13
MT 1134	4.91	RIP	13.73223	0.975	-0.103	2.62	-1.58	1.38	0.17	1.23
MT 1135	4.99	RIP	13.730449	1.003	-0.303	2.74	-2.12	1.43	0.09	1.31
MT 1136	5.05	RIP	13.729113	0.99	-0.192	2.51	-1.83	1.40	-0.07	1.11
MT 1137	5.20	RIP	13.725778	1.014	-0.379	2.41	-1.75	1.34	0.13	1.07
MT 1138	5.28	RIP	13.724	1.298	-0.136	2.42	-1.50	1.33	0.13	1.09
MT 1139	5.34	RIP	13.722667	1.285	0.021	2.53	-1.45	1.25	0.23	1.28
MT 1140	5.45	RIP	13.720222	1.064	0.067	2.59	-1.29	1.22	0.29	1.37
MT 1141	5.54	RIP	13.718222	1.002	-0.109	2.96	-1.73	1.07	0.32	1.89
MT 1142	5.64	RIP	13.716	1.149	-0.057	2.69	-1.66	1.26	0.21	1.44
MT 1143	5.77	RIP	13.713111	1.164	-0.059	2.56	-1.69	1.12	0.18	1.44
MT 1144	5.90	RIP	13.710222	1.282	-0.069	2.57	-1.76	1.24	0.21	1.33
MT 1145	5.91	RIP	13.71	1.429	-0.155	2.65	-1.43	1.30	0.24	1.36
MT 1146	6.01	RIP	13.707778	1.334	-0.25	2.82	-1.50	1.52	0.25	1.30
MT 1147	6.19	RIP	13.703778	1.226	-0.17	2.80	-1.39	1.49	0.33	1.31
MT 1148	6.30	RIP	13.701333	1.273	-0.251	2.59	-1.28	1.69	0.30	0.90
MT 1149	6.46	RIP	13.697778	1.453	-0.029	2.70	-1.70	1.52	0.27	1.18
MT 1150	6.55	RIP	13.695778	1.438	-0.11	2.65	-1.52	1.47	0.33	1.18
MT 1151	6.67	RIP	13.693111	1.775	0.145	2.69	-1.63	1.60	0.25	1.09

MT 1152	6.78	RIP	13.690667	1.723	0.119	2.65	-1.85	1.43	0.41	1.22
MT 1153	6.89	RIP	13.688222	1.93	0.325	2.67	-1.71	1.35	0.35	1.32
MT 1154	6.98	RIP	13.686222	1.897	0.389	2.30	-2.05	1.52	0.37	0.78
MT 1155	7.06	RIP	13.684444	1.901	0.147	2.34	-1.43	1.31	0.28	1.04
MT 1156	7.18	RIP	13.681778	1.575	0.174	2.53	-1.47	1.18	0.41	1.35
MT 1157	7.35	RIP	13.678	1.499	0.259	2.58	-1.71	1.26	0.29	1.32
MT 1158	7.42	RIP	13.676444	1.722	0.187	2.55	-1.41	1.57	0.30	0.99
MT 1159	7.54	RIP	13.673778	2.008	0.355	2.63	-1.52	1.43	0.40	1.20
MT 1160	7.70	RIP	13.670222	1.937	0.446	2.59	-1.01	1.38	0.55	1.21
MT 1161	7.84	RIP	13.667111	1.386	0.234	2.25	-1.21	1.18	0.28	1.07
MT 1162	7.91	RIP	13.665556	1.162	0.063	2.96	-1.20	0.90	0.36	2.07
MT 1163	8.02	RIP	13.663111	1.204	0.049	2.41	-1.38	1.01	0.25	1.40
MT 1164	8.08	RIP	13.661778	1.274	0.021	2.39	-1.39	0.97	0.40	1.42
MT 1165	8.22	RIP	13.658667	1.259	-0.04	2.02	-1.33	1.18	0.25	0.84
MT 1166	8.32	RIP	13.656444	1.087	-0.191	1.89	-1.44	1.04	0.21	0.86
MT 1167	8.45	RIP	13.653556	0.715	-0.302	1.99	-1.39	0.73	0.27	1.26
MT 1168	8.54	RIP	13.651556	0.869	-0.712	1.81	-1.48	1.26	0.24	0.55
MT 1169	8.65	RIP	13.649111	1.362	-0.375	2.31	-1.15	1.12	0.17	1.19
MT 1170	8.76	RIP	13.646667	0.872	-0.63	1.92	-1.19	1.08	0.17	0.83
MT 1171	8.87	RIP	13.644222	1.148	-0.065	2.91	-1.48	1.36	0.46	1.55
MT 1172	8.95	RIP	13.642444	1.116	-0.296	2.35	-1.06	1.01	0.59	1.34
MT 1173	9.09	RIP	13.639333	0.85	-0.079	2.52	-1.47	0.87	0.24	1.64
MT 1174	9.20	RIP	13.636889	0.898	-0.072	2.75	-1.92	1.06	0.36	1.70
MT 1175	9.24	RIP	13.636	1.035	0.046			0.48	0.28	
MT 1176	9.34	RIP	13.633778	0.77	-0.039	2.43	-2.13	0.84	0.24	1.59
MT 1177	9.48	RIP	13.630667	0.76	-0.475	1.92	-1.87	0.97	0.12	0.95
MT 1178	9.59	RIP	13.628222	0.955	-0.404	2.39	-1.84	1.07	0.15	1.32
MT 1179	9.74	RIP	13.624889	1.03	-0.178	2.70	-1.48	1.24	0.24	1.46
MT 1180	9.84	RIP	13.622667	0.594	-0.297	2.49	-1.43	0.91	0.43	1.57

MT 1180A	9.91	RIP	13.621111	0.366	-0.312	2.25	-1.45	0.98	0.11	1.27
MT 1181	10.03	RIP	13.618444	0.39	-0.338	2.57	-1.53	1.12	0.37	1.44
MT 1182	10.21	RIP	13.614444	0.721	-0.368	2.35	-1.58	0.94	0.24	1.40
MT 1183	10.34	RIP	13.611556	0.942	-0.359	2.34	-1.58	1.04	0.37	1.31
MT 1184	10.44	RIP	13.609333	0.943	-0.462	2.39	-1.96	1.14	0.22	1.25
MT 1185	10.56	RIP	13.606667	1.164	-0.423	2.39	-1.68	1.10	0.18	1.29
MT 1186	10.66	RIP	13.604444	1.078	-0.257	2.27	-1.52	1.30	0.65	0.97
MT 1187	10.70	RIP	13.603556	1.188	-0.362	2.35	-1.61	1.11	0.10	1.24
MT 1188	10.82	RIP	13.600889	1.149	-0.105	2.53	-1.73	1.08	0.15	1.45
MT 1189	10.91	RIP	13.598889	1.218	-0.096	2.55	-1.55	1.08	0.06	1.47
MT 1190	11.03	RIP	13.596222	1.071	-0.229	2.36	-1.40	1.07	0.16	1.29
MT 1191	11.15	RIP	13.593556	1.123	-0.322	2.56	-1.65	1.11	0.18	1.45
MT 1192	11.23	RIP	13.591778	1.254	-0.298	2.50	-2.01	1.11	0.22	1.38
MT 1193	11.33	RIP	13.589556	1.286	-0.339	2.66	-1.91	1.41	0.14	1.26
MT 1194	11.43	RIP	13.587333	1.215	-0.378	2.55	-1.72	1.15	0.14	1.39
MT 1195	11.52	RIP	13.585333	1.263	-0.165	2.87	-2.00	1.25	-0.13	1.62
MT 1196	11.61	RIP	13.583333	1.382	-0.299	2.64	-1.44	1.28	0.27	1.36
MT 1197	11.72	RIP	13.580889	1.379	-0.102	3.05	-1.64	1.31	0.24	1.74
MT 1198	11.85	RIP	13.578	1.178	-0.052	2.92	-1.83	1.20	0.17	1.71
MT 1199	11.95	RIP	13.575778	1.286	-0.002	2.77	-1.53	1.39	0.14	1.37
MT 1200	12.07	RIP	13.573111	1.015	-0.011	2.44	-1.50	1.24	0.14	1.20
MT 1201	12.12	RIP	13.572	1.179	-0.017	2.68	-1.36	1.38	0.18	1.30
MT 1202	12.22	RIP	13.569778	1.27	-0.634	2.34	-1.90	0.95	0.20	1.39
MT 1203	12.36	RIP	13.566667	1.299	-0.365	2.26	-1.99	1.08	-0.02	1.18
MT 1204	12.45	RIP	13.564667	0.955	-0.211	2.27	-1.56	0.94	0.33	1.33
MT 1205	12.58	RIP	13.561778	0.791	-0.243	2.26	-1.58	0.91	0.14	1.35
MT 1206	12.70	RIP	13.559111	0.214	-0.582	2.29	-1.86	0.64	0.06	1.64
MT 1207	12.81	RIP	13.556667	0.151	-0.648	2.78	-1.99			2.78
MT 1208	12.87	RIP	13.555333	0.257	-0.58			0.46	-0.03	

MT 1209	12.91	RIP	13.554444	0.583	-0.394	2.07	-1.73	0.90	0.08	1.17
MT 1210	13.02	RIP	13.552	0.745	-0.382	2.28	-2.04	0.62	0.05	1.66
MT 1211	13.10	RIP	13.550222	0.68	-0.694	1.63	-1.36	0.91	0.13	0.72
MT 1212	13.19	RIP	13.548222	0.688	-0.686	2.00	-1.93	0.91	0.20	1.10
MT 1213	13.26	RIP	13.546667	0.848	-0.675	1.74	-1.68	0.51	0.09	1.23
MT 1214	13.33	RIP	13.545111	0.65	-0.492	1.70	-2.03	1.13	0.43	0.57
MT 1215	13.43	RIP	13.542889	0.553	-0.491	2.29	-1.08	1.01	0.33	1.28
MT 1216	13.53	RIP	13.540667	0.691	-0.64	2.78	-1.93	0.73	0.05	2.05
MT 1217	13.65	RIP	13.538	0.743	-0.637	1.85	-1.70	0.81	-0.40	1.03
MT 1218	13.77	RIP	13.535333	0.632	-0.599	1.94	-1.75	0.61	0.06	1.32
MT 1219	13.88	RIP	13.532889	0.904	-0.226	2.18	-1.72	0.75	-0.18	1.43
MT 1220	14.01	RIP	13.53	0.708	-0.231	2.08	-1.47	0.98	-0.21	1.09
MT 1221	14.08	RIP	13.528444	0.61	-0.234	2.53	-2.12	1.05	-0.34	1.48
MT 1222	14.24	RIP	13.523394	0.545	-0.131	2.55	-2.04	0.83	-0.03	1.72
MT 1223	14.32	RIP	13.520761	0.661	-0.251	2.32	-1.85	0.88	-0.02	1.44
MT 1224	14.35	RIP	13.519774	0.644	-0.33	1.97	-1.54	1.04	-0.13	0.93
MT 1225	14.51	RIP	13.51451	0.469	-0.243	1.99	-1.59	0.56	0.12	1.43
MT 1226	14.61	RIP	13.511219	0.489	-0.168	1.86	-1.90	0.78	0.13	1.08
MT 1227	14.70	RIP	13.508258	0.586	-0.433	1.95	-1.48	0.44	0.15	1.50
MT 1228	14.72	RIP	13.5076			1.70	-0.87			1.70
MT 1228A	14.79	RIP	13.505297	0.573	-0.186	1.60	-1.01	0.62	0.38	0.99
MT 1229	14.84	RIP	13.503652	0.577	-0.188	2.02	-1.09	0.54	0.29	1.48
MT 1230	14.93	RIP	13.50069	0.439	-0.287	2.12	-1.17	0.78	0.31	1.34
MT 1231	15.05	RIP	13.496742	0.524	-0.266	2.28	-1.19	1.01	0.15	1.27
MT 1232	15.18	RIP	13.492465	0.523	-0.276	2.42	-1.52	1.00	0.14	1.41
MT 1233	15.30	RIP	13.488516	0.634	-0.311	2.58	-1.47	0.92	0.18	1.66
MT 1234	15.36	RIP	13.486542	0.652	-0.341	2.52	-1.48	0.99	0.26	1.53
MT 1235	15.35	RIP	13.486871	0.647	-0.31	2.54	-1.60	0.99	0.16	1.55
MT 1236	15.45	RIP	13.483581	0.709	-0.296	2.51	-1.72	1.03	0.20	1.48

MT 1237	15.52	RIP	13.481277	0.814	-0.184	2.39	-1.47	0.93	0.28	1.46
MT 1238	15.59	RIP	13.478974	0.942	0.053	2.47	-1.48	0.96	0.25	1.52
MT 1239	15.67	RIP	13.476342	1.163	0.039	2.39	-1.16	0.95	0.41	1.43
MT 1240	15.79	RIP	13.472394	1.21	-0.251	2.48	-1.48	1.12	0.11	1.36
MT 1241	15.87	RIP	13.469761	1.217	-0.252	2.77	-1.39	1.03	0.24	1.74
MT 1242	15.95	RIP	13.467129	1.328	-0.194	2.47	-1.20	1.25	0.01	1.22
MT 1243	16.04	RIP	13.464168	1.294	-0.308	2.53	-1.40	1.04	0.24	1.50
MT 1244	16.13	RIP	13.461206	1.337	0.017	2.46	-1.15	1.11	0.17	1.35
MT 1245	16.20	RIP	13.458903	1.292	0.025	2.36	-1.02	0.97	0.34	1.39
MT 1246	16.27	RIP	13.4566	1.232	-0.003	2.60	-1.23	1.05	0.34	1.56
MT 1247	16.37	RIP	13.45331	1.352	0.033	2.58	-1.26	1.11	0.43	1.47
MT 1248	16.48	RIP	13.44969	1.295	0.1	2.31	-1.36	1.09	0.42	1.22
MT 1249	16.53	RIP	13.448045	1.418	-0.042	1.71	-2.14	1.02	0.30	0.69
MT 1250	16.65	RIP	13.444097	1.494	-0.052	2.17	-2.05	1.30	0.13	0.87
MT 1251	16.72	RIP	13.441794	1.362	-0.138	2.32	-1.45	0.78	0.28	1.54
MT 1252	16.83	RIP	13.438174	1.343	-0.106	2.47	-1.98	0.73	0.17	1.74
MT 1253	16.94	RIP	13.434555	0.866	-0.037			0.67	0.19	
MT 1254	17.01	RIP	13.432252	0.825	-0.069	2.22	-1.66	0.69	0.12	1.53
MT 1255	17.12	RIP	13.428632	0.705	-0.237	2.08	-1.58	0.25	0.04	1.83
MT 1256	17.18	RIP	13.426658	0.737	-0.091	1.71	-1.39	0.56	-0.06	1.15
MT 1257	17.32	RIP	13.422854	0.912	-0.011	1.47	-1.46	0.47	0.04	1.01
MT 1258	17.41	RIP	13.420495	0.869	-0.043	2.12	-1.52	0.48	0.09	1.64
MT 1259	17.48	RIP	13.41866	0.918	0.065	2.10	-1.55	0.60	0.06	1.50
MT 1260	17.58	RIP	13.416039	1.172	0.255	2.25	-1.44	0.65	0.10	1.61
MT 1261	17.65	RIP	13.414204	1.149	0.388	2.09	-1.12	0.99	0.04	1.10
MT 1262	17.72	RIP	13.412369	1.349	0.329	2.23	-1.18	0.96	0.16	1.28
MT 1263	17.79	RIP	13.410534	1.146	0.409	2.27	-1.36	1.09	0.18	1.18
MT 1264	17.90	RIP	13.40765	1.187	0.44	2.25	-1.41	1.01	0.10	1.24
MT 1265	17.97	RIP	13.405816	0.779	-0.09	1.72	-1.63	0.63	0.16	1.09
MT 1266	18.09	RIP	13.40267	0.918	-0.064	1.87	-1.65	0.62	0.13	1.25

MT 1267	18.17	RIP	13.400573	1.117	0.085	2.16	-1.76	0.67	0.22	1.49
MT 1268	18.25	RIP	13.398476	1.135	0.269	2.18	-1.45	0.88	0.28	1.30
MT 1269	18.32	RIP	13.396641	0.93	0.421	2.39	-1.63	0.78	0.47	1.60
MT 1270	18.45	RIP	13.393233	0.977	0.34	2.26	-1.49	0.67	0.28	1.59
MT 1271	18.55	RIP	13.390612	0.889	0.167	2.06	-1.57	0.66	0.21	1.40
MT 1272	18.65	RIP	13.38799	0.81	0.19	2.22	-1.63			2.22
MT 1273	18.70	RIP	13.38668	0.768	0.256	2.05	-1.48	0.66	0.24	1.39
MT 1274	18.80	RIP	13.384058	0.809	0.163	1.92	-1.51			1.92
MT 1275	18.89	RIP	13.381699	0.799	0.362	2.00	-1.73			2.00
MT 1276	18.94	RIP	13.380388	0.805	0.211	1.95	-1.64	0.79	0.17	1.16
MT 1277	19.06	RIP	13.377243	0.785	0.15	1.80	-1.71			1.80
MT 1278	19.14	RIP	13.375146	1.066	0.265	1.96	-1.57	0.70	0.17	1.26
MT 1279	19.23	RIP	13.372786	0.78	0.434	2.34	-1.87	0.79	0.22	1.55
MT 1280	19.36	RIP	13.369379	1.037	0.394	2.33	-1.57			2.33
MT 1281	19.45	RIP	13.367019	0.875	0.326	2.21	-1.55	0.96	0.10	1.24
MT 1282	19.54	RIP	13.36466	0.82	0.303	2.19	-1.56	0.87	0.60	1.32
MT 1283	19.63	RIP	13.362301	0.59	-0.304	1.70	-1.28	0.98	0.25	0.72
MT 1284	19.71	RIP	13.360204	0.535	-0.272	1.77	-1.51	0.61	0.04	1.16
MT 1285	19.78	RIP	13.358369	0.587	-0.052	1.38	-1.29	0.44	0.17	0.95
MT 1286	19.88	RIP	13.355748	0.715	0.065	1.86	-1.62	0.79	0.18	1.08
MT 1287	19.94	RIP	13.354175	0.711	0.104	2.28	-1.97	0.94	0.15	1.34
MT 1288	20.10	RIP	13.349981	0.827	0.052	2.25	-1.75	0.66	0.27	1.59
MT 1289	20.23	RIP	13.346573	0.642	0.064	1.99	-1.61	0.62	0.25	1.37
MT 1290	20.33	RIP	13.343951	0.611	0.197	1.87	-1.50	0.72	0.16	1.15
MT 1291	20.48	RIP	13.340019	0.669	0.082	1.81	-1.75	0.87	0.19	0.95
MT 1292	20.58	RIP	13.337398	0.665	0.192	1.68	-1.46	0.67	0.28	1.01
MT 1293	20.68	RIP	13.334777	0.701	0.226	1.70	-1.50	0.59	0.18	1.11
MT 1294	20.76	RIP	13.33268	0.817	0.331	1.72	-1.45	0.48	0.25	1.24
MT 1295	20.83	RIP	13.330845	0.867	0.303	1.65	-1.48	0.76	0.20	0.89
MT 1296	20.92	RIP	13.328485	0.801	0.316	1.51	-1.14	0.57	0.29	0.94

MT 1297	21.00	RIP	13.326388	0.796	0.304	1.59	-1.22	0.58	0.27	1.01
MT 1298	21.11	RIP	13.323505	0.813	0.173	1.82	-1.13	0.81	0.27	1.02
MT 1299	21.19	RIP	13.321408	0.782	0.179	1.82	-1.32	0.79	0.26	1.03
MT 1300	21.31	RIP	13.318262	0.766	0.158	2.10	-1.39	0.84	0.29	1.27
MT 1301	21.43	RIP	13.315117	0.641	0.252	2.05	-1.39	0.89	0.33	1.16
MT 1302	21.54	RIP	13.312233	0.689	0.25	2.19	-1.36	0.86	0.33	1.33
MT 1303	21.64	RIP	13.309612	0.555	0.307	2.19	-1.43	0.86	0.36	1.33
MT 1304	21.74	RIP	13.30699	0.667	0.244	2.17	-1.39	0.80	0.36	1.37
MT 1305	21.86	RIP	13.303845	0.78	0.288	2.45	-1.50	0.83	0.41	1.62
MT 1306	21.88	RIP	13.30332	0.917	0.222	2.34	-1.32	0.76	0.32	1.58
MT 1307	21.91	RIP	13.302534	0.802	0.318	2.47	-1.64	0.82	0.37	1.65
MT 1308	22.01	RIP	13.299913	0.834	0.463	2.35	-1.59	0.82	0.35	1.53
MT 1309	22.12	RIP	13.297029	0.855	0.46	2.10	-1.70	0.89	0.34	1.21
MT 1310	22.25	RIP	13.293621	0.994	0.164	1.93	-1.67	0.75	0.21	1.18
MT 1311	22.33	RIP	13.291524	0.791	0.121	1.84	-1.52	0.68	0.24	1.16
MT 1312	22.43	RIP	13.288903	0.823	0.093	1.74	-1.29	0.62	0.18	1.11
MT 1313	22.55	RIP	13.285757	0.823	0.2	2.35	-1.62	1.06	0.11	1.29
MT 1314	22.67	RIP	13.282612	0.967	0.308	2.48	-1.54	1.09	0.16	1.39
MT 1315	22.76	RIP	13.280252	1.053	0.387	2.24	-1.19	0.99	0.19	1.25
MT 1316	22.90	RIP	13.276583	1.121	0.456	2.47	-1.53	1.09	0.20	1.38
MT 1317	23.01	RIP	13.273699	1.225	0.365	2.16	-1.39	1.00	0.24	1.16
MT 1318	23.10	RIP	13.27134	0.911	0.107	2.22	-1.23	1.02	0.16	1.19
MT 1319	23.18	RIP	13.269243	0.474	-0.216	1.63	-1.28	0.95	0.22	0.68
MT 1320	23.28	RIP	13.266621	0.542	-0.211	1.55	-1.25	0.87	0.05	0.68
MT 1321	23.40	RIP	13.263476	0.862	-0.18	1.83	-0.92	1.01	0.14	0.82
MT 1322	23.47	RIP	13.261641	0.661	-0.258	2.12	-1.47	0.79	0.16	1.33
MT 1323	23.58	RIP	13.258757	0.487	-0.345	2.06	-1.31			2.06
MT 1324	23.66	RIP	13.25666	0.398	-0.141	1.90	-1.66	0.85		1.05
MT 1325	23.76	RIP	13.254039	0.462	-0.125	1.92	-1.35	0.61	0.26	1.31
MT 1326	23.84	RIP	13.251942	0.606	-0.027	1.87	-1.41	0.92	0.12	0.95

MT 1327	23.90	RIP	13.250369	0.585	-0.046	1.87	-1.32	0.61	0.10	1.26
MT 1328	23.84	RIP	13.251942	0.554	-0.106	2.01	-1.57	0.79	0.11	1.21
MT 1329	23.93	RIP	13.249583	0.655	-0.466	1.56	-1.69			1.56
MT 1330	24.01	RIP	13.247485	0.171	-0.689	1.21	-1.59			1.21
MT 1331	24.10	RIP	13.245126	0.386	-0.453					0.00
MT 1332	24.25	RIP	13.241194	0.907	-0.219	1.96	-1.17	0.95	0.07	1.01
MT 1333	24.35	RIP	13.238573	0.892	0.128	1.91	-1.52	0.88	0.11	1.03
MT 1507	24.41	RIP	13.237	0.928	0.067	1.91	-1.61	0.88	-0.02	1.04
MT 1508	24.52	RIP	13.234117	0.729	0.129	1.95	-1.43	0.88	0.12	1.06
MT 1509	24.54	RIP	13.233592	0.681	-0.003	1.92	-1.27	0.98	0.07	0.94
MT 1510	24.65	RIP	13.230709	0.673	-0.053	2.09	-1.39	0.79	0.14	1.29
MT 1511	24.76	RIP	13.227825	0.648	0.072	2.17	-1.67	0.76	0.09	1.41
MT 1512	24.86	RIP	13.225204	0.529	0.069	2.18	-1.61	0.83	0.03	1.34
MT 1513	24.96	RIP	13.222583	0.458	-0.078	1.92	-1.55	0.75	0.08	1.17
MT 1514	25.06	RIP	13.219961	0.534	-0.182	1.63	-1.20			1.63
MT 1515	25.16	RIP	13.21734	0.478	-0.118	1.87	-1.08	0.70	0.18	1.17
MT 1516	25.28	RIP	13.214194	0.435	0.102	2.04	-1.34	0.96	0.24	1.08
MT 1517	25.38	RIP	13.211573	0.451	0.084	1.90	-1.44	0.78	0.21	1.11
MT 1518	25.46	RIP	13.209476	0.651	0.165	1.95	-1.30	0.65	0.30	1.29
MT 1519	25.53	RIP	13.207641	0.684	0.171	1.82	-1.12	0.79	0.26	1.03
MT 1520	25.63	RIP	13.205019	0.319	-0.065	1.83	-1.42	0.73	0.29	1.11
MT 1521	25.71	RIP	13.202922	0.462	-0.21	2.05	-1.70	0.76	0.14	1.29
MT 1522	25.82	RIP	13.200039	0.303	-0.313	1.50	-1.34	0.78	0.21	0.71
MT 1523	25.91	RIP	13.19768	0.439	-0.209	1.79	-1.44	0.59	-0.17	1.20
MT 1524	25.98	RIP	13.195845	0.414	-0.12	2.11	-1.73	0.86	0.17	1.25
MT 1525	26.08	RIP	13.193223	0.425	-0.197	2.05	-1.65	0.98	0.18	1.07
MT 1526	26.17	RIP	13.190864	0.44	-0.127	2.04	-1.51	1.06	0.15	0.98
MT 1527	26.27	RIP	13.188243	0.619	-0.189	2.01	-1.27	0.92	0.24	1.09
MT 1528	26.36	RIP	13.185883	0.469	-0.019	2.01	-1.40	0.81	0.28	1.20
MT 1529	26.45	RIP	13.183524	0.47	-0.107	2.14	-1.45	0.77	0.32	1.37

MT 1351	26.49	RIP	13.182457	0.687	0.076	2.03	-1.54	0.74	0.37	1.29
MT 1352	26.62	RIP	13.178926	0.635	0.03	2.01	-1.55	0.74	0.38	1.27
MT 1353	26.69	RIP	13.177025	0.857	-0.098	1.69	-1.11	0.88	0.36	0.82
MT 1354	26.74	RIP	13.175667	0.674	-0.125	1.90	-1.46	0.77	0.31	1.13
MT 1355	26.78	RIP	13.174581	0.775	-0.237	1.51	-1.41	0.62	0.32	0.89
MT 1356	26.88	RIP	13.171865	0.921	-0.232	1.73	-1.69	0.51	0.36	1.22
MT 1357	26.99	RIP	13.168878	0.982	-0.084	2.11	-1.91	0.76	0.33	1.34
MT 1358	27.09	RIP	13.166162	0.694	-0.18			0.98	0.36	
MT 1359	27.24	RIP	13.162088	0.637	0.076	2.31	-1.68	0.90	0.29	1.41
MT 1360	27.37	RIP	13.158558	0.578	0.092	2.32	-1.82	0.92	0.28	1.40
MT 1361	27.44	RIP	13.156656	0.403	0.116	2.03	-1.59	0.93	0.24	1.10
MT 1362	27.53	RIP	13.154212	0.482	-0.27	2.05	-1.70	1.00	0.18	1.04
MT 1363	27.61	RIP	13.15204	0.551	-0.419	1.91	-2.12	0.90	0.19	1.00
MT 1364	27.73	RIP	13.148781	0.4	-0.092	1.89	-1.87	0.70	0.24	1.18
MT 1365	27.79	RIP	13.147151	0.605	-0.095	1.93	-1.44	0.67	0.33	1.26
MT 1366	27.89	RIP	13.144435	0.318	0.145	1.91	-1.29			1.91
MT 1367	27.99	RIP	13.141719	0.268	0.067	1.79	-1.21	0.42	0.35	1.37
MT 1368	28.38	RIP	13.131128	0.071	-0.193	1.72	-1.87	0.42	0.33	1.30
MT 1368A	28.50	RIP	13.127869	0.171	-0.221	1.40	-1.67	0.35	0.26	1.06
MT 1369	28.66	RIP	13.123523	0.232	-0.478	1.17	-2.09	0.49	0.35	0.67
MT 1370	28.81	RIP	13.11945	0.056	-0.658	1.16	-2.03	0.09	0.29	1.07
MT 1371	28.93	RIP	13.116191	0.119	-0.508	1.01	-2.31			1.01
MT 1372	29.03	RIP	13.113475	0.154	-0.48	0.95	-1.89			0.95
MT 1373	29.13	RIP	13.110759	0.214	-0.381	1.20	-2.03			1.20
MT 1374	29.24	RIP	13.107772	0.353	-0.04	2.02	-1.77	0.91	0.22	1.12
MT 1375	29.32	RIP	13.105599	0.245	-0.132	1.63	-1.67	0.72	0.25	0.90
MT 1376	29.42	RIP	13.102883	0.567	0.019	1.99	-1.72	0.80	0.21	1.19
MT 1377	29.54	RIP	13.099624	0.288	-0.055	1.92	-1.94	0.86	0.26	1.07
MT 1378	29.67	RIP	13.096094	0.406	-0.368	2.10	-2.04	0.65	0.31	1.45

MT 1379	29.81	RIP	13.092291	0.535	-0.005	2.14	-1.59	0.87	0.40	1.28
MT 1380	29.86	RIP	13.090933	0.672	0.026	2.04	-1.78	0.73	0.40	1.31
MT 1381	29.94	RIP	13.088761	0.578	0.127	2.19	-1.56	0.97	0.29	1.22
MT 1382	30.05	RIP	13.085773	0.683	0.173	1.64	-1.26	0.71	0.31	0.93
MT 1383	30.17	RIP	13.082514	0.66	0.059	1.69	-1.45	0.72	0.34	0.96
MT 1384	30.31	RIP	13.078712	0.702	0.044	1.38	-1.31	0.73	0.34	0.66
MT 1385	30.48	RIP	13.074095	0.957	0.068	1.66	-1.63	0.72	0.35	0.94
MT 1386	30.53	RIP	13.072737	0.864	0.036	1.52	-1.21	0.75	0.29	0.78
MT 1387	30.62	RIP	13.070293	0.852	0.174	2.03	-1.42	1.10	0.27	0.93
MT 1388	30.70	RIP	13.068121	0.642	0.119	1.89	-1.17	0.72	0.37	1.17
MT 1389	30.79	RIP	13.065676	0.523	0.213	1.95	-1.32	0.92	0.32	1.03
MT 1390	30.86	RIP	13.063775	0.77	0.113			0.73	0.36	
MT 1391	30.96	RIP	13.061059	0.644	0.298	2.03	-1.68	0.64	0.45	1.39
MT 1392	31.10	RIP	13.057257	0.502	0.247	2.12	-1.79	0.65	0.35	1.47
MT 1393	31.16	RIP	13.055628	0.494	0.215	1.98	-1.59	0.55	0.49	1.43
MT 1394	31.29	RIP	13.052097	0.557	0.071	1.96	-1.60	0.74	0.46	1.22
MT 1395	31.37	RIP	13.049924	0.403	0.366	1.98	-1.74	0.76	0.41	1.22
MT 1396	31.46	RIP	13.04748	0.401	0.19	1.65	-1.70	0.48	0.49	1.17
MT 1397	31.55	RIP	13.045036	0.533	0.121	1.42	-1.45	0.49	0.54	0.93
MT 1398	31.66	RIP	13.042049	0.873	0.161	1.96	-1.34	0.88	0.40	1.08
MT 1399	31.78	RIP	13.03879	0.779	0.02	1.80	-1.32	0.80	0.38	1.01
MT 1400	31.90	RIP	13.035531	0.722	0.303	1.87	-1.61	0.73	0.35	1.14
MT 1401	32.00	RIP	13.032815	0.597	0.163	2.07	-1.51	0.64	0.33	1.43
MT 1402	32.06	RIP	13.03106	0.536	-0.182	1.66	-1.07	0.69	0.34	0.97
MT 1403	32.16	RIP	13.027929	0.517	-0.333	1.86	-1.43	0.80	0.20	1.07
MT 1404	32.24	RIP	13.025423	0.486	0.029	1.67	-1.23	0.80	0.37	0.87
MT 1405	32.33	RIP	13.022605	0.595	0.224	1.79	-1.36	0.66	0.37	1.12
MT 1406	32.40	RIP	13.020413	0.262	0.112	1.92	-1.53	0.60	0.32	1.32
MT 1407	32.50	RIP	13.017281	0.147	-0.07	1.90	-1.64	0.66	0.33	1.24
MT 1408	32.61	RIP	13.013836	0.44	0.014	1.83	-1.50	0.66	0.34	1.17

MT 1408A	32.71	RIP	13.010704	0.291	-0.047			0.40	0.32	
MT 1409	32.80	RIP	13.007886	0.423	0.039	1.84	-1.53	0.74	0.37	1.10
MT 1410	32.92	RIP	13.004127	0.284	-0.011	1.75	-1.55	0.55	0.25	1.21
MT 1411	33.02	RIP	13.000996	0.505	-0.121	1.61	-1.28	0.57	0.33	1.04
MT 1412	33.11	RIP	12.998177	0.494	0.031	1.60	-1.23	0.53	0.26	1.06
MT 1413	33.17	RIP	12.996298	0.454	0.174	1.65	-1.26	0.60	0.32	1.05
MT 1414	33.22	RIP	12.994732	0.599	0.142	1.77	-1.57	0.70	0.36	1.07
MT 1415	33.34	RIP	12.990974	0.66	0.222	1.79	-1.36	0.68	0.38	1.11
MT 1416	33.42	RIP	12.988469	0.655	0.212	2.02	-1.54	0.77	0.46	1.24
MT 1417	33.56	RIP	12.984084	0.666	-0.071	1.89	-1.18	0.63	0.42	1.26
MT 1418	33.61	RIP	12.982518	0.506	-0.067	2.00	-1.17	0.91	0.47	1.09
MT 1419	33.70	RIP	12.9797	0.665	0.037	1.93	-1.15	1.09	0.39	0.84
MT 1420	33.84	RIP	12.975315	0.722	0.106					
MT 1421	33.91	RIP	12.973123	0.582	0.177					
MT 1422	33.99	RIP	12.970618	0.493	0.051					
MT 1423	34.09	RIP	12.967486	0.553	0.13					
MT 1424	34.11	RIP	12.96686	0.592	0.165					
MT 1425	34.18	RIP	12.964667	0.869	0.199					
MT 1426	34.27	RIP	12.961849	0.864	0.153					
MT 1427	34.37	RIP	12.958717	0.83	0.39					
MT 1428	34.45	RIP	12.956212	0.846	0.516					
MT 1429	34.54	RIP	12.953393	0.477	0.277					
MT 1430	34.57	RIP	12.952454	0.178	0.135					
MT 1431	34.67	RIP	12.949322	0.512	0.172					
MT 1432	34.75	RIP	12.946816	0.357	0.163					
MT 1433	34.84	RIP	12.943998	0.407	-0.069					
MT 1434	34.94	RIP	12.940866	0.292	-0.047					
MT 1435	35.04	RIP	12.937734	0.547	-0.066					
MT 1436	35.14	RIP	12.934603	0.452	0.205					

MT 1437	35.22	RIP	12.932097	0.339	0.008					
MT 1438	35.31	RIP	12.929279	0.605	0.135					
MT 1439	35.43	RIP	12.925521	0.502	0.204					
MT 1440	35.53	RIP	12.922389	0.573	-0.151					
MT 1441	35.61	RIP	12.919883	0.355	-0.007					
MT 1442	35.70	RIP	12.917065	0.396	0.193					
MT 1443	35.81	RIP	12.91362	0.32	0.011					
MT 1444	35.95	RIP	12.909235	0.512	0.079					
MT 1445	36.05	RIP	12.906104	0.36	0.142					
MT 1446	36.16	RIP	12.902659	0.552	-0.07					
MT 1447	36.27	RIP	12.899214	0.636	-0.059					
MT 1448	36.34	RIP	12.897022	0.832	-0.676					
MT 1449	36.44	RIP	12.89389	0.679	0.129					
MT 1450	36.56	RIP	12.890132	0.666	0.205					
MT 1451	36.65	RIP	12.887313	0.715	0.252					
MT 1452	36.76	RIP	12.883868	0.691	0.359					
MT 1453	36.89	RIP	12.879797	0.454	0.218					
MT 1454	36.96	RIP	12.877605	0.453	0.082					
MT 1455	37.06	RIP	12.874473	0.468	0.139					
MT 1456	37.13	RIP	12.872281	0.431	0.174					
MT 1457	37.21	RIP	12.869775	0.452	0.265					
MT 1458	37.31	RIP	12.866644	0.848	0.235					
MT 1459	37.45	RIP	12.862259	0.609	0.079					
MT 1460	37.53	RIP	12.859754	0.658	0.208					
MT 1461	37.68	RIP	12.855056	0.468	-0.034					
MT 1462	37.73	RIP	12.85349	0.569	-0.319					
MT 1463	37.84	RIP	12.850045	0.586	-0.315					
MT 1464	37.97	RIP	12.845974	0.752	-0.231					
MT 1465	38.07	RIP	12.842842	0.544	-0.05					
MT 1466	38.16	RIP	12.840024	0.765	-0.06					

MT 1467	38.26	RIP	12.836892	0.335	-0.135					
MT 1468	38.35	RIP	12.834073	0.61	-1.602					
MT 1469	38.46	RIP	12.830629	0.414	-0.725					
MT 1470A-B	38.51	RIP	12.829063							
MT 1470	38.55	RIP	12.82781	0.161	-0.406					
MT 1471	38.66	RIP	12.824365	0.294	-0.327					
MT 1472	38.74	RIP	12.82186	0.046	-0.534					
MT 1473	38.85	RIP	12.818415	-0.488	-0.547					
MT 1473A	38.94	RIP	12.815596	0.563	-0.322					
MT 1474	39.04	RIP	12.812464	0.423	-0.417					
MT 1475	39.17	RIP	12.808393	0.493	-0.297					
MT 1476	39.28	RIP	12.804948	0.531	-0.365					
MT 1477	39.37	RIP	12.80213	0.483	-0.28					
MT 1478	39.47	RIP	12.798998	0.542	-0.117					
MT 1479	39.58	RIP	12.795553	0.896	-0.303					
MT 1480	39.67	RIP	12.792734	0.787	-0.134					
MT 1481	39.76	RIP	12.789916	0.826	-0.164					
MT 1482	39.86	RIP	12.786784	0.893	-0.118					
MT 1483	39.98	RIP	12.783026	0.845	-0.078					
MT 1484	40.05	RIP	12.780834	0.825	-0.05					
MT 1485	40.18	RIP	12.776762	0.834	-0.107					
MT 1486	40.30	RIP	12.773004	0.659	-0.289					
MT 1487	40.39	RIP	12.770186	0.574	-0.258					
MT 1488	40.50	RIP	12.766741	0.459	-0.14					
MT 1646	40.50	RIP	12.766741							
MT 1647	40.55	RIP	12.765175	0.498	-0.418					
MT 1648	40.65	RIP	12.762043	0.715	0.337					
MT 1649	40.75	RIP	12.758911	0.758	-0.029					
MT 1650	40.85	RIP	12.75578	0.606	-0.171					

MT 1651	40.94	RIP	12.752961	0.643	-0.037					
MT 1652	41.09	RIP	12.748263	0.722	-0.046					
MT 1653	41.19	RIP	12.745132	0.859	0.044					
MT 1654	41.27	RIP	12.742626	0.896	0.033					
MT 1655	41.37	RIP	12.739495	0.992	0.02					
MT 1656	41.47	RIP	12.736363	1.086	0.404					
MT 1657	41.56	RIP	12.733544	1.079	0.139					
MT 1658	41.68	RIP	12.729786	1.015	0.181					
MT 1659	41.78	RIP	12.726654	1.061	0.199					
MT 1660	41.88	RIP	12.723523	0.775	0.152					
MT 1661	42.01	RIP	12.719451	0.337	0.062					
MT 1662	42.15	RIP	12.715067	0.343	0.017					
MT 1663	42.24	RIP	12.712248	0.384	-0.135					
MT 1664	42.31	RIP	12.710056	0.581	-0.182					
MT 1665	42.44	RIP	12.705985	0.726	-0.08					
MT 1666	42.53	RIP	12.703166	0.927	0.052					
MT 1667	42.63	RIP	12.700035	0.966	0.14					
MT 1668	42.74	RIP	12.69659	0.98	0.03					
MT 1669	42.88	RIP	12.692205	0.842	-0.032					
MT 1670	43.00	RIP	12.688447	1.058	0.015					
MT 1671	43.13	RIP	12.684376	1.058	-0.31					
MT 1672	43.25	RIP	12.696862	1.215	0.078					

Appendix 3.2 Trace element ratios from planktic species *Trilobatus trilobus*. 25 to 30 individual specimens used to generate the record. Height for the MRSF section according to Lourens (2022) and RIP section Badger et al., (2013)

Sample no	Section	Height in section (m)	Age model (Lourens 2022)	Mg/Ca (mmol/mol)	Li/Ca (µmol/mol)	Sr/Ca (mmol/mol)	Cd/Ca (µmol/mol)	U/Ca (nmol/mol)	Al/Ca (µmol/mol)	Mn/Ca (µmol/mol)	B/Ca (µmol/mol)	Ba/Ca (µmol/mol)	Fe/Ca (µmol/mol)
MT 1674	MRSF	-23.01	14.35249	5.3787	11.6826	1.2993	0.0355	90.6328	145.9228	106.5936	72.0077	1.5482	678.6331
MT1676	MRSF	-22.86	14.35047	6.5916	12.2673	1.3209	0.0361	73.4808	55.0612	102.4473	74.8435	1.434	994.6336
MT1677	MRSF	-22.79	14.34963	7.8421	12.531	1.2322	0.0308	125.7641	204.1146	163.9409	73.8531	1.6756	1097.373
MT1678	MRSF	-22.69	14.34829	6.6755	11.2466	1.2106	0.0539	54.3003	19.5692	172.1537	67.2774	1.3635	459.1641
MT1679	MRSF	-22.59	14.34695	6.1967	12.0725	1.3003	0.0582	164.7235	118.9732	140.5141	72.8917	2.1416	513.1015
MT1680	MRSF	-22.51	14.34594	5.9118	11.8515	1.2869	0.0677	137.3044	32.1261	115.7444	69.2127	1.494	412.3263
MT1681	MRSF	-22.43	14.34494	8.3055	12.0646	1.2813	0.0868	151.406	47.4218	150.6742	71.8771	86.0244	589.2716
MT1682	MRSF	-22.30	14.34326	6.3146	11.8385	1.2578	0.0424	198.4433	0.7182	149.548	67.5633	1.4853	-15.0881
MT1683	MRSF	-22.19	14.34175	5.8597	12.5582	1.32	0.0578	176.7995	66.7854	103.196	75.2012	1.5156	890.0861
MT1684	MRSF	-22.11	14.34074	5.374	12.6942	1.3216	0.0494	73.6502	69.8432	89.2307	75.9455	2.4294	678.5143
MT1685	MRSF	-22.00	14.3394	4.4159	11.4454	1.121	0.0648	71.1594	22.8612	63.7239	36.8419	0.8814	308.1911
MT1686	MRSF	-21.93	14.33839	5.5584	12.4755	1.3213	0.0643	81.4757	22.4882	97.8494	76.2737	1.3595	473.8115
MT1687	MRSF	-21.81	14.33688	6.7527	11.6745	1.2087	0.04	80.5224	46.1949	166.9389	66.9612	1.6796	741.2938
MT1688	MRSF	-21.69	14.33537	7.3361	10.9246	1.1441	0.0031	154.8342	0.6375	181.2371	62.3937	1.4754	3.4103
MT1689	MRSF	-21.60	14.3342	6.6264	12.3099	1.2911	0.0317	93.2167	22.8423	150.1497	70.2795	1.5676	848.8678
MT1690	MRSF	-21.53	14.33319	5.3691	12.0167	1.3599	0.0226	56.7717	24.0955	76.7364	79.2013	1.6933	473.5292
MT1691	MRSF	-21.44	14.33201	5.3445	12.7333	1.3691	0.023	66.0645	0.7156	79.3461	78.2598	1.5967	12.7135
MT1692	MRSF	-21.33	14.33067	7.6306	13.1584	1.3962	0.0569	76.9238	22.0483	80.6716	74.7835	1.6692	702.5778
MT1693	MRSF	-21.23	14.32933	5.2403	12.0651	1.3597	0.0375	55.3383	29.2466	75.7593	79.1317	1.4028	538.8613
MT1694	MRSF	-21.14	14.32815	6.4029	12.6166	1.3216	0.049	85.913	430.9227	99.3165	73.8317	1.4708	708.9403
MT1696	MRSF	-20.94	14.32564	7.0199	12.448	1.3265	0.0519	69.5997	54.0996	97.1489	80.1425	1.7899	896.4343
MT1697	MRSF	-20.85	14.32446	6.477	13.8503	1.3164	0.0354	76.3156	118.307	108.4417	74.0843	1.4335	712.6058
MT1698	MRSF	-20.78	14.32346	8.2613	13.5183	1.3178	0.0444	64.8155	59.6071	99.7088	83.1472	1.9853	859.1885
MT1699	MRSF	-20.70	14.32245	5.4043	12.2535	1.318	0.0244	42.1251	90.8149	78.4324	75.5992	2.0571	617.2538

MT1700	MRSF	-20.66	14.32195	4.7038	12.0158	1.3344	0.0167	46.5707	12.6365	69.1165	77.5621	1.2843	597.6055
MT1704	MRSF	-20.30	14.31725	5.0281	13.7817	1.3983	0.1037	44.1595	118.5571	520.0187	106.2473	2.5128	847.5843
MT1710	MRSF	-19.71	14.3097	5.9473	12.2001	1.3572	0.0198	49.4723	24.0931	84.9962	76.7819	1.7215	602.8958
MT1714	MRSF	-19.29	14.30413	6.4668	12.5529	1.3118	0.0374	77.5064	106.3756	95.6008	76.291	1.8136	595.7526
MT1718	MRSF	-18.87	14.29869	6.5473	12.8241	1.3236	0.0301	77.7324	49.0464	105.729	74.5048	1.6815	969.7533
MT1722	MRSF	-18.40	14.29239	5.7695	12.6554	1.3754	0.0319	76.3087	38.0033	67.348	74.1414	2.4061	579.7746
MT1725	MRSF	-18.06	14.28796	5.8216	12.8898	1.3653	0.0484	73.8544	68.4945	75.5366	80.1665	1.6424	1212.4818
MT1749	MRSF	-16.82	14.25655	5.0105	12.0229	1.4131	0.0149	37.2671	20.6186	72.363	77.292	1.5756	573.1906
MT1757	MRSF	-16.16	14.2339	4.9913	12.2007	1.396	0.043	47.1771	51.4358	68.0441	78.9082	1.4582	976.4647
MT1763	MRSF	-15.61	14.21525	5.2917	12.2853	1.3729	0.0236	48.799	45.2338	59.108	75.8389	1.5813	538.0291
MT1769	MRSF	-15.07	14.20116	7.218	12.6755	1.3403	0.0141	77.7988	67.1749	88.8244	80.6982	1.5854	669.8586
MT1776	MRSF	-14.46	14.18647	5.3047	12.4856	1.3744	0.0084	47.3795	2.3325	75.0274	78.5146	1.5283	7.7418
MT1783	MRSF	-13.87	14.17209	6.6482	12.5575	1.3402	0.0181	56.7957	59.4904	91.855	77.7828	1.8462	592.2024
MT1789	MRSF	-13.31	14.15865	5.6596	11.9494	1.4078	0.0282	55.8352	14.9938	79.0622	76.391	1.7403	491.5313
MT1803	MRSF	-12.12	14.13904	5.5403	12.8714	1.4307	0.0166	53.7664	16.6457	77.7486	85.9263	1.8587	788.2184
MT1808	MRSF	-11.55	14.1305	7.0405	12.4207	1.4024	0.0191	52.7954	55.5191	129.3326	76.6066	2.2427	565.1369
MT1814	MRSF	-10.89	14.12061	4.9547	12.2279	1.4161	0.0116	34.4088	22.1513	92.705	77.6603	2.0341	434.8291
MT1820	MRSF	-10.35	14.11246	6.0821	12.6973	1.353	0.0363	45.392	50.7393	97.7904	78.9726	2.0462	672.0875
MT1827	MRSF	-9.61	14.08474	5.3976	15.435	1.376	0.012	41.4832	67.4888	95.9303	76.069	1.9695	535.6207
MT1834	MRSF	-8.92	14.05779	7.8197	11.68	1.3565	0.0224	44.8206	97.8164	86.7872	76.0398	1.8417	596.3899
MT1841	MRSF	-8.24	14.03184	7.4136	12.6119	1.3377	0.0697	81.3642	104.3967	111.2534	82.0244	4.0054	673.649
MT1844	MRSF	-7.96	14.02086	8.2051	14.6083	1.3566	0.0555	72.6403	230.7561	97.0046	83.6092	1.9254	1072.5556
MT1856	MRSF	-6.81	13.98255	8.4197	13.6741	1.3016	0.0391	88.2101	213.789	119.5652	78.9297	1.7889	1068.4269
MT1863	MRSF	-6.10	13.96587	7.8024	13.8387	1.3671	0.056	106.2537	111.2295	101.7661	86.9718	1.9227	837.2349
MT1870	MRSF	-5.40	13.94949	10.6334	13.1372	1.3825	0.0357	49.0379	47.3699	97.2739	86.0512	1.9306	1155.3883
MT1879	MRSF	-4.54	13.92935	9.3891	13.1966	1.3721	0.0727	133.7557	45.6132	137.0147	90.4589	1.8867	1215.7954
MT1884	MRSF	-3.99	13.91641	9.1404	12.5489	1.2993	0.0727	134.4949	72.75	173.9316	80.5333	2.0756	1414.7696
MT1887	MRSF	-3.60	13.90724	7.9546	13.3961	1.3516	0.0741	86.6616	80.4929	152.8792	81.915	1.9765	1047.8302
MT1892	MRSF	-3.21	13.89968	10.8837	14.1594	1.2971	0.0779	132.8662	203.3715	186.2795	82.6088	1.9789	1815.2744
MT1954	MRSF	-2.28	13.88288	9.5513	13.3237	1.3505	0.0893	99.5351	130.9595	169.2372	85.519	2.0849	1258.9932

MT1956	MRSF	-1.94	13.87679	7.5391	12.5398	1.3057	0.0833	135.594	54.5853	211.4302	82.4269	1.8989	1438.2224
MT1959	MRSF	-1.56	13.86981	7.2781	13.0178	1.3537	0.2209	92.5614	33.5339	179.8194	96.6571	1.8193	996.9639
MT1961	MRSF	-1.33	13.86561	7.2383	12.7025	1.3418	0.0744	124.3157	34.9323	166.7436	90.0787	1.744	1234.6309
MT1962a	MRSF	-1.08	13.86119	6.3724	12.9003	1.3192	0.0159	135.953	0.561	189.699	81.9147	1.8136	15.0065
MT1965	MRSF	-0.72	13.85468	6.13	12.9268	1.3796	0.0897	79.2982	24.1535	130.1276	90.2806	1.8077	968.837
MT1966A	MRSF	-0.35	13.8479	6.6097	12.9885	1.3629	0.0576	116.3075	34.9564	167.6925	91.9341	1.8897	1330.0544
MT1968	MRSF	-0.02	13.84209	5.2333	13.4227	1.3735	0.0518	73.8593	24.2377	154.9231	96.6667	1.8148	1061.8022
MT1970	MRSF	0.30	13.83485	5.5533	14.7431	1.363	0.0538	71.6951	46.4071	156.5082	94.5427	1.9961	5452.1143
MT1972	MRSF	0.61	13.82801	7.562	14.2778	1.3112	0.0523	117.9038	168.8175	327.8162	84.6157	2.0431	2567.6355
MT1974	MRSF	0.95	13.8204	5.8037	14.5986	1.3184	0.0435	75.3878	69.0356	275.5329	90.6402	2.0511	1572.4401
MT1977	MRSF	1.60	13.80595	5.4218	13.7772	1.3884	0.0384	60.1833	28.5349	196.7161	97.5335	2.115	1833.6765
MT1987	MRSF	2.61	13.78337	5.0155	14.7255	1.4243	0.0622	54.697	20.601	424.8595	101.8757	2.3747	932.1055
MT20	RIP	6.65	13.70394	4.5248	14.7133	1.4076	0.0644	53.6172	308.9961	228.7895	107.1149	4.4831	633.9792
MT21	RIP	7.00	13.69674	5.0791	14.8892	1.3954	0.0767	48.2829	545.1922	281.7543	115.0354	8.177	752.6812
MT22	RIP	7.35	13.68954	4.5185	13.1789	1.4255	0.0628	68.9217	129.3535	248.6582	102.6476	2.7494	602.19
MT23	RIP	7.70	13.68235	5.3326	13.1085	4.2009	0.0713	85.6949	76.4523	379.7049	115.3034	108.9697	572.8492
MT24	RIP	8.05	13.67504	4.7239	12.2879	1.385	0.0504	37.3416	181.5631	287.3445	98.9234		518.9511
MT25	RIP	8.40	13.66772	3.9793	12.7096	1.5584	0.0677	108.5246	132.0419	182.6609	98.3374	341.3721	691.5056
MT26	RIP	8.75	13.66039	4.6043	15.7554	1.4033	0.0645	51.5769	185.0598	190.259	110.6468	3.455	489.1691
MT27	RIP	9.10	13.65307	5.3583	13.0176	1.3789	0.0339	59.2529	77.8568	294.8731	93.8001	2.8128	749.9975
MT28	RIP	9.45	13.64574	4.5142	12.7332	1.3819	0.0665	56.5861	141.2077	293.1835	111.6352	16.9396	475.8522
MT29	RIP	9.80	13.63842	4.0417	11.5038	1.3695	0.0812	105.3344	413.5401	206.1109	95.1794	6.6823	714.2137
MT30	RIP	10.15	13.63109										
MT31	RIP	10.50	13.62377	4.749	14.0304	1.3944	0.0567	51.8875	311.1476	343.4334	102.1752	2.9952	557.2321
MT33	RIP	11.20	13.60911	5.9242	13.5185	1.4126	0.0642	94.1565	1388.5127	247.7872	108.6273	4.8441	676.3303
MT34	RIP	11.55	13.60179	5.1871	13.2507	1.3863	0.0521	75.7637	31.1286	598.654	106.9865	2.76	630.187
MT35	RIP	11.90	13.59446	4.821	13.0019	1.4013	0.0627	51.8217	46.2636	379.4977	97.997		533.0869
MT36	RIP	12.25	13.58714	4.9503	13.148	1.3983	0.0538	57.8061	40.0125	406.8079	102.0495	2.7674	621.2
MT37	RIP	12.60	13.57936	4.7084	13.1739	1.3822	0.0672	82.3339	442.6628	319.4977	112.2977	2.3551	719.2364
MT38	RIP	12.95	13.57124	4.0829	12.512	1.3652	0.0609	70.8956	191.3075	161.2662	91.5081	2.4275	427.7538

MT39	RIP	13.30	13.56311	4.2323	12.3737	3.5994	0.0509	88.7677	44.1218	167.2908	86.1975	123.6375	483.0201
MT40	RIP	13.65	13.55499	3.797	12.5004	1.3804	0.0439	68.3892	155.7339	180.9981	86.3747	10.1983	538.2555
MT41	RIP	14.00	13.54687	4.3914	12.7125	1.39	0.0478	76.9821	77.1658	178.1435	91.9828	2.6276	395.9121
MT42	RIP	14.35	13.53875	4.2879	13.1545	2.6516	0.0609	108.2577	168.7569	133.0006	95.9414		605.5003
MT43	RIP	14.70	13.53062	4.8391	11.9829	1.3614	0.0459	69.2116	294.8874	210.2081	87.6951	3.8105	524.444
MT44	RIP	15.05	13.51986	5.0989	13.0163	2.6429	0.0471	89.2945	71.6323	320.59	90.3682	100.0817	680.6126
MT45	RIP	15.40	13.50783	3.6092	11.4393	1.3503	0.0443	179.7283	160.3548	182.1752	74.4368	3.3665	571.1953
MT46	RIP	15.75	13.49581	4.2179	12.4913	1.313	0.0264	68.6422	62.2993	142.7799	99.4453	5.8178	529.6158
MT47	RIP	16.10	13.48378	3.9828	12.805	1.3599	0.0419	53.3983	166.5539	147.8573	103.7842	28.572	472.666
MT48	RIP	16.45	13.47175	3.946	13.3842	1.7597	0.0769	116.1149	27.8781	213.4395	105.0824	48.2329	633.7869
MT49	RIP	16.80	13.45973	4.2644	12.6199	1.3509	0.063	87.5265	322.5865	369.1704	92.6579		651.7579
MT50	RIP	17.15	13.44776	3.6024	12.4649	1.3774	0.081	60.7368	44.4351	323.5687	88.676	2.4035	538.4335
MT51	RIP	17.50	13.43792	4.1743	12.6768	2.6349	0.1178	82.7518	76.3122	299.4915	95.7256	192.5657	535.2092
MT52	RIP	17.85	13.42808	3.8242	12.395	1.3627	0.0486	60.8515	8.525	340.4933	84.5221	2.8241	505.6917
MT53	RIP	18.20	13.41982	3.9252	12.036	1.4712	0.0959	53.5529	103.5332	148.8651	86.0809	32.7834	421.7892
MT54	RIP	18.55	13.41198	4.1069	11.6608	1.3603	0.0536	104.2414	8.1995	263.5341	75.7477	3.4063	557.9518
MT55	RIP	18.90	13.40414	3.5853	11.8446	5.1178	0.0517	44.706	64.1202	172.6059	86.3446	160.4853	259.0737
MT57	RIP	19.60	13.38846	4.0115	12.1927	2.1873	0.0686	89.3959	38.6773	198.9098	87.6731	91.0029	459.4398
MT58	RIP	19.95	13.38062	3.6199	12.706	5.8761	0.078	93.333	64.2669	169.6834	89.6042		629.7295
MT59	RIP	20.30	13.37277	4.5228	12.6779	1.4646	0.0322	22.5755	-9.1646	337.5939	86.6315	72.8517	13.8066
MT60	RIP	20.65	13.36493	4.1626	13.3454	1.4231	0.0579	66.8833	23.39	236.8872	91.2167	23.5282	1417.9124
MT61	RIP	21.00	13.35709	4.4002	13.3372	1.4545	0.0486	40.1282	-28.567	200.8106	88.6558	33.6155	30.4573
MT62	RIP	21.35	13.34925	4.061	12.7433	1.4305	0.0395	2.7275	-16.0062	150.7441	92.7085	27.026	8.6008
MT63	RIP	21.70	13.34141	4.1947	12.5927	1.7076	0.0452	84.0964	29.2952	226.8915	89.8781		648.4966
MT64	RIP	22.05	13.33357	4.2042	12.5147	2.887	0.0361	72.5168	37.6242	317.3548	87.5145	220.7128	642.3746
MT65	RIP	22.40	13.32573	4.992	12.7544	1.4065	0.0305	58.7304	53.8772	255.5904	91.4188	31.1869	533.5594
MT66	RIP	22.75	13.31789	4.1222	12.8255	1.3498	0.0366	53.6734	29.1179	215.7085	85.5709	2.7138	704.3499
MT67	RIP	23.10	13.31005	3.9736	13.0349	1.3788	0.041	116.131	44.2769	295.4326	94.8345	6.4639	739.3963
MT68-	RIP	23.45	13.30221	3.7796	12.3857	1.3946	0.0689	76.059	110.8719	188.9984	85.258		516.0179
MT69	RIP	23.80	13.29437	4.4208	13.0095	2.3981	0.0783	70.537	33.408	314.4997	89.675	101.4345	573.0353

MT70	RIP	24.15	13.28653	4.0277	12.754	1.5061	0.0631	94.7883	6.0307	307.1358	86.0724	64.8381	418.6573
MT71	RIP	24.50	13.27858	3.5336	12.7226	1.4493	0.1115	142.6035	11.6938	166.3522	85.2285	107.2496	653.95
MT72	RIP	24.85	13.27048	4.1117	12.2233	1.3791	0.0559	112.9548	-0.7979	357.7904	77.3928	3.5257	519.1936
MT73	RIP	25.20	13.26238	3.6892	13.1441	1.3941	0.083	140.7667	39.979	221.7322	89.9343	4.0053	648.999
MT74	RIP	25.55	13.25428	3.9573	12.9303	1.4039	0.0875	113.8063	23.8309	336.3176	87.3571	3.4744	556.6125
MT75	RIP	25.90	13.24618										
MT76	RIP	26.25	13.23808	4.3305	12.297	1.3718	0.0541	116.1	29.1409	178.5629	84.8025	2.933	466.1775
MT77	RIP	26.60	13.22998	3.9574	12.6223	1.3495	0.0853	138.5278	25.058	200.0991	96.9798	10.1649	775.6777
MT78	RIP	26.95	13.22188	4.2981	12.0668	1.3673	0.0442	117.6583	157.729	147.134	92.0162	3.1298	541.1204
MT79	RIP	27.30	13.21378	4.1066	12.6993	1.3721	0.0596	76.7473	29.5528	206.5135	91.9192	2.7224	601.7728
MT80	RIP	27.65	13.20568	3.9567	12.9666	1.3784	0.0878	131.8933	75.0274	174.5418	88.9105	2.5293	585.5921
MT81	RIP	28.00	13.19758	4.4273	12.1173	1.3424	0.0481	130.7078	10.3934	387.1781	75.3581	4.7978	552.4758
MT82	RIP	28.35	13.18948	4.0327	12.754	1.3804	0.0472	63.2373	28.2594	322.1103	94.2847	9.3611	853.1908
MT83	RIP	28.70	13.18132	4.0202	14.3135	1.5645	0.0705	130.8624	28.9867	337.5741	100.5984		865.9743
MT84	RIP	29.05	13.17293	3.9095	13.5932	1.3847	0.0446	71.0959	9.0169	561.4994	95.1866	3.2475	445.8408
MT85	RIP	29.40	13.16453	4.3641	13.6469	1.4006	0.0518	46.5508	108.5648	297.527	112.1137	3.3011	489.7399
MT86	RIP	29.75	13.15614	4.0254	13.7637	1.398	0.0513	103.7946	28.1998	220.9125	98.9849	6.7844	637.9585
MT87	RIP	30.10	13.14775	5.3326	13.6251	1.4127	0.0836	216.9127	56.511	403.9318	109.8303	4.9949	796.8023
MT88	RIP	30.45	13.13936	4.5881	13.7336	1.4052	0.0838	118.0419	19.4305	268.3157	108.0508	2.8942	700.8203
MT89	RIP	30.80	13.13096	4.0959	13.4126	1.3761	0.0579	191.4872	-2.1392	299.0868	96.9687	2.641	998.4368
MT90	RIP	31.15	13.12257	4.4915	13.3847	1.3821	0.0614	200.1727	17.7088	328.3773	99.9858	2.9486	820.9988
MT92	RIP	31.85	13.10578	4.3419	13.4604	1.3854	0.0599	120.0565	30.0992	264.5907	98.9598	3.1488	721.3308
MT93	RIP	32.20	13.09739	4.638	13.2511	1.3817	0.0332	64.5925	-18.1593	391.1601	106.541	3.0439	622.5694
MT94	RIP	32.55	13.089	4.585	13.8423	1.4028	0.0567	154.4935	28.1934	356.9907	105.5092	5.2978	888.081
MT95	RIP	32.90	13.08061	4.4223	13.164	3.1876	0.0639	65.7494	32.8248	581.4907	91.9932	251.7292	706.5934
MT96	RIP	33.25	13.07221	4.1043	13.1251	1.5163	0.0575	83.0811	3.7814	527.6037	103.2042	188.1677	779.9462
MT97	RIP	33.60	13.06337	4.2446	13.4993	1.3991	0.0616	101.9259	33.493	282.7696	108.514	2.738	771.1341
MT98	RIP	33.95	13.0534	4.5163	12.9006	1.3935	0.0445	108.7476	53.3829	411.3069	100.9969	3.0377	864.5218
MT99	RIP	34.30	13.04342	4.3862	13.0685	1.391	0.0354	4.2039	-9.4744	304.9938	94.6129	2.8098	37.4282
MT100	RIP	34.65	13.03345	4.024	12.5062	1.3556	0.0488	151.0223	8.0424	373.3877	89.3899	2.754	648.9362

MT101	RIP	35.00	13.02217										
MT102	RIP	35.35	13.01067	3.6762	12.5702	1.3563	0.0472	77.1681	24.536	531.2828	93.5825	2.4836	683.731
MT104	RIP	36.05	12.98767	3.6821	12.6607	1.3871	0.0421	103.2414	44.1065	387.8847	84.5913		800.8297
MT105	RIP	36.40	12.97617										
MT108	RIP	37.45	12.94443	4.0301	13.1335	1.387	0.0465	105.9307	59.0219	258.0156	100.0502	2.7537	789.7331
MT116	RIP	40.25	12.86346	4.5698	15.2834	1.4141	0.0553	119.1217	24.8244	225.7964	119.725	2.7925	654.0946

Appendix 3.3 Trace element ratios from benthic species *Uvigerina* spp. 25 to 30 individual specimens used to generate the record.

Sample no	Section	Height in section (m)	Age model Lourens (2022)	Mg/Ca (mmol/mol)	Li/Ca (µmol/mol)	Sr/Ca (mmol/mol)	Cd/Ca (µmol/mol)	U/Ca (nmol/mol)	Al/Ca (µmol/mol)	Mn/Ca (µmol/mol)	B/Ca (µmol/mol)	Ba/Ca (µmol/mol)	Fe/Ca (µmol/mol)
MT1677	MRSF	-22.79	14.34963	5.5059	11.4924	1.0796	0.0495	91.4785	40.3174	118.559	33.0915	1.0209	684.3813
MT1681	MRSF	-22.43	14.34494	5.4839	12.2914	1.0903	0.0817	148.3522	106.6162	112.3051	32.4467	1.4512	471.5002
MT1683	MRSF	-22.19	14.34175	5.0524	12.4157	1.099	0.0587	104.3037	47.4414	75.5734	35.6766	0.995	470.4223
MT1689	MRSF	-21.60	14.3342	4.7992	12.3684	1.1345	0.0516	102.8573	91.5563	94.5095	34.8746	2.3183	695.8918
MT1699	MRSF	-20.70	14.32245	4.448	11.8288	1.1349	0.0502	67.9344	89.5681	85.2364	34.2279	1.3554	719.5743
MT1710	MRSF	-19.71	14.3097	5.2172	12.2939	1.1508	0.0459	52.182	183.3398	86.9369	33.2361	2.4818	777.2527
MT1722	MRSF	-18.40	14.29239	4.9554	12.5719	1.1062	0.0622	148.5847	81.4707	74.7921	34.9007	1.3931	672.3491
MT1776	MRSF	-14.46	14.18647	3.6711	11.6707	1.1611	0.052	66.6422	21.4491	59.6457	40.3427	1.5729	252.3091
MT1795	MRSF	-12.76	14.14855	4.1572	12.1086	1.1579	0.1207	43.5894	82.6615	44.4739	87.2988	1.4329	229.0286
MT1814	MRSF	-10.89	14.12061	3.7226	12.2692	1.1994	0.0693	32.9855	102.6911	61.0442	36.7991	1.4715	196.6849
MT1834	MRSF	-8.92	14.05779	4.3973	11.4027	1.158	0.0822	61.5178	37.0709	63.0015	35.8497	1.2464	331.0531
MT1863	MRSF	-6.10	13.96587	4.8225	12.2355	1.1544	0.0875	60.1234	38.0864	71.919	39.0266	1.5138	443.8316
MT1875	MRSF	-4.92	13.93827	6.6123	12.6822	1.1909	0.0944	84.5094	65.9668	83.1566	33.1965	2.2462	745.7245
MT1892	MRSF	-3.21	13.89968	5.1491	11.9739	1.1457	0.083	102.2737	43.4158	127.6089	36.645	1.4959	716.4814
MT1951	MRSF	-2.60	13.8889	4.2543	12.6872	1.1463	0.1625	106.6455	65.0242	110.9359	37.4737	2.2388	984.042
MT1972	MRSF	0.61	13.82801	2.8594	11.1297	1.1768	0.0882	51.0139	28.1614	109.7224	25.1386	3.4929	1323.5022
MT1976	MRSF	1.29	13.81279	2.7066	11.3117	1.1909	0.0715	39.4903	11.598	78.0058	26.3701	2.9659	690.6619
MT1978	MRSF	1.77	13.80214	2.649	11.8696	1.2062	0.0813	21.2638	8.6259	100.9925	26.444	2.5671	437.05
MT1979	MRSF	1.84	13.80068	2.3674	11.4326	1.2339	0.0817	21.6068	334.5979	76.5458	30.0675	3.6427	367.7177
MT1987	MRSF	2.61	13.78337	2.4535	11.8519	1.2121	0.094	37.758	37.3354	131.6265	27.3579	32.8564	447.867
MT20	RIP	6.65	13.70394	2.3674	11.4326	1.2339	0.0817	21.6068	334.5979	76.5458	30.0675	3.6427	367.7177
MT28	RIP	9.45	13.64574	2.4535	11.8519	1.2121	0.094	37.758	37.3354	131.6265	27.3579	32.8564	447.867
MT30	RIP	10.15	13.63109	2.8989	12.4244	2.5516	0.1466	141.05	98.077	196.1044	28.0458	36.5224	759.8398
MT33	RIP	11.20	13.60911	2.9368	12.0024	1.1558	0.1234	136.0027	50.447	291.4746	28.7871	2.8174	740.191
MT34	RIP	11.55	13.60179	2.4988	11.8165	1.1779	0.0743	24.025	50.8569	188.2994	24.6179	4.1949	328.899

MT36	RIP	12.25	13.58714	2.4063	11.4497	1.1952	0.0668	17.5152	107.5927	107.4696	22.9529	3.3032	364.1354
MT37	RIP	12.60	13.57936	2.4908	11.7768	1.1671	0.0822	26.0029	101.9296	92.6554	28.2711	2.9562	349.8762
MT42	RIP	14.35	13.53875	2.5569	11.4651	1.1681	0.0699	33.3391	14.3301	50.7445	25.9002	3.0248	316.1013
MT44	RIP	15.05	13.51986	2.4143	11.7734	1.1913	0.0664	40.1993	15.5338	114.0521	29.6044	3.6479	314.2236
MT46	RIP	15.75	13.49581	2.3729	11.9418	1.2263	0.0638	24.2426	82.7818	66.825	25.8017	3.7316	397.6892
MT48	RIP	16.45	13.47175	2.4642	11.7312	1.2025	0.0772	34.571	-6.4958	76.2885	25.326	3.6256	417.5028
MT50	RIP	17.15	13.44776	2.4838	11.7499	1.1961	0.0852	19.255	46.5399	89.5996	28.807	3.2484	304.9546
MT55	RIP	18.90	13.40414	2.5801	11.2469	1.2089	0.0883	41.7091	11.7305	83.4769	26.1782	4.1367	381.8818
MT58	RIP	19.95	13.38062	2.6961	11.7146	1.5501	0.1072	42.1315	68.2277	76.9692	25.6434	128.3306	367.076
MT60	RIP	20.65	13.36493	2.6115	11.6269	1.2333	0.0687	16.2652	99.4537	73.8977	27.5028	33.8581	248.7458
MT61	RIP	21.00	13.35709	2.6669	12.2568	1.2002	0.0692	20.2873	-10.0591	55.5014	27.5879	3.656	320.7396
MT63	RIP	21.70	13.34141	2.6629	12.0783	1.2954	0.0858	30.9351	153.4459	86.6168	33.2791	7.4249	468.3234
MT69	RIP	23.80	13.29437	2.6941	11.9096	1.1899	0.0948	27.885	60.7114	98.1886	29.6895	3.9556	363.6649
MT71	RIP	24.50	13.27858	2.4221	10.9388	1.1746	0.1482	57.2614	27.0613	77.4015	26.7703	16.7749	379.8873
MT74	RIP	25.55	13.25428	2.6829	8.3817	1.202	2.804	9.8397	4.06	36.5133	51.7933	2.744	94.3646
MT75	RIP	25.90	13.24618	2.4747	11.0867	1.1705	0.0757	34.4354	9.133	103.7141	27.6676	3.3655	333.6107
MT77	RIP	26.60	13.22998	2.6167	11.237	1.1868	0.1	80.91	-14.4658	122.7064	26.9073	5.0051	520.6397
MT79	RIP	27.30	13.21378	2.4428	11.3423	1.1939	0.096	25.5565	9.9563	68.4548	29.4881	4.8328	342.076
MT83	RIP	28.70	13.18132	1.4968	10.2564	2.204	1.408	2.9435	11.1997	99.0441	56.8756	294.2026	116.9934
MT88	RIP	30.45	13.13936	2.5719	12.0988	1.2039	0.1049	55.0523	131.3331	94.0608	30.382	4.656	468.3077
MT90	RIP	31.15	13.12257	2.6533	11.5815	1.1697	0.0978	72.194	70.0879	132.3311	24.5611	2.8585	593.9686
MT92	RIP	31.85	13.10578	2.2174	10.8796	1.188	0.0815	53.8608	17.1999	88.3035	24.6249	3.5404	437.2215
MT97	RIP	33.60	13.06337	2.2865	10.6669	1.183	0.0847	48.0215	117.257	102.2237	26.8952	2.99	548.4624
MT98	RIP	33.95	13.0534	2.7472	11.8158	1.1986	0.0603	33.4482	-14.1977	134.1995	26.6203	3.4586	525.2795
MT100	RIP	34.65	13.03345	2.6278	11.68	1.1716	0.0834	162.209	-36.9114	237.0391	24.7358	3.2333	669.14
MT101	RIP	35.00	13.02217	2.4806	10.9522	1.1741	0.1157	83.3725	-3.9693	197.1324	28.6481	2.9369	724.4103
MT105	RIP	36.40	12.97617	2.8522	11.9861	1.2041	0.0781	67.2409	71.3546	242.2657	35.0621	3.3498	648.9525
MT116	RIP	40.25	12.86346	2.5808	11.6578	1.1851	0.0769	34.927	-3.22	86.3434	37.2915	2.8237	420.9465

Appendix 3.4 $[B(OH)_4^-]/[DIC]$ from planktic B/Ca and from salinity corrected planktic B/Ca

Sample no	Section	Age model (Lourens 2022)	B/Ca (µmol/mol)	$B(OH)_4^-$ /[DIC]	B/Ca (µmol/mol) Salinity corrected	$B(OH)_4^-$ /[DIC] Salinity corrected
MT 1674	MRSF	14.35249	72.01	0.06	59.26	0.039
MT1675	MRSF	14.35148				
MT1676	MRSF	14.35047	74.84	0.06	62.09	0.043
MT1677	MRSF	14.34963	73.85	0.06	61.10	0.042
MT1678	MRSF	14.34829	67.28	0.05	54.53	0.032
MT1679	MRSF	14.34695	72.89	0.06	60.14	0.040
MT1680	MRSF	14.34594	69.21	0.05	56.46	0.035
MT1681	MRSF	14.34494	71.88	0.06	59.13	0.039
MT1682	MRSF	14.34326	67.56	0.05	54.81	0.033
MT1683	MRSF	14.34175	75.20	0.06	62.45	0.044
MT1684	MRSF	14.34074	75.95	0.06	63.20	0.045
MT1685	MRSF	14.33940	36.84	0.01	24.09	-0.013
MT1686	MRSF	14.33839	76.27	0.06	63.52	0.045
MT1687	MRSF	14.33688	66.96	0.05	54.21	0.032
MT1688	MRSF	14.33537	62.39	0.04	49.64	0.025
MT1689	MRSF	14.33420	70.28	0.06	57.53	0.037
MT1690	MRSF	14.33319	79.20	0.07	66.45	0.050
MT1691	MRSF	14.33201	78.26	0.07	65.51	0.048
MT1692	MRSF	14.33067	74.78	0.06	62.03	0.043
MT1693	MRSF	14.32933	79.13	0.07	66.38	0.050
MT1694	MRSF	14.32815	73.83	0.06	61.08	0.042
MT1695	MRSF	14.32681				
MT1696	MRSF	14.32564	80.14	0.07	67.39	0.051
MT1697	MRSF	14.32446	74.08	0.06	61.33	0.042
MT1698	MRSF	14.32346	83.15	0.07	70.40	0.056
MT1699	MRSF	14.32245	75.60	0.06	62.85	0.044
MT1700	MRSF	14.32195	77.56	0.07	64.81	0.047
1704tt	MRSF	14.31725	106.25	0.11	93.50	0.090
1710tt	MRSF	14.30970	76.78	0.07	64.03	0.046
1714tt	MRSF	14.30413	76.29	0.06	63.54	0.046
1718tt	MRSF	14.29869	74.50	0.06	61.75	0.043
1722tt	MRSF	14.29239	74.14	0.06	61.39	0.042
1725tt	MRSF	14.28796	80.17	0.07	67.42	0.051
1749tt	MRSF	14.25655	77.29	0.07	64.54	0.047
1757tt	MRSF	14.23390	78.91	0.07	66.16	0.049
1763tt	MRSF	14.21525	75.84	0.06	63.09	0.045
1769tt	MRSF	14.20116	80.70	0.07	67.95	0.052
1776tt	MRSF	14.18647	78.51	0.07	65.76	0.049
1783tt	MRSF	14.17209	77.78	0.07	65.03	0.048
1789tt	MRSF	14.15865	76.39	0.06	63.64	0.046

1803tt	MRSF	14.13904	85.93	0.08	73.18	0.060
1808tt	MRSF	14.13050	76.61	0.06	63.86	0.046
1814tt	MRSF	14.12061	77.66	0.07	64.91	0.048
1820tt	MRSF	14.11246	78.97	0.07	66.22	0.050
1827tt	MRSF	14.08474	76.07	0.06	63.32	0.045
1834tt	MRSF	14.05779	76.04	0.06	63.29	0.045
1841tt	MRSF	14.03184	82.02	0.07	69.27	0.054
1844tt	MRSF	14.02086	83.61	0.08	70.86	0.056
1856tt	MRSF	13.98255	78.93	0.07	66.18	0.049
1863tt	MRSF	13.96587	86.97	0.08	74.22	0.061
1870tt	MRSF	13.94949	86.05	0.08	73.30	0.060
1879tt	MRSF	13.92935	90.46	0.09	77.71	0.067
1884tt	MRSF	13.91641	80.53	0.07	67.78	0.052
1887tt	MRSF	13.90724	81.91	0.07	69.16	0.054
1892tt	MRSF	13.89968	82.61	0.07	69.86	0.055
1954tt	MRSF	13.88288	85.52	0.08	72.77	0.059
1956tt	MRSF	13.87679	82.43	0.07	69.68	0.055
1959tt	MRSF	13.86981	96.66	0.09	83.91	0.076
1961tt	MRSF	13.86561	90.08	0.09	77.33	0.066
1962att	MRSF	13.86119	81.91	0.07	69.16	0.054
1965tt	MRSF	13.85468	90.28	0.09	77.53	0.066
1966Att	MRSF	13.84790	91.93	0.09	79.18	0.069
1968tt	MRSF	13.84209	96.67	0.09	83.92	0.076
1970tt	MRSF	13.83485	94.54	0.09	81.79	0.073
1972tt	MRSF	13.82801	84.62	0.08	71.87	0.058
1974tt	MRSF	13.82040	90.64	0.09	77.89	0.067
1977tt	MRSF	13.80595	97.53	0.10	84.78	0.077
1987tt	MRSF	13.78337	101.88	0.10	89.13	0.084
MT20	RIP	13.70394	107.11	0.11	83.22	0.075
MT21	RIP	13.69674	115.04	0.12		
MT22	RIP	13.68954	102.65	0.10	96.97	0.095
MT23	RIP	13.68235	115.30	0.12	96.45	0.095
MT24	RIP	13.67504	98.92	0.10	94.67	0.092
MT25	RIP	13.66772	98.34	0.10	82.94	0.074
MT26	RIP	13.66039	110.65	0.12	94.88	0.092
MT27	RIP	13.65307	93.80	0.09	75.91	0.064
MT28	RIP	13.64574	111.64	0.12	102.27	0.103
MT29	RIP	13.63842	95.18	0.09		
MT30	RIP	13.63109				
MT31	RIP	13.62377	102.18	0.10		
MT33	RIP	13.60911	108.63	0.11		
MT34	RIP	13.60179	106.99	0.11	101.23	0.102
MT35	RIP	13.59446	98.00	0.10	99.86	0.100
MT36	RIP	13.58714	102.05	0.10	102.07	0.103
MT37	RIP	13.57936	112.30	0.12		
MT38	RIP	13.57124	91.51	0.09	81.84	0.073

MT39	RIP	13.56311	86.20	0.08	93.58	0.090
MT40	RIP	13.55499	86.37	0.08	89.47	0.084
MT41	RIP	13.54687	91.98	0.09	96.76	0.095
MT42	RIP	13.53875	95.94	0.09	96.77	0.095
MT43	RIP	13.53062	87.70	0.08		
MT44	RIP	13.51986	90.37	0.09	78.85	0.068
MT45	RIP	13.50783	74.44	0.06	49.39	0.024
MT46	RIP	13.49581	99.45	0.10	81.37	0.072
MT47	RIP	13.48378	103.78	0.11	97.46	0.096
MT48	RIP	13.47175	105.08	0.11	97.47	0.096
MT49	RIP	13.45973	92.66	0.09		
MT50	RIP	13.44776	88.68	0.08	84.71	0.077
MT51	RIP	13.43792	95.73	0.09	89.31	0.084
MT52	RIP	13.42808	84.52	0.08	89.65	0.084
MT53	RIP	13.41982	86.08	0.08	76.99	0.066
MT54	RIP	13.41198	75.75	0.06	46.09	0.020
MT55	RIP	13.40414	86.34	0.08	72.58	0.059
MT57	RIP	13.38846	87.67	0.08	83.37	0.075
MT58	RIP	13.38062	89.60	0.08	88.14	0.082
MT59	RIP	13.37277	86.63	0.08	70.89	0.056
MT60	RIP	13.36493	91.22	0.09	70.72	0.056
MT61	RIP	13.35709	88.66	0.08	80.24	0.070
MT62	RIP	13.34925	92.71	0.09		
MT63	RIP	13.34141	89.88	0.08	65.70	0.049
MT64	RIP	13.33357	87.51	0.08	69.18	0.054
MT65	RIP	13.32573	91.42	0.09	66.17	0.049
MT66	RIP	13.31789	85.57	0.08	73.05	0.060
MT67	RIP	13.31005	94.83	0.09	78.26	0.067
MT68-	RIP	13.30221	85.26	0.08	77.15	0.066
MT69	RIP	13.29437	89.68	0.08	78.63	0.068
MT70	RIP	13.28653	86.07	0.08	66.05	0.049
MT71	RIP	13.27858	85.23	0.08		
MT72	RIP	13.27048	77.39	0.07	55.53	0.034
MT73	RIP	13.26238	89.93	0.08	51.58	0.028
MT74	RIP	13.25428	87.36	0.08	68.88	0.053
MT75	RIP	13.24618				
MT76	RIP	13.23808	84.80	0.08	74.08	0.061
MT77	RIP	13.22998	96.98	0.10	76.13	0.064
MT78	RIP	13.22188	92.02	0.09	79.25	0.069
MT79	RIP	13.21378	91.92	0.09	66.89	0.051
MT80	RIP	13.20568	88.91	0.08	78.54	0.068
MT81	RIP	13.19758	75.36	0.06	67.71	0.052
MT82	RIP	13.18948	94.28	0.09	75.71	0.064
MT83	RIP	13.18132	100.60	0.10	89.52	0.084
MT84	RIP	13.17293	95.19	0.09	73.22	0.060
MT85	RIP	13.16453	112.11	0.12	103.52	0.105

MT86	RIP	13.15614	98.98	0.10	79.48	0.069
MT87	RIP	13.14775	109.83	0.11	85.97	0.079
MT88	RIP	13.13936	108.05	0.11	86.89	0.080
MT89	RIP	13.13096	96.97	0.10	75.94	0.064
MT90	RIP	13.12257	99.99	0.10		
MT92	RIP	13.10578	98.96	0.10	95.58	0.093
MT93	RIP	13.09739	106.54	0.11	88.87	0.083
MT94	RIP	13.08900	105.51	0.11	65.93	0.049
MT95	RIP	13.08061	91.99	0.09	84.13	0.076
MT96	RIP	13.07221	103.20	0.10	89.02	0.083
MT97	RIP	13.06337	108.51	0.11	98.45	0.098
MT98	RIP	13.05340	101.00	0.10	79.29	0.069
MT99	RIP	13.04342	94.61	0.09	78.56	0.068
MT100	RIP	13.03345	89.39	0.08	67.43	0.051
MT101	RIP	13.02217				
MT102	RIP	13.01067	93.58	0.09	92.08	0.088
MT104	RIP	12.98767	84.59	0.08	64.75	0.047
MT105	RIP	12.97617				
MT108	RIP	12.94443	100.05	0.10	83.36	0.075
MT116	RIP	12.86346	119.72	0.13	112.56	0.119